Unravelling the molecular mechanisms of TFAM and mtSSB variants in mitochondrial diseases : a single molecule approach

Martial Martucci

To cite this version:

Martial Martucci. Unravelling the molecular mechanisms of TFAM and mtSSB variants in mitochondrial diseases : a single molecule approach. Biochemistry, Molecular Biology. Université Clermont Auvergne, 2023. English. NNT : 2023UCFA0152 . tel-04608210

HAL Id: tel-04608210
https://theses.hal.science/tel-04608210

Submitted on 11 Jun 2024

UNIVERSITE CLERMONT AUVERGNE

École doctorale des Sciences Fondamentales

THESE DE DOCTORAT

Présenté à l'Université Clermont Auvergne par

Martial MARTUCCI

En vue de l'obtention du grade de Docteur d'Université

Spécialité : **Milieux dilués et optique**

Soutenue publiquement le 14 décembre 2023

Unravelling the molecular mechanisms of TFAM and mtSSB variants in mitochondrial diseases: a single molecule approach

---

Directeurs de thèse :

Dr Siet VAN DEN WILDENBERG (Laboratoire de Physique de Clermont-Ferrand, UMR CNRS 6533; LMV, Université Jean Monnet Saint Etienne, CNRS, IRD, Université Clermont Auvergne)

Dr Géraldine FARGE (Laboratoire de Physique de Clermont-Ferrand, UMR CNRS 6533, Université Clermont Auvergne)

JURY

Rapporteurs

Dr Cécile DELETTRE	DR INSERM, Institut de Neurosciences de Montpellier
Pr Zdenek LANSKY	DR, Institute of Biotechnology, Czech Academy of Sciences

Examinateurs

Dr Laurence VANDEL	DR CNRS, GReD, Université Clermont Auvergne
Président: Pr Jean ORLOFF	PU, LPC, Université Clermont Auvergne

Laboratoire de Physique de Clermont-Ferrand - UMR CNRS 6533 – Université Clermont Auvergne

Remerciements

Tout d’abord, je remercie l’école doctorale des sciences fondamentales au travers de son président M. Heurteaux Yannick et de sa gestionnaire Mme Habouzit Emilie ainsi que le directeur du laboratoire de physique de Clermont-Ferrand (LPCplus) M. Pallin Dominique, pour m’avoir accordé cette thèse et accueilli dans les locaux du laboratoire.

Je remercie également mon chef d’équipe M. Vernet Patrick pour avoir veillé au bon déroulement de ma thèse et pour avoir été une oreille attentive à mon égard. Merci aussi à ma marraine de thèse Mme Faure Géraldine pour avoir suivi avec bienveillance ma thèse.

Je souhaite bien évidemment remercier mes encadrants de thèse M. van den Wildenberg Siet et Mme Farge Géraldine pour m’avoir fait confiance toutes ces années. Merci de m’avoir confié ce magnifique microscope et AFS avec lesquels je me suis épanouie (même si je l’admets, ils n’ont pas toujours été très réceptifs avec moi). Même s’il y a eu des hauts et des bas, merci à vous deux de m’avoir mis à l’aise rapidement à mes débuts et merci de m’avoir épaulé dans la validation de mes expériences et résultats et de m’avoir transmis votre savoir. Vous avez été à la fois rigoureux et sympathique toutes ses années.

Un grand merci également à toute l’équipe. Merci Guillaume Rivrais, Mathilde Lefevbre, Adèle Porcan pour tous les rires, les blagues et de manière générale, merci pour votre bienveillance et bonne humeur au quotidien. Vous êtes les meilleurs coéquipiers qu’on puisse avoir. Merci aussi à Isabelle Balandier et Frédérique Morel et Phillippe Lachaume pour votre bonne humeur et pour votre savoir qui m’a bien aidé. Merci également à Amandine Moretton, Jade Sutter et Thibaut Tabanou pour les gâteaux en salle de pause.

Même si tu n’es plus au labo, j’aimerais te remercier Louis Debar pour avoir été un fidèle ami et pour avoir fait passer ces années de thèses très rapidement.

Merci aux poilus des Cézeaux pour m’avoir changé les idées à chaque balade le soir. Vous êtes des personnes formidables et merci d’être passés sur ma route.

Merci à toute ma famille pour m’avoir soutenu dans mes études et m’avoir donné les clefs de la réussite.

Le meilleur pour la fin, je souhaite te dire Nastasia que tu es la plus belle chose qui me soit arrivé. Je ne sais pas comment te remercier avec des mots. Merci d’être une épouse merveilleuse et merci d’être la meilleure des mamans qui soit. Je te ne remercierai jamais assez d’avoir fait les nuits de nos enfants pour me soulager. Merci de me supporter sans conditions. Merci d’élever nos enfants avec amour et compassion. Un énorme bisou aussi à mon grand garçon d’amour Elyo et ma pupuce chérie Arya. Vous êtes sans le savoir une très grande source de motivation. Je vous aime tous les trois plus grand que la lune, les étoiles, la galaxie et pour toute la vie.

CONTENT

ABBREVIATIONS

TABLE OF FIGURES

ABBREVIATIONS

AAG : Alkyladenine DNA Glycosylases

AAV : Adeno-associated Viral vector

AFM : Atomic Force Microscopy

AFS : Acoustic Force Spectroscopy

AP site : Apurinic or Apyrimidinic site

ATP : Adenosine Triphosphate

BER : Base Excision Repair

BLI : Bio-Layer Interferometry

bp : base pair

CACT : Carnitine-Acyl Carnitine Translocase

CCD : Charge Coupled Device

CSB : Conserved Sequence Box

CTD : Carboxy-Terminal Domain

DNA : Deoxyribonucleic acid

DOA : Dominant Optic Atrophy

DREEM : Dual-Resonance-frequency-Enhanced Electrostatic Force Microscopy

DSB : Double Strand Break

dsDNA : Double stranded DNA

Eco : Escherichia coli

EMCCD : Electron Multiplying Charge Coupled Device

ETC : Electron Transport Chain

FAD : Flavin Adenine Nucleotide

FAO : Fatty Acids Oxidation

Fd : Force detachment

FITC : Fluorescein Isothiocyanate

FJC : Freely Jointed Chain model

Fu : Force unwrapping

FRET : Förster Resonance Energy Transfer

GFP : Green Fluorescent Protein

HMG : High Mobility Group

HR : Homologous Recombination

HsmtSSB : Human Mitochondrial Single Stranded Binding protein

HSP : Heavy Strand Promoter

IDL : Intrinsically Disordered Linker

ITC : Isothermal Calorimetry

kDa : kiloDalton

Lc : Contour Length

LHON : Leber's Hereditary Optic Neuropathy

Lp : Persistence Length

LS : Leigh syndrome

LSP : Light Strand Promoter

MDMD : Mitochondrial DNA Maintenance Defects

MELAS : Mitochondrial Encephalomyopathie Lactic Acidosis and Stroke like episodes

MERRF : Myoclonic Epilepsy with Ragged Red Fibers

MMR : Mismatch Repair

mRNA : RNA messenger

MSD : Mean Squared Displacement

Mt : Mitochondrial

MTERF1 : Mitochondrial Termination Factor 1

NA : Numerical Aperture

NAD : Nicotinamide Adenine Dinucleotide

NER : Nucleotide Excision Repair

NCR : Non Coding Region

NGS : Next-Generation Sequencing

NHEJ : Non-Homologous End Joining

nt : nucleotide

NTE : N-Terminal Extension

NTD : Amino-Terminal Domain

OB : Oligonucleotide/Oligosaccharide Binding

OGG1 : 8-oxo Guanine Glycosylase 1

OriH : Heavy strand Origin of replication

OriL : Light strand Origin of replication

OXPHOS : Oxidative Phosphorylation

PALM : Photo-Activated Localization Microscopy

PEO : Progressive External Ophthalmoplegia

pN : piconewton

PPR : Pentatricopeptide Repeat Domain

PSF : Point Spread Function

RITOLS : Ribonucleotide Incorporation Throughout the Lagging Strand

RMS : Root Mean Square

RNA : Ribonucleic acid

ROS : Reactive Oxygen Species

RPA : Replicative Protein A

rRNA : ribosomal RNA

SDM : Strand Displacement Model

siRNA : small interfering RNA

Sm : Single molecule

SMaRT : Spliceosome Mediated RNA Trans-splicing

SMB : Single Molecular Buffer

SSB : Single Stranded Binding protein

ssDNA : Single stranded DNA

STED : Stimulated Emission Depletion

STORM : Stochastic Optical Reconstruction Microscopy

TALENs : Transcription Activator-Like Effector Nucleases

TAS : Termination Associated Sequence

TCA : Tricarboxylic Acid Cycle

TFAM : Mitochondrial Transcription Factor A

TFB2M : Mitochondrial Transcription Factor B2

TEFM : Mitochondrial Transcription Elongation Factor

TIRF : Total Internal Reflection Fluorescence

TPM : Tethered Particle Motion

tRNA : transfert RNA

UNG : Uracil N-Glycosylase

WES : Whole Exome Sequencing

WLC : extensible Worm Like Chain model

WT : Wild-Type

YFP : Yellow Fluorescent Protein

ZFN : Zinc Finger Nucleases

List of figures & tables

1. INTRODUCTION

1.1. The mitochondria

Mitochondria are essential organelles found in most eukaryotic cells. They are known to be « the powerhouses » that supply cells in energy by producing ATP molecules that the cells use to cover their cellular needs. The average number of mitochondria per cell can vary from hundreds to thousands, depending on the energetic needs of tissues. The mitochondria organelle is composed of two membranes, an outer membrane separating mitochondria from the cytoplasm of the cell and an inner membrane shaped with invaginations called cristae where the aerobic respiration takes place. Although mitochondria conduct ATP synthesis, they are involved in many other cellular pathways including, for example, apoptosis via regulation of cellular calcium and cytochrome C, amino acid and nucleotide metabolism and fatty-acid catabolism (Andrew J. Roger et al., 2017). Moreover, mitochondria possess their own genome localized in the matrix. In humans, mitochondrial DNA is circular and 16 kb of length, encoding only 13 proteins whereas its proteome is estimated at more than 1000 proteins (Nils Wiedemann et al., 2017). This difference illustrates a close link between the cell and the mitochondria where the majority of mitochondrial proteins are in fact synthesized in the nucleus and exported to the mitochondria.

1.1.1. Origin of mitochondria

The origins of the mitochondrial lineages are conventionally associated with a global atmospheric change about two billion years ago (Andersson *et al.*, 2002). At that time, the atmosphere of the Earth was mainly composed of carbon dioxide along with reduced forms of sulphur, nitrogen and carbon with very low concentrations of oxygen. At some point, there was an accumulation of oxygen, presumably from the activity of oceanic photosynthetic cyanobacteria that led to a major crisis for life on Earth, where anaerobic life forms had to find a way to protect themselves from the toxicity of oxygen (Andersson *et al.*, 2002, Rubey 1951, Holland 1994). In 1970, Lynn Margulis published a book entitled « Origin of Eukaryotic Cells » where she proposed that eukaryotic organelles like mitochondria and chloroplasts evolved from endosymbiosis between a bacteria and an eukaryotic cell (Roger *et al.*, 2017). Indeed, the breakthrough of mitochondrial DNA (Nass and Nass, 1963) distinct from nuclear DNA, followed by phylogenetic analyses of mitochondrial genes (Bonen *et at,* 1977) supports that

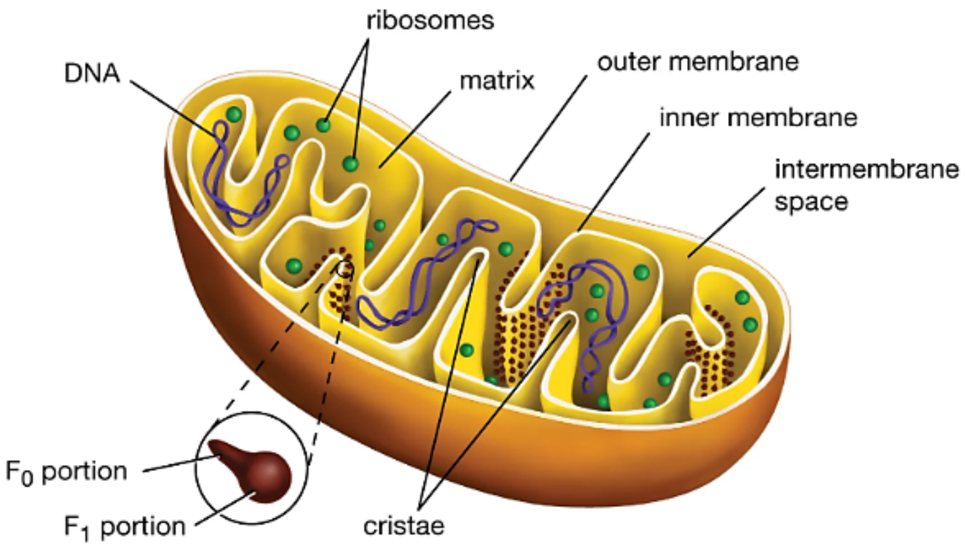

Figure 1: The mitochondria. Cartoon of a cross section of a mitochondria showing the double membranes (the inner membrane forming cristae and the outer membrane) that separate the intermembrane space and the mitochondrial matrix. Mitochondrial DNA resides in the matrix and the electron transport chain symbolised by the ATP synthase (brown pear shape) is anchored in the inner membrane (from: https://www.britannica.com/science/cell-biology/Regulation-of-RNA-after-synthesis).

mitochondria arise from an endosymbiosis between an α-Proteobacterium and an archaeal cell (Grey, 2012).

1.1.2. Structure of mitochondria

In the early 1950s, Sjostrand and Palade used electron microscopy to examine mitochondria, and they concluded that mitochondria contained more than one membrane (Palade 1953, Sjostrand 1953). In Palade's model that is currently depicted in textbooks, mitochondria are two membranes organelles: an outer membrane separates mitochondria from the cell's cytosol, and an inner membrane forming invaginations called mitochondrial cristae that harbor oxydative phosphorylation system (OXPHOS) (**Figure 1**). These two membranes define two internal compartments, the intermembrane space between the outer and inner membrane, and the matrix within the inner membrane where the mitochondrial DNA resides (Frey *et al.*, 2002) and where metabolic pathways of the β-oxidation of fatty acids and the citric acid cycle take place.

As the human mitochondrial proteome consists of about 1500 different proteins and only 13 of those are encoded by the mitochondrial DNA, protein exchanges from cytosol towards mitochondria must occur. Import and sorting of mitochondrial proteins are handled by translocators, which are membrane protein complexes in the outer and inner membrane. For example, the translocator complex TOM40 and TOB/SAM are localized in the outer membrane, whereas TIM 22 and TIM23 are localized in the inner membrane, and Mia40/TIM401-Erv1 in the intermembrane space (Endo 2009, Wiedemann *et al.,* 2017). Mitochondrial proteins synthesized in the cytosol hold a specific amino acids sequence at their N-terminal region called mitochondrial targeting sequence that enables them to move through the membranes via the translocators (Omura *et al.*, 1998).

The number of mitochondria present in a cell depends on the cellular energetic needs. However, they should not be taken as a single unit, but instead they form a so-called « mitochondrial network » within the cell. This network is the result of a dynamic equilibrium between fusion and fission. Indeed, mitochondria can fuse (referred as fusion) or split (referred as fission) in order to regulate their number, subcellular distribution, morphology and function. Similarly, the mitochondrial content of a cell arises from the balance between mitochondrial biogenesis and mitochondrial degradation (Meyer *et al.,* 2017).

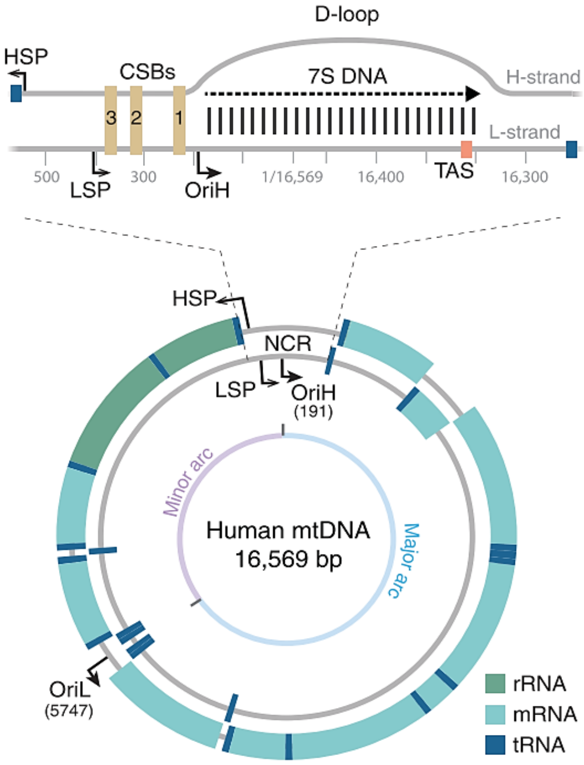

Figure 2: Structure of the human mitochondrial genome. Mitochondrial genome is circular and 16.6 kbp long. It is composed of an heavy strand (H-strand, outer circle) and a light strand (L-strand, inner circle) that both harbour a promoter sequence HSP and LSP as well as an origin of replication OriH and OriL for the corresponding H and L strand. The non-coding region (NCR) is represented at the top (extracted from Falkenberg and Gustafsson, 2020).

1.1.3. The mammalian mitochondrial genome

Mitochondria possess their own genome, and genome replication is independent of the cell life cycle. MtDNA is a circular double-stranded supercoiled genome of 16,6 kbp (Boore, 1999), and it is thus relatively small compared to the 3 billion base pairs of the human genome. The mtDNA is packed into nucleoprotein complexes called nucleoids that are anchored to the inner membrane on the matrix side. The proteins bound to the mtDNA are involved in its maintenance and expression. Nucleoids are found in multiple copies inside mitochondria, and the estimated number of mtDNA molecules per nucleoid is approximately 1.4 in human cells and 1.1-1.5 in mouse cells, suggesting that it often contains only a single mtDNA molecule. Since a cell contains multiple mitochondria, it has been shown that, for example, a human fibroblast can contain around 1880 nucleoids leading to around 2721 mtDNA copies that are evenly distributed in the cell (Kukat et al., 2011).

mtDNA contains 37 genes of which 13 encode subunit proteins of the ETC complexes, 22 transfer RNA (tRNA) genes, and 2 ribosomal RNA (rRNA) genes (Boore, 1999). Despite this low amount of proteins encoded by mtDNA that are essential for the OXPHOS system, it has been estimated that mitochondria contain approximately 1200 proteins of which several hundred are involved in mtDNA expression, thus highlighting the important number of nuclear encoded proteins and the exchange between the cytosol and the mitochondria (Gustafsson et al., 2016). The two strands of the mtDNA have a different nucleotide distribution, one strand is richer in guanine and is referred to as the heavy strand (H), the other one is referred to as the light strand (L), their different weights makes it possible to separate the strands by density centrifugation (**Figure 2**). A control region of 1 kbp called NCR for non-coding region harbours the H and L strand promoters for initiating the polycistronic transcription of mtDNA, the origin of the H-strand replication (OriH), as well as a number of conserved sequence boxes (CSB) and the termination associated sequence (TAS) involved in event regulation. Within the NCR, there is an approximately 650 nt long DNA sequence called 7S DNA that forms a triple strand DNA region called the D-loop that its function still remains unclear. Instead, the origin of the L-strand replication (OriL) is localized 11 kbp downstream of OriH, thus dividing the mtDNA into two parts: the major and minor arcs (Ayman et al., 2017, Falkenberg and Gustafsson, 2020).

1.2. Metabolism

1.2.1. Krebs cycle and β-oxidation pathway

Fatty acids are one of the substrates an organism can use to generate energy. To this end, fatty acids are degraded via an oxidation pathway called « Fatty acids oxidation FAO » or β-oxidation pathway. The oxidation of fatty acids takes place in mitochondria where the oxidation of the long fatty acid carbon chain results in its shortening on carbon β releasing an acetyl-CoA and an acid with two carbons in less. Fatty acids cannot penetrate the mitochondrial outer membrane, therefore they have to be activated in the cytosol of the cell requiring energy to form acyl-coAs and then enter the mitochondria using the carnitine-acyl carnitine translocase (CACT) (Bartlett and Eaton, 2004). During the import, an acyl-CoA is converted in an acyl-carnitine via a outer membrane protein (CPT1), then enter the mitochondria via CACT in exchange of a free carnitine, and finally is reconverted by an inner membrane protein (CPT2) in acyl-CoA that can undergo FAO. The oxidation proceeds in four enzymatic reactions : (i) an acyl-CoA ester is dehydrogenated into a trans-2-enoyl-CoA, reducing a flavin adenine nucleotide (FAD) into $FADH_2$, (ii) then it is hydrated to form a L-β-hydroxyacyl CoA, (iii) followed by the oxidation of L-β-hydroxyacyl CoA by a dehydrogenase releasing a β-ketoacyl-Coa and a nicotinamide adenine dinucleotide (NADH), (iiii) finally thiolytic cleavage of β-ketoacyl-Coa releases a two-carbon chain-shortened acyl-CoA that will undergo another cycle plus an acetyl-CoA that will enter the citric acid cycle (Houten and Wanders, 2010).

Acetyl-CoA molecules are at the center of metabolic crossroads. Indeed, during glycolysis, glucose is oxidized in the cytosol via a number of enzymatic reactions in pyruvate that is further oxidized in acetyl-CoA in the mitochondria, a process during which ATP and NADH is generated. In FAO, fatty acids are degraded in mitochondria to form acetyl-CoA and some amino acids metabolic pathways are also oxidized to generate acetyl-CoA. In the mitochondrial matrix, an acetyl-CoA will enter the citric acids cycle (also known as Krebs cycle or tricarboxylic acid cycle TCA) in which a total of eight enzymatic reactions per cycle will lead to the formation of two CO_2, three NADH, two $FADH_2$ and one GTP (Judge and Dodd, 2020). NADH and FADH2 cofactors will provide electrons to the electron transport chain (ETC) localized in the inner membrane that will serve to produce ATP by the ATP synthase via oxidative phosphorylation (OXPHOS) (van der Bliek *et al.*, 2017).

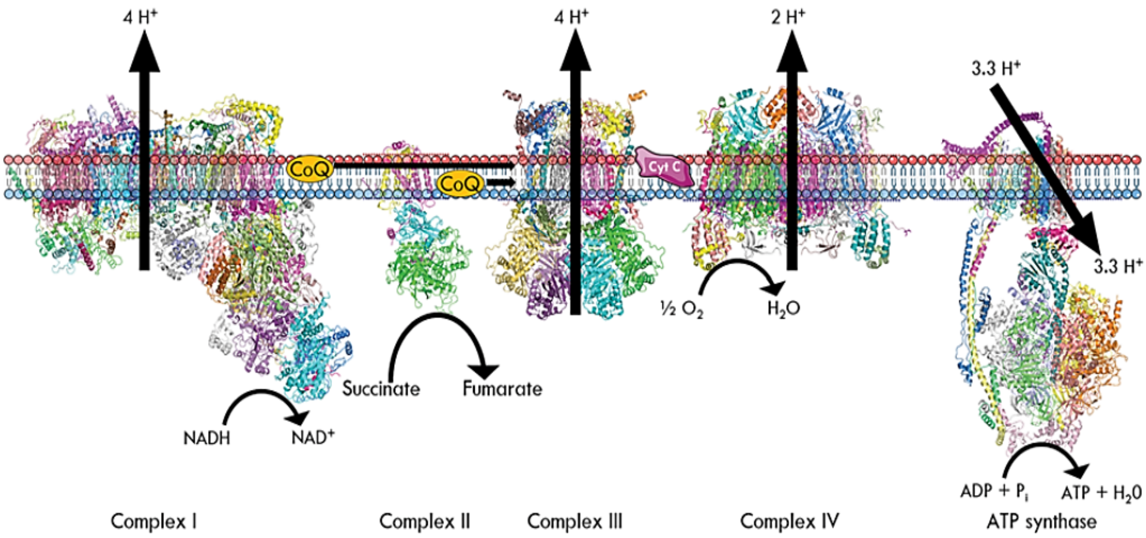

Figure 3: Electron transport chain (ETC). Reduced cofactors NADH and FADH2 from glycolysis, TCA and FAO are oxidized by the ETC. Electrons are transported through a series of complexes (I-IV) to a final electron acceptor that is oxygen. Electron transport is coupled to the translocation of protons that generates an electrochemical gradient between the intermembrane space and the matrix, this gradient is used by the ATP synthase to synthesize ATP (from Judge and Dodd, 2020).

1.2.2. Oxidative phosphorylation (OXPHOS)

Oxidation of molecules that occur during catabolism processes such as glycolysis, β-fatty acids oxidation or citric acid cycle is used to generates ATP molecules that can directly be used to fuel reactions, but these oxidations also reduce cofactors such as NADH or FADH2 which are high energy potential electron carrier that will give its electrons to the electron transport chain (ETC) localized in the mitochondrial inner membrane (van der Bliek et al., 2017). Oxidative phosphorylation encompass both the ETC and the ATP synthase (**Figure 3**). Electrons are transported through a serie of complexes (I-IV) to a final electron acceptor that is oxygen. As electrons flow through the complexes, they lost potential energy that is used by complexes to pump protons from the matrix to the inter membrane space. As the inner membrane is impermeable to protons, an electrochemical gradient is created, that drives ATP synthesis by the ATP synthase with phosphorylation of ADP into ATP, with formation of H2O in the matrix (Judge and Dodd, 2020). As said, the ETC is composed of four protein complexes plus the ATP synthase. Complex I or NADH-Ubiquinone oxidoreductase (sometimes named NADH dehydrogenase) is a 44 subunit complex of which seven are encoded by mtDNA. It catalyses the oxidation of NADH,H+, transferring two electrons to the ubiquinone (or coenzyme Q) coupled with the translocation of four protons to the inter membrane space. Complex II or Succinate-Ubiquinone oxidoreductase is the only complex that is entirely nuclear encoded. It is a small complex (4 subunits) that catalyses the oxidation of succinate to fumarate in the TCA cycle, but also transfers electrons from FAD to another Q without pumping protons through the inner membrane. Complex III or Ubiquinol-Cytochrome C oxidoreductase is a 11 subunits complex with only one subunit (Cytochrome b) is encoded by mtDNA and in which the oxidation of ubiquinol takes place. Electrons from ubiquinol oxidation are transferred to cytochrome c coupled with the translocation of four protons in the inter membrane space. Finally, complex IV or Cytochrome c oxidase is composed of 14 subunits of which COX1, COX2 and COX3 are the mitochondrial genome encoded catalytic subunits. It transfers electrons from cytochrome c to a final electron acceptor, the oxygen, reducing it in H_2O plus translocating four protons. Hence, the electrochemical gradient that is formed by the differential H^+ concentrations between the matrix and the inter membrane space generates potential energy that is used by the ATP synthase to phosphorylate ADP + P_i to ATP (Xin Tang *et al.*, 2020).

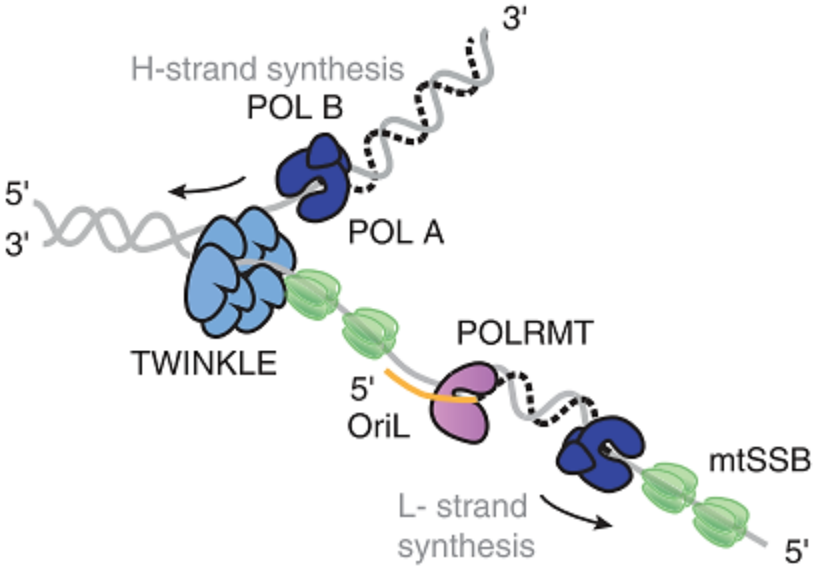

Figure 4: The mtDNA replication fork. The helicase TWINKLE (light blue) leads the unwinding of the dsDNA in the 5'-3' direction. mtSSB (green) binds to ssDNA and stimulates POLγ (dark blue) DNA synthesis. POLRMT (purple) synthesizes the RNA primers needed for the replication initiation of POLγ (from Falkenberg and Gustafsson, 2020).

1.3. Mitochondrial replication and repair

1.3.1. mtDNA replication factors

Mammalian mtDNA is replicated by replication factors that are different from those that are needed for nuclear DNA replication, although they have a nuclear origin. Many are related to replication factors that belong to the bacteriophage family such as the replicative mitochondrial polymerase POLγ, the helicase TWINKLE or the RNA polymerase POLRMT (Gustafsson *et al.*, 2016). Both H and L strand synthesis is only performed by POLγ which is a heterotrimer composed of two accessory subunits (POLγB) of 55 kDa and one catalytic subunit (POLγA) of 140 kDa. However, it should be noticed that the structure of POLγ varies depending on the species. For instance, in *Drosophila melanogaster* POLγ is a heterodimer, whereas only POLγA is found in *Saccharomyces cerevisiae* (Ravichandran et al.. 2004; Fan et al.. 2006). The polymerase also harbours a 3'-5' exonuclease activity that is useful for proofreading and thus possesses a high accuracy with a frequency of misincorporation lower than 10^{-6} (Falkenberg, 2018). However in order to initiate mtDNA synthesis, POLγ needs a RNA primer as starting template (Fusté *et al.*, 2010). This primer is synthesized by POLRMT, which is involved in the mtDNA transcription (Gaspari *et al.,* 2004, Wanrooij *et al.,* 2008). Moreover, POLγ is unable to progress on dsDNA and the mitochondrial helicase TWINKLE is required to unwind the mtDNA (Korhonen *et al.*, 2003). TWINKLE forms a hexamer of 420 kDa that unwinds dsDNA in the 5'-3' direction requiring a fork structure (**Figure 4)** (Falkenberg and Gustafsson, 2020).

Another essential factor in mtDNA replication is the mitochondrial single stranded binding protein (mtSSB). mtSSB is a homotetramer of 60 kDa that binds to ssDNA during the replication process. It prevents reannealing and degradation of the displaced strand, but also enhances mtDNA replication by stimulating TWINKLE activity and improving the processivity of POLγ at the replication fork (mtSSB will be treated at section 1.7). At the replication fork, TWINKLE uses energy to unwind dsDNA followed by POLγ that synthesises the nascent strand that is bound by mtSSB to protect it against nucleases and prevent secondary structure formation (Falkenberg 2018).

1.3.2. Strand displacement model of replication

A model for mtDNA replication was proposed in 1972 by Vinograd and co-workers. In this model, DNA synthesis occurs continuously on both H and L strand, where the H strand is displaced to initiate the replication; this model is thus called the strand displacement model of replication (SDM) (Robberson *et al.*, 1972). As mentioned above, both strands have their own origin of replication: OriH for the heavy strand and OriL for the light strand. Replication first begins at OriH that is localized in the NCR region. To start replication, the transcription machinery initiates transcription at LSP. POLRMT synthesises a short RNA and passes by CSB2 that is a G-rich conserved sequence. During transcription of CSB2, the RNA folds into a G-quadruplex structure with non-template DNA forming a stable hybrid RNA-DNA triple-stranded structure, referred to as R-loop (Wanrooij *et al.,* 2012). The R-loop structure causes the POLRMT to dissociate, leading to a premature transcription termination just downstream of the CSB2 region. However, POLγ cannot use the R-loop to initiate replication because the 3' end is inaccessible (Posse *et al.*, 2019). Therefore, it was proposed that the R-loop is processed by the nuclease RNase H1. RNase H1 can cleave the R-loop both in vitro and in vivo and the 3'end can be used by POLγ to start DNA synthesis (Posse *et al.*, 2019). Once DNA synthesis is started, only a few replication events reach full length mtDNA. Indeed, about 95% of all events are prematurely terminated after about 650 nt at a conserved sequence in the NCR region named TAS (termination associated sequence) (Nicholls and Minczuk, 2014; Bogenhagen and Clayton, 1978; Doda *et al.*, 1981). This results in a short DNA sequence of approximately 650 bases long that is called 7S DNA, which remains annealed to the parental DNA forming a triple-stranded displacement loop referred to as the D-loop (**cf Figure 2**). The role of the D-loop in mtDNA maintenance is not well understood. It was proposed to be an aborted product of nascent H strand synthesis and or could serve as a regulator to control the amount of events that reach full mtDNA replication, and thus the number of mtDNA molecules (Ruhanen *et al.*, 2010; Jemt *et al.*, 2015). Although it is still not clearly understood how the abundance of 7S DNA is determined nor monitored, it was shown that knockdown of mtSSB in HeLa cells caused a severe and rapid decrease of 7S DNA synthesis, suggesting that mtSSB is involved in the regulation of the D-loop (Ruhanen *et al.*, 2010). Interestingly, a recent study with a mtSSB variant (R107Q) has been shown to impaired replication initiation (Jiang *et al.*, 2021), that may support that 7S DNA could play a role in mtDNA replication regulation.

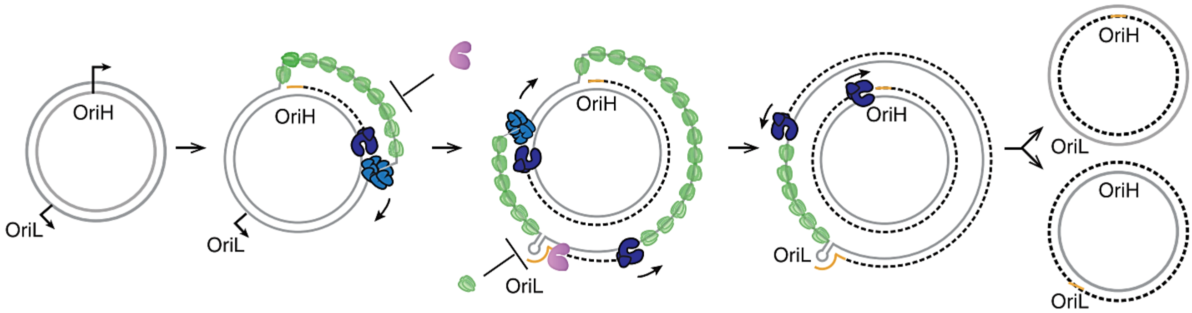

Figure 5: Strand-displacement mtDNA replication. Replication of the nascent H-strand is initiated at OriH and proceeds unidirectionally from 5’ to 3’. The parental H-strand is displaced and bound by mtSSB. Upon reaching the OriL, the H-strand folds into a stem-loop structure that is used by POLRMT to prime L-strand synthesis by POLγ until full-circle and two new full-length circular daughter molecules are formed (from Falkenbeg and Gustafsson, 2020).

During the replication elongation, TWINKLE moves on the parental H-strand and unwinds mtDNA, of which the single stranded L-strand is covered by mtSSB. TWINKLE is followed by POLγ that continuously synthesises a H-strand copy until reaching OriL 11000 bp downstream OriH (Gustafsson *et al.*, 2016). At this moment, OriL becomes single-stranded and folds into a stem loop structure (an 11 bp stem and a 12 nt loop) (Fuste *et al.*, 2010; Falkenberg and Gustafsson, 2020). This stem-loop structure can be used by POLRMT to start RNA synthesis that will serve to prime POLγ to start L-strand synthesis (**Figure 5**) (Fuste *et al.*, 2010) Note that the mechanism of replication of the H and L strand is different. Indeed, during H strand synthesis, the template is dsDNA that needs to be unwind by TWINKLE. In contrast, the L strand synthesis uses a single stranded template that does not need the intervention of TWINKLE and during the processing of POLγ, mtSSB has to be displaced (Falkenberg and Gustafsson, 2020). Also, because the L-strand synthesis uses a single stranded template, the POLRMT processivity is low and it dissociates after about 25 nt, that favours the synthesis of primers for POLγ, and thus mtDNA synthesis and not transcription events (Wanrooij *et al.*, 2008).

Two other alternative modes of replication have been proposed based on the observation in certain cell-types of other replication intermediates. One of these models is the RITOLS model for Ribonucleotide Incorporation Throughout the Lagging Strand, which proposes that RNA molecules (rRNA, tRNA and mRNA with its poly A tails) cover the displaced H-strand by hybridation during mtDNA replication (Yasukawa *et al.*, 2006; Reyes *et al.*, 2013). The other model is the Strand-coupled model, which suggests that L-strand synthesis starts at multiple locations on the parental H-strand (Holt et al., 2000). These two models are still strongly debated therefore, I will not detail them more, as also they minimise the involvement of mtSSB in the replication process.

1.3.3. Replication termination

In order to finish a complete replication, the two daughter molecules have to be ligated at the two origins of replication and separated. In addition, prior to ligation, all RNA primers have to be removed and the gaps have to be filled by POLγ until the 3' end of the nascent DNA reaches the 5' end. They then can be ligated by the mitochondrial Ligase 3 (Lakshmipathy *et al.*, 1999). However, mechanisms of primer removal at OriH and OriL are not similar but in both is involved RNase H1 (Holmes *et al.*, 2015).

At OriL, primers are almost entirely removed by RNase H1, however 1-3 ribonucleotides are left behind the 5' junction and this still impaired ligation (Holmes *et al.*, 2015; Uhler *et al.*, 2016). Therefore, another nuclease should intervene in order to process these remaining nucleotides. Moreover, since POLγ normally synthesizes a few nucleotides into duplex regions, the 5' end substrate that needs to be ligated should be a flap end, thus the missing nuclease may be a flap nuclease (Falkenberg and Gustafsson, 2020). EXOG was proposed to be this missing nuclease as it has a mitochondrial localization and it has been shown the protein could efficiently remove the last ribonucleotides at OriL *in vitro* (Wu *et al.,* 2019).

At OriH, primers are processed by two nucleases: MGME, which belongs to the RecB family and displays a strong preference for ssDNA, and RNaseH1. RNAseH1 removes the primers the same way as at OriL, leaving 1-3 ribonucleotides. In a second step, the nuclease MGME1 removes the remaining ribonucleotides and a stretch of the nascent 5' end. It can cleave flaps ends and also RNA-DNA flaps that are long enough (2-5 nt) (Uhler *et al.*, 2016; Falkenberg and Gustafsson, 2020). However, how the nascent strand is displaced in order to be processed by MGME1 has not been reported yet. Finally, after ligation by Ligase 3 the two daughter molecules are separated by the topoisomerase TOP3A via the formation of a hemicatenane intermediate in the OriH region (Nicholls *et al.*, 2018).

1.3.4. Existing repair mechanisms and mtDNA degradation

As mentioned in the above section, nucleic acids can be damaged by various chemical or physical agents, for example reactive oxygen species (ROS) which are highly reactive molecules formed from diatomic oxygen (O2) or UV light and radiation for an example of physical agent. ROS are especially present in the mitochondria due to the oxidative phosphorylation in the matrix where the mtDNA resides. Therefore, the environment in which mtDNA is processed could be at the origin of mtDNA damages such as point mutations or strand breaks. It is also important to note that mtDNA is continuously replicated independently of the cell cycle, increasing the chances of mtDNA to be damaged. In the nucleus, DNA damages can be repaired by several complexes and robust repair mechanisms such as base excision repair (BER), nucleotide excision repair (NER) or mismatch repair (MMR) for multiple base damages or single-strand break and double-strand break repair such as homologous recombination (HR) or non-homologous end joining (NHEJ) (Chatterjee *et al.*, 2017).

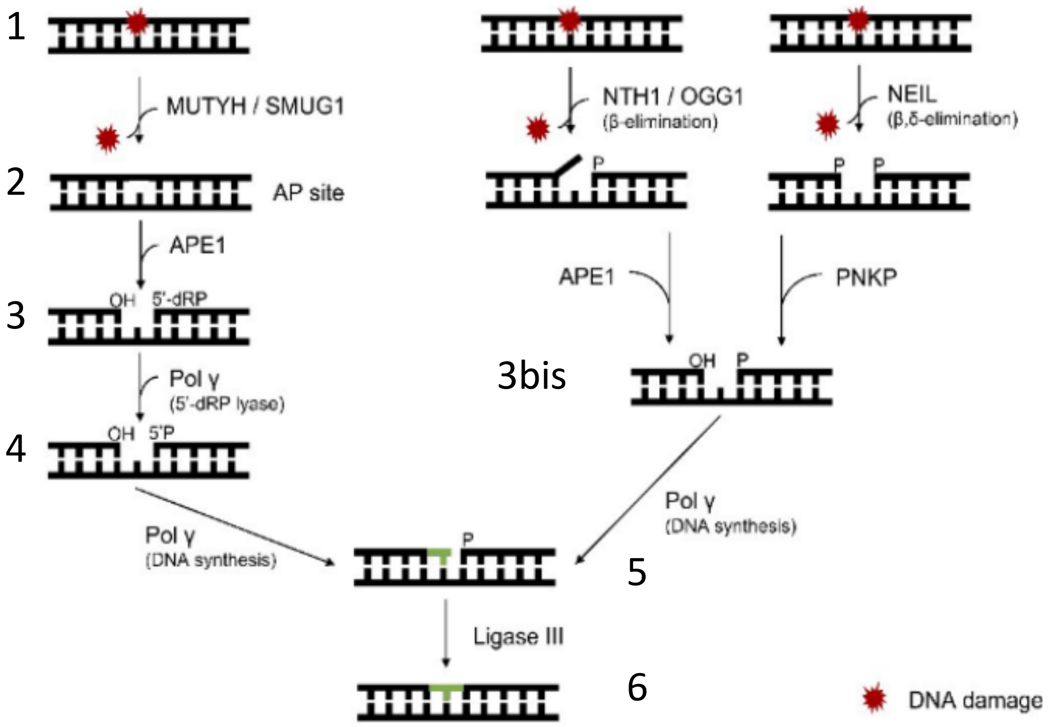

Figure 6: The Base excision repair (BER) mechanism in mitochondria. (**1**) First, glycosylases target and remove the damage base, resulting is the formation of an AP site. Depending on the DNA damage (alkylation, deamination or oxidation), there are different types of glycosylases that will be involved. Also, two types of glycosylases exist, mono (left panel) and bifunctional (right panel), of which the last harbour an AP endonuclease activity. (**2**) An AP site is generated in the case of monofunctional glycosylases. Bifunctional glycosylases, on the contrary, create a gap in the strand. (**3**) The AP site is incised by AP endonuclease APE1. (**3bis**) The AP site is processed by APE1 or polynucleotide kinase 3'-phosphatase PNKP to generate 3'OH end in the case of bifunctional glycosylase repair. (**4**) Polγ processes the 5' end in the case of monofunctional glycosylase repair. (**5**) Polγ incorpores newly nucleotides to fill the gap. (**6**) The ligation is performed by Ligase III (Drawing comes from Boguszewska et al, 2020).

The BER mechanism is the only repair mechanism that has been comprehensively characterised in mitochondria (**Figure 6**). It is a repair pathway that is also present in the nucleus and repairs non-bulky lesions generated by oxidation, deamination, and alkylation. The removal of the damaged base is carried out by glycosylases that are exported to the mitochondria (Prakash and Doublié, 2015). Glycosylases can recognize and clip damaged bases from DNA phosphodiester backbone depending on the nature of the damage, for instance 8-oxo Guanine glycosylase 1 (OGG1) for oxidative damages, Uracil N-glycosylase (UNG1) for uracil misincorporation, or Alkyladenine DNA glycosylases (AAG) that recognize alkylated and deaminated DNA bases like 3-methyladenine and hypoxanthine. The removal of the damage base leaves an apurinic or apyrimidinic site (AP site). Then, an AP endonucleases enzyme cleaves the phosphodiester backbone at the AP site, which leaves a 3' OH end that provides a starting point for POLG to fill the gap. Ligation is carried out by Ligase III that ends the process. Note that Glycosylases involved oxidative damages repair are bifunctional and possess an associated lyase activity whereas it is not the case for glycosylases involved in alkylated and deaminated damages (Prakash and Doublié, 2015). TFAM has been suggested to be involved in the BER mechanism by modulating BER activity via DNA binding. Indeed, it was found *in vitro* and in cell-based assays, using TFAM knockdown and binding-defective TFAM mutant, that TFAM binds preferentially oxidatively damaged DNA but inhibits BER activity by limiting access to DNA to BER proteins. Repair could thus be affected by modulation of the TFAM/DNA affinity by interacting proteins like the tumour suppressor protein p53 (Canugovi *et al.*, 2010).

Other mtDNA repair mechanisms have been shown to take place within mitochondria. For example, in mitochondria from *Saccharomyces cerevisiae*, DSBs can be repaired by HR (Stein *et al.*, 2015). Nevertheless, it is still not clear if DSBs repair exists in mammalian mitochondria, but as discussed in section 1.5.1, mtDNA rearrangements have been observed after DSBs induction coupled with knockdown of nucleases supposed to play a role in linear fragment degradation (Peeva *et al.*, 2018, Nissanka *et al.*, 2018). This suggests that a rudimentary end-joining repair mechanism could take place in mammalian mitochondria if damaged mtDNA are not rapidly degraded or it could be as simple as a ligation of the free ends by Ligase III (Nissanka *et al.*, 2019).

In mammalian mitochondria, unlike in the nucleus, heavily damaged mtDNA molecules (like strand breaks) often undergo a rapid degradation (Bayona-Bafaluy *et al.*, 2005; Moretton *et al..,* 2017). Indeed, the multicopy feature of mtDNA allows the degradation of damaged mtDNA molecules without generating issues within the mitochondria. As mentioned before, the degradation pathway could be less energetic than a complex repair mechanism, preferring to replicate healthy mtDNA copies (Nissanka *et al.*, 2019). Actors of the degradation of linear mtDNA have not been clearly highlighted yet, but studies have evidenced that gene silencing of POLγ, Twinkle and MGME1 nucleases impact the degradation of mtDNA molecules (Peeva *et al.*, 2018, Nissanka *et al.*, 2018). Indeed, it has been shown that mtDNA molecules in which a DSB occurred are rapidly degraded as linear fragments resulting from DSB are only seen during the first 2 hours but the actors involved in the degradation were not identified (Bayona-Bafaluy *et al.*, 2005). Attempts to identify these actors were conducted with *in vitro* model of mitochondrial-targeted restriction endonuclease (*Pst1*) induced DSBs coupled with knockdown of nucleases such as MGME1, DNA2, EXOG, ENDOG or FEN1 (Moretton *et al.*, 2017). However, a similar study using a comparable *in vitro* system observed a delayed mtDNA fragment degradation 4 hours after the induction of the DSB in MGME1 knockdown cells, as well as in POLG and TWINKLE knockdowns (Peeva *et al.*, 2018). Authors also observed a delayed degradation up to 18 hours in cells that are either deficient for MGME1 or expressed a mutant version of POLγ that has lost its 3'-5' exonuclease activity. These results suggest that MGME1, Twinkle and POLγ may be involved in mtDNA degradation in addition to their role in mtDNA replication. Moreover, as the degradation process was disturbed in this study, mtDNA rearrangements were observed by PCR analysis across the breakpoints. Other studies support that in some instances, DSBs could be re-ligated by an end-joining activity within the mammalian mitochondria, resulting in rearranged molecules that harbour a deletion (Nissanka *et al.*, 2019). Therefore, DSBs could be a mechanism by which mtDNA deletion could be generated.

1.4. Mitochondrial transcription

1.4.1. Transcription factors

Mitochondrial transcription machinery is composed of several proteins that are translated in the cytosol and exported into the mitochondria. The main proteins involved in mtDNA transcription are the mitochondrial RNA polymerase POLRMT, the mitochondrial transcription factor A (TFAM), B2 (TFB2M), the mitochondrial elongation factor (TEFM), and the mitochondrial termination factor 1 (MTERF1) (Gaspari *et al.,* 2004; Gustafsson and Falkenberg, 2016).

Mitochondrial RNA polymerase POLRMT is a 130 kDa protein that belongs to the polymerase A family and is related to phage T7 RNA polymerase, which can open DNA and initiate transcription by itself instead of mitochondrial one that needs two transcription factors (TFAM and TFB2M) (Cheetham et al., 1999; Hillen 2017). Indeed, in a recombinant in vitro transcription system, both transcription factors act synergistically and increase transcription efficiency 100-200-fold as compared with POLRMT alone (Litonin et al., 2010). POLRMT contains a carboxy-terminal domain (CTD), which is the catalytic domain that is conserved in all single-stranded RNA polymerases, an amino-terminal domain (NTD), a pentatricopeptide repeat domain (PPR) which serves to bind RNA, and a flexible N-terminal extension (NTE) (Ringel et al., 2011). Its NTD is involved in the separation of RNA from DNA during transcription elongation, this is different from the T7 NTD which contains an intercalating hairpin like structure which melts DNA during transcription initiation. Moreover, the NTE domain is a specificity of the POLRMT structure that is not found in phage polymerases (Gustafsson et al., 2016). This NTE is involved in POLRMT recruitment on promoters as it interacts with the transcription factor A (TFAM) that recognizes upstream promoter sequences (14-35 bp upstream LSP transcription start site) and thus stabilizes the polymerase on DNA (Hillen et al., 2017).

TFAM is a 24 kDa protein of 246 amino acids that is exported to the mitochondrial matrix. TFAM is the most abundant protein that composed the mitochondrial nucleoid (1 TFAM per 16-17 bp of mtDNA in mammalian cells), and it is thus considered as one of the core components of the mitochondrial nucleoid (Farge and Falkenberg, 2019). TFAM belongs to the High Mobility Group (HMG) proteins, which are subdivided in three groups, HMG-A, HMG-box (HMGB) and HMG-N. They are abundant and ubiquitous DNA binding proteins

within cells that intervene in the DNA maintenance process, in which TFAM belongs to the HMGB group (Malarkey and Churchill, 2012). The functions and mechanisms of TFAM will be described in detail in section 1.6. Another transcription factor is required to initiate mtDNA transcription: TFB2M. Its role is to melt the promoter where POLRMT is bound and stabilise the open DNA strand (Litonin et al., 2010). TFB2M as well as its homologous TFB1M are related to methyltransferase that are required to methylate 12 S rRNA, a component of mitochondrial ribosomes. However, instead of TFB2M, TFB1M has conserved its methyltransferase activity and in vitro studies report that it stimulates transcription initiation 10-100 fold less than TFB2M , thus supporting its non-involvement in mtDNA transcription. Finally, transcription elongation and termination are handled by TEFM and MTERF, respectively. TEFM has been proposed to regulate the switch between transcription termination to prime POLγ for replication initiation and processive near genome-length mtDNA transcription, but it may also be involved in mtRNA processing as it can interact with multiple RNA processing factors (Agaronyan et al., 2015; Jian et al., 2019). Indeed, in mouse heart cells in which TEFM has been knockout, the levels of promoter-distal mitochondrial transcripts drastically decreased and promoter-distal transcripts are increased but they mostly terminated before the switch region between transcription and replication, reducing also the levels of mtDNA replication. Moreover, in addition to impaired transcription elongation, there was also an accumulation of unprocessed transcripts (Jian et al., 2019). Dynamics studies proposed that TEFM enhances transcription elongation by modifying mtRNAP pausing dynamics by enhancing the stall force of mtRNAP and by reducing the polymerase long-pauses frequency and shortening their durations (Yu et al., 2018). On another hand, the polyadenylated non coding 7S RNA molecule has been shown, using cryo-EM, to act like a negative regulation factor of transcription initiation by inducing POLRMT dimerization upon interaction by the polymerase with 7S RNA, and that POLRMT no longer can recognize promoter sequence in a dimer form (Zhu *et al.*, 2022).

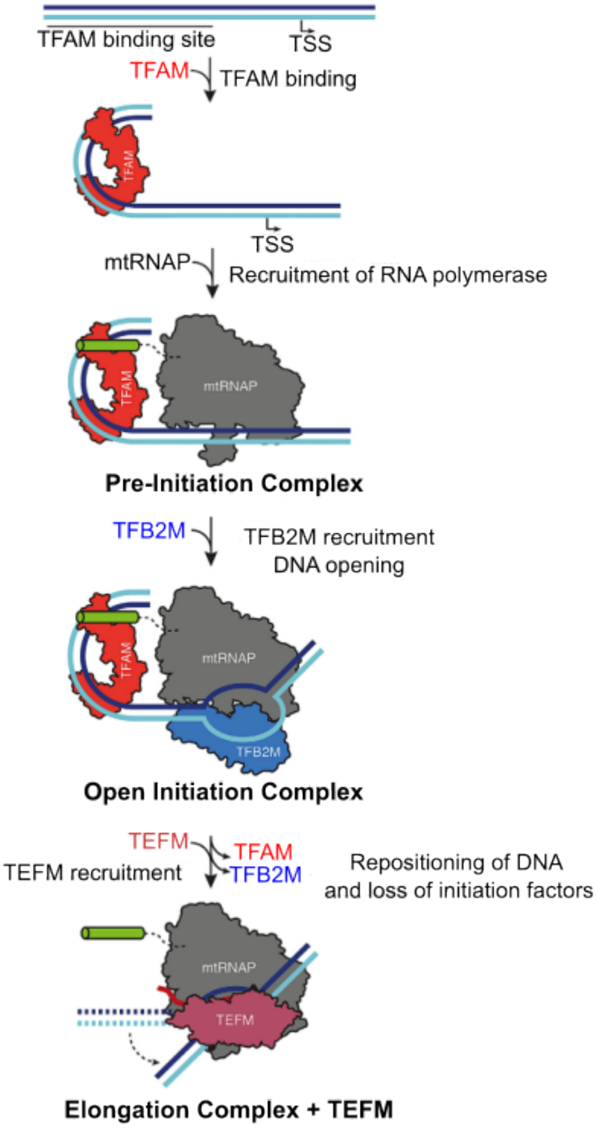

Figure 7: Model for transcription initiation in human mitochondria. TFAM binds DNA and bends it at 180° and recruits the RNA polymerase (mtRNAP) to form the pre-initiation complex. Next, TFB2M is recruited and assists mtRNAP in opening DNA. Then TFAM and TFB2M dissociate and TEFM interacts with mtRNAP to form the elongation complex. How transcription termination is regulated is still not clear but MTERF is proposed to be involved in the process (from Hillen *et al*, 2017).

1.4.2. Transcription overview

Mitochondrial transcription leads to the formation of two long polycistronic transcripts without introns that correspond to the transcription of the heavy and light strand, starting at the promoters HSP and LSP both localized in the NCR region (Gustafsson *et al.*, 2016). However, an additional light strand promoter LSP2 has been recently found in the human mitochondrial genome at the NCR 3' end, that questions the consensus that mitochondrial replication primers and transcription both arise from a single LSP (Tan *et al.*, 2022). LSP2 will not be discussed thereafter. Transcription initiation starts by the recognition of promoters by TFAM, at 16-39 nt upstream of the transcription start site (TSS). TFAM bends the DNA backbone and induces a 180° turn, i.e. U-turn (**Figure 7**) (Ngo et al., 2011; Rubio-Cosials et al., 2011). Next, TFAM recruits POLRMT and anchors it to the promoter region via the interaction of the HMG Box B domain with the N-terminal tail of POLRMT that is called "the tether helix" (Hillen et al., 2017). Then TFB2M is recruited and assists POLRMT in opening the DNA. TFB2M induces conformational changes in the polymerase that stabilizes it and helps its intercalating hairpin to open the DNA. Moreover, TFB2M traps the non-template DNA strand to further help in the opening of DNA (Hillen et al., 2017). Finally, the transition between initiation and elongation occurs via a DNA rearrangement instead of a conformational change of the mtRNAP like it is the case for T7 RNAP (Yin and Steitz, 2002; Schwinghammer et al., 2013). During this process, TFB2M and TFAM dissociate and TEFM interacts with POLRMT to start the elongation as it increases POLRMT processivity (Posse et al. 2015). A protein, MTERF1 for mitochondrial termination factor 1 has been proposed to be involved in this process (Terzioglu et al., 2013; Asin-Cayuela et al., 2005) in *in vitro* assays. The transcription termination could occur by MTERF1 with a base flipping stepwise fashion (Byrnes et al., 2016). However, *in vivo* studies with knockout MTERF1 in human and mouse cells revealed that steady-state levels of rRNA and mRNA transcripts from HSP remained unchanged and that relative RNA levels between rRNA and mRNA could rather be explained by differences in stability. Moreover, knockout mouse model showed that MTERF1 prevents antisense transcription from entering the rRNA region (Shi et al., 2016). Therefore, MTERF1 may be involved in LSP transcription termination but may not be involved in termination from HSP. Overall, mechanisms for transcription termination are still unclear.

1.5. Mitochondrial defects and associated pathologies

1.5.1. Mitochondrial diseases and therapies

Due to the ubiquitous feature of mitochondria, mitochondrial disorders can affect any organ systems and manifest at any age displaying a multi-systemic syndromes; but can also result in tissue-specific symptoms. For these reasons, mitochondrial diseases are particularly difficult to diagnose. Mitochondrial diseases, defined as disorders due to a defect in the oxidative phosphorylation chain (OXPHOS), are the most common maternally inherited diseases of metabolism (in the case of mutation occurring within mitochondrial DNA) (Jardel and Rucheton, 2018). As these disorders impair the OXPHOS process, that results in a deficiency in energy production, organs and tissues that need a high amount of energy, for example, the nervous system, cardiac and skeletal muscles or liver, will be affected first. This is why mitochondrial diseases often involved neurological impairment and muscle weakness. Mitochondrial disorder manifestations observed can be, for example, cognitive impairment, optic atrophy, encephalomyopathy, epilepsy, cardiac and skeletal myopathies, nephropathies, hepatopathies or endocrinopathies (El Hattab *et al.*, 2017).

A characteristic feature of mitochondrial disorders that is directly linked to the multicopy nature of mtDNA is that cells can contain both wild-type and mutant mtDNA populations. This phenomenon is called heteroplasmy. Therefore, within mitochondria, a number of mtDNA could be damaged leading to mutated proteins but this may be compensated by wild-type proteins produced by healthy mtDNA copies. Similarly, if some mitochondria are damaged in a cell, there is still a high number of healthy mitochondria to support mitochondrial functions. For these particular situations, mitochondrial disorder leads to a disease if a threshold is exceeded between the amount of defective mitochondria and healthy ones. Mitochondrial disorders can thus be difficult to diagnose, and even more so by the prevalence of these disorders, with one in five thousand births (Jardel and Rucheton, 2018). Moreover, the degree of heteroplasmy above the threshold can also have an impact in the severity of phenotypes. As an example for mtDNA mutation affecting ATPase6, a low mutant load causes retinopathy, ataxia and neuropathy in adults whereas a high mutant load causes Leigh syndrome in infants (Nunnari and Suomalainen, 2012). The maternally inherited Leigh syndrome (LS) is a neurometabolic mitochondrial disease affecting 1 in 36.000 newborns and causes lactic

acidosis and lesions in the central nervous system. LS usually leads to intellectual disability and muscle weakness, with a peak of mortality before three years of age (Baldo and Vilarinho, 2020; Di Donfrancesco *et al.*, 2022). This disease has a dual origin as mutations had been found in more than 75 nuclear or mtDNA genes coding proteins subunits involved in the complex one and four of the electron transport chain.

As mentioned with the LS syndrome, human mitochondrial disorders are genetic diseases due to the mutation of very diverse genes located either on the mitochondrial DNA (mtDNA) or on the nuclear genome, leading to mitochondrial dysfunctions at multiple stages, for examples mtDNA maintenance defects, mitochondrial dynamics defects in fusion-fission or incapacity in maintaining a balanced mitochondrial nucleotide pool (El-Hattab *et al.*, 2017). Mitochondrial disorders can arise at any age and are usually progressive. For instance, Leber's hereditary optic neuropathy (LHON) is a frequent maternally inherited disease associated with homoplasmic mtDNA mutations which causes blindness in young people, in which 95% of all cases are due to mutations in ND1, ND4 and ND6 mitochondrial genes coding complex 1 subunits (Meyerson *et al.*, 2015). Myopathy like myoclonic epilepsy with ragged red fibers (MERRF) can be caused (among others) by a mtDNA mutation of the gene MT-TK coding tRNA^{lys} or in the nuclear gene coding POLG polymerase (Chinnery *et al.*, 1997; Jardel and Rucheton, 2018). Else, encephalomyopathy like MELAS for mitochondrial encephalomyopathy lactic acidosis and stroke like episodes are usually caused by mtDNA mutation in gene coding tRNA^{Leu} (Moraes *et al.*, 1992; Jardel and Rucheton, 2018; Di Donfrancesco *et al.*, 2022), and dominant optic atrophy (DOA) is a progressive neurodegeneration of the optic nerves that typically starts during the first decade of life and is caused by mutations in OPA nuclear genes coding for mitochondrial proteins involved in mitochondrial fusion and membrane dynamics (Lenaers *et al.*, 2012).

Moreover, a' mutation in the same mitochondrial protein can lead to different phenotypes, which can also depend on the age of onset. For instance, flaws in respiratory complex I can generate atrophy of the optic nerve in adulthood or subacute necrotizing encephalopathy in childhood (Nunnari and Suomalainen, 2012). Another example is that different point mutations in the mitochondrial tRNA $^{\text{Leu}}$ can lead to different diseases such as MELAS, progressive kidney failure or progressive external ophthalmoplegia (PEO) (Moraes *et al.*, 1992; Jansen *et al.*, 1997; Rossmanith and Karwan, 1998).

Nowadays, there is still no efficient curative treatment for mitochondrial disorders. Therapies are focused primarily on restorative or preventative strategies like Q10 supplementation or restoring NAD+ levels, upregulating mitochondrial biogenesis or increasing mitophagy to reduce heteroplasmy levels, or modulating the production of ROS by scavenger molecules (Russel *et al.*, 2020). Another promising approach that has been developed in recent decades is gene therapy. Gene therapy represents an attractive, straightforward therapeutic approach for monogenic recessive diseases. However, there are several challenging issues that have hindered advances in this approach. Extensive review from Di Donfrancesco *et al.* in 2022 explains the challenges and advances of gene therapy in the treatment of mitochondrial diseases. Delivering and expressing an ectopic gene throughout the whole body is still challenging and current technologies can target selected cells or tissues to achieve a therapeutic effect. While most preclinical and clinical studies focus mainly on discrete organs or tissues, such as the nervous system or the eye, the treatment of many mitochondrial diseases would require widespread systemic gene expression that, together with the challenges in delivering genetic material or proteins into the mitochondria, makes developing an effective therapeutic strategy an arduous task. Most mitochondrial diseases are multi-systemic syndromes. Therefore, a widespread, if not ubiquitous, gene expression of the vector carrying the therapeutic transgene should be required to achieve a significant recovery of the patient's condition, with related issues regarding toxicity and immunogenicity. Another main issue with the drug delivery system is to efficiently cross the mitochondrial membrane, and as mitochondrial disorders frequently affect the central nervous system, another difficulty is to penetrate the blood-brain barrier. In addition, regarding the high doses of vectors needed to achieve widespread effects across multiple tissues, another critical limit is the cost of the treatment (Di Donfrancesco *et al.*, 2022).

Different gene delivery approaches are in progress, employing either viral or non-viral systems, of which viral gene delivery is for now the most efficient tool for gene therapy. The most commonly used viral vector systems are based on lentiviruses (retroviruses), adenoviruses, and adeno-associated viruses. Gene therapy is still essentially at a preclinical stage with successful reported results with mouse model and with adeno-associated viral vectors (AAV) delivery system in particular. However, recently in 2020 and 2021, phase 3 clinical trials on patients suffering Leber's hereditary optic neuropathy and using AAV for the allotopic expression of ND4 showed encouraging results (Di Donfrancesco *et al.*, 2022).

Another current promising strategy is to selectively target mutated molecules of mtDNA and induce their degradation, a methodology referred to as heteroplasmy shifting. Briefly, this can be done using zinc-finger nucleases (ZFNs) or transcription activator-like effector nucleases (TALENs) proteins modified with a mitochondrial targeting sequence and fused to another nuclease. These proteins can be engineered to recognize a specific target sequence (containing the mutation) and, linked with a nuclease, allows the cleavage and degradation of mutant mtDNA molecules; or linked with an engineered interbacterial toxin named DddA, allowing the C-G to T-A conversion for gene editing (Joung and Sander, 2013; Lee *et al.*, 2021).

Another therapeutic approach is to focus on RNA molecules repair rather than replacing the mutated gene. Spliceosome-Mediated RNA trans-splicing (SMaRT) is a technique based of RNA repair or reprogramming, which involved the spliceosome and the target pre-RNA transcript that are naturally provided by the cells and a pre-mRNA trans-splicing molecule that is artificially engineered (Yang and Walsh, 2005). Spliceosome-mediated pre-RNA trans-splicing can results in repair from the mutated target pre-mRNA transcript via exon replacement. Recently in 2022, it has been developed an ocular gene therapy based on trans-splicing OPA1 pre-mRNA. Therapeutic *in vitro* experiments on fibroblasts of patients affected by dominant optic atrophy (DOA) have demonstrated the trans-splicing ability to restore physiological levels of OPA1 isoforms and mitochondrial fusion (Le Dantec *et al.*, 2022).

Finally, advances in genome sequencing, like the development of whole genome sequencing and next-generation sequencing, have helped to prevent transmission of mitochondrial mutations. Indeed, a way to decrease mitochondrial disorders is to help and inform, by genetic counselling, families with genetic predisposition (Russel *et al.*, 2020).

1.5.2. Mitochondrial DNA maintenance defects (MDMD)

As this thesis aim to uncover the molecular mechanisms of two mitochondrial maintenance proteins TFAM and mtSSB, focus will be particularly on mitochondrial DNA maintenance defects (MDMD) that is a group of mitochondrial disorders that imply mutation on nuclear encoded proteins involved in the maintenance of mtDNA.

The mitochondrial genome is replicated independently of the nuclear genome, and mtDNA is continuously synthesized throughout the cell cycle. However, constant replication can lead to

Table 1 : MDMD in replication machinery. Table illustrating some examples of clinical features of mitochondrial DNA maintenance defects due to abnormalities in mtDNA replication machinery (from El-Hattab et al, 2017).

Clinical features of mitochondrial DNA maintenance defects due to abnormalities in mtDNA replication machinery.

	Inh.	Onset	MtDNA	Clinical manifestations
Defects in mitochondrial DNA polymerization				
POLG-related Alpers-Huttenlocher syndrome	AR	Early childhood	Depletion	Encephalopathy, neuropathy, and hepatopathy
POLG-related MNGIE	AR	Infancy or childhood	Depletion and multiple deletions	Gastrointestinal dysmotility, myopathy, and neuropathy
POLG-related MEMSA	AR	Young adulthood	Multiple deletions	Epilepsy, myopathy, neuropathy, and ataxia
POLG-related ANS	AR	Young adulthood	Multiple deletions	Ataxia, neuropathy, and encephalopathy
POLG-related ARPEO	AR	Adolescence or young adulthood	Multiple deletions	Ophthalmoplegia
POLG-related ADPEO	AD	Adulthood	Multiple deletions	Ophthalmoplegia and myopathy
POLG2-related myopathic MDMD	AD	Infancy to adulthood	Multiple deletions	Myopathy and ophthalmoplegia
TWNK-related IOSCA	AR	Infancy	Depletion	Ataxia, encephalopathy, and neuropathy
TWNK-related hepatocerebral MDMD	AR	Neonatal period or infancy	Depletion	Encephalopathy and hepatopathy
TWNK-related ADPEO	AD	Early adulthood	Multiple deletions	Ophthalmoplegia and myopathy
TFAM-related hepatocerebral MDMD	AR	Neonatal period	Depletion	Hepatopathy
Defects in mitochondrial nucleases				
RNASEH1-related encephalomyopathic MDMD	AR	Early adulthood	Depletion and multiple deletions	Encephalopathy and myopathy
MGME1-related myopathic MDMD	AR	Childhood or early adulthood	Depletion and multiple deletions	Myopathy
DNA2-related myopathic MDMD	AD	Childhood or early adulthood	Multiple deletions	Myopathy
DNA2-related Seckel syndrome	AR	Birth	NA	Dwarfism

Inh.: inheritance; AR: autosomal recessive; AD: autosomal dominant; MDMD: mitochondrial DNA maintenance defects; MNGIE: mitochondrial neurogastrointestinal encephalopathy; MEMSA: myoclonic epilepsy-myopathy-sensory ataxia; ANS: ataxia-neuropathy spectrum; ARPEO: autosomal recessive progressive external ophthalmoplegia; ADPEO: autosomal dominant progressive external ophthalmoplegia; IOSCA: infantile-onset spinocerebellar ataxia.

the apparition of mutations and increase the frequency of replication errors generating defective mtDNA. Therefore, mtDNA integrity has to be maintained in order to have an adequate number of mtDNA copies in cells for the production of ETC complexes proteins and ensure energy production. Mitochondrial genome maintenance is handled by nuclear encoded proteins that are translated in the cytosol of the cell and are then exported to the mitochondrial matrix by translocators. Pathogenic variants of proteins such as POLγ, TWINKLE, TFAM or mtSSB can be at the origin of impaired mtDNA synthesis leading to quantitative (referred to as mtDNA depletion) or qualitative (referred to as mtDNA deletions) defects in mtDNA (El-Hattab *et al.*, 2017). These kinds of flaws are called mitochondrial DNA maintenance defects (MDMD). MDMDs are genetic diseases that are inherited in an autosomal recessive or dominant manner. As mitochondria are present in all mammalian tissues (except erythrocytes) at various numbers, the phenotypes of MDMDs have a broad spectrum, appearing in childhood or adulthood ranging from mild ophthalmoplegia to severe hepatic failure. MDMDs have multiple origins depending on the pathogenic variants. It can be due to abnormalities in mtDNA replication machinery, in maintaining a balanced mitochondrial nucleotide pool or in mitochondrial dynamics such as mitochondrial fusion (El-Hattab and Scaglia, 2013; Spinazzola 2011). For instance, mutations in the *POLG* gene encoding the POLγA subunit result in a reduction of its activity and leads to stalling at the replication fork and mtDNA depletion and deletions (El-Hattab *et al.*, 2017). Also mutations in *POLG2* encoding POLγB subunits can lower their affinity and impair their interaction with POLγA, leading to an overall reduced processivity of the polymerase and a defected replication generating multiple mtDNA deletions (Young *et al.,* 2011; Craig *et al.*, 2012). In a same manner, mutations in the *TWNK* gene that encode the Twinkle helicase can lead to mtDNA depletion syndrome and/or multiple mtDNA deletions via a disruption of Twinkle activity resulting in mtDNA replication stalling (Goffart *et al.*, 2009; Wanrooij *et al.*, 2007). Another example of MDMD due to abnormalities in mtDNA replication machinery is pathogenic variants of TFAM protein that are linked to mtDNA depletion syndrome with a decrease in number of mitochondrial nucleoids and impaired mtDNA synthesis (Stiles *et al.*, 2016). A summary of clinical features of MDMD caused by pathogenic variants involved in mtDNA replication machinery can be found in **Table 1** (El-Hattab *et al.*, 2017). Recent clinical studies have used exome sequencing to find pathogenic variants of mtSSB in patients that also result in mtDNA depletion syndrome (cf. section 1.7.6) (Pyro-Mégy *et al.*, 2020; Del Dotto *et al.,* 2020).

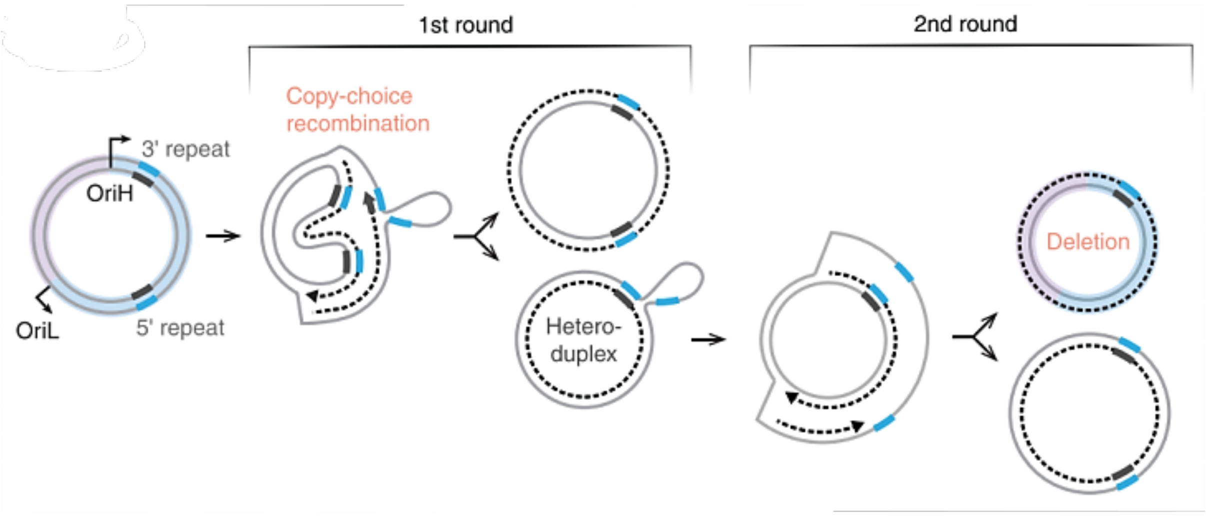

Figure 8: Formation of mtDNA deletion by copy-choice recombination. During replication, repeat sequences in the parental H-strand are exposed. If POLγ stalls and dissociates after the replication of the first repeat sequence closest to OriL, the nascent strand may unpair from the template and mispair with the second repeat that is located closest to OriH on the same strand. If the replication is resumed from the mispaired 3'end, a heteroduplex is formed leading to a mtDNA deletion after a second round of replication (from Falkenberg and Gustafsson, 2020).

The mechanisms involved in mtDNA deletions have been studied and several models have been proposed. The most frequent circular deletion in human cells causes the loss of a 5 kb region between position 8470 and position 13447 in mtDNA; that is located between two repeat sequences of 13 bp where one is retained whereas the other is lost during deletion formation (Falkenberg and Gustafsson, 2020). These two sequence repeats are located in the major arc of the mitochondrial genome between OriH and OriL. Recently, it has been suggested that mtDNA deletions could be formed during L-strand mtDNA synthesis via a mechanism named copy choice recombination (Falkenberg and Gustafsson, 2020). During strand displacement replication, the two repeat sequences are exposed since the displaced H-strand is single stranded. If POLγ stalls and dissociates after the replication of the first repeat sequence closest to OriL, the nascent strand may unpair from the template and mispair with the second repeat that is located closest to OriH on the same strand. If the replication is resumed from the mispaired 3'end, a heteroduplex is formed leading to a mtDNA deletion after a second round of replication (**Figure 8**). Copy-choice recombination could explain why mtDNA deletions occur frequently in the major arc.

A similar model has been observed in *E.coli* in which during lagging strand synthesis, the single stranded template may form secondary structures thereby increasing the chance that the polymerase dissociates and resumes afterward further downstream by reannealing to a similar region (Canceill and Ehrlich, 1996). Another kind of mtDNA deletions that has been observed are linear mtDNA deletions. These deletions are found when the gene encoding the nuclease MGME1 is mutated, leading to the loss of the major arc fragment (Nicholls *et al.*, 2014; Matic *et al.*, 2018). The mechanism proposed for this deletion involved the strand displacement model in which the replication termination at OriH requires the cooperation of POLγ and MGME1 to create a nick that could be ligated by Ligase III. In a scenario where the H-strand is not fully ligated, a next round of replication will lead to a double strand break during the L-strand synthesis (Falkenberg and Gustafsson, 2020).

Double strand break (DSB) followed by a supposed DNA repair mechanism has also been proposed recently in mtDNA deletions formation as it was mentioned in section 1.3.4, after mtDNA rearrangements were observed after silencing of actors of the mtDNA degradation process in human HEK cells (Peeva *et al.*, 2018).

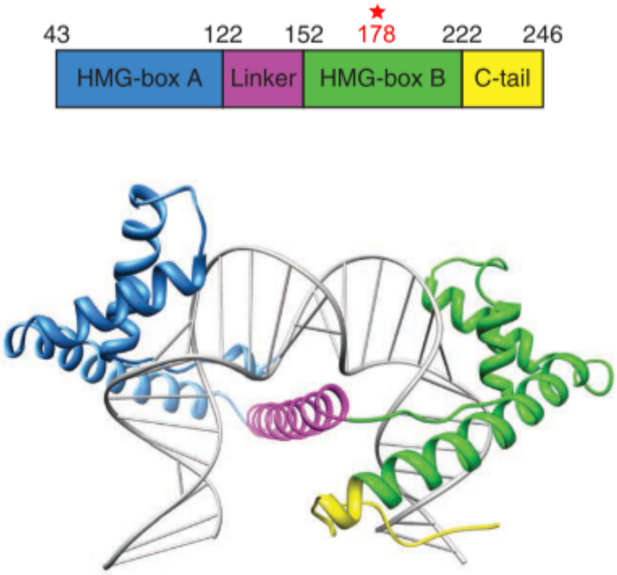

Figure 9: TFAM amino acids sequence and structure. (**Top)** TFAM is a 246 amino acids protein that harbours two HMG box, A and B (**blue and green**), a linker (**purple**) and a C-terminal tail (**yellow**). The mutation P178L is indicated in red. Note that the MTS is not shown and corresponds to the amino acids from 1 to 43. (**Bottom**) Is illustrated the TFAM structure, bound to a dsDNA during transcription initiation, in which colours are related to the protein sequence (from Ngo et al, 2011).

1.6. Mitochondrial Transcription Factor A (TFAM)

1.6.1. Structure

TFAM is one of the core components of the mitochondrial nucleoid. In mammalian mitochondria, about 1000 TFAM molecules are present per mtDNA molecule, which implies that there is 1 TFAM per 16-17 bp of mtDNA (Farge and Falkenberg, 2019). As mentioned before, TFAM belongs to the High Mobility Group, specifically the HMGB group (Malarkey and Churchill, 2012), it is a 24 kDa protein of 246 amino acids that is encoded by nuclear DNA and exported to the mitochondrial matrix via the recognition of its MTS, which is cleaved upon arrival in the mitochondria. The structure of TFAM was revealed by crystallography, which showed that TFAM is composed of two HMG boxes named HMG box A and B (sometimes called 1 and 2) that bind the DNA, a linker region that connects these two boxes and a C-terminal tail involved in transcription activation and specific promoter sequence recognition (Gangelhoff *et al.*, 2009; Ngo *et al.*, 2011; Rubio-Cosials *et al.*, 2011) (**Figure 9**). Structural analyses of the HMG box domains revealed that they interact with DNA under an L shape form of three-helix domain that binds to DNA in the minor groove and dramatically bends the DNA by 90° each into a U-shape, favorizing the recruitment of POLRMT during the initiation of mtDNA transcription (Ngo *et al.*, 2011; Rubio-Cosials *et al.*, 2011; Hillen *et al.*, 2017). The short L-arm is composed of two short antiparallel α-helices and the long L-arm consists of an elongated segment of six to seven amino acids from the N terminus of the domain that is packed against a C-terminal α-helix (Gangelhoff *et al.*, 2009). It has been shown that HMG box A binds independently to a DNA fragment containing LSP whereas HMG box B fails to bind suggesting that HMG box A initiates the binding to DNA (Gangelhoff *et al.*, 2009). However, HMB box B has been shown to recruit POLRMT via the interaction with the N-terminal tail of the polymerase named “the tether helix” (Hillen *et al.*, 2017). Interestingly, HMB box proteins that bind specific sequences usually have one HMG domain whereas those that bind non-specific sequences usually have two, but TFAM shows both specific and non-specific DNA binding. For instance, TFAM’s counterpart in yeast Abf2p is structurally close to TFAM with two HMG box domains, a linker and a C-terminal tail, and has been shown to be the main actor of the yeast mtDNA compaction by inducing U-turn of the DNA backbone; but no role in transcription activation has been highlighted yet (Farge and Falkenberg, 2019).

Moreover, crystal structure analyses revealed that TFAM was in a monomeric state in solution, but higher oligomeric states were observed when it was bound to DNA, for example a dimeric

state in human cells or tetrameric in Xenopus *laevis* cells during transcriptional activation (Gangelhoff *et al.*, 2009). There are diverging propositions for the functions of the TFAM dimerization in human cells. Indeed, *in vitro* gel mobility shift assays using high concentrations of TFAM (WT or tagged with a GST protein) and DNA substrates (containing LSP sequence) suggest that TFAM binds LSP promoter in a dimer form (Gangelhoff *et al.*, 2009). But in the other crystal structure analyses with size exclusion chromatography with in-line multi-angle light scattering analysis (SEC-MALS), researchers found that in preformed 1:1 ratio TFAM-DNA complexes, TFAM is bound as a monomer; or that a second TFAM would not fit in the DNA substrate. Dimers are then possible through protein-protein interactions that would allow DNA loops in addition to DNA bends (Ngo *et al.*, 2011; Rubio-Cosials *et al.*, 2011). Moreover, in an *in vitro* study implying a dimer defect TFAM variant (TFAM-DM), it was shown that TFAM-DM had no effect on transcription but showed reduced compaction activity for linear DNA. This suggests that TFAM dimerization may play an important role in mtDNA compaction rather than transcription (Ngo *et al.*, 2014).

1.6.2. Compaction of mitochondrial DNA and nucleoid formation

Cells of all organisms encounter a spatial issue that is; to fit a longer DNA than the space required hosting it. As an example, the human genome has a length of about 3 billion nucleotides and the mitochondrial genome a length of 16500 nucleotides. Assuming that two nucleotides are spaced by 0,34 nm, this yields lengths of human genome and mitochondrial DNA of around 1 cm and 5 µm, respectively. Now consider that a cell has a length of about 15-20 µm and a mitochondria 0.5-1 µm much smaller than the length of their respective genomes. This indicates that DNA compaction is indispensable. However, the mechanisms and degree of compaction may vary. For instance, nuclear DNA is wrapped around histones to form a nucleosomal fiber that is folded into a chromatin fiber and further compacted into chromatin and chromosome. Mammalian mtDNA compaction differs from nuclear DNA organisation and is more similar to the eubacterial DNA conformation. In bacteria, the bacterial chromosome is organized by nucleoid-associated proteins (NAPs) or bacterial chromatin proteins that compact bacterial DNA with bends, wraps and bridges, forming a structure referred to as the nucleoid (Farge and Falkenberg, 2019).

Electron microscopy images of *in vitro* reconstituted nucleoids, obtained by mixing mtDNA and TFAM, showed that TFAM alone can fully compact mtDNA via similar mechanisms as

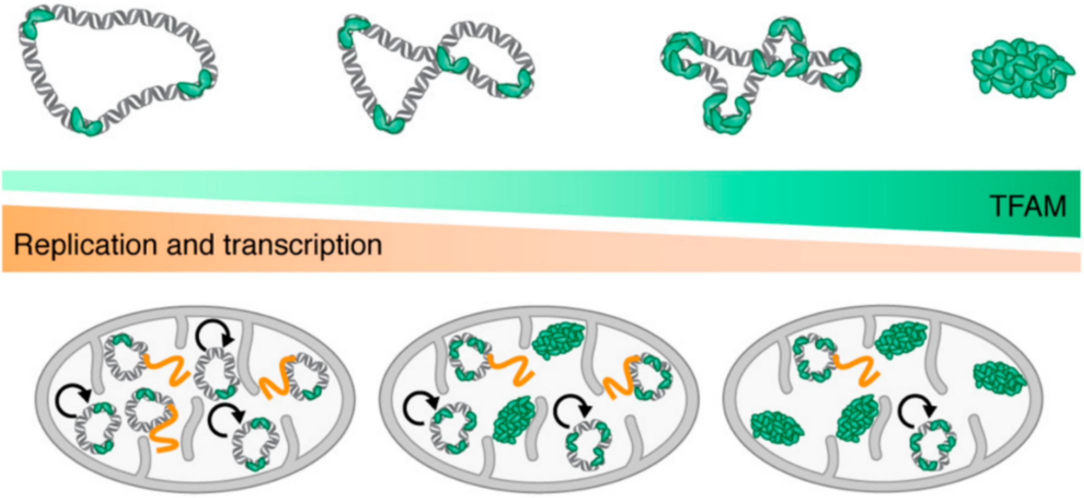

Figure 10: TFAM regulates replication and transcription by controlling mtDNA compaction. (**Top**) Model illustrating compaction of mtDNA as a function of TFAM concentration. (**Bottom**) mtDNA compaction by TFAM is proposed to regulated both replication and transcription depending on the compaction degree of mtDNA compaction. Compacted nucleoids are suggested to be a storage form that coexist with active nucleoids (**Above)** (from Farge and Falkenberg, 2019).

bacterial NAPs, i.e., via bends, wraps and bridging distal DNA strands forming DNA loops (Kukat *et al.*, 2015). Similarly, using tether particle motion (TPM), it was shown that TFAM is able to compact by itself mtDNA. Using optical tweezer assays it was shown that TFAM can decrease the persistence length of mtDNA via local melting of DNA strand, leading to an increase of the overall mtDNA flexibility (Farge *et al.,* 2012; Ngo *et al.*, 2014). This interesting feature may explain how TFAM can handle both transcription activation and mtDNA compaction at the same time (Farge *et al.,* 2012).

The development of super-resolution microscopy made it possible to image the l mammalian mitochondrial nucleoid, which has an irregular ellipsoidal shape with an approximately diameter of 100 nm and typically contains a single copy of mtDNA. The shape of the nucleoids depends on their TFAM coverage and thus their degree of compaction, with fully compacted mtDNA (with high TFAM coverage) or larger nucleoids with less TFAM bound to mtDNA (Brown *et al.,* 2011; Kukat *et al.*, 2015; Farge *et al.*, 2014). TFAM's ability to compact mtDNA could be related to its dimerization. *In vivo* fluorescence microscopy with monomeric Kusabira-Green fluorescence protein reporter has been used to detect TFAM-TFAM interaction in cells. This revealed that the HMG box A was sufficient for dimerization, and that the expression of a dimer-defective mutant induced enlarged mtDNA nucleoids by 46 % (Kasashima and Endo, 2015). These results suggest that TFAM could play an important role in the distribution of mtDNA molecules. An earlier study performed with the same TFAM dimer defective mutant also reported a reduced compaction activity for linear DNA but found no effect on transcription activity (Ngo *et al.*, 2014). However, the same TFAM mutant has also been observed in electron microscopy and super-resolution microscopy and it behaved similarly to wild type TFAM, and increasing concentrations of the dimer defective TFAM led to increased sizes of TFAM patches and fully compacted mtDNA molecules, but to a lesser extent than with wild type TFAM (Kukat *et al.*, 2015). Therefore, the requirement of TFAM dimers for efficient mtDNA compaction needs further investigation.

Moreover, in vitro reconstituted nucleoids showed that in a fully compacted nucleoid, TFAM forms stable protein filaments and can block mitochondrial replication as well as transcription and that small changes in TFAM concentration levels can change the number of mtDNA molecules available for mtDNA transcription and replication (**Figure 10**) (Farge et al., 2014). Based on these results, it has been suggested that TFAM may function as an epigenetic regulator that could control the number of mtDNA molecules that can undergo transcription

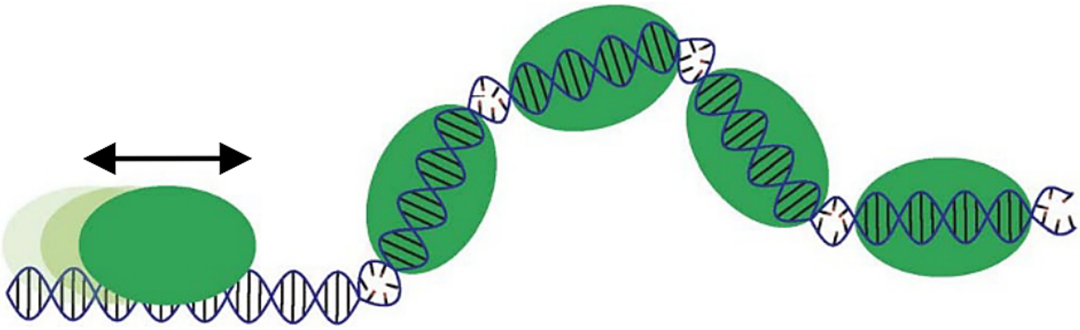

Figure 11: Model of TFAM patches formation and increase of DNA flexibility. Illustration of TFAM cooperativity via sliding mechanism of TFAM monomers and patches formation. DNA flexibility is increased via local DNA melting between TFAMs (from Farge et al, 2012).

and replication or mtDNA molecules that should remain compacted as a storage form (Farge and Falkenberg, 2019). This was further supported by *in vivo* multi-color STED super-resolution microscopy where observations in human cells demonstrated that only a minority of nucleoids were active and physically larger, whereas inactive nucleoids correlated with high ratio of TFAM to mtDNA and may represent a storage pool (Brüser *et al.*, 2021).

1.6.3. Dynamics of TFAM

In mammalian mitochondria, TFAM has been seen to diffuse rapidly over long distances (several micrometers) on double stranded DNA and it exhibits cooperative binding. In optical tweezer coupled with fluorescence microscopy or super-resolution microscopy with Stimulated Emission Depletion (STED), it has been shown that TFAM can diffuse rapidly in a sliding mechanism (Farge *et al.*, 2012; Heller *et al.*, 2013). MSD analysis of TFAM diffusion from Farge *et al.,* 2012 experiments indicated a linear fit corresponding to a random diffusion with a diffusion coefficient around $8.6.10^4$ nm^2 s^{-1}. Moreover, it has been shown that TFAM binds as a monomer (as previously supported in Ngo *et al.*, 2011; Rubio-Cosials *et al.*, 2011) and diffuse rapidly, while multimers formed immobile patches (Farge *et al.*, 2012; Heller *et al.*, 2013). In addition, dual-colour experiments evidenced that when a TFAM monomer collides with a stationary patch of TFAM, it stops its movement and aggregates with this patch (Farge *et al.*, 2012). Moreover, in electron microscopy imaging of *in vitro* interaction between TFAM and mtDNA showed that an increasing TFAM concentration led to the accumulation of enlarged aggregates instead of an even distribution of TFAM over all mtDNA molecules, this is consistent with a cooperative binding (Kukat *et al.*, 2015). Quantification of the cooperative binding of TFAM to DNA was estimated using the McGhee-von Hippel model to fit the concentration dependence of the persistence length of the DNA (which is a measure for the flexibility of the DNA, cf. section 1.9) (McGhee and von Hippel, 1974). It was found that TFAM is 100 times more likely to stably bind next to an already bound TFAM than to bare DNA (Farge *et al.*, 2012).

The model proposed for the cooperative patch formation is the following. TFAM binds as a monomer and diffuses along the DNA and, upon collisions between TFAM molecules TFAM patches are formed, which induce local melting bubbles in the DNA of 2-3 bp between neighbouring TFAM molecules, thus increasing DNA flexibility and enhancing DNA compaction (**Figure 11**) (Farge *et al.*, 2012). It was shown that higher TFAM oligomerization states (like dimers) could also diffuse on the DNA but with a slower diffusion coefficient

(Heller *et al.*, 2013). The capability of TFAM to rapidly diffuse on DNA could also be a way to scan for promoter regions on mtDNA.

1.6.4. Activity regulation of TFAM

In section 1.6.2, we discussed that TFAM could fine tune the regulation of mtDNA replication and transcription by controlling the number of nucleoids that are active and in a storage form. This task of TFAM may be regulated by modifications such as acetylation and phosphorylation of the TFAM molecule. It has been demonstrated that TFAM can be acetylated and phosphorylated within HMG box A (Lu et al., 2013; King et al., 2018). These modifications decrease the binding affinity of TFAM for non-specific DNA sequences.

In this context, mimics of TFAM with acetylation and phosphorylation (will be named as TFAM$_{\text{Ace}}$ and TFAM$_{\text{Pho}}$) were studied in single molecule assays combining fluorescence microscopy with dual-trap optical tweezers (King et al., 2018). The observed decrease in binding affinity for TFAM$_{\text{Ace}}$ was explained by a sharp lower on-rate and for TFAMPho by both a 3.5 flow lower on-rate and a 2 fold higher off-rate relative to WT. Moreover, TFAM$_{\text{Pho}}$ was found to diffuse 6.5 fold faster than TFAM WT and 4.5 fold faster than TFAMAce. However, both modified TFAM displayed similar cooperativity than the WT and exhibited the same flexible-hinge mechanism and could compact DNA, but required different protein concentration to achieve a given extent of compaction. TFAM phosphorylation was also performed by extracellular signal regulated protein kinases (ERK1/2) within HMG box B and led to a decrease in promoter binding and transcription, but not in the non-selective binding of mtDNA (Wang *et al.*, 2014). Regarding these results, the authors suggested that TFAM phosphorylation may be involved in transcription regulation by decompacting nucleoids, as well as accelerating the scan of the promoter region by TFAM, or impairing promoter binding. In addition, acetylation could impair free TFAM to rebind, and the lower binding affinity caused by both modifications could regulate TFAM concentration via Lon degradation and, thereby, tune the level of nucleoids available for replication or transcription.

Indeed, it was described that TFAM is degraded by Lon mitochondrial protease when not bound to dsDNA (Matsushima et al., 2010; Lu et al., 2013). Also, TFAM could be degraded by 20S proteasome in the cytosol as the level of TFAM dimer-defect mutant is restored when using epoxomicin (that is a 20S proteasome inhibitor but does not inhibit Lon) in transfected HeLa cells. Moreover, TFAM dimer-defect mutant levels were also restored when using Lon

inhibitor (Kasashima and Endo, 2015). Interestingly, this observation suggests TFAM dimerization may be a way to control TFAM stability.

1.6.5. Pathologies associated with TFAM mutants

A reported TFAM variant (TFAM P178L) has been identified in human siblings and they were affected by neonatal-onset liver failure progressing to demise and mtDNA depletion in liver and skeletal muscle (Stiles et al., 2016). This variant was the subject of experimental studies in this thesis. TFAM levels and mtDNA copy number have been demonstrated to be directly linked. In mice, heterozygous mutation of TFAM generates a decrease of about 40 % in mtDNA copy number in vivo, and homozygous mutation was found to be embryonically lethal (Kang et al., 2018). Moreover, important decreased levels of mtDNA or TFAM have been observed in patient populations that were affected by Parkinson's, Huntington's and Alzheimer's disease and even just in ageing, describing an association of mtDNA and TFAM levels with neurodegeneration (Kang et al., 2018). Recently, a recessive variant in TFAM (Arg232Cys) has been shown to cause mtDNA depletion associated with primary ovarian insufficiency, seizures, intellectual disability and hearing loss in a consanguineous family which expands the repertoire of mitochondrial disease phenotypes (Ullah *et al.*, 2021).

1.7. Mitochondrial Single Stranded Binding protein (mtSSB)

1.7.1. Structure

Single-stranded DNA binding proteins (SSBs) are found in all three domains of life, *i.e* Eukarya, Eubacteria, Archaea as well as in viruses. Depending on the organism, SSBs are involved in DNA metabolism at different degrees including DNA replication and transcription, DNA recombination and DNA repair such as NER, BER, DSBr and MMR (Broderick et al., 2010; Guo and Malik, 2022). Single-stranded DNA (ssDNA) is less stable than double-stranded DNA and is prone to mutations and damages, but also to form secondary structures that may block the action of polymerases. Nevertheless, ssDNA is frequently exposed during essential cellular processes as mentioned above and is thus vulnerable to chemical attack and nucleolytic degradation. Therefore, there is a critical importance to protect ssDNA and to maintain genome integrity that is ensured by the SSB family. Among this family, known SSBs are SSB from bacteriophage T4 (gp32) and T7 (gp2.5), SSB from *E. coli* (EcoSSB), replication

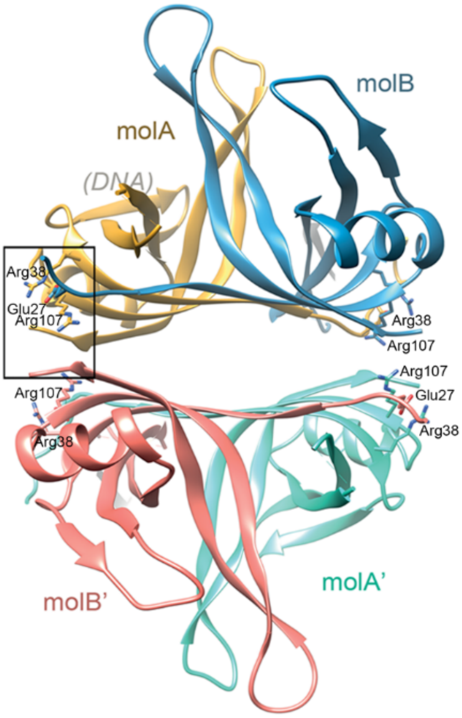

Figure 12: HsmtSSB structure. HsmtSSB is assembled as a homotetramer, in which the four monomers (molA, A', B and B') form a dimer to dimer structure. In the box, some mutation positions found in mitochondrial disorders are indicated, where they stand at the dimer interface (from Piro-Mégy et al., 2020).

protein A (RPA) or POT1 from telomere end-binding protein family in eukaryotes, to name a few (Guo and Malik, 2022). Four main structural folds in the ssDNA-binding domains of SSB were characterised, which are oligonucleotide/oligosaccharide-binding folds (OB), K homology (KH), whirly domains and RNA recognition motifs (RRMs) (Dickey et al., 2013). The crystal structure of human mitochondrial single-stranded DNA binding protein (HsmtSSB) was solved in 1997 and highlighted a homotetrameric structure formed by two dimers interacting head-to-head with a D2 symmetry (Yang et al., 1997) (**Figure 12**). In mammals, mtSSB is a 148 amino acids protein of 16 kDa that displays a MTS and harbours one OB folds domains as binding domain for ssDNA, allowing ssDNA to be wrapped around the tetramer. (Wu et al., 2016). Depending on the number of OB fold domains, SSBs can be classified into two groups, simple SSBs which contain one OB fold domain like mtSSB or ecoSSB, and higher order SSBs which contain multiple OB fold domains like RPA1, RPA2 and RPA3 (Wu et al., 2016).

As HsmtSSB contains one OB fold domain as binding site, only this structural fold will be described here. Although OB folds domains in different proteins have a low degree of sequence similarity and can vary in length from 70-150 amino acids, they all share structural features (Flynn and Zou, 2010). The structure of OB folds consists of five-stranded β-sheets coiled to form a closed β-barrel that is capped by an α-helix located between the third and fourth strands (Murzin, 1993). HsmtSSB shows a high degree of structural similarity, despite displaying low sequence identity with EcoSSB, therefore, EcoSSB constitutes a good model of comparison (Webster et al., 1997). Indeed EcoSSB is 177 amino acids long and also binds ssDNA as a tetramer. It has one OB fold domain and the main difference between HsmtSSB is the presence of a C-terminal disordered domain that may explain the physicochemical properties between the two proteins (described in section 1.7.2) (Webster et al., 1997; Qian and Johnson, 2017).

1.7.2. Binding modes

The number of ssDNA nucleotides bound by SSBs can be modulated by the environmental conditions, such as the concentration and type of salt, the pH and temperature, the SSB to ssDNA ratio, as well as the binding partners (Antony and Lohman, 2019). Depending on these conditions, it has been found that HsmtSSB displays at least two binding modes: a low binding mode SSB_{50} and a high binding mode SSB_{70} where the subscript numbers indicate the average number of nucleotides occluded by the tetramer (Curth et al., 1994). In a recent study involving optical tweezer experiments to characterise and compare the structure

of preformed HsmtSSB-ssDNA complexes with ssDNA generated during an artificial replication fork, it was confirmed that HsmtSSB displayed a low and a high binding mode on preformed complexes. The low binding mode was favoured by a high ratio of SSB to ssDNA and by a low concentration of NaCl, whereas the high binding mode was favoured by a low ratio of SSB to ssDNA and a high concentration of NaCl (Morin, et al., 2017). However, the average nucleotides number found for these binding modes may vary depending on the experimental setting and salt type. The authors also noticed that HsmtSSB31 and HsmtSSB53 found in specific conditions are remarkably similar to EcoSSB low binding mode EcoSSB35 and high binding modes EcoSSB$_{56}$ or EcoSSB$_{65}$ (Morin et al., 2017; Lohman and Ferrari, 1994). Moreover, during strand displacement synthesis implying Phi29 DNA polymerase, SSB bound to the ssDNA only in the low binding mode, suggesting that gradual release of ssDNA during DNA synthesis may be a key regulator to determine the wrapping state of ssDNA by HsmtSSB (Morin et al., 2017). The fact that HsmtSSB and EcoSSB share structural similarities and binding modes modulation may suggest that their binding kinetics are similar.

Dual-Resonance-frequency-Enhanced Electrostatic Force Microscopy (DREEM) experiment, showed that, when HsmtSSB or EcoSSB was incubated with 90 nt ssDNA, the ssDNA was wrapped in either a single turn or two turns around the SSB tetramers.s (Kaur et al., 2017). This interesting feature might correspond to the ssDNA wrapping transition from the high and the low binding modes, but it was not specified by the authors. Binding modes of EcoSSB have been shown to be modulated by the interaction of proteins with its C-terminal tip. Several studies have demonstrated that PriA and PriC DNA helicases as well as RecQ helicase, involved in the replication restart process, promote the transition from the fully wrapped state EcoSSB65 to the partially wrapped state EcoSSB35 (Antony and Lohman, 2019). This mechanism could be important to free space on ssDNA to allow proteins of DNA maintenance to access ssDNA.

The EcoSSB structure contains one OB fold per monomer as binding domain, a C-terminal tip that mediates protein-protein interactions and in between, an intervening non-conserved intrinsically disordered linker (IDL) shaped in a globular conformation that is necessary for EcoSSB tetramers cooperativity (Antony and Lohman, 2019). EcoSSB has been observed to bind to ssDNA in a highly cooperativity manner, instead no cooperativity was seen for HsmtSSB (Kaur et al., 2018). Single molecule assays using Total Internal Reflection Fluorescence microscopy (TIRF) also showed that EcoSSB can compact ssDNA beyond the

expectation of the simple transition of binding mode, that is consistent with a tetramer-tetramer interaction (Bell et al., 2015). The IDL was proposed to be mainly involved in this cooperativity through direct interaction between other IDLs of tetramers (Figure 13). This is consistent with non-cooperative binding of HsmtSSB to ssDNA, since HsmtSSB lacks the IDL (Kozlov *et al.*, 2017). However, SSB from Plasmodium falciparum (PfSSB), which shows structurally similarities with EcoSSB and HsmtSSB, like homotetramer conformation with one binding domain per monomer, harbours an IDL, but does not show any cooperativity (Antony et al., 2012; Antony and Lohman, 2019). This absence of cooperativity from PfSSB could be related to the difference in sequence and structure of its IDL compared to EcoSSB's IDL. In a chimeric version of EcoSSB, in which PfSSB IDL is replaced from EcoSSB IDL, EcoSSB lost its cooperativity feature (Kozlov et al., 2017). Thus, it is tempting to say that PfSSB may be also a good model to study HsmtSSB as they share several characteristics as discussed in Kaur *et al.*, 2017.

Kinetic and thermodynamic with equilibrium titration, stop-flow kinetic and isothermal titration calorimetry (ITC) of HsmtSSB revealed a $HsmtSSB_{30}$ and $HsmtSSB_{60}$ binding mode. The low binding mode ($HsmtSSB_{30}$) is inhibited in presence of Mg^{2+}, which is more efficient in shielding negative charges on the DNA backbone, indicating the importance of the electrostatic charges for HsmtSSB stability (Qian and Johnson, 2017). Moreover in this study, they used FRET and stop-flow kinetic assays to show that HsmtSSB can (i) bind two dT_{30} in two sequential steps, (ii) rapidly wrap a dT_{60} around its four monomers, (iii) can directly transfer from one ssDNA molecule to another via an intermediate state with two ssDNA molecules bound to the same HsmtSSB. The ability of HsmtSSB to potentially exchange ssDNA molecules is interesting and may offer the ability to be redistributed along the mtDNA molecule.

Finally, it has been shown that EcoSSB binding modes can be modulated by interacting proteins. PriA DNA helicase was shown, using FRET, to binds to EcoSSB and promotes the transition from the fully to partially wrapped state (Bhattacharyya *et al.*, 2013). Likewise, PriC and RecQ helicases were also shown to bind to EcoSSB and promote the low binding mode (Wessel *et al.*, 2013; Mills *et al.*, 2017). The transition from the high to the low binding mode facilitated by interacting protein could be a way partially gain access to the buried ssDNA. As the low binding mode was seen to be promoted by proteins actors of the replication machinery, it was suggested that EcSSB low binding mode may be favour in the replication process

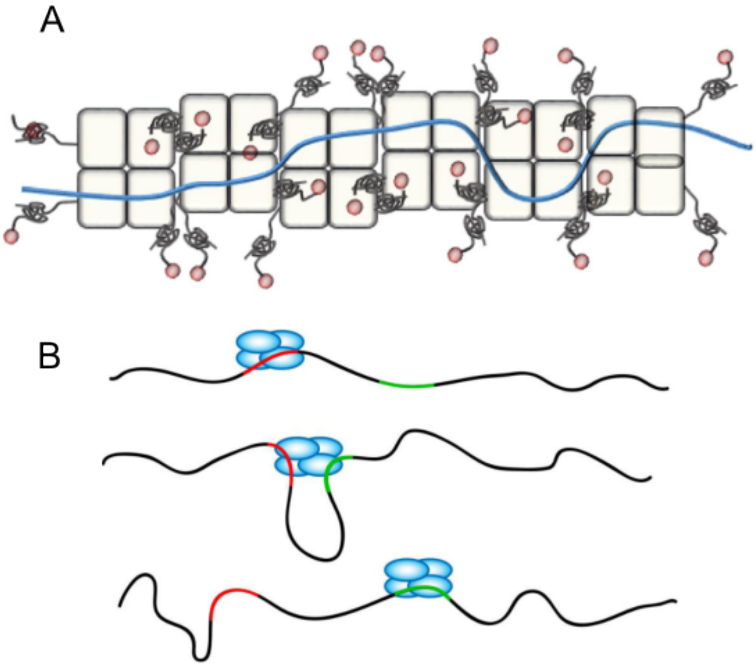

Figure 13: Model of EcoSSB cooperativity and diffusion mechanism. (**A**) Schema displaying binding cooperativity of EcoSSB in the low binding mode on ssDNA (**bleu**) via tetramer (**squares**) interactions by their IDL (**black globular segment**). The C-terminal tip of EcoSSB is represented in pink. Reptation diffusion mechanism could be imaged by EcoSSB tetramers sliding on ssDNA. (**B**) Model of intersegment transfer mechanism in which EcoSSB (**in blue**) bound to a ssDNA site (**in red**) interacts with another distant site of the same ssDNA molecule (**in green**) and dissociates from the original site, leading to large displacements (from Lee et al. 2008 and Antony and Lohman, 2019).

(Antony and Lohman, 2019). Others studies showed that human mtSSB only shows the low binding mode in a strand displacement assay with the bacteriophage Phi29 DNA polymerase in an optical tweezers experiment (Morin *et al.*, 2017); and from another study, that EcoSSB variant unable to form high binding mode was able to functionally complement wild-type EcoSSB, but as a trade-off an accumulation of mutation in DNA (Waldman *et al.*, 2016). This last result, supported by the fact that the conditions that favourised EcoSSB high binding mode correlate with the propensity of the RecA recombinase to perform strand exchange (Roy *et al.*, 2010), suggest that a role of the high binding mode in DNA repair and recombination cannot be ruled out (Antony and Lohman, 2019).

1.7.3. Dynamics

Several SSB proteins have been observed to diffuse on ssDNA (Lee *et al.*, 2014; Zhou *et al.*, 2011; Nguyen *et al.*, 2014). In single molecule assay with optical tweezers, EcoSSB diffusion mechanism has been proposed, in which EcoSSB is redistributed along long ssDNA via intersegment transfer (**Figure 13**), a mechanism that may allow EcoSSB to be recycled and rapidly transfer between Okazaki fragments (Lee *et al.*, 2014). Additionally, in experiments with optical tweezers coupled with Förster Resonance Energy Transfer (FRET), it was shown that EcoSSB can diffuse by sliding on the ssDNA molecule via a reptation mechanism resulting in an apparent diffusion coefficient of 270 nt^2/s at 37°C, even when tightly bound and it can serve as a platform to carry interacting proteins for use in DNA metabolism (Zhou *et al.*, 2011). Eukaryotic protein RPA is also able to diffuse with an approximately diffusion coefficient of 5000 nt^2/s at 37°C (Nguyen *et al.*, 2014). However, for the moment, there is no evidence that HsmtSSB can diffuse on ssDNA. SSB motion might not always be an intrinsic characteristic as it was shown for example with the T7 SSB protein (gp2.5) that was found to be relatively immobile on ssDNA in dual-trap optical tweezers combined with fluorescence (Xu *et al.*, 2023).

Finally, it has been shown that EcoSSB can be moved directionally on the ssDNA by the action of a nucleic acid motor protein such as an ATP-dependent translocase or a polymerase (Sokoloski *et al.*, 2016). It is possible that such directional pushing of HsmtSSB by POLγ also occurs during mtDNA L-strand synthesis.

1.7.4. Mechanical study of mtSSB binding to ssDNA under tension

General binding properties of SSB, such as footprint, on rates, off rates, can be probed with both bulk assay and single molecule techniques. However, the binding mechanics of SSB proteins to ssDNA under tension can be investigated exclusively with single molecule force spectroscopy tools (cf. section 1.9). Insight into the binding mechanics can be obtained by analysing the stretching of mtSSB-ssDNA complexes as a function of applied force. Force-stretching of ssDNA can be achieved using DNA manipulation methods such as optical and magnetic tweezers or acoustic force spectroscopy (cf. section 1.9.2). For instance, Zhou *et al.* has concluded by measuring DNA extension changes with dual optical traps at constant force that EcoSSB is highly sensitive to force tension. The unwrapping of the DNA occurs at tensions as low as 1 pN and complete dissociation between 7 and 13 pN at 500mM Na+.

The tension-dependent wrapping behaviour of EcoSSB has revealed three distinct force regimes namely: loading, wrapping and protein removal (Xu *et al.,* 2023; Suksombat *et al.*, 2015; Naufer *et al.*, 2021). Correlation between the number of nucleotides wrapped and the force level showed that as the applied tensions increases, fewer nucleotides are wrapped around EcoSSB. This decrease of the number of wrapped nucleotide with increasing force occurs in several stable modes, namely at 65 nt for low force (<1 pN), 56 nt (at 1-5 pN), 35 nt at 3-8 pN, and 17 nt at 8-11 pN (Xu *et al.*, 2023; Suksombat *et al.*, 2015). Interestingly, these values correspond to the EcoSSB binding modes that were determined previously (section 1.7.2), and that may suggest that SSB binding modes (here EcoSSB but might be extendable) could also be modulated by the tension that is exerted on the ssDNA molecule, and it could be an explanation why HsmtSSB only displays the low binding mode during a strand displacement (Morin *et al.*, 2017).

Morin *et al.* has investigated the force sensitivity of HsmtSSB with a series of stretch-relax cycles in which force was incremented by 1 pN in each consecutive cycle. The minimum force triggering mtSSB unwrapping (F_u) was determined as the average force value above which the stretch-relax cycle presented hysteresis, but consecutive cycles exhibited the same original extensions. The minimum force that begins to promote protein detachment (F_d) was determined as the average force value above which consecutive stretching cycles show different extensions. F_u and F_d were found to be dependent on the SSB/NaCl ratio, with both forces increasing as the ratio increased. At lowest ratios, overall unwrapping and protein detachment

began at force values around 6 and 8 pN. At highest ratios, F_u and F_d were around 9 and 14 pN. These results suggest that mtSSB stability is dependent on the protein/salt concentration conditions but is also dependent on the mechanical tension that is exerted on the ssDNA strand. Moreover, Morin *et al.,* 2017, have shown that the removing of hysteresis within the force distance curve of a ssDNA molecules bound with HsmtSSB at high salt concentration (which promotes secondary structure within ssDNA) is an evidence that HsmtSSB efficiently removes secondary structures (as EcoSSB, Bell *et al.*, 2015) that is an important feature for the mitochondrial replication process. To assess binding stability, energetic variation of SSB protein binding to ssDNA can be measured by analysing its force distance curve using the relationship: $1\ k_bT \sim 4.1$ pN.nm at 25°C (Bell *et al.*, 2015). Measurement of energetic changes can be used to get insight of environmental influence on SSB binding stability like binding partners or salt conditions (Bell *et al.*, 2015, Morin *et al.*, 2017)

The binding affinity can also be probed on ssDNA under tension. Xu *et al.* in 2023 have shown with optical tweezers experiments that the T7 SSB (gp2.5 protein) displayed three binding states determined as short, intermediate and long-live states that depend on the binding duration of gp2.5 on ssDNA. For all states, on rates seemed to decrease with increasing tensions (from 3 to 12 pN), but tension seemed to have no influence on the off rate between 3 and 18 pN but rather on the proportion of SSB protein that belongs to intermediate and long-lived states. Moreover, the authors showed that a net dissociation starts at 25 pN.

Mechanical tension is also an important parameter for other players in the mtDNA maintenance process. As an example, mechanical tension has been shown to play a key role in Polγ strand displacement activity. The activity of Polγ is hampered by the mechanical tension exerted on the polymerase due to the strands reannealing pressure at the fork, enhancing by the 3'-5' exonuclease activity of Polγ. In this context, mtSSB has been shown to lower the energy barrier for the strands unwinding (Plaza *et al.*, 2023).

Studying mechanical tensions at the replication fork could be a lead to investigate the disease-causing mechanism of mtSSB protein variants involved in defects at the mitochondrial replication initiation like mtSSB R107Q mutant.

1.7.5. Roles in the mitochondrial DNA maintenance

It has been discussed in section 1.3 that mammalian mtSSB is a key component of the mitochondrial DNA protein maintenance. In the strand displacement model of replication, mtSSB is required to protect the displaced parental H-strand. Indeed, SSBs proteins, such as mtSSB, bind ssDNA with a high specificity and one of their roles is to protect the single stranded DNA from damages such as nucleolytic degradation or chemical attacks. However, the involvement of mtSSB in DNA maintenance should not be only restricted to a passive role of protection, but rather mtSSB should be considered as an active actor of the mtDNA metabolism.

For instance, in 2009, HsmtSSB was identified as a binding partner of the tumour suppressor p53 protein within mitochondria and was found to enhance its exonuclease activity, especially in hydrolysing 8-oxodG. This suggests, besides that p53 is involved in mtDNA repair, that HsmtSSB participates actively in the mtDNA repair mechanism (Wong et al., 2009). HsmtSSB is also actively involved in mtDNA replication as it removes secondary structures that may occur as DNA goes single stranded and thus can cause the replication process to stall (Morin et al., 2017). By removing these secondary structures, HsmtSSB organises the DNA template and was found to stimulate both Twinkle and Polγ activity / processivity (Ciesielski et al., 2015; Korhonen et al., 2003). This feature seems common among SSBs family, since it was also observed for RPA and EcoSSB (for example, Nguyen et al., 2014; Roy et al., 2010). Furthermore, single molecule assay showed Polγ displays a robust DNA unwinding mechanism and that HsmtSSB can stimulate the strand displacement DNA synthesis by Polγ via imposing destabilization energy on the DNA junction leading to an increase of the pause-free rate of the polymerase and a reduction of the DNA fork regression pressure on it (Plaza-G.A *et al.*, 2023).

An interesting finding was that HsmtSSB and Twinkle were not restricted to the nucleoid and were found to be colocalized in mtRNA granules. MtRNA granules are nucleic acids-proteins structures found in the mitochondrial matrix either in close association with the nucleoids or as discrete structures, and they are involved in mitochondrial RNA processing and ribosome biogenesis (Hensen et al., 2019). Depletion of HsmtSSB and GRFS1 in HEK cells by siRNA knockdown greatly increased the level of mtRNA breakdown products as well as dsRNA and RNA/DNA hybrids (Hensen et al., 2019). From this result, the authors proposed the GRFS1-

Table 2: Clinical manifestations of some HsmtSSB mutations (from Gustafson et al., 2019).

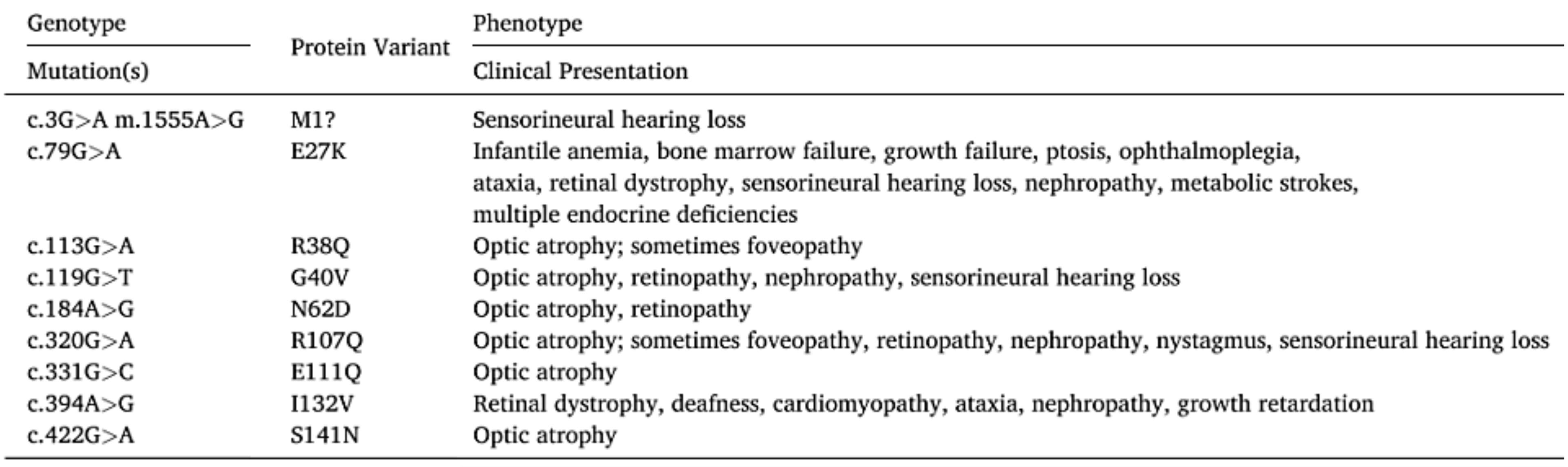

Genotype	Protein Variant	Phenotype
Mutation(s)		Clinical Presentation
c.3G>A m.1555A>G	M1?	Sensorineural hearing loss
c.79G>A	E27K	Infantile anemia, bone marrow failure, growth failure, ptosis, ophthalmoplegia, ataxia, retinal dystrophy, sensorineural hearing loss, nephropathy, metabolic strokes, multiple endocrine deficiencies
c.113G>A	R38Q	Optic atrophy; sometimes foveopathy
c.119G>T	G40V	Optic atrophy, retinopathy, nephropathy, sensorineural hearing loss
c.184A>G	N62D	Optic atrophy, retinopathy
c.320G>A	R107Q	Optic atrophy; sometimes foveopathy, retinopathy, nephropathy, nystagmus, sensorineural hearing loss
c.331G>C	E111Q	Optic atrophy
c.394A>G	I132V	Retinal dystrophy, deafness, cardiomyopathy, ataxia, nephropathy, growth retardation
c.422G>A	S141N	Optic atrophy

mtRNA degradosome pathway in which HsmtSSB is involved to remove G-quadruplex structures.

Additionally, using a mouse knockout model as well as in vitro replication reconstitution it was shown that mammalian mtSSB was essential for initiation of mtDNA replication (Jiang et al., 2021). Indeed, Falkenberg and co-workers concluded that in the absence of mtSSB, transcription from LSP is strongly up-regulated and that no replication primers are formed (Jiang et al., 2021). Using mutant versions of mtSSB, they showed that initiation of mtDNA replication is impaired via the inefficiency of mutants to prime replication. They, therefore, suggested that mtSSB is essential to actively drive mtDNA replication over transcription by restricting and optimising primer formation at both origins of mtDNA replication.

1.7.6. Pathologies associated with mtSSB mutants

As discussed above, as one of the core components of the mtDNA maintenance machinery, mammalian mtSSB binds and protects ssDNA, and also interacts with the essential core replication protein Polγ. Furthermore, mtSSB colocalized in mtRNA granules, suggesting that it plays an important role in mtRNA processing. It is thus not surprising that any variation of mtSSB levels can cause mtDNA depletion as seen in vivo (Ruhanen et al., 2010). Recently, several mtSSB variants have been reported to cause autosomal dominant mitochondrial optic neuropathy/atrophy and retinal dystrophy with or without mitochondrial DNA depletion. These mutations have been found, so far, in more than 80 patients across around 20 families, and with the development of whole exome sequencing (WES) and next-generation sequencing (NGS), these numbers are rapidly rising (Kullar et al., 2018; Del Dotto et al., 2019; Pyro-Mégy et al., 2019; Jurkute et al., 2019; Gustafson et al., 2021). One mutation was particularly of interest, the mutation 320 G>A in SSBP1 leading to the variant mtSSB R107Q, as it shows the most severe mtDNA depletion and was found in a number of patients (**Table 2**). The phenotypes can range from optic disorders like optic atrophy, foveopathy or retinopathy, to kidney disorders with nephropathy, and also sensorineural hearing loss. This variant was the subject of experimental studies in chapter three of this thesis.

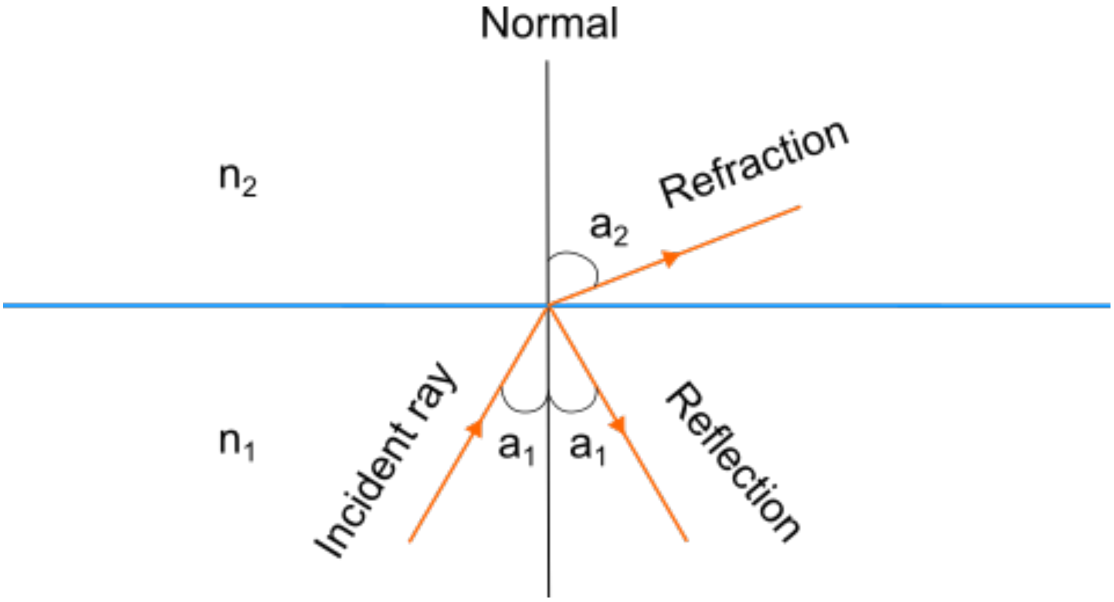

Figure 14: The Snell-Descartes laws. In the same plan, an incident ray with an angle a_1 to the normal and in a medium with a refractive index n_1 will be refracted with an angle a_2 in a medium with a refractive index n_2 by the relation : $n_1.\sin(a_1) = n_2.\sin(a_2)$; and a portion will be reflected with the same angle a_1.

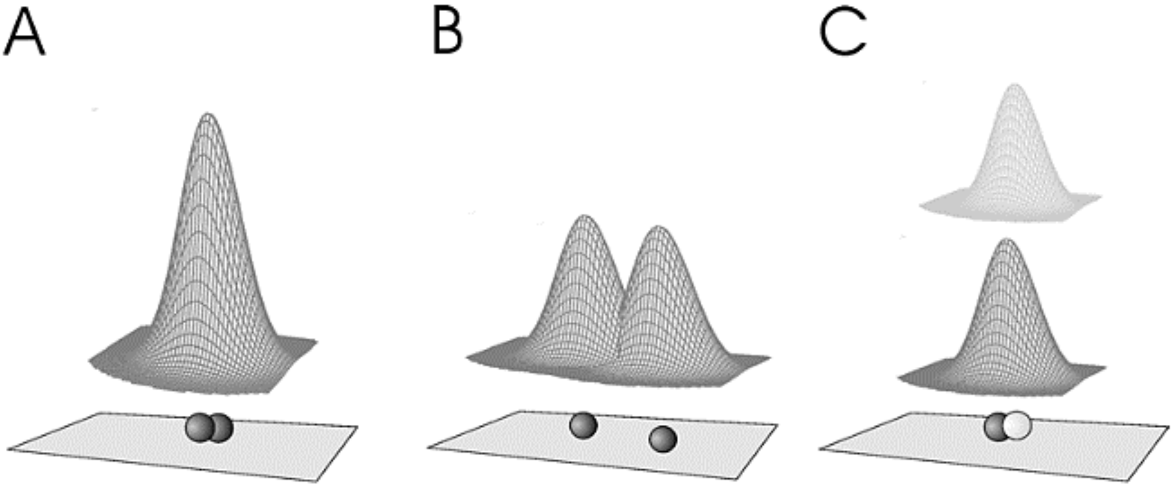

Figure 15: Scheme of the diffraction limit. (**A**) The Point spread function (PSF) of two molecules cannot be resolved because d<Rayleigh criterion. The PSF display is the result of the sum of the PSF of both molecules. (**B**) Two objects separated by the Rayleigh criterion. (**C**) Two molecules can be differentiated by using two different colours and image them sequentially (Scheme was extracted from van den Wildenberg, 2011).

1.8. Fluorescence microscopy

1.8.1. Introduction to optic

The way we see objects relies on the physical properties of light. In the XVII and XVIII centuries, the nature of light has been debated. According to Huygens' theory, the nature of light is undulatory and acts like waves, whereas Newton proposed a corpuscular nature of light that is made up of small discrete particles that travel in a straight line with finite velocity. For instance, undulatory theory can explain the diffraction of light whereas the corpuscular theory introduces the reflexion and refraction of light. Refraction of light can be described by Snell-Descartes laws. Considering a plan with a boundary composed of two mediums with different refractive index n_1 and n_2, an incident ray with an angle a_1 to the normal will be reflected with the same angle a_1 and refracted with an angle a_2 (**Figure 14**) by the relation : $n_1.\sin(a_1) = n_2.\sin(a_2)$. There exists a critical angle a_1 for which $a_2 = 90°$ which is equal to: $a_1 = \arcsin(n_2/n_1)$. Beyond this critical angle, the light is totally reflected. This particular angle is required in Total Internal Reflection Fluorescence (TIRF) microscopy, which is one of the methods in the thesis (cf. section 1.9.3 and chapter 1 in 2.1).

The diffraction of light is an important characteristic that explains how we see objects through a microscope. For instance, a fluorescent molecule will emit photons in all directions and only a fraction will be collected by the objective. The circular aperture of the objective will diffract the transmitted light and as a result, only an Airy disc can be imaged instead of a finite small point. The 3D representation of an Airy disc is called a Point Spread Function (PSF). In light microscopy, because of the diffraction of light, there is a minimal distance under which two objects can no longer be resolved (**Figure 15**). The minimal distance d (called the Rayleigh criterion) between two objects illuminated by a light source with a wavelength λ through an objective with a numerical aperture (NA) is determined by the Abbe's law : $d = \frac{\lambda}{2NA}$. By this relation, the resolution of a microscope only depends on the light source and the numerical aperture of the objective. As the visible spectrum is ranged from approximately 400 to 800 nm, taking a light source of 400 nm and a NA of 1.49, the resulting resolution is around 135 nm.

Nevertheless, there are several ways to overcome this limitation in resolution: (i) do it optically with super resolution microscopy or (ii) overcome resolution limit by doing a mathematical trick. We will focus on the second option. In that case, if the objects are sufficiently separated,

the position of a single object can be determined with precision much below the size of its airy disk. This is because the center of the emission pattern from the object can be determined by fitting its PSF using a two-dimensional Gaussian function, resulting in a precision of several nanometers in the x-y plane (Yildiz and Selvin, 2004). The standard error of the mean (sem) of the PSF can serve as a precise location of the molecule. A theoretical calculation of the sem (σ) in fluorescence microscopy is determined by the relation :

$$\sigma^2 = \frac{s^2}{N} + \frac{(\frac{a^2}{12})}{N} + \frac{8\pi s^4 b^2}{a^2 N^2}$$

with a the size of pixels, N the number of photons, b the background noise, s the standard deviation of the PSF. The final term corresponds to the background noise involvement. This is why reducing background noise is an important lead of development in wide-field fluorescence microscopy and that TIRF microscopy is of interest in single molecule fluorescence study (cf. section 1.9.3).

Even though super-resolution microscopy has led to great advancements in biophysics and their importance has been recognized by a shared Nobel prize in chemistry in 2014, I will only discuss them briefly below. Super-resolution microscopy allows to overcome the light diffraction limit by using innovative optical methods, and achieving spatial resolution far beyond the classical limit set by the diffraction of light. Among these methods, the most known techniques are Stochastic Optical Reconstruction Microscopy (STORM), Photo-Activated Localization Microscopy (PALM) and Stimulated Emission Depletion (STED) microscopy. PALM and STORM are based on stochastically switching individual fluorescent molecules (photoswitchable proteins) between a fluorescent and a dark state whereas STED spatially modulates the illumination light of a fluorophore with a laser beam that is used to deplete a large area surrounding the fluorophore (Betzig *et al.*, 2006; Kamiyama and Huang, 2012). However, breaking diffraction limit has a cost, and the biggest disadvantage of these techniques is that, to date, the commercialy available models are very expensive compared to more “routine” devices like TIRF microscopes.

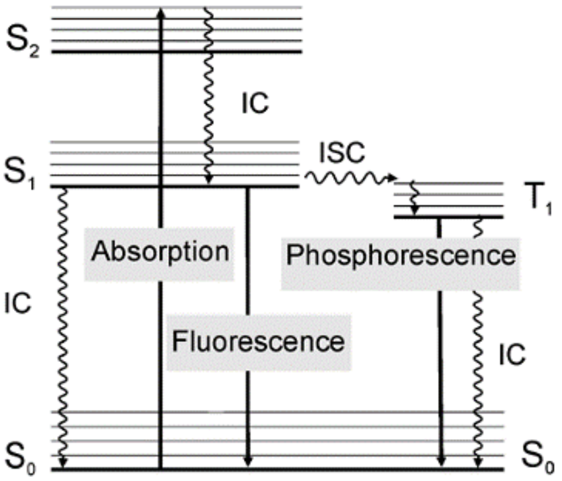

Figure 16: Scheme of the Jablonski diagram. Electronic states (S_0, S_1, S_2) and their corresponding vibronic states are displayed as horizontal lines. Wavy lines illustrate non radiative transition whereas straight lines show radiative emission (Scheme taken from van den Wildenberg, 2011).

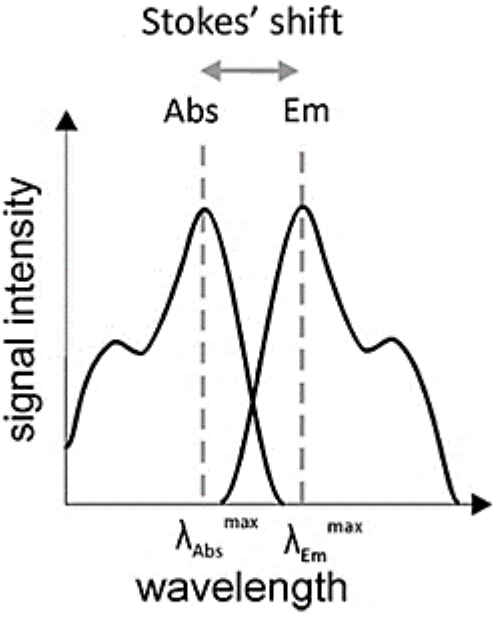

Figure 17: Illustration of the Stoke's shift. The excitation wavelength required for a fluorophore to absorb light (λ_{Abs}) is lower than the emission wavelength of light emitted by the same fluorophore (λ_{Em}). The peaks at which the maximum amount of light is absorbed and emitted are separated by a length called the Stoke's shift (Scheme taken from van den Wildenberg, 2011).

1.8.2. Fluorescence principles

Fluorescence is a process in which matter absorbs light and re-emits at a different wavelength. The process of fluorescence was first introduced by Sir George Gabriel Stoke in 1852 and was explained in 1933 by the professor Aleksander Jablonski in its diagram of his name: the Jablonski diagram. An example is shown in **figure 16**. When a fluorophore absorbs photons, its electrons will go through several electronic states of different energy levels (S_0, S1, S_2); from a relaxation state (S0 ground state) to an excited state (S_1, S_2). When electrons are excited in higher singlet electronic states (S1, S2), they will spontaneously relax by different mechanisms such as vibrational relaxation inside the same electronic state (10^{-14}-10^{-12} s, relax to a lower electronic state by internal conversion (IC), by re-emitting photons that is fluorescence (10^{-9}-10^{-7} s) or by intersystem crossing (ISC) involving a triplet state (T) resulting in phosphorescence (10^{-3}-10^{2} s).

When electrons relax from higher to lower electronic states, they lose energy. That is why for the fluorescence mechanism, the energy of the excitation light (photons) is always lower than the energy of the emitted light by the fluorophore. This phenomenon is characterised by the relation of Planck, who determined that the energy of a photon E is the product of the constant of Planck h and the speed of light c divided by its wavelength λ : $E=(h.c)/\lambda$. This explains why fluorophores always display an excitation wavelength that is lower than the emission wavelength that is illustrated by the Stoke's shift (**Figure 17**).

Fluorescence microscopy relies on four main components, which are: (i) a light source that can be of different natures like LED lamps or lasers, (ii) a filter cube that is composed of an excitation filter, an emission filter and a dichroic mirror, (iii) an objective with a specific magnification, numerical aperture NA and light aberration correction, and (iv) a detector that is usually a camera. In epifluorescence microscopy cameras like charge coupled device (CCD) and electron multiplying charge coupled device (EMCCD that is useful in single molecule fluorescence microscopy) are used, while confocal microscopes may use point detectors.

Fluorescence microscopy has blossomed with the discovery and the development of the Green Fluorescence Protein GFP initially presents in the jellyfish Aequorea victoria and other derived fluorescent protein like the enhanced Green Fluorescent Protein (eGFP) or the Yellow Fluorescent Protein (YFP) by the co-Nobel Prizes of chemistry in 2008: Roger Tsien, Osamu Shimomura and Martin Chalfie. Fluorescence microscopy has become a robust tool that is often

used in biology research, for instance to localise a molecule within a cell or to analyse specific interaction between molecules such as protein-protein interactions and characterised protein displacement.

1.8.3. Dye properties

A crucial aspect of the conduct of a microscopy experiment is the choice of the adequate fluorophore. First, fluorophores can be classified by their nature. We can distinguish synthetic dyes such as Cy3, Alexa Fluors and ATTO dyes, or fluorescein isothiocyanate (FITC), fluorescent proteins like enhanced green fluorescent protein (eGFP) or yellow fluorescent protein (YFP) that contain a chemical structure with fluorescent properties, quantum dots that are semiconductor nanocrystal structures, and natural fluorophores such as chlorophyll or flavin (van den Wildenberg et al., 2011). For single molecule fluorescence assays, synthetic dyes are commonly preferred over fuzed fluorescent proteins as they are smaller and less likely to not perturb the protein of interest. Furthermore, synthetic dyes can be covalently bound in a simple way to the protein of interest, they display less sensitivity to buffer conditions and their chemical and photophysical properties are usually well defined in the commerce (Modesti, 2011).

Fluorophores have important properties that will have an influence on the experiments and results, and they thus should be chosen carefully. Each fluorophore displays an absorption and an emission spectrum that must fit the optical configuration of the microscope that includes the available absorption and emission filters and dichroic mirrors. It is preferable to use fluorophores that are spectrally well separated as it will be easier to accurately filter the light (for instance if multiple dyes are used during an experiment).

Other important features are the quantum yield, the molar extinction coefficient and the brightness as well as the excited state lifetime. The quantum yield corresponds to the ratio of absorbed versus emitted photons. The higher it is (tends to 1) the better it is, as it will re-emit almost all the light absorbed. The molar extinction coefficient measures the quantity of light absorbed by a mole of fluorophore. The product of the quantum yield by the molar extinction coefficient will give the brightness of the fluorophore.

Also, the size of fluorophore is important, especially if it is used as a label for a protein for example. Synthetic dyes usually have a size of around 1 nm length and fit well for labelling protein. On the contrary, quantum dots are around 10-15 nm length and can potentially disturb

a protein activity. Thus, it is important to select the right dye depending on the experimental objectives. Note that the characteristics of fluorescent molecules can also be affected by the local environment such as pH, polarity, ions or interaction with other molecules that could quench the fluorophore or hinder its capacity to penetrate the cell. A well-known limitation in fluorescence microscopy experiments is photobleaching. Photobleaching is the loss of the capacity of a dye to fluoresce caused by a permanent photochemical alteration often due to the interaction with ROS in solution generated by the illumination. However, there exists anti-fading agents that can be used to minimise photobleaching, increasing the lifetime of the fluorophores and allowing longer experiments.

Importantly, fluorophores have also been developed to visualize double stranded DNA molecules. DNA has no fluorescent properties and thus, it has to be stained for single molecule detection. Novel dyes have been developed and commercialised for dsDNA detection that remain largely non-fluorescent in solution and display a large increase in their fluorescent quantum yield upon binding DNA. Among these are YOYO-1 and SYTOX Orange dyes that have greatly enhanced single molecule fluorescence detection of DNA-protein interactions (Kaur *et al.*, 2019). To date, there is no dye available to image ssDNA.

1.9. Single molecule approaches to assess DNA-protein interactions

1.9.1. Introduction

Single molecule biophysics was born with an experimental challenge : Is it possible to examine and study a single biological molecule? Over the last decade, single molecule techniques have experienced remarkable growth in the field of biology and can be divided into two main categories: (i) force spectroscopy and (ii) fluorescence spectroscopy. Single molecule research in biophysics has been rewarded by a shared Nobel prize of chemistry in 2014 granted to Stefan Hell, Eric Betzig and William Moerner, and in 2018 by a Nobel prize in physics granted to Arthus Ashkin for his work on optical tweezers.

Single molecule assays give complementary information to classical biochemical assays. These techniques, such as micromanipulation or fluorescence imaging, allow to eliminate the spatial and temporal averaging effects inherent to overall measurements and provide access to rare or transient events, difficult to observe by overall measurements. The term "single molecule

experiments" refers to the experiments that focus on the investigation of properties of individual molecules. In the past two decades, biophysics techniques have emerged and have made possible the manipulation of DNA and the imaging of DNA-proteins complexes in real time.

Single molecule fluorescence techniques proved to be particularly relevant to visualise and quantify protein motion. The motion of individual molecules can be quantified by calculating the mean squared displacement (MSD). In fluorescence single molecule assays, the point spread function of molecules can be tracked in time with nanometer precision using two-dimensional Gaussian fit of the intensity profile in each frame for the tracking molecule (cf. section 1.8). Positions are then connected to form a trajectory from which the displacement is calculated for different time intervals. The MSD is then determined by averaging the squared displacement per time interval for one trajectory and the diffusion coefficient D can be determined by the equation $\mathrm{MSD}(\tau) = 2D\tau \bullet d + V^2\tau^2$ in which d is the dimension of freedom and τ the time value and V the drift constant velocity (Qian *et al.*, 1991). MSD not only determine the diffusion coefficient but also give information about the maximum range of displacement of the particle as well as the situation the particle is in, such as random motion or directional movement. In addition, single molecule fluorescence spectroscopy methods provide information on the location and dynamics of proteins binding to a ligand, such as their on and off rates, or conformational changes within molecules (Gross *et al.*, 2010).

Single molecule force spectroscopy such as optical and magnetic tweezers are commonly used to study the mechanical properties of biopolymers like DNA and their interactions with other molecules. These methods grant access to study mechanical parameters of DNA (like its flexibility or its length) but they may also give information about the kinetics and mechanochemistry of bound proteins like DNA polymerases for instance (Gross *et al.*, 2010). A combination of force manipulation and fluorescence spectroscopy such as Dual-optical fluorescence tweezers with fluorescence microscopy or single molecule Forster Energy Transfer (smFRET) have greatly enhanced our knowledge of DNA-protein interaction mechanisms. This provided insights into biological events by monitoring and visualising the dynamic behaviour of individual biomolecules interacting with others. Today, some of these techniques are becoming standard techniques, with many commercial solutions available and with technical support.

Single molecule experiments had a craze especially because in bulk assays (such as gel electrophoresis) millions of biomolecules are subjected to analysis, and therefore, the results reveal the average behaviour of a large number of molecules (Takahashi et al., 2021). Instead, single molecule experiments not only reveal the average behaviour, but they also provide information on the dynamic behaviours of these molecules during a biological process in which the same molecule can act in several ways. For example, during mtDNA transcription, it has been shown that POLRMT can "pause", and that TEFM enhances transcription elongation by modifying POLRMT pausing dynamics (Yu et al., 2018); or else that HsmtSSB displays only the low binding mode during a strand displacement initiated by the polymerase Phi29 (Morin et al., 2017).

One of the main limitations of single molecule techniques is that often many experiments are required in order to provide large numbers of observations and adequately study the sample distributions, subpopulations and rare events (Hill *et al.*, 2017). To overcome this limitation, single molecule techniques have been developed that are competitive in high-throughput data analysis. Examples of these are DNA curtains, acoustic force spectroscopy, zero-mode waveguide and magnetic tweezers.

1.9.2. DNA manipulation

Physical properties of DNA

During biological events such as DNA replication, transcription and repair, DNA is constantly handled by maintenance proteins that bend, torque, compact or unwind it. Understanding the physical properties of DNA under tension is then necessary for the study of DNA-protein interactions involved in these events. The physical form of the DNA molecules fluctuates in solution without external forces due to its flexibility and Brownian motion. DNA manipulation techniques offer the possibility to control the DNA conformation by trapping DNA ends and/or by exerting external forces on it. This allows for the measurement of tensions and torque on DNA, as well as the displacement and force extension of DNA. DNA manipulation techniques coupled with fluorescence microscopy allow the analysis of the motion of proteins on DNA, conformational changes of the DNA, and proteins binding to specific DNA sequences (Takahashi *et al.*, 2021; Xu *et al.*, January and May 2023). To analyse the stretching of DNA under applied force, dsDNA has been modelled as a long semi-flexible polymer in the worm-like chain model (WLC) and the extensible WLC (eWLC) in the case of

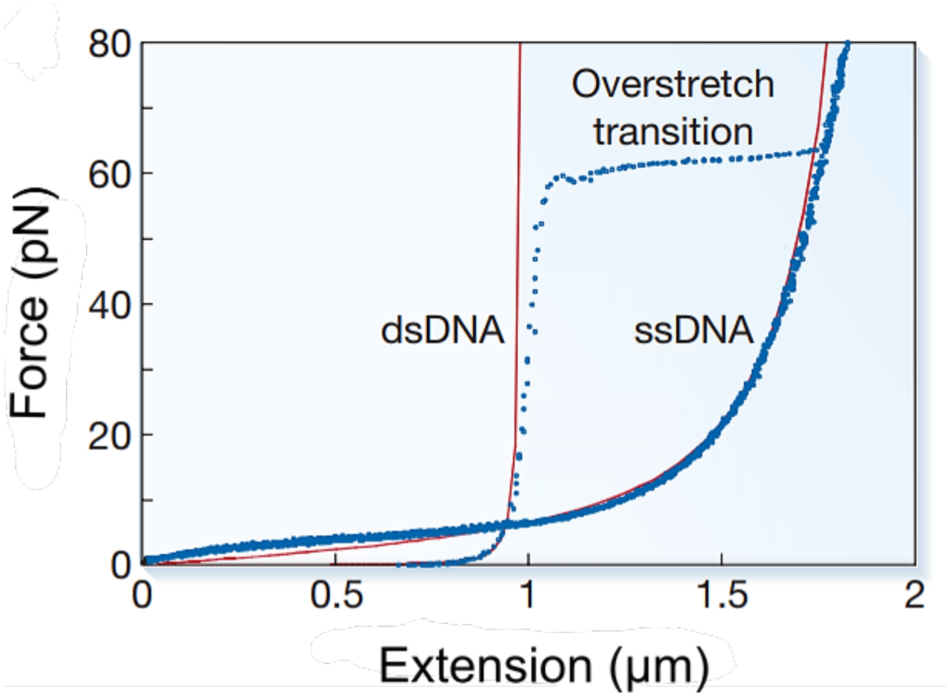

Figure 18: Force distance curve. Graph of a force distance curve that is generated by following the displacement of the object tethered to dsDNA or ssDNA (usually a microbead) in function of applied force, leading to a curve that depicts DNA molecules flexibility and length (from Bustamante et al., 2003).

external forces up to 20-30 pN. This model describes the elastic behaviour of dsDNA. By measuring the DNA extension (x) during a stretching process (the end to end distance of the DNA) in function of the force (F), the eWLC informs on the persistence length of the DNA (Lp) and its contour length (Lc) with the relationship (Odijk, 1995) :

where kbT is the Boltzmann’s constant times absolute temperature and K the stretch modulus of dsDNA (sometimes written S). For ssDNA, the extensible Freely Jointed Chain model

$$x = L_c \left[1 - \frac{1}{2} \sqrt{\left(\frac{k_b T}{F L_p} \right)} + \frac{F}{K} \right]$$

(eFJC) is applicable (Smith *et al.*, 1996) with the following relationship :

$$x = L_{ss} \left[coth \left(\frac{Fb}{k_b T} \right) - \frac{k_b T}{F_b} \right] \left(1 + \frac{F}{S} \right)$$

where L_{ss} is the contour length of the ssDNA, b is the Kuhn length which is equal to twice the persistence length when the contour length of the DNA molecule is much longer than its persistence length (Lee *et al.*, 2007), and S is the stretch modulus of ssDNA. With single molecule force spectroscopy, mechanical features of DNA were characterised, and it was shown that dsDNA has an approximative persistence length of 45-50 nm and that DNA melting occurs at around 60 pN, referring to the overstretching plateau during DNA force stretching (**Figure 18).** Several single molecule force spectroscopy as well as single molecule fluorescence microscopy techniques involving DNA manipulation will be detailed thereafter.

Optical tweezers

The conformation of the DNA fluctuates in solution due to its flexibility and due to Brownian motion. For instance, DNA supercoiling conformation can be easily induced by thermal agitation at room temperature (Takahashi et al., 2021). Therefore, it is challenging to study DNA/protein interaction or localisation without controlling the DNA conformation state, nor its end to end distance, that represents the distance separating the DNA molecule ends which should not be mistaken with the contour length of the DNA that is its characteristic length. Several methods have been developed for single DNA molecule manipulation, so called single molecule force spectroscopy. The most common and powerful tool is the DNA manipulation by optical tweezers introduced by Ashkin (Ashkin, 1992). This method relies on

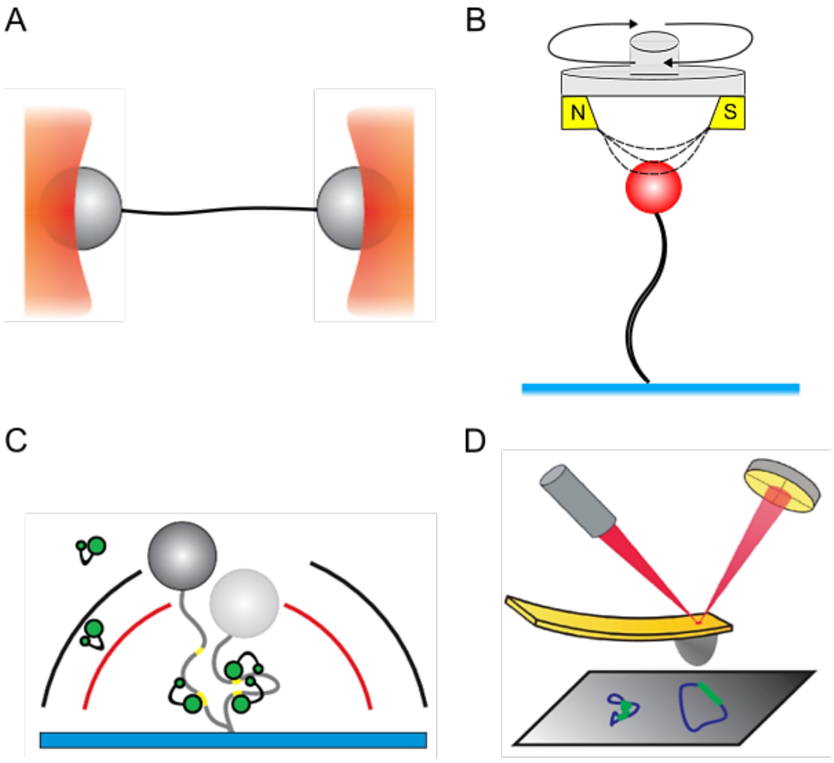

Figure 19 : Common single molecule techniques. (**A**) Dual-trap optical tweezers. (**B**) Magnetic tweezers. (**C**) Tethered Particle Motion (TPM). (**D**) Atomic Force Microscopy (AFM) (Magnetic tweezers schema adapted from Takahashi et al., 2021).

the use of an extremely bright laser beam that will trap a microparticle by exerting a force on it caused by refraction of photons. By attaching each end of a linear DNA molecule to a particle, and trapping the particles in a dual-trap optical tweezer, the DNA molecule can be indirectly manipulated by moving the trapped particles, thus a force can be exerted on a DNA molecule (**Figure 19A**). This method presents the great advantage over other trapping methods that it can be coupled with fluorescence microscopy and second, DNA molecules are not fixed to a surface, decreasing the chances of undesirable interactions with the surface. However, a drawback of this technique is the low number of DNA molecules that can be manipulated at the same time, thus necessitating to repeat experiments many times to have sufficient amounts of data. Optical tweezers have been particularly useful to study DNA organisation flexibility and compaction as well as DNA-protein assembly into nucleoprotein structure (Gross *et al.*, 2010; Heller *et al.,* 2013; Farge et al., 2012; Morin *et al.*, 2017; Plaza *et al.*, 2023). It also allows to study protein binding affinity and kinetics, cooperativity, protein dissociation, DNA strand displacement synthesis and unwinding mechanism, polymerase processivity and interaction with protein partner, protein binding modes, as examples (Farge et al., 2012; King et al., 2018, Plaza-G.A et al., 2023; Naufer et al., 2021; Morin et al., 2017). Another interesting feature of this method is the feasibility to generate single stranded template from double stranded DNA via force melting as force intensity can be subtlety controlled (Candelli et al., 2013).

Magnetic tweezers

A variation of optical tweezers called magnetic tweezers allows DNA manipulation by using a magnetic bead attached to one end of DNA whereas the second end is anchored to a glass surface. The magnetic bead is manipulated using a magnet above it, exerting force on the DNA molecule (**Figure 19B**). An interesting feature of this method is the ability to rotate the magnet, inducing the rotation of the magnetic bead that leads to the rotation of the DNA tether. In this way, magnetic tweezers can be a useful tool to control DNA supercoiling and induce torque of the DNA backbone and consequently study the behaviour of topoisomerase proteins for instance (Gunn et al., 2018). They are also useful to study DNA compaction and other interacting proteins enhancing compaction effects (Bell *et al.*, 2015). Magnetic tweezers have the advantage over the optical tweezers to generate more data per experiment as more DNA molecules can be followed at the same time.

Atomic Force Microscopy

Unlike the previous DNA manipulation techniques, atomic force microscopy is usually used for imaging rather than DNA manipulation. AFM allows imaging of biological samples (like DNA molecules) on the nanoscale resolution while the sample remains fully hydrated. Imaging process relies on a nanotip connected to a cantilever that probes the sample. A laser beam is reflected onto a position-sensitive photodiode detector as the cantilever moves in response to the sample topography (**Figure 19D**). However, it can be used as a single molecule method as the cantilever and the mica surface can be functionalised (i.e. chemically engineered to interact with sample of interest) to tether DNA molecules (or antibodies) and use the cantilever movement to apply and measure forces using a molecular force probe (Chung *et al.*, 2013; Morfill *et al.*, 2007). As example, AFM was used to study affinity of antibody-antigen couple (Morfill *et al.,* 2007) or to study the rupture force of a DNA-peptide interaction (Chung *et al.*, 2013).

With the emergence of high-speed AFM (HS-AFM), real-time nanoscale dynamics of DNA-protein interactions is possible in millisecond timescale conditions. Other advantages of AFM is that samples are not fixed and remain in fluid environments, thus buffer composition can be controlled such as protein concentrations, pH or cation types. As examples, AFM was used to assess mtSSB and EcoSSB cooperativity, DNA shortening and compaction by TFAM, binding localisation of SSB as well as binding mode transition depending on ionic environment (Kaur et al., 2018; Hamon et al., 2007; Farge et al., 2014). The great advantage of AFM is therefore to directly visualise dozens of individual DNA molecules interacting with proteins at a nanoscale resolution without strong fixation nor dehydration.

Acoustic Force Spectroscopy

There are other high-throughput single molecule DNA manipulation techniques that allows analysis of a large number of DNA molecules at the same time such as Acoustic Force Spectroscopy (AFS), High-Speed Atomic Force Microscopy (HS-AFM). AFS methodology relies on attaching DNA molecules that are tethered at one end to a glass surface and at the other end to microbeads, usually polystyrene beads, in a microfluidic chamber (cf. chapter one in 2.1). The manipulation of the DNA is done indirectly by exerting an acoustic force in pN on the beads via a piezo element situated above the glass slide which is connected to a generator that generates acoustic waves. The beads then move towards the acoustic node exerting a

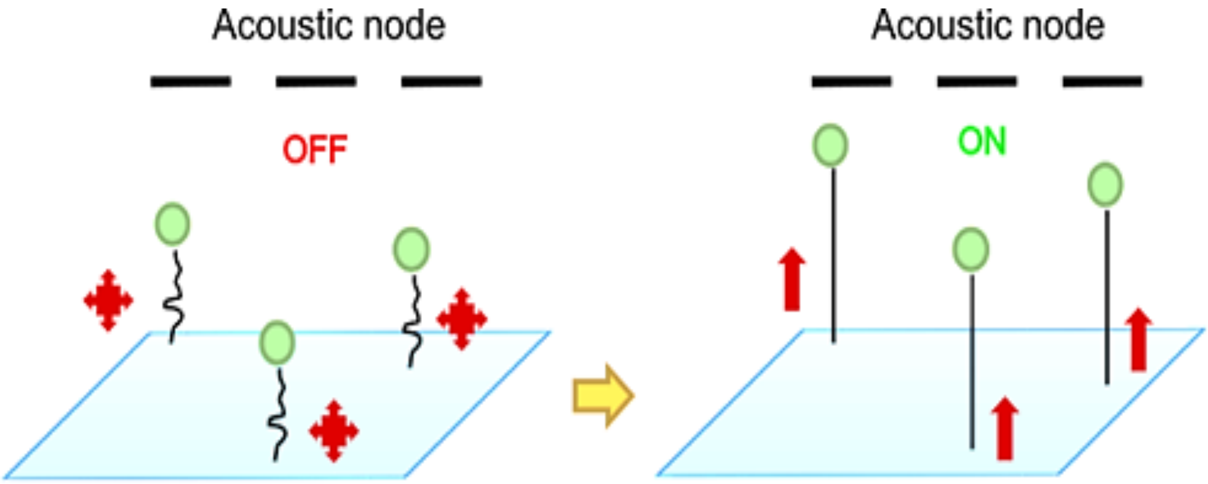

Figure 20: Acoustic Force Spectroscopy. Illustration of the AFS method. DNA molecules are anchored to a glass surface in a microfluidic chamber that has been functionalized. The other end of the DNA molecules are tethers to microbeads. DNA manipulation is done indirectly by exerting a force on microbeads via acoustic waves. Beads are pushed toward the acoustic node, resulting in the stretching of DNA molecules. Without force, AFS can act like TPM by simply measuring beads position in x,y,z plans that are submitted to Brownian motion.

stretching force on the DNAs (Sitters et al., 2014) (**Figure 20**). The DNA motion and stretching is monitored by following the bead motion similar to in magnetic tweezers using brightfield illumination with an inverted microscope. A Look-up table is generated by imaging the diffraction pattern of the beads within a range of z-steps in nanometers related to increased force steps in pN, allowing to know the displacement of the beads during DNA force extension in x, y and z plans. AFS has been used to analyse DNA flexibility and compaction by architectural proteins such as histone-like nucleoid-structuring proteins (Lin *et al.*, 2018), or analyse step assembly mechanism of virus-like particles (Rosmalen *et al.*, 2020). As the DNA tethers are in a microfluidic chamber, buffer exchanges can be easily done, as well as introducing protein partners or inhibitors, and temperature can also be controlled (to some extent) with an appropriate device. Therefore, AFS is a promising tool to study DNA-protein and protein-protein interactions. Note that AFS is not limited to DNA-protein interaction and displays a lot of different applications. For instance, AFS can also be used with cells in the microfluidic chamber and study interactions with molecules of interest like CD4 T lymphocytes to fibronectin modulated by interleukin (Kamsma *et al.*, 2018).

Tethered Particle Motion (TPM)

Single DNA molecule manipulation techniques like optical and magnetic tweezers and acoustic force spectroscopy (AFS) share a common step that is the trapping of the DNA molecules to microbeads. This step is important as it allows the stretching of the DNA tethers via external forces exerting on the beads. However, it is not always necessary to apply a force to measure DNA-protein interaction and dynamics. DNA tethers that are not subject to force move according to the Brownian motion of beads. By analysing the Root Mean Square of the beads (RMS), conformational changes of DNA tethers induced by proteins can be monitored over time such as DNA compaction and flexibility and consequently study binding protein affinity (**Figure 19C)** (Henneman et al., 2018; Driessen et al., 2014; Kovari et al., 2018). This method has the advantages of being simple, cheap and allows to monitor a high number of tethers simultaneously.

Note there exist other single molecule DNA manipulation techniques that will not be detailed such as DNA manipulation by orientation forces using Coulomb forces, DNA manipulation of terminal immobilized DNA by electric field that is similar in methodology to fluid flow (explained in section 1.9.3), DNA manipulation by interface movement, DNA origami and nanopores. Review of these techniques can be found in Takahashi et al., 2021.

1.9.3. Single molecule fluorescence microscopy

Fluorescence microscopy became an indispensable and common tool for biologists, since it can be used to observe and localise biomolecules within cells. However, what it is observed in standard fluorescence microscopy is millions of molecules. Consequently, a question has been raised: is it possible to accurately observe the fluorescence emitted by a single molecule? To this end, molecules should be separately manipulated (discussed in section 1.9.2) and illumination should be controlled to excite only the molecules desired. Single molecule fluorescence microscopy thus relies on the accurate detection of the fluorescence emitted by one or more single molecules in real-time, while putting efforts to limit background signal to increase the signal to background noise ratio. Indeed, to gather more detailed and clear information, it is important to have the highest possible signal to noise ratio. Approaches to do this include the design of fluorophores with high brightness and develop microscopy methods to decrease background signal and probe only small volumes around the molecule of interest.

Single molecules fluorescence microscopy can be classified into two broad categories that are (i) confocal fluorescence microscopy where an image is generated by scanning a sample with a focussed laser, while a pinhole in front of the detector blocks out of focus light and (ii) wide-field fluorescence microscopy where a larger region around the sample is excited (Gross *et al.*, 2010). But how can we reduce background signal in wide field fluorescence microscopy? A successful method is Total Internal Reflection Fluorescence (TIRF) microscopy that has been developed by Axelrod and coworkers (Axelrod *et al.*, 1983). This method was used in this thesis. TIRF microscopy relies on the Snell and Descartes law (cf. section 1.8) in which a laser beam can be totally reflected on contact to a surface if it arrives with a particular angle called the critical angle. At the contact point, an evanescence wave is generated and its energy decays exponentially as it goes through the medium in which the sample remains. As a result, only the molecules in the region between the surface and 100-200 nm above it are excited, greatly improving the signal to background noise ratio since molecules in solution are not excited. TIRF microscopy is well suited with DNA manipulation requiring DNA anchoring to a glass surface and flow stretching. Combined with DNA manipulation techniques, single molecule fluorescence microscopy techniques have greatly improved our understanding of mechanisms underlying DNA-protein and protein-protein interactions. Presented below are single molecule fluorescence techniques that are commonly used to study DNA-protein interaction dynamics (**Figure 20**).

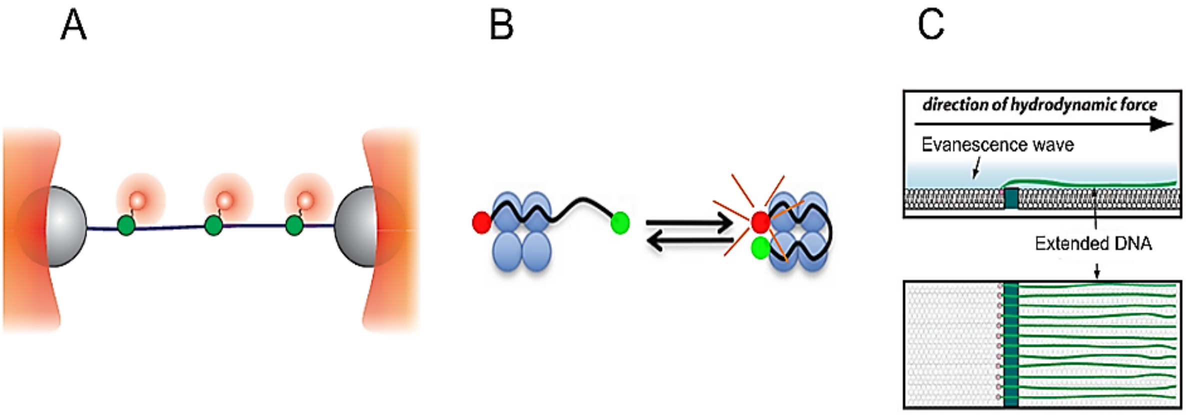

Figure 21: Single molecule fluorescence microscopy common techniques. (**A**) Schema of dual-trap optical tweezers. A DNA molecule is trapped at both end by microbeads that usually interact with biotin-streptavidin linkage. Both microbeads are then manipulated by laser beams (red beam) allowing DNA manipulation. Fluorescent protein of interest can be used and visualised by different types of illumination such as wide-field, confocal or super-resolution STED. (**B**) FRET illustration with a fluorophore couple. Conformational change of the protein in blue is seen as the two fluorophores reached a sufficient distance that allow green dye to transfer its energy to the red dye that emits fluorescence that is captured by the microscope devices. (**C**) Cartoon of the DNA curtains technique. In a microfluidic chamber functionalized with a lipid bilayer, DNA molecules are tethered to the lipid bilayer. The last are pushed by fluid flow toward a nanobarrier that will stop their progression and lead to the alignment of the DNA molecules (FRET illustration adapted from Qian and Johnson, 2017 and DNA curtains schema from Fazio et al., 2008).

Optical tweezers combined with fluorescence

Optical tweezers can combine force (cf. section 1.9.2) and fluorescence spectroscopy, with fluorescent-labelled proteins or with FRET constructs (smFRET) and even with super-resolution microscopy like STED. As mentioned before in section 1.9.2, this method relies on the use of an extremely bright laser beam that will trap a microparticle by exerting a force on it caused by refraction of photons. By attaching each end of a linear DNA molecule to a particle, and trapping the particles in a dual-trap optical tweezer, the DNA molecule can be indirectly manipulated by moving the trapped particles, thus a force can be exerted on a DNA molecule Fluorescence illumination can be wide-field or use confocal microscopy (Gross *et al.*, 2010) (**Figure 21A**). The combined fluorescence microscopy allows visualising in real-time protein functions and interactions in a tense environment. Hence, this method is useful for instance to study diffusion mechanism, force binding and dissociation dependency and binding kinetics and stability, sequence specific binding, footprint, cooperativity, DNA compaction or conformational changes within proteins (Suksombat *et al.*, 2015; Xu *et al.*, January and May 2023; King *et al.*, 2018; Heller *et al.*, 2013; Farge *et al.*, 2012).

Single molecule FRET (smFRET)

Using small-molecule organic fluorophores, Förster Resonance Energy Transfer (FRET) is widely used to probe biomolecular interactions and conformational dynamics *in vitro* and increasingly in living cells by detecting nanoscale conformational changes as well as ligand binding events (Juette *et al.*, 2014). FRET is based on energy transfer from a donor fluorophore to a nearby acceptor leading to fluorescence emission of the acceptor with partial quenching of the donor. The transfer efficiency depends on the distance between the two fluorophores that need to be in close proximity (10 - 90 Ångstrom) (**Figure 21B**). Therefore, it is possible by measuring the FRET signal to infer changes in the positions of the two complementary fluorescent probes, positions that are designed experimentally in order to get information about molecules interactions (Juette *et al.*, 2014). smFRET is usually combined with wide-field TIRF microscopy. It was used for examples, to study EcoSSB motion and binding modes transition (Suksombat *et al.*, 2015; Roy *et al.*, 2010; Zhou *et al.*, 2011). smFRET is evolving with multiple colours FRET with three or four fluorescence molecules to enable the study of multiple protein interactions but it tends, in return, to limit the signal-to-noise ratio and thus the interpretation (Juette *et al.*, 2014). FRET is thus a powerful tool to study DNA-protein interactions and combined with DNA manipulation methods, single molecule FRET

(smFRET) is a promising technique to challenge the difficulty to image complex systems of multitude of pairwise interactions at biologically relevant timescales.

DNA curtains

DNA curtains is a DNA manipulation method that was developed by Eric Greene and coworkers (Fazio *et al.*, 2008) and that is combined with wide-field fluorescence microscopy, generally TIRF microscopy. This method allows thousands of DNA molecules to be aligned and stretched by fluid flow simultaneously in real-time in a microfluidic chamber, thus providing very high throughput data measurements (**Figure 21C**). The method is explained in Silverstein *et al.*, 2014. Briefly, metallic patterns are first deposited on a fused silica microscope slide by electron-beam lithography and then the slide is connected to a microfluidic chamber. These metallic patterns serve as a nanoscale diffusion barrier. The slide surface is then passivated by deposition of a lipid bilayer in which a fraction of the lipid head group has been functionalized with streptavidin, which allows biotinylated DNA substrate to be attached to the bilayer surface. The lipid bilayer also greatly limits non-specific surface adsorption and provides an inert environment. Finally by fluid flow, the DNA tethers are pushed towards the nano-barrier which stops the lipid diffusion. It results in DNA molecules to be aligned along the nano-barrier and can be stretched and bound with fluorescent labelled proteins. DNA curtains technique has demonstrated to be particularly relevant for studying protein motion on dsDNA and ssDNA as well as tracking proteins that switch between DNA strand by cross-strand disposition or visualise DNA recombination and protein partner interactions (Silverstein *et al.*, 2014; Fazio *et al.*, 2008, Gibb *et al.*, 2012; Ma *et al.*, 2017; Qi *et al.*, 2016).

2. Aims of this thesis

There is still a lot to understand about mitochondrial DNA metabolism and mitochondria functions within the cells. More interest was generated for mitochondria since the development of NGS that greatly helped the diagnosis of mitochondrial diseases. Mitochondrial diseases are rare genetic diseases, usually inherited, with an estimated prevalence of 1/5000 new-borns. They display a large clinical heterogeneity due to the ubiquitous nature of mitochondria in organs and tissues. Genetic mutations leading to mitochondrial diseases can occur either in nuclear DNA or in mitochondrial DNA, affecting a large number of proteins involved in different process, such as mitochondrial DNA maintenance, mitochondrial fusion, ATP synthesis by the electron transport chain, maintain of a balanced pool of nucleotides, or homeostasis regulation. Diseases can be studied at different levels: organ and tissues level, cell level, or molecular level. In the past two decades, single molecule methods have arisen and enabled the investigation of DNA-protein interaction mechanisms at a single molecule level. In this thesis we used two single molecule techniques, namely acoustic force spectroscopy (AFS) and total internal reflection fluorescence microscopy (TIRFm) coupled with DNA flow stretching, as well as biochemical assays to characterize the molecular mechanisms of diseases caused by TFAM P178L and mtSSB R107Q, two mtDNA maintenance protein variants implicated in human disease.

The first chapter of this thesis is a technical description of our single molecule TIRF and AFS set-ups and experiments. Protocols to analyse protein-DNA binding interaction and protein motion on DNA are described. In this chapter are also discussed issues that may be encountered during such experiments and propose ways to avoid or overcome them.

In the second chapter we have studied the disease-causing mutant TFAM P178L that was shown to be involved in mtDNA depletion in patients. We performed biochemical experiments such as *in vitro* replication assay (rolling circle), *in vitro* transcription at HSP and LSP, electromobility shift assay (EMSA), structure modelisation and thermofluor stability assay as well as protease degradation assay by LON. Altogether, our results allowed the characterisation of TFAM P178L functions in replication and transcription, its stability and specific and unspecific binding affinity. We also analysed TFAM ability to bind and compact DNA using acoustic force spectroscopy (AFS). Finally, we carried out fluorescence experiments to assess TFAM motion by determining characteristic diffusion events as well as quantifying diffusion coefficient and oligomeric states. Our results show that the P178L mutation has no effects on

DNA binding, but mildly affects DNA compaction. In vitro transcription revealed that the amino acid change severely impairs TFAM capacity to initiate transcription at both heavy and light strand promoters. Molecular modelling suggests that both promoter sequence recognition and interaction between TFAM and the tether helix of POLRMT are altered by the mutation. Furthermore, the motion of TFAM P178L on DNA is unchanged but it seems that dimerization could be affected.

The third chapter focused on the study of the human mitochondrial SSB variant R107Q that was recently clinically investigated and is involved in mitochondrial maintenance defects like mtDNA depletion and deletion associated with autosomal dominant mitochondrial optic atrophy and retinal dystrophy. Since 2018, several clinical reports have described mutations of mtSSB that are associated with human diseases. In this chapter, we have studied the functional consequence of one of the most severe variants, R107Q. We first studied the oligomeric state of this variant and observed that the R107Q mutant is still able to form stable tetramers. On the other hand, we showed, using complementary single molecule approaches, that mtSSB R107Q displays a lower intramolecular ssDNA compaction ability and a higher ssDNA dissociation rate than the WT protein. We also directly visualized R107Q and WT SSB competing in real time for ssDNA and observed a marked advantage for the WT SSB. Combined, these results show that the R107Q mutation significantly impaired the ssDNA wrapping and compacting ability of SSB. These features are in line with our molecular modelling of SSB on ssDNA showing that the R107Q mutation results in an electronegative spot that interrupts an ssDNA-interacting-electropositive patch, thus reducing the potential SSB-ssDNA interaction sites.

The work in this thesis on these two main actors of the mtDNA maintenance might facilitate the understanding of the molecular origin of mitochondrial maintenance defects involving TFAM and mtSSB as well as the understanding of their roles in mtDNA metabolism in health.

Chapter 2.1: Quantify DNA compaction and TFAM dynamics using AFS and TIRF microscopy (Paper I)

Total Internal Reflection Fluorescence (TIRF) microscopy was developed in response to a problematic: How to improve signal to noise ratio in fluorescence microscopy? Confocal microscopy greatly improves signal to noise ratio by blocking photons that do not come from the laser focal plane, increasing axial resolution. However, time acquisition can be long and light power is usually high, limiting the use of low fluorophore concentrations and movie records, useful to study particle motion. This is where TIRF stands out. TIRF microscopy relies on a laser beam that exits from the objective lens under a particular angle (called the critical angle) leading to a total reflection of the laser at the interface between the glass and the sample (cf. section 1.8). At the contact point, an evanescence wave is generated of which its energy decays exponentially as it goes through the sample, illuminating fluorophores in 200 nm of depth with low energy power. Therefore, TIRF greatly improves axial resolution and signal to noise ratio by exciting only a small region of interest. Coupled with DNA manipulation by fluid flow, TIRF is a powerful tool to visualise a high number of DNA molecules anchored to a glass surface simultaneously, and with a low illumination power, it is a method of choice to record single particle motion interacting with DNA.

Acoustic Force Spectroscopy (AFS) is a single molecule force spectroscopy technique that allows the manipulation of multiple DNA tethers simultaneously in a microfluidic chamber. A great advantage of AFS is that it combines Tether Particle Motion (TPM) with DNA force stretching. Allowing buffer exchanges, it is a good technique to analyse DNA-protein interactions with buffer composition variations or by flushing in protein partners. One end of the DNA tethers is attached to the glass surface of the chamber and to the other end to a microbead. By exerting acoustic forces on beads, we indirectly manipulate DNA tethers, stretching them or maintaining them static at a constant force. By correlating displacement of the beads with the applied forces, we obtained a force distance curve that gives insights of the mechanical properties of DNA tethers, with or without proteins bound.

In this paper, we extensively described in two protocols to study TFAM binding, compaction, and motion on individual double-stranded DNA molecules with AFS and TIRF microscopy. In a first step, we explained how to perform DNA trapping and how to measure TFAM effects on dsDNA using Root Mean Square (RMS) and force extension curve analysis. In a second step, we described how to perform two-colour TIRF microscopy with our customized experimental

setup, from TFAM labelling with fluorophore, DNA manipulation by fluid flow stretching in a microfluidic chamber, TFAM tracking on dsDNA. Finally, this paper gives advice to avoid some experimental issues and help to troubleshoot issues that can be encountered during such experiments (publication 2.1).

Chapter 10

How to Quantify DNA Compaction by TFAM with Acoustic Force Spectroscopy and Total Internal Reflection Fluorescence Microscopy

Martial Martucci, Louis Debar, Siet van den Wildenberg, and Geraldine Farge

Abstract

Mitochondrial transcription factor A (TFAM) plays a key role in the organization and compaction of the mitochondrial genome. However, there are only a few simple and accessible methods available to observe and quantify TFAM-dependent DNA compaction. Acoustic Force Spectroscopy (AFS) is a straightforward single-molecule force spectroscopy technique. It allows one to track many individual protein-DNA complexes in parallel and to quantify their mechanical properties. Total internal reflection fluorescence (TIRF) microscopy is a high-throughput single-molecule technique that permits the real-time visualization of the dynamics of TFAM on DNA, parameters inaccessible with classical biochemistry tools. Here we describe, in detail, how to set up, perform, and analyze AFS and TIRF measurements to study DNA compaction by TFAM.

Key words Acoustic Force Spectroscopy (AFS), Total Internal Reflection Microscopy (TIRF), mitochondrial DNA compaction, mitochondrial Transcription Factor A (TFAM), Single molecule biophysics

1 Introduction

The mitochondrial genome is organized in protein-DNA complexes called nucleoids [1]. The most abundant protein found in these nucleoids is mitochondrial transcription factor A (TFAM) [2]. TFAM plays two crucial roles in mtDNA maintenance: *(i)* a role in transcription initiation, where it interacts specifically with the promotor regions of mtDNA [3]; and, *(ii)* a role in DNA compaction, for which it displays strong non-sequence-specific DNA binding [4, 5]. The latter function, DNA compaction, has been studied over the years using different techniques such as X-ray crystallography [6, 7], electron microscopy [8], or AFM [9].

Thomas J. Nicholls et al. (eds.), *Mitochondrial DNA: Methods and Protocols*, Methods in Molecular Biology,
vol. 2615, https://doi.org/10.1007/978-1-0716-2922-2_10,

With these techniques, researchers have established the structure of TFAM bound specifically and nonspecifically to DNA. They have also been able to propose different modes of compaction by TFAM, such as bending, loop formation, or bridging [10–12]. However, these techniques do not typically explore the dynamics of the TFAM-DNA interactions. In contrast, single molecule techniques give the possibility to manipulate and follow DNA-TFAM filaments in real time, providing valuable tools to study their structure and dynamics. For instance, a combination of optical tweezers and fluorescence microscopy has been used to study the DNA compaction mode of WT and modified TFAM [13, 14]. It was also possible to show that TFAM diffuses rapidly on nonspecific DNA via a 1D sliding mechanism, which may provide a way for TFAM to locate the mtDNA promoters and initiate transcription [13]. Similarly, Tethered Particle Motion (TPM), a high-throughput single molecule technique, has successfully been used to study DNA compaction induced by WT TFAM and some TFAM variants [10, 13].

In this chapter, we describe two powerful, complementary, and high-throughput single molecule techniques to quantify and visualize TFAM-DNA interactions, namely AFS (Acoustic Force Spectroscopy) and TIRF (Total internal Reflection Fluorescence) microscopy. AFS is a newly developed technique that uses acoustic waves to apply force simultaneously on multiple single tethered molecules [15–18]. In our assay, we tether single DNA molecules between a glass slide and a bead. We first describe how to prepare a DNA substrate containing a portion of the mitochondrial genome and how to label it at one end of the DNA with digoxigenin and at the other end with biotin to attach it to the glass surface and to the bead, respectively. We then describe a typical AFS measurement to study DNA compaction. We first measure the *RMS* (Root mean square) values of the tethered molecules. The tethered beads undergo Brownian motion that is restricted by the reach of the DNA tether. Changes in the amplitude of these Brownian fluctuations will reflect a change in DNA tether length. By tracking the position of the tethered bead over time, we can determine the *RMS* and thus monitor the DNA length's variation in real time. We then apply acoustic force to the tethers, and we perform an overstretching curve of DNA in order to determine the DNA's persistence length (L_p). The persistence length of TFAM-coated DNA is considerably decreased compared to naked DNA molecules and thus constitutes a fingerprint of DNA compaction by TFAM [13].

In TIRF microscopy, an evanescent wave is created, which excites only the fluorophores near the glass surface. This results in the elimination of out-of-focus fluorescence, thus making it possible to achieve single molecule detection [19, 20]. TIRF microscopy allows the visualization of biological events at the single molecule scale, such as, for example, the real-time observation of rolling-

circle DNA replication [21, 22]. In the second part of this chapter, we describe in detail how to perform a two-color TIRF experiment on DNA molecules coated with TFAM. We explain how to label a DNA template with biotins to attach it to the glass surface and with YOYO-1 to visualize it. We also provide a protocol to fluorescently label TFAM with Alexa-555. Finally, we describe step-by-step how to perform a TIRF experiment and how to analyze the obtained data.

2 Materials

2.1 TFAM Purification and Labeling

1. Purified recombinant human TFAM.
2. Dialysis buffer: 25 mM $NaPO_4$ (pH 7), 10% glycerol, 0.2 M NaCl.
3. Dialysis device: Slide-A-Lyzer MINI dialysis units 7000 MWCO (Thermo Scientific).
4. Alexa Fluor 555 C2-maleimide (Invitrogen).
5. Illustra Microspin-G25 columns (GE Healthcare).
6. 1 M Dithiothreitol (DTT).
7. Spectrophotometer (NanoDrop or similar device).

2.2 DNA Production and Labeling

2.2.1 Template for AFS Experiments

1. 10 μM Digoxygenin-labeled forward primer: 5′-[DIG]GCT[DIG]AAACCTAGCCCCAAACC-3′.
2. 10 μM Biotin-labeled reverse primer: 5′- [Bio]T[BiodT]GTGTTGAGGGTTATGAGAGTAGC-3′.
3. LongAMP buffer (5X) (NEB) and LongAMP polymerase (NEB).
4. 10 mM dNTPs.
5. Nuclease-free water.
6. Template DNA (10–30 ng).
7. PCR clean-up Macherey-Nagel kit.
8. PCR tubes.
9. Thermocycler.

2.2.2 Template for TIRF Experiments

1. Klenow buffer (10X) and Klenow DNA polymerase exo- (Promega).
2. 0.4 mM Biotin 14-dATP (Invitrogen).
3. 0.4 mM Biotin 14-dCTP (Invitrogen).
4. 10 mM dGTP and dTTP (Promega).
5. 250 μg/mL λDNA (Roche).
6. YOYO™-1 Iodide (491/509) (ThermoFisher).

7. Nuclease-free water.
8. Illustra Microspin S-400 HR columns (GE Healthcare).

2.3 Preparation of the Flow Cells

2.3.1 For AFS Experiments

1. Acetone.
2. 0.5 M Sodium thiosulfate.
3. Alkaline hypochlorite solution: 0.2% sodium hypochlorite (Sigma).
4. PBS buffer: 137 mM NaCl, 2.7 mM KCl, 10 mM phosphate pH 7.4, supplemented with 5 mM NaN_3 and 0.5 mM EDTA.
5. Anti-digoxygenin from sheep: 20 μg/mL in PBS (Roche).
6. 1% BSA (Sigma) in PBS buffer.
7. 5% Pluronic (F127) (Sigma) in PBS buffer.
8. 0.1% BSA and 0.25% Pluronic in PBS buffer.
9. 1% Casein (Sigma) in PBS buffer.
10. Buffer A: PBS buffer with 0.02% casein and 0.02% Pluronic.
11. Buffer B: 75 mM NaCl, 10 mM Tris–HCl pH 7.0, 0.5% glycerol.
12. Streptavidin-coated polystyrene beads (4.4 μm) (0.5%) (Spherotech).
13. 1 M NaOH.
14. Sigmacote.
15. Regal water: nitric acid and hydrochloric acid in a molar ratio of 1:3.

2.3.2 TIRF Experiments

1. Buffer C: 20 mM TrisOAc (pH 8), 20% sucrose, 10 mM dithiothreitol (DTT).
2. 10 mg/mL BSA-biotin (Sigma).
3. Alkaline hypochlorite solution: 0.2% sodium hypochlorite (Sigma).
4. 1 mg/mL Streptavidin (EMD Millipore).
5. 1.5 mg/mL Blocking reagent (Roche).
6. Nuclease-free water or MilliQ water.
7. 5 M NaCl.
8. 1 M NaOH.
9. Anhydrous DMSO.

2.4 Hardware

1. Isolation table.
2. Syringe pump (New Era Pump Systems).
3. AFS experimental setup: AFS experiments are performed on the AFS stand-alone G2 from LUMICKS B.V. It includes an inverted microscope, camera, controller box, and a stage

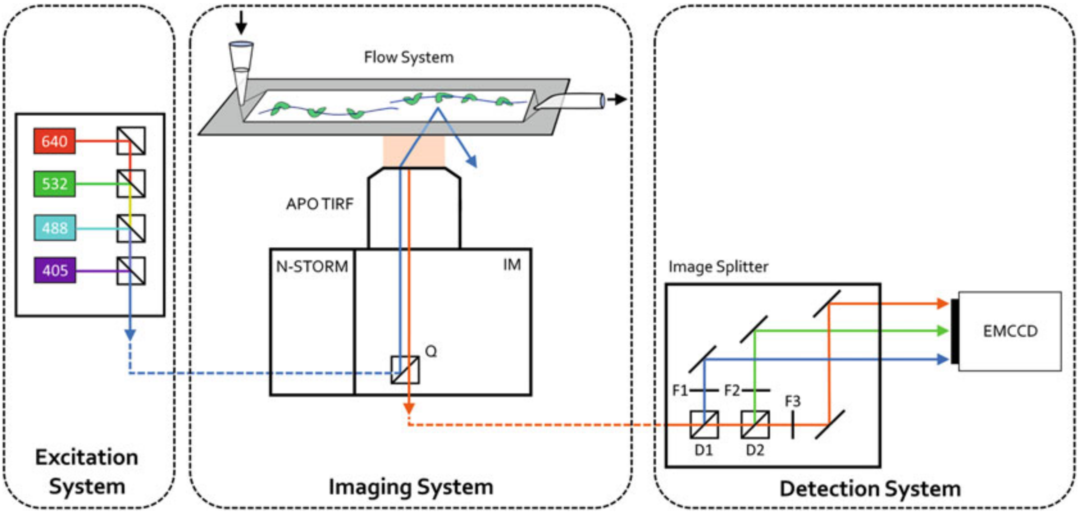

Fig. 1 Simplified diagram of the experimental TIRF setup. Includes excitation lasers (Oxxius laser base), flow system (Lumicks), inverted microscope (*IM*) (Ti2E, Nikon), and detection system (Image splitter: Optosplit III, Cairn Research; EMCCD: iXon 888, ANDOR). *Q*: Quad Band TIRF filters (405/488/532/638–647), *F1*: filter 550/88, *F2*: filter 580/60, *F3*: filter 676/29, *D1*: dichroic 552 nm, *D2*: dichroic 650 nm

holding a chip holder and a chip. The AFS is connected to a desktop computer.

4. TIRF setup: TIRF experiments are performed on an inverted microscope TI2-E (Nikon) connected to a computer. The microscope contains the following parts (*see* schematic Fig. 1):
   - CFI Plan APO TIRF objective (100X, NA = 1.49, oil) (Nikon).
   - Excitation lasers: 405–100 mW, 488–100 mW, 532–100 mW, 638–150 mW (OXXIUS).
   - Highly sensitive camera for fluorescence detection: EMCCD (iXon 888, ANDOR).
   - Image Splitter (Optosplit III, Cairn Research).
   - Excitation and emission filters optimized for the fluorophores of interest (Chroma).
   - Flow cell and flow cell holder (Lumicks).
   - Perfect focus system (PFS, Nikon).
   - 96-well plate holder (TI2-S-HW, Nikon).

2.5 Software

1. ImageJ.
2. MatLab.
3. NIS-Elements (Nikon).
4. Lumicks Tracking and Analysis software (Tracking software is freely available http://figshare.com/articles/AFS_software/1195874).

3 Methods

3.1 Assessing DNA Compaction by TFAM with AFS

The DNA template used is a ~9 kb fragment of the human mitochondrial genome (position 1671 to 10,600 nt) obtained and labeled by PCR. Amplification is performed using total DNA extracted from HEK cells (HEK 293, Invitrogen) and primers containing two biotins on one end and two digoxigenin on the other end (*see* **Note 1**).

3.1.1 DNA Labeling

Mix DNA template (10 ng of total cellular DNA), dNTPs (10 mM each final concentration), fwd and rev primers (10 μM each final concentration), LongAMP Taq polymerase (5 units), in 1X Long Amp PCR reaction buffer. Perform the amplification according to Table 1.

Purify the PCR products with the Macherey-Nagel PCR clean-up kit. Elute DNA in 2 × 20 μL with elution buffer heated at 70 °C. Measure the DNA concentration on the Nanodrop and store at 4 ° C for a short period of time, or at −20 °C for longer term storage.

3.1.2 Flow Cell Functionalization

The flow cell used is a glass flow cell with one channel (volume ~ 5 ul). If handled gently, one flow cell can be reused for tens of experiments. The following cleaning and functionalization protocols are the manufacturer's protocols with minor modifications and can be performed with the flow cell mounted on the microscope stage of AFS G2 setup (except the regal water step, which should be performed under a fume hood). For that, put the flow cell on the stage and connect the inlet to a reservoir containing the buffers and the outlet to the pump via a tubing (*see* **Note 2**). Use a flow rate of 100 μl/min for the washing, then, upon adding of the biological sample (from Subheading 3.1.2, **step 2** onward), decrease the flow rate to 40 μL/min to avoid damaging the sample with too high shear/drag forces (*see* **Note 3**).

Table 1
PCR amplification for DNA labeling

Temperature	Duration	Cycles
94 °C	30 s	1×
94 °C	15 s	30×
60 °C	30 s	
65 °C	50 s/kb	
65 °C	10 min	1×
10 °C	∞	1×

1. *Cleaning:* Connect a 3 mL syringe to the outlet of the flow cell. Insert 400 μL of alkaline hypochlorite solution. Incubate for 20 min (*see* **Note 4**). Insert 400 μL of 0.5 M sodium thiosulfate. Incubate for 5 min. Insert 400 μL of 1 M NaOH and incubate for 5 min. Rinse with nuclease-free water or MilliQ water between each step. Insert 50 μL of siliconizing reagent (Sigmacote) into the flow cell. Incubate for 1 min and air-dry the flow cell. Wash with acetone (*see* **Note 5**) and rinse thoroughly with nuclease-free water of MilliQ water.
2. *Incubation of anti-digoxigenin:* Insert 50 μL of anti-digoxigenin (20 μg/mL) into the flow cell. Incubate for 20 min.
3. *Passivation of the glass surface:* Insert in the flow cell 250 μL of PBS solution with 0.1% BSA and 0.25% Pluronic. Incubate for 15 min. Repeat this step twice.
4. *Anchoring DNA template to the glass surface:* Insert 200 μL of buffer A in the flow cell. Then insert 50 μL of 0.02 ng/μL DNA solution in the flow cell and let it incubate for 20 min. Rinse with 200 μL of buffer A.
5. *Washing the polystyrene beads:* Add 10 μL of the bead solution to 1 mL of buffer A, mix by vortexing, and spin down the beads at 2000 × *g* for 2 min. Discard the supernatant. Resuspend the beads in 130 μL of buffer A. Repeat the washing step two times.
6. *Attaching the beads:* Gently insert the beads in the flow cell at a rate of 3 μL/min. Incubate 10 min.

3.1.3 AFS on TFAM-Coated DNA

1. *Getting started:* Start the AFS and the tracking and analysis softwares (Lumicks).
2. *Mounting the flow cell on the microscope stage:* If this step has not been performed yet, first proceed as explained in Subheading 3.1.2. Then, when the flow cell is mounted, rinse the flow chamber with 400 μL buffer A to remove the beads that are not attached to DNA. Rinse the flow chamber with 50 μL buffer B.
3. *Finding a field of view with tethered beads:* Adjust the focus of the objective (20X) to a position where the beads appear out of focus (overfocus). Move the microscope stage to an area of the flow cell with multiple beads with a good spatial distribution (*see* **Note 6**). Select regions of interest (ROI) around the beads manually or automatically (*see* **Note 7**). Track the x and y positions of the beads using the Lumicks tracking software. For measuring the z position, make a look up table (LUT) (*see* **Note 8**).
4. *Measuring RMS and FD curves on naked and TFAM-coated DNA*. A typical experimental workflow is depicted in Fig. 2a.

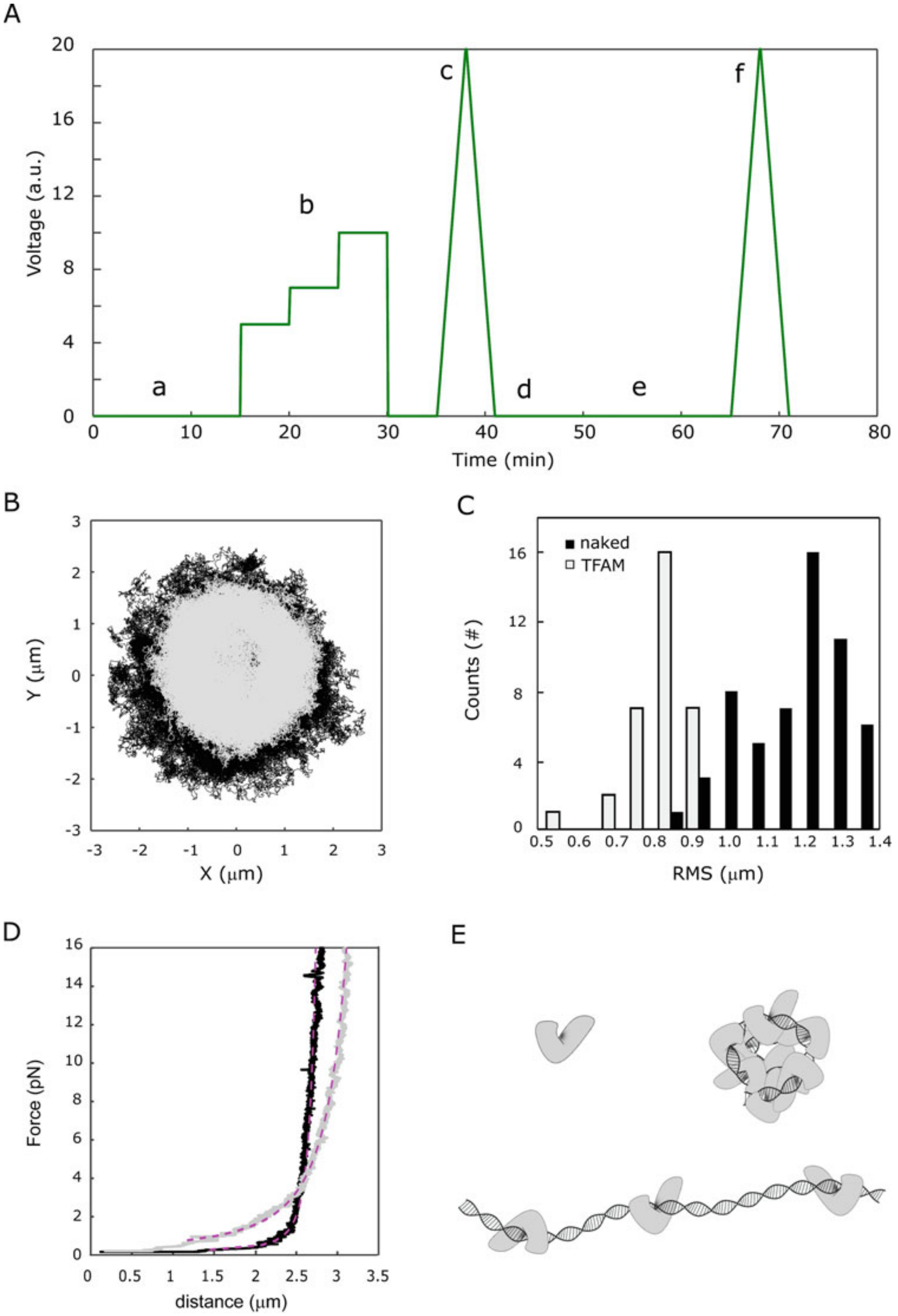

Fig. 2 AFS data analysis. (**a**) Schematic of the workflow of a typical AFS experiment. a: determination of the *RMS* for DNA tethers in the absence of TFAM and determination of the anchor point for the force calibration, b: force calibration, c: force ramp, d: incubation (with flow) with TFAM (this step can also be performed while applying a small force of about 2pN), e: determination of *RMS* for DNA tethers in the presence of TFAM, f: force ramp. (**b**) XY plot of tethered particles in the absence (black trace) and presence (gray trace) of 1 μM TFAM. The calculated *RMS* is 1.35 and 1.07 μm in the absence and presence of TFAM, respectively. (**c**) Histogram of

Track the x and y positions of the beads (without force) for 15–30 min in the absence of protein. Typically, an x-y plot of a single tether is round (Fig. 2b) and the area probed by the tethered bead depends on the length of the tether. Calculate the anisotropic ratio α (Eq. 1) and the root mean square displacement (*RMS*) (Eq. 2) for all tethers using LUMICKS analysis software.

$$\alpha = \frac{l_{\mathrm{major}}}{l_{\mathrm{minor}}} \tag{1}$$

where l_{major} and l_{minor} are the length of the major and minor axis of the x-y scatter plot, respectively [23].

$$\mathrm{RMS} = \sqrt{\frac{1}{n}\sum_{i=1}^{n}\left[(x-\overline{x})^2 + (y-\overline{y})^2\right]} \tag{2}$$

where x and y are the coordinates of the bead position and n the total number of positions recorded [23].

Select tethers with an α below 1.4 (tethers with α above 1.4 are likely double tethers). For the selected tethers, determine the position where the DNA is anchored to the surface (i.e., the anchor point) from the bead position traces (*see* **Note 9**). Perform a force calibration by applying successively three different constant acoustic amplitudes to the DNA for 5 min each. For each amplitude, create a power spectrum of the bead position fluctuations and fit this power spectrum with quenched Brownian motion to obtain the force and subsequently deduce the Force/Amplitude ratio (use LUMICKS analysis software). After completing the force calibration, perform a force ramp (*see* **Note 10**) and generate a force-distance curve (Fig. 2d). Insert 1 μM TFAM (diluted in buffer B, *see* **Note 11**) in the flow cell at a flow rate of 0.6 μL/min for 15 min, stop the flow and then track again the x and y positions of the beads for 15–30 min. Determine the *RMS* for all tethers. Perform once again a force ramp and generate a force-distance curve for TFAM-coated DNA (*see* **Note 12**). At the end of the experiment, rinse the flow cell extensively with 1 M NaOH. Leave the NaOH overnight.

Fig. 2 (continued) the *RMS* values is obtained for one experiment; the values in the absence of TFAM are depicted in black and the values in the presence of TFAM are depicted in gray. (**d**) Typical force-extension curves for DNA in the absence (black trace) and presence (gray trace) of 1 μM TFAM. The pink dashed line represents the eWLC fit to our data, yielding a persistence length (*Lp*) of 43.0 nm in the absence of TFAM and 3.83 nm in the presence of TFAM and a contour length (L_c) of 2.78 in the absence of TFAM and 3.52 nm in the presence of TFAM, in agreement with earlier observations [13]. (**e**) DNA compaction by TFAM. TFAM molecules (gray) bind to DNA and compact it [5]

5. *Data representation and data analysis:* To compare naked and TFAM-coated DNA molecules, plot the values of the average *RMS* with and without TFAM in a histogram (Fig. 2c). Fit the FD curves using the extensible wormlike chain model (eWLC) [24] which describes the dsDNA elastic behavior up to around 20 pN (Eq. 3) (we use a custom-written MatLab program).

$$x = L_c\left[1 - \frac{1}{2}\sqrt{\left(\frac{k_b T}{F L_p}\right)} + \frac{F}{K.}\right] \tag{3}$$

where x is the extension (end-to-end distance) of the DNA, L_c is the contour length, $k_b T$ is Boltzmann's constant times absolute temperature, F is the force, L_p the persistence length, and K the stretch modulus of DNA (set at 1200 pN). Determine the persistence length (L_p) and the contour length (L_c) of the DNA molecules in the presence and absence of TFAM. The decrease of the *RMS* and of the L_p both reflect DNA compaction upon TFAM binding (Fig. 2e).

3.2 Assessing TFAM Dynamics with TIRF Microscopy

In this protocol, we use λDNA, a linear molecule of 48,502 bp with two single-stranded 12-nt overhangs on both 5′-ends. λDNA is first labeled on both ends with biotins to attach it to the glass surface, then labeled with YOYO-1 for visualization. TFAM is labeled by covalently attaching a fluorophore to the -SH group (thiol) of the cysteines residues of the protein.

3.2.1 DNA Biotin Labeling

Mix λDNA (7 μg) with Klenow buffer (10X), Biotin 14-dATP (64 μM final concentration), Biotin 14-dCTP (64 μM final concentration), dGTP / dTTP (0.1 mM final concentration), and Klenow DNA polymerase exo- (5 units) in a total volume of 50 μL. Incubate 30 min at 37 °C. Then inactivate the reaction at 70 °C for 15 min. Purify the DNA on Illustra Microspin S-400 HR columns following the manufacturer's protocol. Measure DNA concentration on the Nanodrop and store at 4 °C.

3.2.2 TFAM Labeling

Dialyze TFAM in dialysis buffer for 1.5 h using a Slide-A-Lyzer MINI dialysis unit 7000 MWCO. Dissolve Alexa Fluor 555 C2-maleimide in anhydrous DMSO and add to the TFAM solution at a fivefold molar excess of dye over the protein. Incubate rotating at 4 °C for at least 2 h. The reaction should be protected from light as much as possible. Remove the excess dye using a G-25 Microspin column following the manufacturer's protocol. Measure the degree of labeling spectrophotometrically (*see* **Note 13**). Add 1 mM DTT, aliquot the sample and store at −80 °C in aluminum foil after flash freezing in liquid nitrogen.

3.2.3 Flow Cell Functionalization

The flow cell holder is mounted on a 96-well plate holder. The inlet of the flow cell is connected to a 3 mL syringe and the outlet of the flow cell is connected to a pump. The cleaning and DNA anchoring protocols are adapted from [25].

1. *Cleaning:* All the cleaning steps are performed at a flow rate of 50 μL/min. Wash the flow cell with alkaline hypochlorite solution for 20 min (*see* **Note 14**). Rinse with nuclease-free water. Insert 200 μL of 1 M NaOH and incubate 10 min. Rinse with nuclease-free water. Wash with 200 μL of Buffer C.
2. *Flow cell passivation:* Insert 250 μL of Buffer C supplemented with 1 mg/mL BSA-Biotin in the flow cell and incubate for 15 min. Repeat this step twice. Insert 250 μL of Buffer C supplemented with 0.1 mg/mL streptavidin in the flow cell and incubate 15 min. Repeat this step twice. Insert 300 μL of blocking reagent in the flow cell and incubate for 15 min. Rinse the flow cell with 200 μL buffer C.

3.2.4 Anchoring DNA Template to the Glass Surface

Mix biotinylated λDNA (0.25 ng/μL final concentration) with YOYO-1 (0.5 nM) in buffer C. Insert 100 μL of this solution in the flow cell (40 μL/min) and incubate for 20 min. Flush in at least 200 μL of buffer C at 100 μL/min to stretch the DNA molecules at the surface of the flow cell (*see* **Note 15**). Rinse with buffer C to remove the YOYO-1 in excess.

3.2.5 Sample Preparation

Dilute labeled TFAM in buffer C without salt to a concentration of 5–20 nM (*see* **Notes 16** and **17**). Insert 100 μL of diluted labeled TFAM in the flow cell (50 μL/min) and incubate for 5 min. Wash with buffer C supplemented with 25 mM NaCl to remove the excess of free TFAM. Start imaging immediately.

3.2.6 Imaging

Images are acquired in total internal reflection mode, through a Nikon Plan APO TIRF objective (*see* Subheading 2.4), on an EMCCD camera. The images are split using an image splitter into separate spectral components which are aligned side by side on the camera chip (size of each image is 1024 × 340 pixels) (Fig. 3a). Start recording a movie. Excite the YOYO-1 with the 488 nm laser (laser power: 9 mW, exposure time: 500 ms, gain 200, 2–10 frames) (*see* **Note 18**). Turn off the 488 nm laser and turn on the 532 nm laser to excite Alexa555 (laser power: 2.6 mW, exposure time: 500 ms, gain 200, 40–300 frames). Record until the molecules of interest are bleached (*see* **Note 19**). Stop recording the movie. Move to another area of the flow cell and record another movie.

3.2.7 Data Analysis

Quantifying the Intensity of a Single Fluorophore Take a DNA molecule with a dense TFAM coverage (*see* **Note 17**). For each visible fluorescent TFAM particle, plot the intensity of the particle versus time. Use bleaching steps to determine the intensity of a

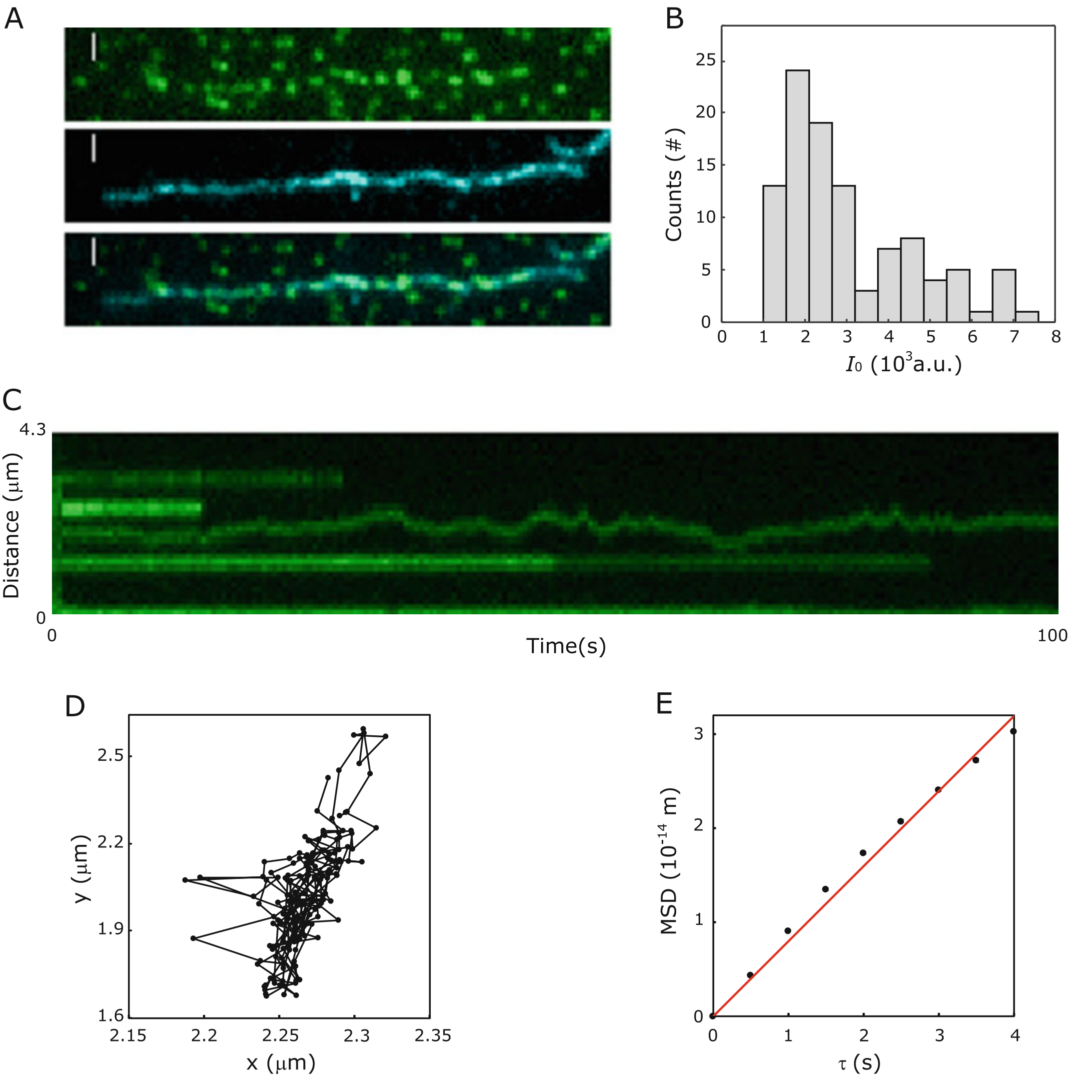

Fig. 3 TIRF data analysis. (**a**) Two color TIRF fluorescence images of a DNA molecule coated with TFAM. Upper image (green): DNA labeled with YOYO-1 excited with the 488 nm laser. Middle image (blue): Fluorescent TFAM-Alexa555 excited with 532 nm laser. Lower image: Merge of the two images. Scale bar: 1 μm. (**b**) Intensity histogram of single step bleaching. The fluorescence intensity was measured for 103 fluorescent particles. We obtain a mean fluorescence value for a single fluorophore of approximately 2000 a.u. (**c**) Kymograph created from TFAM spots on a DNA molecule (as shown in (**a**)) showing the diffusion of fluorescent TFAM on DNA. Time (s) and distance (μm) are indicated at the bottom and left of the kymograph, respectively. (**d**) Representative trajectory generated from tracking the motion of a single TFAM on DNA. (**e**) Mean-squared displacement (*MSD*) of a TFAM molecule (same molecule as in (**d**)) versus time interval (τ). The diffusion coefficient calculated for this molecule from the linear fit (red line) to the *MSD* plot is 7×10^3 nm^2 s^{-1}

single fluorophore. Perform this analysis on at least 30 molecules. Build a histogram of the steps found (example Fig. 3b) (*see* **Note 20**).

Creating a Kymograph Select a DNA molecule with a sparse TFAM coverage. Create a kymograph (*see* **Note 21** and Fig. 3c) for each DNA molecule selected. Use the tool “Image>ND processing>create a kymograph by line” if using the Nikon software (*see* **Note 22**).

Selecting Single TFAM Molecules Determine the initial intensity of the fluorescent particles detectable on the kymograph. Select the molecules with an intensity corresponding to a single TFAM (i.e., to two fluorophores, *see* **Note 13**).

Tracking Single Particles Track single TFAM molecules (*see* **Note 23**). Take only traces with a minimal length of 30 frames. Determine the trajectory of the moving spots (Fig. 3d), and the MSD (Fig. 3e). Calculate the diffusion constant (D) from the MSD plot ($\mathrm{MSD} = 2D\tau + \mathrm{offset}$), where τ is the time interval and the offset indicates the position accuracy.

4 Notes

1. We chose a portion of mtDNA that does not contain any specific binding sites, but other regions of mtDNA can be amplified following the same protocol and using primers flanking the region of interest. For PCR amplification of a portion of human mtDNA, it is possible to use as template DNA extracted from any other human cell line available in the lab.
2. Make sure to always keep liquid in the tank. To improve the flow in the tubing, wash the microtube with ethanol before connecting it to the flow cell outlet.
3. The washing steps can be performed by directly connecting a syringe to the outlet of the flow cell. The pump can be connected only at **step 2** of Subheading 3.1.2.
4. In case a bacterial lawn remains stuck to the surface, insert 500 μL of 25% regal water in the flow cell and incubate for 15 min.
5. Be careful to not drop acetone on the piezo element as it can damage welding spots.
6. The beads should not be too close, otherwise they will interfere with each other in the tracking, yet there should be enough beads in the field of view, typically in the order of 30 beads.

7. The diffraction rings of the beads should be included in the ROI. The size of the ROI will depend on many parameters, such as the bead size, the objective used, etc. Typically for a 4.4 μm bead and using a 20× magnification objective, we select ROIs of about 60 nm. For the automatic bead detection, a reference bead has to be preselected first.
8. The range of the LUT has to be bigger than the size of the extended DNA molecule. In our case, the DNA molecule is 3 μm long and we make the LUT over 10 μm.
9. The anchor point should be carefully determined for a good force calibration.
10. For the force ramp, we usually set a linear force ramp (back and forth) of 5000 steps, over 30 s, and the maximum force reached at 15 pN.
11. Buffer B contains glycerol as TFAM stock protein is stored in 10% glycerol. Be careful not to use more than 0.5% glycerol in the assay, as a higher glycerol concentration may result in more surface interactions. In case the protein is stored in high glycerol concentration, or the volume of protein used in the assay is important, first dialyze the protein against a buffer containing not more than 0.5% glycerol.
12. To clearly observe the effect of the protein on the DNA, make sure to measure the *RMS* and the force-distance on the same good tethers before and after addition of TFAM.
13. Wild-type human TFAM contains two cysteines. We typically obtain a ratio of two dyes per TFAM monomer, suggesting that the two cysteines of TFAM are exposed to the solvent and can be labeled.
14. In case of bacterial contamination, this step can be performed overnight. It is also possible to use regal water diluted in water (1:3 v/v) for 15 min.
15. If the DNA is not stretched enough, it is possible to stop the flow 2 or 3 times for 2 min during this step.
16. Always keep TFAM and the TFAM dilutions on ice to prevent loss of function. Perform the dilution of TFAM just prior to use and briefly centrifuge the sample to remove possible aggregates.
17. To obtain single-molecule resolution and to be able to follow the diffusion of the TFAM molecules on DNA, the concentration of TFAM used should be low, resulting in a sparse coverage of the DNA (typically we use 5 nM). On the contrary, for measuring the intensity of a single fluorophore, it is better to start with a DNA molecule with a denser TFAM coverage, so we use a higher TFAM concentration (typically we use 20 nM). At these concentrations, TFAM forms patches that are

immobile, making it possible to follow its fluorescence in time without the risk that it is blurred by any movement [13].

18. This is just to determine the position of the DNA molecules, so only take a few frames.
19. The laser power and exposure time should be chosen according to the process that is investigated. For example, to obtain a diffusion coefficient for molecules moving along the DNA molecule, the movies should be significantly long (in our experience at least 30 frames) and laser power should thus be low to limit photobleaching. In contrast, fast processes such as binding/unbinding may require short exposure times (and consequently higher laser powers).
20. In our hands a single fluorophore has an intensity of about 2000 a.u.
21. A standard way of following a particle moving in one dimension, in this case to follow the diffusion of TFAM molecules on DNA, is to create a kymograph. A kymograph takes the pixels along a DNA molecule in the video and stacks them as time progresses.
22. There are also many free plug-ins available for ImageJ to create kymographs.
23. There are many different tracking softwares available in the single molecule labs or otherwise in the literature. Some tracking softwares are based on 2D Gaussian fit of the fluorescent spot, others on applying image filtering (e.g., the ImageJ plugin "Particle Tracker 2D/3D" [26]).

Acknowledgments

The authors thank Maria Falkenberg for valuable support. This work was supported by the University Clermont Auvergne (UCA), the Laboratoire de Physique de Clermont (LPC), the Region Auvergne-Rhône-Alpes et l'Union Européenne dans le cadre du Fonds Européen de Développement Régional (FEDER), and the Association Française Contre les Myopathies Téléthon (AFM) (#21411 to GF and #22765 to LD).

References

1. Spelbrink JN (2010) Functional organization of mammalian mitochondrial DNA in nucleoids: history, recent developments, and future challenges. IUBMB Life 62:19–32. https://doi.org/10.1002/iub.282
2. Gustafsson CM, Falkenberg M, Larsson N-G (2016) Maintenance and expression of mammalian mitochondrial DNA. Annu Rev Biochem 85:133–160. https://doi.org/10.1146/annurev-biochem-060815-014402
3. Falkenberg M, Gaspari M, Rantanen A, Trifunovic A, Larsson N-G, Gustafsson CM (2002) 2 Mitochondrial transcription factors B1 and B2 activate transcription of human

mtDNA. Nat Genet 31:289–294. https://doi.org/10.1038/ng909

4. Wang YE, Marinov GK, Wold BJ, Chan DC (2013) Genome-wide analysis reveals coating of the mitochondrial genome by TFAM. PLoS One 8:e74513. https://doi.org/10.1371/journal.pone.0074513
5. Farge G, Falkenberg M (2019) Organization of DNA in mammalian mitochondria. Int J Mol Sci 20. https://doi.org/10.3390/ijms20112770
6. Ngo HB, Kaiser JT, Chan DC (2011) The mitochondrial transcription and packaging factor Tfam imposes a U-turn on mitochondrial DNA. Nat Struct Mol Biol 18:1290–1296. https://doi.org/10.1038/nsmb.2159
7. Rubio-Cosials A, Sidow JF, Jiménez-Menéndez N, Fernández-Millán P, Montoya J, Jacobs HT, Coll M, Bernadó P, Solà M (2011) Human mitochondrial transcription factor A induces a U-turn structure in the light strand promoter. Nat Struct Mol Biol 18:1281–1289. https://doi.org/10.1038/nsmb.2160
8. Kukat C, Davies KM, Wurm CA, Spåhr H, Bonekamp NA, Kühl I, Joos F, Polosa PL, Park CB, Posse V, Falkenberg M, Jakobs S, Kühlbrandt W, Larsson N-G (2015) Cross-strand binding of TFAM to a single mtDNA molecule forms the mitochondrial nucleoid. Proc Natl Acad Sci U S A 112:11288–11293. https://doi.org/10.1073/pnas.1512131112
9. Kaufman BA, Durisic N, Mativetsky JM, Costantino S, Hancock MA, Grutter P, Shoubridge EA (2007) The mitochondrial transcription factor TFAM coordinates the assembly of multiple DNA molecules into nucleoid-like structures. Mol Biol Cell 18:3225–3236. https://doi.org/10.1091/mbc.e07-05-0404
10. Ngo HB, Lovely GA, Phillips R, Chan DC (2014) Distinct structural features of TFAM drive mitochondrial DNA packaging versus transcriptional activation. Nat Commun 5:3077. https://doi.org/10.1038/ncomms4077
11. Rubio-Cosials A, Battistini F, Gansen A, Cuppari A, Bernadó P, Orozco M, Langowski J, Tóth K, Solà M (2018) 9 protein flexibility and synergy of HMG domains underlie U-turn bending of DNA by TFAM in solution. Biophys J 114:2386–2396. https://doi.org/10.1016/j.bpj.2017.11.3743
12. Malarkey CS, Bestwick M, Kuhlwilm JE, Shadel GS, Churchill MEA (2012) Transcriptional activation by mitochondrial transcription factor A involves preferential distortion of promoter DNA. Nucleic Acids Res 40:614–624. https://doi.org/10.1093/nar/gkr787
13. Farge G, Laurens N, Broekmans OD, van den Wildenberg SMJL, Dekker LCM, Gaspari M, Gustafsson CM, Peterman EJG, Falkenberg M, Wuite GJL (2012) Protein sliding and DNA denaturation are essential for DNA organization by human mitochondrial transcription factor A. Nat Commun 3:1013. https://doi.org/10.1038/ncomms2001
14. King GA, Hashemi Shabestari M, Taris K-KH, Pandey AK, Venkatesh S, Thilagavathi J, Singh K, Krishna Koppisetti R, Temiakov D, Roos WH, Suzuki CK, Wuite GJL (2018) Acetylation and phosphorylation of human TFAM regulate TFAM-DNA interactions via contrasting mechanisms. Nucleic Acids Res 46:3633–3642. https://doi.org/10.1093/nar/gky204
15. Kamsma D, Creyghton R, Sitters G, Wuite GJL, Peterman EJG (2016) Tuning the music: acoustic force spectroscopy (AFS) 2.0. Methods 105:26–33. https://doi.org/10.1016/j.ymeth.2016.05.002
16. Sitters G, Kamsma D, Thalhammer G, Ritsch-Marte M, Peterman EJG, Wuite GJL (2015) Acoustic force spectroscopy. Nat Methods 12:47–50. https://doi.org/10.1038/nmeth.3183
17. Kamsma D, Wuite GJL (2018) Single-molecule measurements using acoustic force spectroscopy (AFS). Methods Mol Biol 1665:341–351. https://doi.org/10.1007/978-1-4939-7271-5_18
18. Lin S-N, Qin L, Wuite GJL, Dame RT (2018) Unraveling the biophysical properties of chromatin proteins and DNA using acoustic force spectroscopy. Methods Mol Biol 1837:301–316. https://doi.org/10.1007/978-1-4939-8675-0_16
19. Kudalkar EM, Davis TN, Asbury CL (2016) Single-molecule total internal reflection fluorescence microscopy. Cold Spring Harb Protoc 2016. https://doi.org/10.1101/pdb.top077800
20. van den Wildenberg SMJL, Prevo B, Peterman EJG (2018) A brief introduction to single-molecule fluorescence methods. Methods Mol Biol 1665:93–113. https://doi.org/10.1007/978-1-4939-7271-5_5
21. Tanner NA, van Oijen AM (2009) Single-molecule observation of prokaryotic DNA replication. Methods Mol Biol 521:397–410. https://doi.org/10.1007/978-1-60327-815-7_22
22. Tigano M, Phillips AF, Sfeir A (2020) Single-molecule analysis of mtDNA replication with

high resolution. Methods Cell Biol 155:401–414. https://doi.org/10.1016/bs.mcb.2019.10.005

23. Henneman B, Heinsman J, Battjes J, Dame R (2018) Quantitation of DNA-binding affinity using tethered particle motion: methods and protocols. In: Methods in molecular biology (Clifton, N.J.), pp 257–275
24. Odijk T (1995) Stiff chains and filaments under tension. Macromolecules 28:7016–7018. https://doi.org/10.1021/ma00124a044
25. Bell JC, Liu B, Kowalczykowski SC (2015) Imaging and energetics of single SSB-ssDNA molecules reveal intramolecular condensation and insight into RecOR function. elife 4. https://doi.org/10.7554/eLife.08646
26. Ewers H, Smith AE, Sbalzarini IF, Lilie H, Koumoutsakos P, Helenius A (2005) Single-particle tracking of murine polyoma virus-like particles on live cells and artificial membranes. Proc Natl Acad Sci U S A 102:15110–15115. https://doi.org/10.1073/pnas.0504407102

Chapter 2.2 : TFAM P178L disease causing mutant

2.2.1: Disease causing mutation (P178L) in mitochondrial transcription factor A results in impaired mitochondrial transcription initiation (Paper II)

Mitochondrial transcription factor A (TFAM) is a core component of the mammalian mitochondrial nucleoid and is actively involved in the organization and expression of mitochondrial DNA (mtDNA). Disease causing mutations affecting mitochondrial replication factors are common, but for a long time, no mutations affecting TFAM were identified Recently, a pathogenic homozygous variant of TFAM has been associated with a severe mtDNA depletion syndrome leading to neonatal liver failure and early death (Stiles *et al.*, 2016). The mutation generates a single amino acid change from Proline to Leucine (P to L) at position 178 within the primary protein sequence.

In this paper, we have performed a biochemical and biophysical characterization of a cloned and expressed TFAM variant P178L in order to understand the molecular basis for the pathogenicity of this mutation. Binding ability, DNA compaction efficiency and ability to activate transcription were monitored in comparison with TFAM WT. Mutation effects on the protein stability have also been studied and a structural model has been performed.

Our results reported a severe mtDNA depletion in patient primary skin fibroblast cells accompanied by a decrease in TFAM protein level as it was shown in Stiles *et al.*, 2016. Interestingly, using Southern blot to detect mtDNA levels, we demonstrated that 7S DNA level is increased relative to mtDNA level in patient cells. By performing acoustic force spectroscopy, we determined and compared DNA's flexibility changes induced by the mutant, such as the persistence length and contour length of individual DNA molecules. The results suggest that DNA flexibility is only mildly affected by the P178L amino acid change. However, analysis of replication in a reconstituted in vitro system containing POLγ, mtSSB and TWINKLE, demonstrated that TFAM P178L was unable to efficiently block progression of the replication fork as compared to TFAM WT (as it was shown in Farge et al., 2014). This observation supports TFAM's ability to compact mtDNA is affected by the amino acid change. In addition, we performed an *in vitro* transcription assay with POLRMT, TFB2M and TFAM on a dsDNA template, containing the cloned mitochondrial HSP/LSP promoter cassette, to monitor the effects the P178L mutation might have on transcription initiation. Remarkably, the

mutation severely impairs mtDNA transcription initiation at the mitochondrial heavy and light strand promoters. Transcript run off from both promoters were reduced up to 2.5 fold. Finally, we modeled the structure of TFAM P178L using the already solved crystal structure. Our molecular modelling suggests the P178L mutation induces a turn between a6 and a7. This structural change may affect the positioning of the C-terminal tail, disrupt promoter sequence recognition and the interaction between TFAM and the tether helix of POLRMT, thus explaining transcription initiation deficiency.

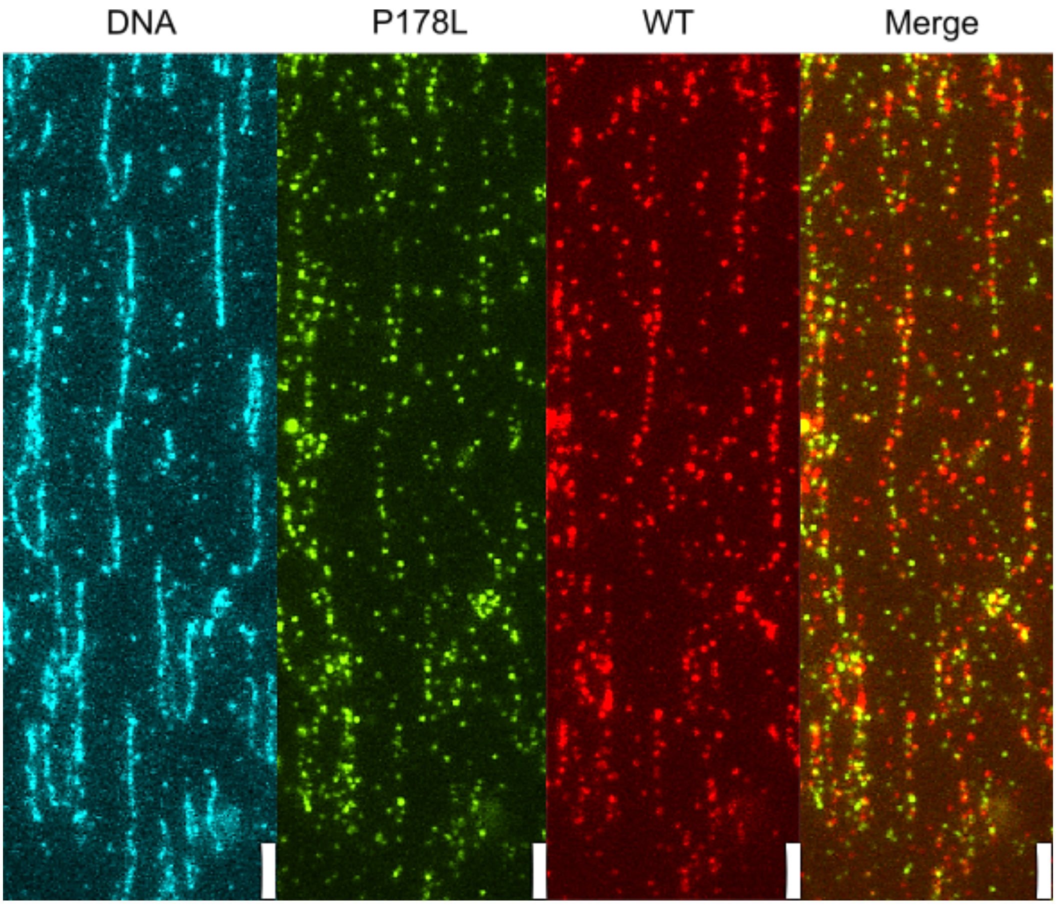

Figure 22: Typical three colours TIRF view. Double stranded Lambda DNA (16µm) is flow stretched and labelled with YOYO-1 (**blue**) excited with a 488nm laser. TFAM WT is labelled with Alexa 647 (**red**) and TFAM P178 with Alexa 555 (**green**) and are excited with 638nm and 532nm lasers respectively. Movies of the moving TFAM molecules on DNA are recorded with a EMCCD camera. Scale bar : 5 µm.

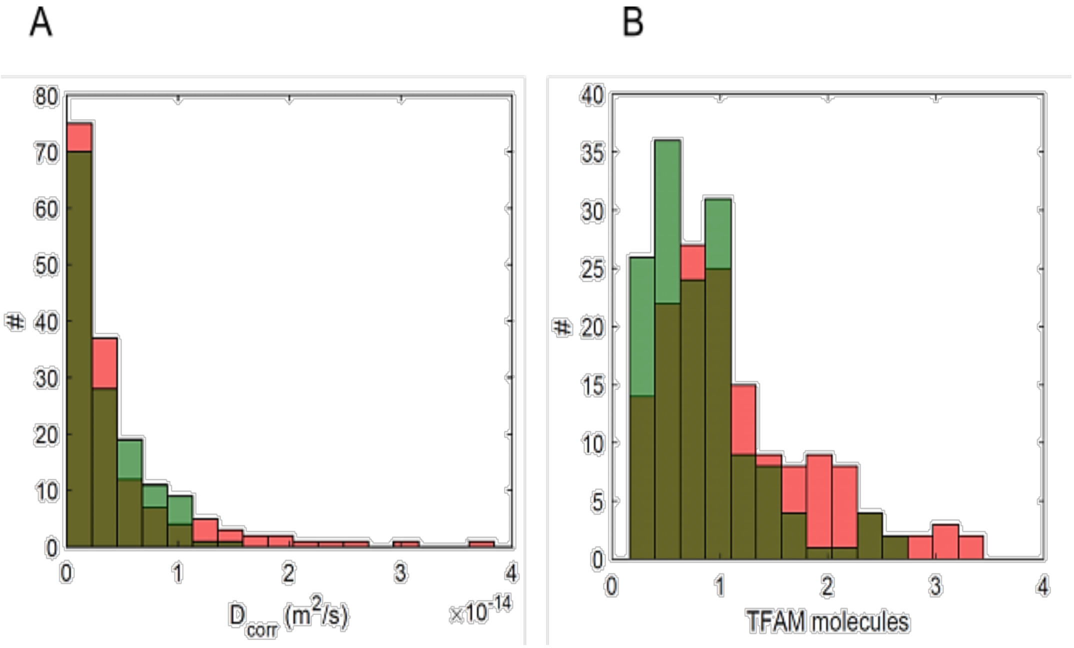

Figure 23: TFAM Diffusion coefficient and oligomeric measurement. (**A**)We tracked a hundred of TFAM molecules and calculated their diffusion coefficient D. No significant difference between TFAM WT and TFAMP178L were observed (D = 0.5e-14 m²/s). (**B**) Oligomeric state of moving TFAM (P178L in green, WT in red).

2.2.2: TFAM supplementary results and outlook

To go further in the characterization of the P178L mutant, we studied the real-time interaction dynamics of WT and P178L on dsDNA using TIRFm. For this, long dsDNA molecules were anchored to a glass surface by fluid flow stretching and the movement of fluorescent proteins on DNA was followed in real time. We investigated the effects of the P178L mutation on the dynamical properties of TFAM, such as its (diffusive) motion and dissociation, as well as protein-protein interactions. Using TIRF microscopy, we tracked individual TFAM P178L and WT fluorescent proteins on individual dsDNA labelled with YOYO-1 to evaluate (in comparison with WT) if the mutation has an impact on its motion. A typical TIRF experiment can be seen on **figure 22** in which dsDNA is labelled with YOYO-1 in cyan, TFAM P178L in green labelled with Alexa Fluor 555 and TFAM WT in red labelled with Alexa Fluor 647.

Quantification of TFAM diffusion

TFAM proteins were expressed and purified as explained in the publication (cf. section 2.2.1). To quantify TFAM WT and P178L motion, we labelled the proteins with Alexa Fluor 555 and recorded their movement on flow stretched dsDNA in separated experiments. For this, 100µL of 0.15 ng/µL of biotinylated λ dsDNA were flow stretched at the surface of the microfluidic chamber and incubated with YOYO-1 at 0.5 nM during 20 min and incubated with either 30 µL of TFAM WT or TFAM P178L at 1 or 5 nM in single molecular buffer (SMB) (cf. chapter 2.1). Then, 200 µL of SMB buffer supplemented with 25 mM NaCl was added to rinse the microfluidic chamber and remove the excess of protein. Tracking of individual TFAM molecules was done using following criteria: (i) particles must stay on a DNA molecule (ii) particles should not blink (iii) selected particles should not collide with each other (iv) tracking particles must be a monomer and (v) tracking must be done on particle moving during at least 20 s. The tracking of TFAM individuals was performed using a ImageJ free plugin called Particle Tracker 2D/3D in order to extract x and y particle positions (Sbalzarini and Koumoutsakos, 2005). With x and y position, we measured the mean squared displacement (MSD) of each tracked particle with a home-made Matlab programme. TFAM WT and P178L appeared to have the same diffusion coefficient D of 0.5e-14 m^2/s (**Figure 23A**). Therefore, the disease-causing mechanism may not involve TFAM motion. TFAM's diffusion coefficient calculated here is lower by a factor 4 than the one calculated by Heller et al., 2013 with optical tweezers and STED microscopy. This difference is not very surprising as

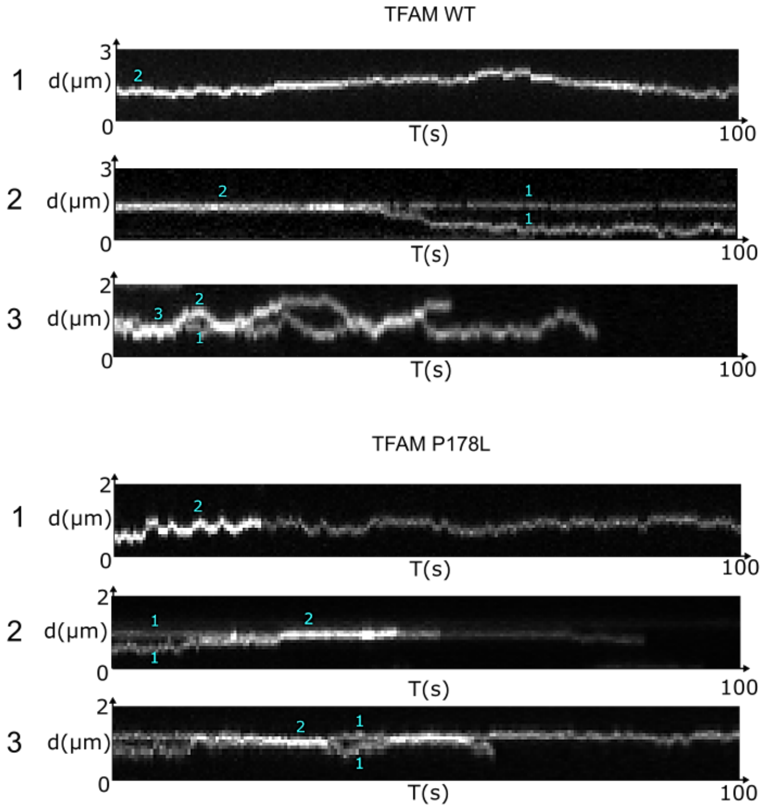

Figure 24: TFAMs typical diffusion events. Kymographs of moving TFAM molecules showing moving dimer (Lane 1 WT and P178L), and association/dissociation (events lane 2 and 3). Above, TFAM P178L showing same events. Number in blue indicates the number of TFAM molecules.

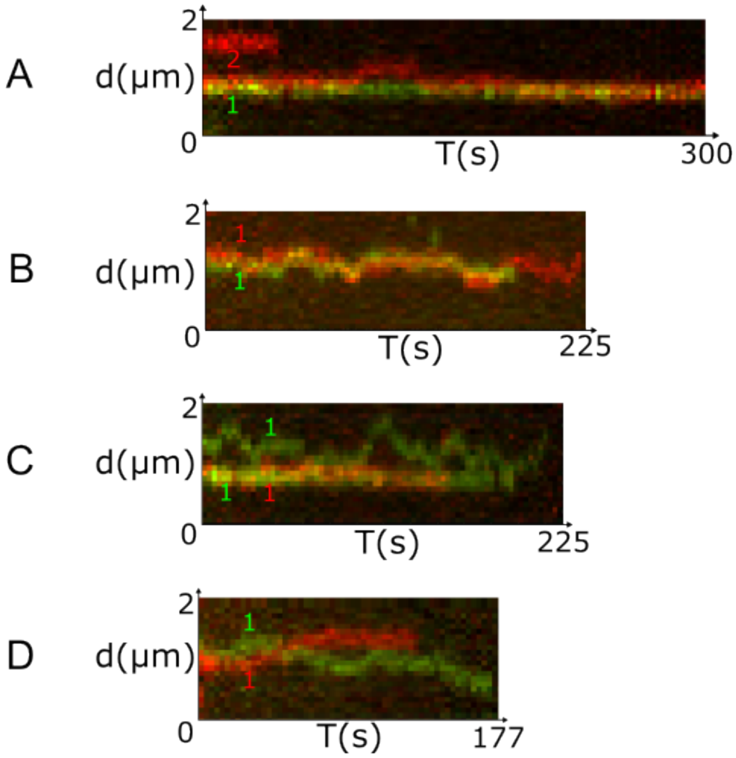

Figure 25: TFAM WT and P178L interactions. Kymographs showing interactions between TFAM P178L (**green**) and TFAM WT (**red**) (DNA in blue not shown). (**A**) Association–dissociation of TFAM WT dimer from a single TFAM P178L. (**B**) Moving dimer of WT and P178L. (**C**) P178L bouncing on a patch formed by WT and P178L. (**D**) WT and P178L crossing.

in our experiment, glass surface interaction may hinder TFAM motion, which is not the case with optical tweezers. We then analysed intensity of hundreds of TFAMs molecules (not only monomers) that diffuse on DNA molecules, and observed a non-negligible fraction of TFAM WT dimers that diffuse on dsDNA, which was not found in the same proportion for TFAM P178L (**Figure 23B**). It should be noticed that intensity steps measurements to quantify single molecule intensity steps were not done with AutoStepFinder v2.1.0 from Loeff-Kerssemakers and coworkers like it is explained in chapter 2.3 on mtSSB. Using intensity profiles of fluorescent TFAM on dsDNA, steps quantification was done by subtracting the mean of intensities of apparent plateaus.

As a slight decrease in the number of TFAM P178L dimers has been observed, it could indicate that the P178L mutation could affect the dimerization of TFAM, even though more experiments are necessary to confirm this result. This dimerization defect could also be involved in the impairment of transcription initiation as the role of TFAM dimerization in transcription is subject to debate (Gangelhoff *et al.*, 2009; Ngo *et al.*, 2014). Moreover, another study has shown that levels of dimer-defect TFAM were restored *in vivo* during inhibition of Lon protease and cytosol 20S proteasome, suggesting TFAM dimerization could be involved in its stability (Kasashima and Endo, 2015). Finally, as TFAM-TFAM interactions is important to efficiently compact mtDNA molecules (Kukat *et al.*, 2015), hindered TFAM dimerization and higher oligomeric states formation could be a lead of investigation, that could explain to a certain extent the TFAM depletion observed in patients (Stiles *et al.,* 2016).

Noticeable diffusion events

During diffusion experiments, we observed for both TFAM version characteristic diffusion events such as static patches, moving dimers and more rarely higher oligomers as well as TFAMs association with and dissociation from other TFAMs. These events were captured using kymographs on dsDNA molecules with the NIS-Elements Nikon software (**Figure 24**). The nature and the proportion of these events were similar for WT and P178L. We decided to study the TFAM WT and P178L interactions on dsDNA. To this end, we performed a triple colours TIRF experiment with dsDNA labelled with YOYO-1, TFAM WT with Alexa Fluor 647 and TFAM P178L with Alexa Fluor 555. DNA molecules were stretched and incubated with YOYO-1 in a first step. Then both TFAM were mixed at 5 nM in SMB each and flushed in the microfluidic chamber where the DNA molecules were attached (**Figure 25**). The microfluidic chamber was rinsed with 200 µl of SMB supplemented with 25 mM

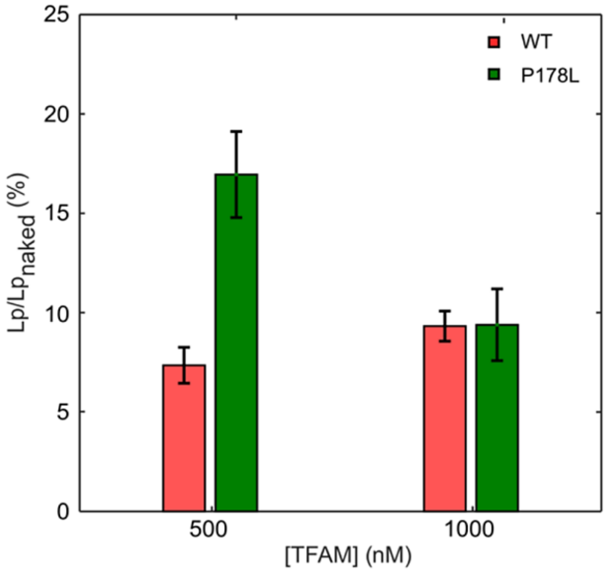

Figure 26: Persistence length of dsDNA as a function of TFAM concentration. Persistence length of dsDNA molecules were measured with TFAM WT (**red**) and P178L (**green**) at 500 nM and 1µM of proteins concentration.

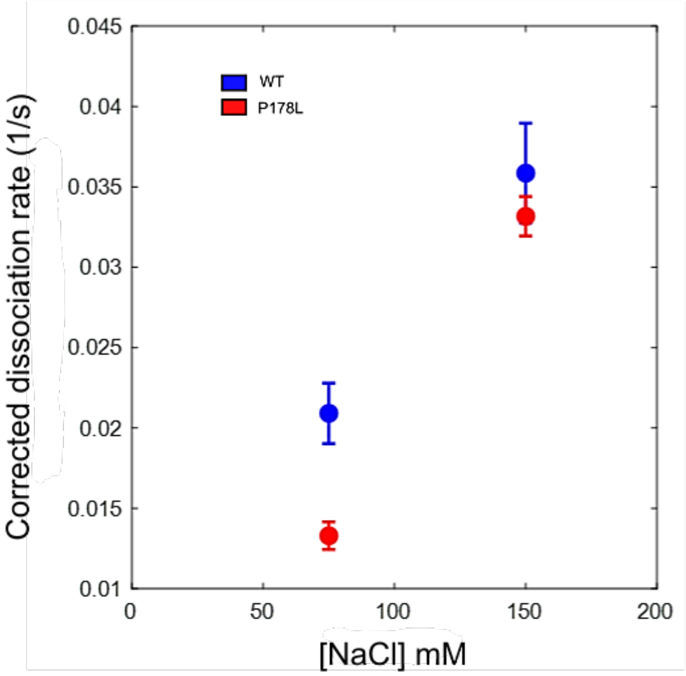

Figure 27: TFAMs dissociation rate. TFAMs dissociation rates (WT in **blue**, P178L in **red**) were calculated at 75 and 150 mM NaCl. Dissociation rate was corrected with the photobleaching rate.

NaCl. Interaction events were captured using kymographs on dsDNA molecules with the NIS-Elements Nikon software as well. Interestingly, the same TFAM interaction events were seen as in the separately TFAM tracking experiments (**Figure 24**), however less often. Among these interactions, we can find: (i) TFAM static patches and moving dimers of WT and mutant (**Figure 25A and B**) (ii) association and dissociation of TFAMs molecules (**Figure 25A**), (iii) bouncing of a TFAM molecule on a nearly static patch (**Figure 25C**), (iv) Crossing of TFAM WT and P178L (**Figure 25D**). However, it seems that the proportion of colocalized red and green light (corresponding to WT and P178L) is low, suggesting that both TFAMs do not interact much (**Figure 22**). Colocalization evaluation could be done to validate this idea, as well as other interaction quantification techniques such as isothermal calorimetry (ITC) or bio-layer interferometry (BLI). This hypothesis goes in line with the lower proportion of P178L dimers from **figure 23B**, supporting that the mutation could impaired TFAM-TFAM interaction. Moreover, TFAM-TFAM interactions has been proposed to be important in mtDNA model of compaction (cf. section 1.6.2 and 1.6.3), that could partly explain the difference of DNA persistence length displayed in AFS experiments between TFAM WT and P178L at 500 nM of concentration (publication 2.2 and **figure 26**).

Salt dissociation experiment

It was shown that the TFAM dissociation rate increases with increasing salt concentration (Farge *et al.*, 2012). To study if the mutation impacts the salt dependence dissociation rate of TFAM, we performed a salt dissociation assay with TFAM WT and TFAM P178L labelled with Alexa Fluor 555. In this assay, TFAM WT and P178L are studied separately. TFAM proteins were flushed in the microfluidic chamber at a concentration of 100 nM in the presence of label free and stretched DNA molecules (**Figure 28**). Then, the dissociation experiment starts with adding NaCl at various concentrations (75 mM and 150 mM) during 2 min following with 1 min incubation time without flow. Intensities of DNA molecules coated by TFAM (n~50) were measured over time and data were fit with the equation : $I(t)=I(0)\bullet\exp(-t/\tau_{\text{dissociation}})\bullet\exp(-t/\tau_{\text{photobleaching}})$ to extract the dissociation rate, corrected with the photobleaching rate. Overall, at 75 and 150 mM NaCl concentration, there is no relevant difference between TFAM WT and P178L, indicating that TFAM P178L displays the same salt dependence dissociation (**Figure 27**).

We conducted another experiment in which both version of TFAM were mixed together at the same concentration of 5 nM, with WT labelled with Alexa 647 and R107Q with Alexa 555, and added with pre-stretched dsDNA molecules labelled with YOYO-1. When we observed

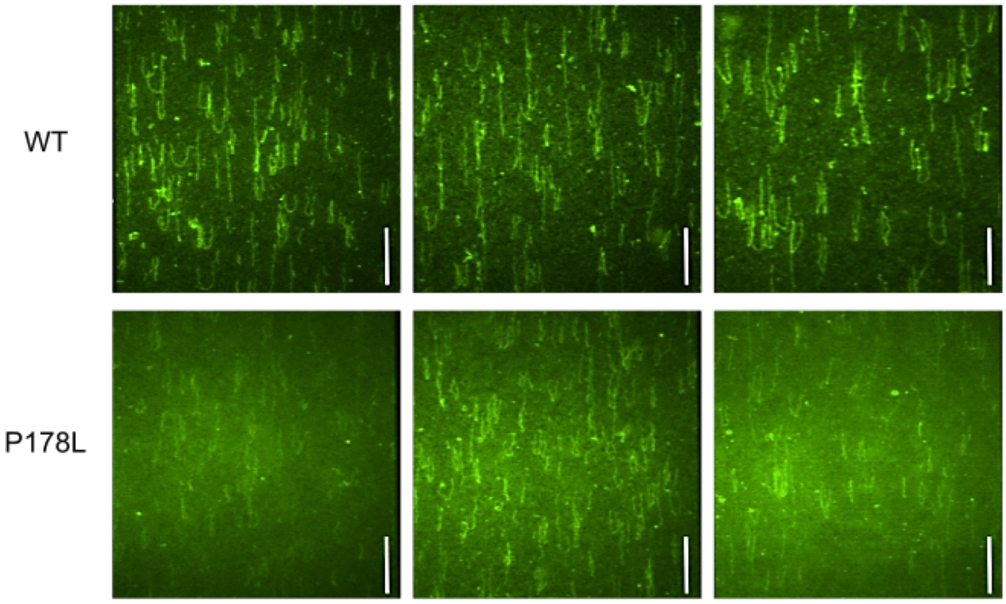

Figure 28: WT and P187L TIRF view before salt dissociation assay at 0 mM NaCl. TFAM WT and P178L labelled with Alexa 555 were used, at a concentration of 100 nM. DNA concentration was 0.15 ng/µL. DNA were pre-stretched, prior adding TFAM proteins. Scale bar = 10 µm.

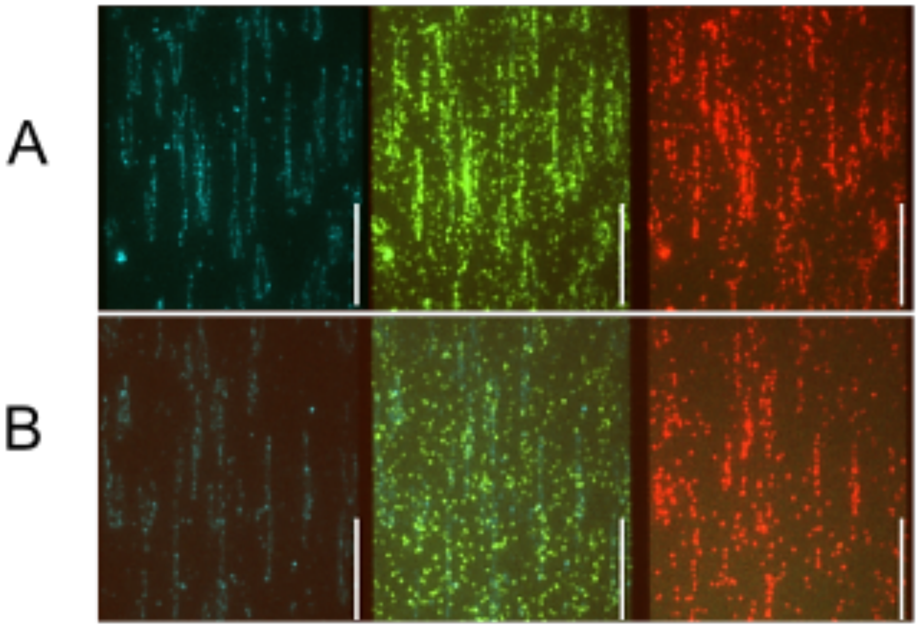

Figure 29: TFAMs binding at 0 or 25 mM NaCl. TIRF view of DNA (**blue**), P178L (**green**) and WT TFAM (**red**) at 5 nM of proteins. (**A**) Picture taken at 0 mM NaCl. (**B**) Picture taken at 25 mM NaCl from a different ROI. Scales bars = 10µm.

both TFAMs in the three colours experiments without salt and after adding 25 mM salt (**Figure 29**), it appears that both TFAM coats well DNA molecules without salt but upon addition of 25 mM NaCl, P178L seems to be scattered in comparison to WT in which we can still distinguish DNA shape through WT binding. These observations show that P178L dissociation may be enhanced by salt concentration which is not in line with our salt dissociation data analysis (**Figure 27**), but this difference should be carefully study as both experiments are not the same as in the three colours assay, both TFAM are competing for dsDNA. It should also be noted that a more accurately dissociation analysis could be done with background subtraction. A more detailed study and analysis is necessary to address this issue. Also, more data should be gathered with lower TFAM concentrations.

Finally, when we acquired images (that were used to measure dissociation) of TFAM WT versus P178L before adding salt, it appears that DNA coverage seems lower with P178L (**Figure 28**). The DNA coverage needs to be quantified to estimate the number of bound TFAM WT and P178L the same way as we did for mtSSB in chapter 2.3. If we could demonstrate that TFAM P178L shows a lower on-rate than WT, this could explain the difference of persistence length values between WT and P178L, as a higher concentration of P178L is required to decrease in a same extent as the WT the DNA persistence length. Overall, our results eventhough preliminary, tend to suggest that motion on DNA of TFAM P178L is not impaired but that the mutation might affect TFAM protein-protein interactions as well as TFAM salt dependence binding affinity.

Outlook

For perspectives, in a short-term, quantification of DNA coverage by TFAM P178L as a function of TFAM concentration as well as quantification of DNA persistence length as a function of TFAM concentration could give insight in cooperativity and binding affinity. In the long-term, a cellular model expressing TFAM P178L could be obtained with gene editing with CRISPr. This would allow the *in vivo* study of replication using EdU and transcription using BrU, or the analysis of the expression of main actors of the replication such as POLγ or mtSSB via western blot.

Interestingly, 7S DNA level was found to be increased relatively to WT. The role of 7S DNA in replication is still not completely understood. However, it was shown that 7S DNA is more present in “active nucleoids” (Nicholls *et al.,* 2014). As the P178L mutation seems to mildly impair DNA compaction, the proportion of active nucleoids could be increased relatively to

nucleoids in a “storage form”. Indeed it was shown that TFAM compaction can block mtDNA replication (Farge *et al.*, 2014). As nucleoids in a storage form were seen to be in a greater numbers than active nucleoids (Brüser *et al.*, 2021), the increased level of 7S DNA relatively to mtDNA degradation could result from a switch between the storage form to active nucleoids as TFAM is depleted. Multi-color STED super-resolution microscopy on human cells expressing TFAM P178L could be way to analyse nucleoids activity. Associated with LON and proteasome 20S inhibitors, information on P178L degradation in the cytosol could be studied. Indeed, it was shown that the level of a dimer-defective variant (Kasashima *et al.*, 2015) was restored *in vivo* using protease inhibitor, thus supporting that TFAM dimerization could be involved in its stability. Therefore, dimerization impairment could explain the P178L decreased level in patient fibroblasts.

BBA - Molecular Basis of Disease 1868 (2022) 166467

Contents lists available at ScienceDirect

BBA - Molecular Basis of Disease

journal homepage: www.elsevier.com/locate/bbadis

Disease causing mutation (P178L) in mitochondrial transcription factor A results in impaired mitochondrial transcription initiation

Majda Mehmedović [a], Martial Martucci [b], Henrik Spåhr [c,e,f], Layal Ishak [a], Anup Mishra [a], Maria Eugenia Sanchez-Sandoval [a], Carlos Pardo-Hernández [a], Bradley Peter [a], Siet M. van den Wildenberg [b,d], Maria Falkenberg [a,*], Geraldine Farge [b,*]

[a] *Department of Medical Biochemistry and Cell Biology, University of Gothenburg, P.O. Box 440, SE-405 30 Gothenburg, Sweden*
[b] *Université Clermont Auvergne, CNRS, Laboratoire de Physique de Clermont, F-63000 Clermont-Ferrand, France*
[c] *Department of Mitochondrial Biology, Max Planck Institute for Biology of Ageing, 50931 Cologne, Germany*
[d] *Université Clermont Auvergne, CNRS, IRD, Université Jean Monnet Saint Etienne, LMV, F-63000 Clermont-Ferrand, France*
[e] *Department of Medical Biochemistry and Biophysics, Karolinska Institutet, Stockholm 17177, Sweden*
[f] *Max Planck Institute for Biology of Ageing - Karolinska Institutet Laboratory, Karolinska Institutet, Stockholm 17177, Sweden*

ARTICLE INFO

Keywords:
TFAM
Mitochondria
Disease causing mutation
Transcription initiation
mtDNA depletion

ABSTRACT

Mitochondrial transcription factor A (TFAM) is essential for the maintenance, expression, and packaging of mitochondrial DNA (mtDNA). Recently, a pathogenic homozygous variant in TFAM (P178L) has been associated with a severe mtDNA depletion syndrome leading to neonatal liver failure and early death. We have performed a biochemical characterization of the TFAM variant P178L in order to understand the molecular basis for the pathogenicity of this mutation. We observe no effects on DNA binding, and compaction of DNA is only mildly affected by the P178L amino acid change. Instead, the mutation severely impairs mtDNA transcription initiation at the mitochondrial heavy and light strand promoters. Molecular modeling suggests that the P178L mutation affects promoter sequence recognition and the interaction between TFAM and the tether helix of POLRMT, thus explaining transcription initiation deficiency.

1. Introduction

Mitochondrial DNA (mtDNA) maintenance defects (MDMDs) are caused by a dysfunction of nuclear-encoded mtDNA maintenance factors and are characterized by low levels and/or multiple deletions of mtDNA in affected tissues and organs [1]. MDMDs are transmitted in an autosomal recessive or dominant manner, and the clinical phenotypes are heterogeneous, ranging from mild adult-onset weakness of the extra-ocular muscles (ophthalmoplegia) to severe early-onset hepatic failure. Several pathogenic variants have been associated with this class of diseases, most of them reported in genes involved maintaining the mitochondrial/cytosolic nucleotide pool, mtDNA synthesis/transcription or mitochondrial dynamics (reviewed by [2]).

mtDNA is a circular molecule comprised of a light strand and a heavy strand, each containing its own origin of replication (O_L and O_H, respectively) and promoters for transcription (LSP and HSP, respectively). It is replicated and transcribed by relatively simple enzymatic machineries distinct from those involved in nuclear DNA replication and transcription. These processes are linked in mitochondria, since POLRMT generates the RNA primers required to initiate mtDNA replication [3,4]. First, the mitochondrial transcription factor A (TFAM) binds specifically to a promoter element upstream of the transcription start site and induces a U-bend in the DNA [5,6]. This structural change allows the mitochondrial RNA polymerase (POLRMT) to bind to the promoter and form a closed pre-initiation complex [7,8]. A structure of the initiation complex showed that a high mobility box domain of TFAM, HMG2, interacts with the N-terminal region of POLRMT, also known as the 'tether helix', thereby anchoring the active site of POLRMT near the transcription start site where the initial melting takes place [9]. The mitochondrial transcription factor B2 (TFB2M) can then induce structural changes in POLRMT that eventually lead to the formation of the open initiation complex and initiation of RNA synthesis.

TFAM monomers have been shown to diffuse rapidly along non-specific DNA sequences via 1D sliding, a potential mechanism by

---

* Corresponding authors.
E-mail addresses: maria.falkenberg@medkem.gu.se (M. Falkenberg), geraldine.farge@uca.fr (G. Farge).

https://doi.org/10.1016/j.bbadis.2022.166467
Received 13 March 2022; Received in revised form 31 May 2022; Accepted 9 June 2022
Available online 15 June 2022

which they locate the mtDNA promoters to initiate transcription [10,11]. TFAM also has an essential role in the packaging of mtDNA into nucleoids [12,46]. In contrast to its role in transcription initiation where TFAM interacts specifically with the promotor regions, DNA compaction depends on TFAM's ability to bind non-sequence-specifically to DNA. These two activities are balanced by mitochondrial TFAM levels, i.e. lower TFAM concentrations favor transcription, whereas high amounts lead to compaction, which eventually may shut down transcription completely [13]. TFAM level is believed to be regulated by Lon Peptidase 1 (LONP1) that degrades TFAM not bound to mtDNA [48].

Despite its central role in mtDNA maintenance, only a few mutations in TFAM have been associated with human disease. Expression of a truncated TFAM protein missing the last 149 amino acids (TFAM$^{\Delta149}$) has been reported to cause mtDNA depletion and micro-satellite unstable colorectal cancer [14]. Furthermore, a homozygous variant of TFAM with the amino acid substitution arginine (R) to cysteine (C) at position 232 (TFAM^{R232C}) was identified by whole-exome sequencing in patients with Perrault syndrome, a rare heterogeneous condition characterized by sensorineural hearing loss and premature ovarian insufficiency [15]. Finally, the amino acid substitution proline (P) to leucine (L) at position 178 in TFAM (TFAM^{P178L}) was identified in a consanguineous family and shown to cause neonatal-onset liver failure progressing to demise and mtDNA depletion in liver and skeletal muscle [16].

Here we investigate the functional consequences of the P178L mutation. We report that the mutation leads to a severe depletion of mtDNA in patient fibroblast cells. Furthermore, while the P178L mutation only marginally affects TFAM's ability to bind and compact DNA, its ability to support transcription initiation is severely impaired. We discuss these findings in the light of a structural molecular model.

2. Experimental procedures

2.1. Cell culture

Primary human skin fibroblast cells from healthy donors and patients with P178L phenotype were obtained from the J.E. Abdenur group [16]. The cells were grown on plates in DMEM (1×) + GlutMAX™ (Gibco) medium containing 15 % FBS and 1 % Pen Strep (Gibco), at 37 °C and 5 % CO_2.

2.2. Southern blotting

Total DNA from cells was extracted using the High Pure PCR template preparation kit for genomic DNA (Roche) according to the manufacturer's instructions. Extracted DNA was treated with RNase A (Thermo Fisher Scientific) and *BamHI* or *PuvII* in 1× Cutsmart buffer (NEB) at 37 °C for 1 h. A total of 1 μg of treated DNA was separated by electrophoresis on a 1 % agarose gel in 1 × TBE running buffer. After incubation in depurination, denaturation, and neutralization buffers, DNA was transferred to a charged nylon membrane (Hybond-N+-membrane, GE Healthcare) and cross-linked with UV exposure (254 nm UV, 200 mJ/cm^2). Probes against mtDNA positions 16,262–16282 (FW: 5′-CTC ACC CAC TAG GAT ACC AA-3′) and 128–109 (REV: 5′-GAT ACT GCG ACA TAG GGT GC-3′) within the D-loop were radioactively labeled with [γ-P^{32}] ATP at the 5′-end and hybridized to the membrane. As a control, the housekeeping nuclear gene 28S rRNA was targeted (FW: 5′-GCC TAG CAG CCG ACT TAG AAC TGG 3′; REV: 5′ GGG CCT CCC ACT TAT TCT ACA CCT C-3′). Quantification was performed using Multi Gauge analysis software.

2.3. Western blotting

Total cell lysates were analyzed by SDS PAGE followed by immunoblotting using the iBind system (ThermoFisher). Primary antibodies used were as follows: TIM23 (BD biosciences, 611222), 1:1000; TFAM (homemade), 1:2000; actin (Abcam, ab6276), 1:2000. Secondary antibodies were as follows: Goat (HRP) anti-mouse (ThermoFisher 31430) and Goat (HRP) anti-rabbit (Invitrogen 65612). The detection of proteins was performed using Pierce ECL western blotting Substrate (ThermoFisher).

2.4. Fluorescence microscopy

Cells were grown on 12 mm coverslips for 24 h. Cells were fixed using 4 % paraformaldehyde (PFA) in cell culture medium for 20 min, washed 3 times in PBS, and permeabilized for 10 min with 1 % Triton X100. Primary and secondary antibodies were incubated at the following concentrations: COXIV (cell signaling, 4850), 1:200; anti-DNA antibody (AC 30-10, Sigma-Aldrich), 1:200; secondary goat-anti-mouse IGM AlexaFluor 488 (Invitrogen), 1:250; and goat-anti-rabbit IgG AlexaFluor 594 (Cell signaling), 1:250. Cell nuclei were counterstained with 300 nM 4′,6-diamidino-2-phenylindole (DAPI) before mounting in ProLong Diamond. A Zeiss LSM 880 equipped with an Airyscan detector was used for image acquisition.

2.5. Protein purification

Recombinant proteins mtSSB, POLγA, POLγB, TWINKLE, POLRMT, TFB2M, and LONP1 were expressed and purified as described previously [4,17–19]. The DNA sequence lacking the mitochondrial targeting sequence coding for TFAM (amino acids 43–246) was cloned into the pJ477 plasmid (Atum) containing a TEV cleaving site, MBP- and His-tag sequences. Mutagenesis of TFAM was performed using the QuikChange Lightning site-directed mutagenesis kit (AgilentTechnologies), and confirmed by sequencing (Eurofins MWG Operon). All versions of TFAM were expressed in *E. coli* pLys-Rosetta cells in Luria-Bertani medium containing 25 μg/mL kanamycin and 34 μg/mL chloramphenicol. The proteins were induced with 0.5 mM IPTG at OD_{600} ~0.6 and grown at 37 °C with shaking for 2 h before harvesting. The proteins were purified with Ni^{2+}-sepharose, cleaved with TEV enzyme and run on HiTrap™ Heparin HP and HiTrap™ SP HP columns (GE Healthcare). All TFAM versions were stored in a stock buffer (25 mM HEPES pH 7.2, 10 % glycerol, 0.6 M NaCl, 1 mM DTT, and 0.5 mM EDTA).

2.6. Thermofluor stability assay

The fluorescent dye Sypro Orange (Invitrogen) was used to monitor the temperature-induced unfolding of TFAM^{WT}, TFAM^{P178L} and TFAM$^{\Delta25C}$. Proteins (2 μM final) were set up in 96-well PCR plates in reaction buffer (10 mM HEPES pH 7.2, 50 mM NaCl, 1 mM DTT and 5 × SYPRO Orange). Differential scanning fluorimetry was performed in a C1000™ Thermal Cycler using the CFX96™ real time software (Bio-Rad). Scans were recorded using the HEX emission filter (560–580 nm) between 4 °C and 95 °C in 0.5 °C increments with a 5 s equilibration time. The melting temperature (Tm) was determined from the first derivative of a plot of fluorescence intensity *versus* temperature [47].

2.7. Modeling of mutation effects on the structure

Structure prediction of TFAM^{P178L} was performed using AlphaFold [20]. Prediction of protein stability and flexibility upon mutation was performed using Dynamut [21]. Structural analysis was based on PDB ID: 3TMM [5] and PDB ID: 6ERP [9].

2.8. DNA compaction

The DNA template for compaction studies was prepared by digesting pUC18 plasmid with *HindIII* and *SspI*, yielding a linear fragment of 584 bp with a 5′ overhang and a blunt end. The linearized fragment was extracted from a 1 % agarose gel in 1 × TAE buffer using the QIAquick Gel Extraction kit (Qiagen). The template was subsequently labeled with [α-P^{32}] dCTP using the large Klenow fragment (ThermoFisher) to fill in

the 5′ overhang. The experiment was carried out utilizing electrophoresis mobility shift assays (EMSA) where reactions were performed in a reaction buffer containing 10 mM HEPES pH 7.2, 50 mM NaCl, 1 mM DTT, 0.5 mM EDTA, 100 μg/mL BSA, 5 mM $MgCl_2$, and 10 % glycerol in a total volume of 20 μL. The indicated concentrations of TFAM (0 nM, 3.65 nM, 7.3 nM, 14.6 nM, 292 nM, and 584 nM) were incubated with labeled DNA template (10 fmol) for 10 min in 25 °C. Reactions were then analyzed on a native 4 % polyacrylamide gel (PAGE) in 0.5 × TBE buffer.

2.9. DNA binding and K_d value determination

For the determination of K_d values, a dsDNA template (22 bp) containing the mtDNA HSP sequence was designed using two oligonucleotides (oligonucleotide 1: 5′-GGT TGG TTC GGG GTA TGG GGT T-3′, oligonucleotide 2: 5′-AAC CCC ATA CCC CGA ACC AAC C-3′). Oligonucleotide 1 was labeled with [γ-P^{32}] ATP at the 5′-end using T4 polynucleotide kinase (NEB). It was then annealed to the complementary ssDNA oligonucleotide 2 to obtain a labeled dsDNA template. The reactions were performed and analyzed as described above with the indicated TFAM concentrations (0, 1, 2, 4, 5, 10, 15, 20, 40, 50, 75, and 100 nM) per reaction. K_d values were calculated using GraphPad Prism 8 software, using non-linear one-site specific binding analysis with a constraint of Bmax = 1.

2.10. Competition assays

Cold (unlabeled) dsDNA template was obtained by annealing oligonucleotide 1 with oligonucleotide 2 (see above). Competition assays were performed using the same EMSA reaction conditions as described above. Labeled dsDNA (22 bp) was added to the reaction mixture (10 fmol). For a negative control 20 μL of reaction mixture was removed containing only 10 fmol hot DNA template. After adding TFAM (50 nM), the reaction mixture was incubated for 10 min at 25 °C then put on ice and 20 μL was removed as a positive control containing only TFAM and hot DNA. Subsequently 19 μL of the reaction mixture was removed and added to 1 μL of cold DNA template at the indicated concentrations (10 fmol, 100 fmol, 1 pmol, 10 pmol) and incubated again at 25 °C for 10 min, then put on ice before loading the samples for analysis on a native 4 % PAGE in 0.5 × TBE. For competition assays with a longer DNA template (197 bp), pUC18 plasmid was cleaved with *Xma*I and *Sfo*I giving rise to a 5′ overhang and 3′ blunt end. The template was subsequently labeled with the large Klenow fragment and reactions were performed as described above in presence of 40 nM TFAM (2.5 bp/TFAM).

2.11. Rolling-circle DNA replication

Rolling-circle reactions were performed in a reaction mixture containing 25 mM HEPES pH 7.6, 10 mM $MgCl_2$, 10 mM DTT, 100 μg/mL BSA, 4 mM ATP, 100 BSA, 4 mM ATP, 100 μM dATP, 100 μM dTTP, 100 μM dGTP, 10 μM dCTP, 10 fmol rolling circle template, and [α-P^{32}]-dCTP. The final volume was 25 μL and the reactions were performed as previously described [3]. TWINKLE (200 fmol, calculated as a hexamer), POLγA (250 fmol), POLγB (500 fmol, calculated as a dimer), and mtSSB (3 pmol, calculated as a tetramer) were present in the reactions. The TFAM (0 nM, 156 nM, 195 nM, 260 nM, 390 nM, 780 nM) added to the reactions was calculated as a ratio to DNA, as indicated. The total amount of salt was calculated to account for the salt in the protein solutions. The reactions were performed at 37 °C and stopped after 60 min by adding 10 μL alkaline gel loading buffer (300 mM NaOH, 6 mM EDTA, 18 % Ficoll, 0.05 % Xylene Cyanol FF) and 1 μL 0.5 M EDTA to the samples. These were then analyzed on an alkaline gel (0.8 % agarose, 50 mM NaOH, 1 mM EDTA).

2.12. TFAM proteolysis assay

In vitro TFAM proteolysis assays were performed in 10 μL reaction volumes. LONP1 (240 nM, calculated as a monomer) and 1.3 μM of $TFAM^{WT}$ or $TFAM^{P178L}$ were incubated at 37 °C for 0–30 min in a buffer containing 50 mM Tris-HCl pH 8.0, 10 mM MgCl2, 0.1 mg/mL BSA, 2 mM ATP and 1 mM DTT. The reactions were stopped by the addition of SDS-PAGE loading buffer. Samples were run in a precast 4–20 % gradient SDS-PAGE gel.

2.13. In vitro transcription

The DNA template for *in vitro* transcription was obtained by PCR, amplifying the mitochondrial genome sequence 1–740 nt with following primers (FW: 5′-ATC CCG GGA TGG ATC CGA TCA CAG GTC TAT CA-3′; REV: 5′-ATG GCG CCA TAA GCT TTC GTG GTG ATT TAG AG-3′). The PCR fragment was purified with PCR purification kit (Qiagen) before use. *In vitro* transcription (in a total volume of 25 μL) was performed and analyzed as described previously [7,13] with POLRMT (500 fmol), TFB2M (1 pmol), and TFAM present at various concentrations (31 nM, 62 nM, 124 nM, 248 nM, 495 nM, 990 nM) to obtain the indicated TFAM to DNA ratio. The transcription run off was quantified and normalized by the number of UMPs (U) present in the run off from each promoter (108 U for LSP and 50 U for HSP, respectively).

2.14. Acoustic force spectroscopy

For AFS experiments, DNA tethers were made by attaching DNA molecules between a glass surface and 4.5 μm polystyrene beads. A detailed description of the AFS instrumentation (LUMICKS B.V., Amsterdam, the Netherlands) can be found in [22,23]. DNA substrates were made by PCR amplification (PCR Long Amplification Taq PCR kit, NEB) of a 9 kb fragment of human mitochondrial genome (position 1671–10600) using total DNA from HEK293 cells, and modified primers with either two digoxygenins (DIG) or two biotins (BIO) at their 5′-end: 5′-DIG-DIG-GCT AAA CCT AGC CCC AAA CC-3′ and 5′-T(BIO)-T(BIO)-GTG TTG AGG GTT ATG AGA GTA GC-3′. Flow cell (LUMICKS B.V., Amsterdam, the Netherlands) cleaning, passivation, and beads tethering were performed as described in [24] with some minor changes.

On average, 20 single DNA tethers were measured simultaneously in a buffer containing 10 mM Tris HCl pH 7.8, 75 mM NaCl, and 0.25 % glycerol. A typical assay was performed as follows: (i), the r.m.s (root-mean-square) amplitude of the Brownian motion of the beads was measured for 20 min with bare DNA; (ii), force calibration was performed; (iii), stretching (force-distance) curves were generated. These steps with bare DNA constituted our control and were done for each assay. Proteins of interest were then flushed in the flow cell with a flow rate of 1 μL/min for 15 min, beads r.m.s was recorded for 20 min, and stretching curves were generated. Data acquisition was performed using AFS Tracking G2 and AFS Analysis G2 software (LUMICKS B.V., Amsterdam, the Netherlands).

2.15. Analysis

We used the extensible worm-like chain (eWLC) model [25] to approximate the dsDNA elastic behavior according to:

$$x = L_C\left[1 - \frac{1}{2}\sqrt{\left(\frac{k_bT}{FL_p}\right)} + \frac{F}{K}\right],$$

where x is the extension (end-to-end distance) of the DNA, L_c is the contour length, k_BT is Boltzmann's constant times absolute temperature, F is the force, L_p the persistence length, and K the stretch modulus of DNA (set at 1200 pN). A custom-written MATLAB program was used to fit the stretching curves up to ~20 pN.

3. Results

3.1. mtDNA depletion in TFAM^{P178L} patient cells

The homozygous mutation P178L has been correlated with mtDNA depletion in both liver and skeletal muscle tissues in a pair of sibling patients [16]. We thus sought to confirm that we could observe a similar phenotype in fibroblast cells obtained from one of these patients. In wild-type (WT) cells, approximately 95 % of replication initiation events initiated at O_H are prematurely terminated, and the resulting DNA fragment of about 650 bp is denoted 7S DNA [26,27]. We performed Southern blot to observe and quantify mtDNA in healthy control and patient primary skin fibroblast cells (Fig. 1A and B) using probes against the D-loop region of mtDNA. In agreement with the reported case [16], we noticed a severe depletion of full-length mtDNA in patient cells (~20 % of control cell levels), which was confirmed by immunofluorescence using an antibody targeting DNA (Fig. 1C). This decrease in mtDNA content in patient fibroblasts was accompanied by a marked decrease of TFAM protein level (Fig. 1D). Interestingly, 7S DNA levels remained unchanged compared to control cells and were increased relative to mDNA in patient cells (Fig. 1B).

3.2. The P178L mutation is predicted to affect the structure of TFAM

To understand the pathogenicity of the P178L variant, we cloned and expressed recombinant TFAM^{P178L} (Fig. 2A). For comparison, we also cloned and expressed a TFAM mutant lacking the C-terminal tail (TFAM$^{\Delta25C}$) that has been characterized previously [28]. TFAM$^{\Delta25C}$ has a 100-fold reduced transcription activity compared to TFAM^{WT} [29] and a reduced ability to bind DNA [28]. A thermofluor assay revealed that both TFAM^{P178L} and TFAM$^{\Delta25C}$ showed near TFAM^{WT} stability (Fig. 2B) (WT Tm = 35 °C, P178L Tm = 35.5 °C, Δ25C Tm = 36 °C). Moreover, as TFAM that is not bound to mtDNA is rapidly degraded by the LONP1 [30], we performed a proteolysis assay in which we incubated TFAM^{WT} or TFAM^{P178L} with LONP1 for increasing times (Fig. S1). Our results showed a similar sensitivity to LONP1-mediated proteolysis for TFAM^{WT} and TFAM^{P178L}.

A recent study showed that TFAM recognizes a minimal motif in mtDNA consisting of two guanines separated by 10 random nucleotides ($GN_{10}G$), which is essential for transcription initiation [31]. Interestingly, the main chain carbonyl of P178 forms a sequence specific hydrogen bond with the base of G-31 of the $GN_{10}G$ motif at LSP or HSP. We performed molecular modeling, which predicts that the P178L mutation would lead to a clash between the bulky side chain of leucine and the bases of G-31 and G-30 of LSP in an initiation complex and would therefore be unable to form the sequence specific bond (Fig. 2C). Instead, the side chain of leucine forms a hydrophobic interaction with F170 that give rise to a local stabilization at the mutation site, an increase in flexibility in surrounding regions and a shift in position of helix α6 (Fig. 2C–D). A change in position of α6 may affect the interaction between TFAM and the tether helix of POLRMT as W122 of the tether helix is inserted into a binding pocket formed by A167, V164, and E168 of α6 in TFAM (Fig. 2C).

3.3. The P178L mutation does not impair the ability of TFAM to bind dsDNA

We measured the ability of TFAM^{WT} and its two variants to bind dsDNA with an electrophoresis mobility shift assay (EMSA), using a short dsDNA template (22 bp) containing the TFAM binding site at HSP and increasing TFAM concentrations (Fig. 3A). Only minor variations in the dissociation constant (K_d) were observed for TFAM^{WT}, TFAM^{P178L}, and TFAM$^{\Delta25C}$ (12.23 ± 0.11 nM, 13.08 ± 0.10 nM and 15.08 ± 0.12 nM, respectively), indicating similar DNA binding capabilities. Interestingly, TFAM$^{\Delta25C}$ displayed a double shift on the gel (Fig. 3A). This could be because the lack of the C-terminal tail can enable more TFAM molecules to bind on a short DNA stretch.

3.4. The ability of TFAM to compact DNA is slightly reduced in the P178L variant

As TFAM plays an essential role in packaging mtDNA into nucleoids [12], we used EMSA to visualize the level of mtDNA compaction by TFAM^{WT} and its variants. We employed a longer, linear non-specific DNA fragment (585 bp) as a template because a distinct nucleoprotein complex corresponding to fully compacted mtDNA can be observed as a distinct band. Even though TFAM^{P178L} and TFAM$^{\Delta25C}$ bind to DNA as efficiently as TFAM^{WT}, we found that their ability to compact DNA was slightly affected (Fig. 4A). While a distinct band appeared at a ratio of 10 bp/TFAM for TFAM^{WT}, a more dispersed band was observed for TFAM^{P178L} and TFAM$^{\Delta25C}$ at the same concentration, suggesting that the nucleoprotein structures are not as compacted compared to TFAM^{WT}. This seemingly less effective DNA compaction by TFAM^{P178L} and TFAM$^{\Delta25C}$ could be due to faster dissociation of TFAM^{P178L} and TFAM$^{\Delta25C}$ from the DNA than TFAM^{WT}. To test this hypothesis, we performed competition assays using either a short DNA template (22 bp) or a longer DNA fragment (197 bp) (Fig. S2) but observed no major differences between TFAM^{WT}, TFAM^{P178L}, and TFAM$^{\Delta25C}$.

TFAM^{WT} compacts double stranded DNA (dsDNA) by increasing its flexibility, as indicated by a decrease in the dsDNA's persistence length [10]. To investigate whether TFAM^{P178L} or TFAM$^{\Delta25C}$ could modify the elastic properties of dsDNA in a similar manner, we used acoustic force spectroscopy (AFS) to measure the force-extension behavior of individual dsDNA molecules (~9 kb) at two different TFAM concentrations (Fig. S3). As expected [10,32], we found that, upon addition of TFAM, the mechanical response of the DNA changed significantly. The TFAM-induced changes of DNA were then quantified by fitting each FD curve to the extensible worm-like chain (eWLC) model, which describes the force-extension properties of dsDNA using three parameters: Lp (the persistence length), Lc (the contour length) and S (the stretch modulus). Our results presented in Fig. 4B and C show that an intermediate TFAM^{WT} concentration (500 nM) leads to an important decrease in Lp (Lp/Lp naked = 6 %). At this concentration, the persistence length of dsDNA coated with TFAM^{P178L} or TFAM$^{\Delta25C}$ also decreased, but to a lesser extent (Lp/Lp naked = 16 % and 17 %, respectively). We can thus conclude that TFAM^{P178L} and TFAM$^{\Delta25C}$ have a slightly impaired capacity to increase DNA flexibility, confirming our EMSA results. However, at a saturating protein concentration (1 μM), the Lp of dsDNA coated with TFAM^{WT}, TFAM^{P178L} or TFAM$^{\Delta25C}$ was more consistent (Lp/Lp naked = 8 %, 9 %, and 6 %, respectively). Additionally, TFAM^{P178L} and TFAM$^{\Delta25C}$ could both induce an equally small increase in Lc as TFAM^{WT} (Fig. 4C).

3.5. Higher TFAM^{P178L} concentrations are required to block replication progression

We have previously demonstrated that TFAM^{WT} can block the progression of the DNA replication machinery by compacting the dsDNA template [13]. Using an *in vitro* DNA replication assay [18], we investigated the capacity of TFAM^{P178L} and TFAM$^{\Delta25C}$ to block DNA replication in a similar manner. On a circular dsDNA template (4 kb) with a preformed replication fork, POLγ, TWINKLE, and mtSSB can support DNA replication, generating long stretches of single stranded DNA molecules. We found that adding increasing concentrations of TFAM^{WT} (Fig. 4D) led to a progressive decrease in replication starting at a ratio of 10 bp per TFAM molecule, which reached a complete abolishment of DNA replication at a ratio of 4 bp/TFAM. At ratios between 8 and 4 bp/TFAM, both TFAM^{P178L} and TFAM$^{\Delta25C}$ were less efficient in blocking replication progression than TFAM^{WT}. However, at a very high ratio (2 bp/TFAM), TFAM^{P178L} and TFAM$^{\Delta25C}$ could inhibit replication progression through compaction similar to TFAM^{WT}.

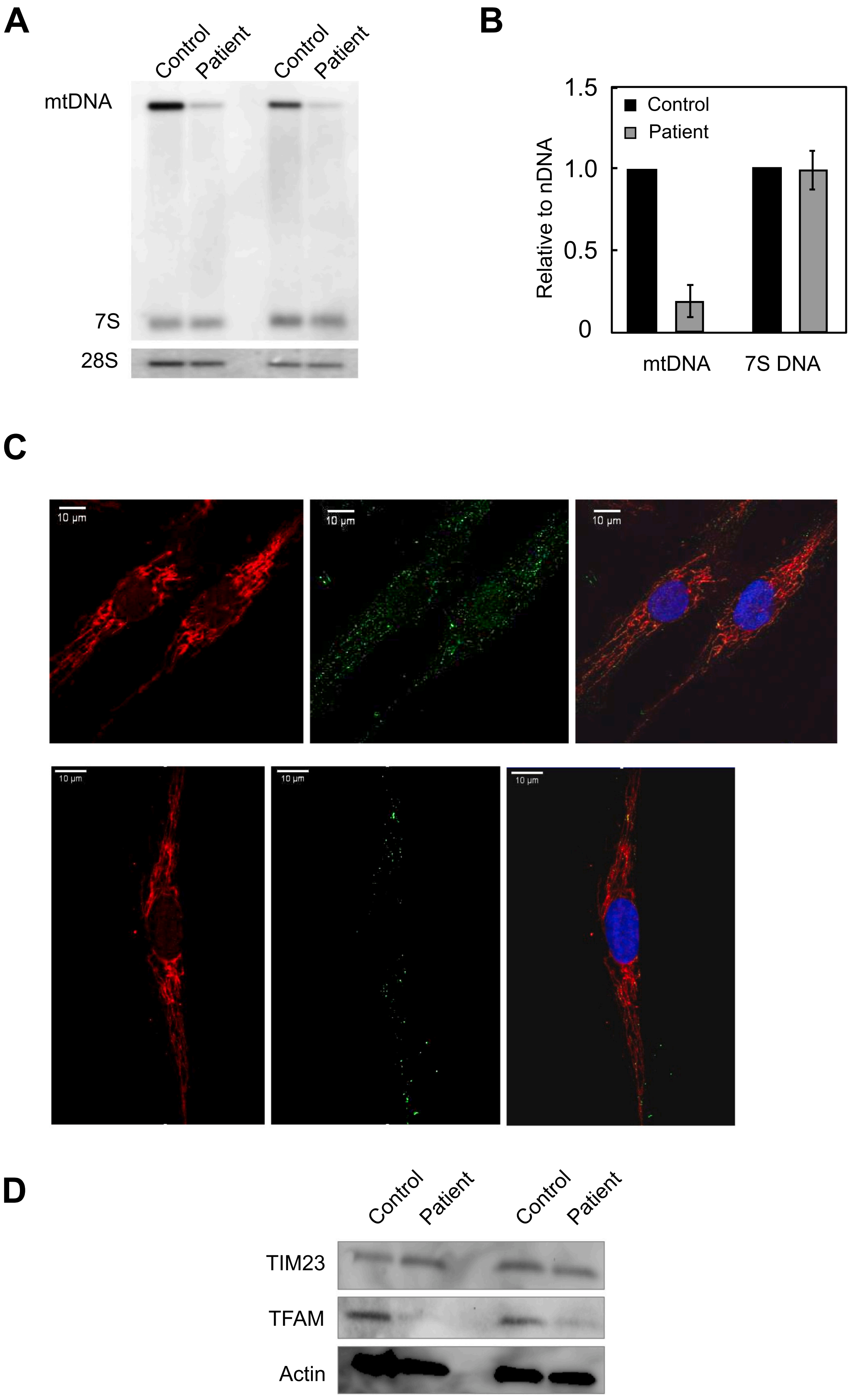

(caption on next page)

Fig. 1. Depletion of mtDNA and TFAM protein levels in patient cells. (A) Southern blot of control and patient cells, in duplicates. mtDNA, 7S DNA, and housekeeping 28S are indicated. (B) Quantification of mtDNA in control cells and in TFAM^{P178L} patient cells based on Southern blot. Data was normalized to the housekeeping nuclear gene 28S (mean ± s.e.m., $N = 4$). (C) Representative immunofluorescence microscopy images of mitochondrial morphology (COX IV antibody, red) and mtDNA staining (anti-DNA antibody, green) in control (upper panel) and patient cells (lower panel). In blue: nuclear staining with DAPI. (D) Western blot analysis showing decreased level of TFAM in patient cells compared to control. TIM23 was used as a mitochondrial control and actin as a loading control. (For interpretation of the references to colour in this figure legend, the reader is referred to the web version of this article.)

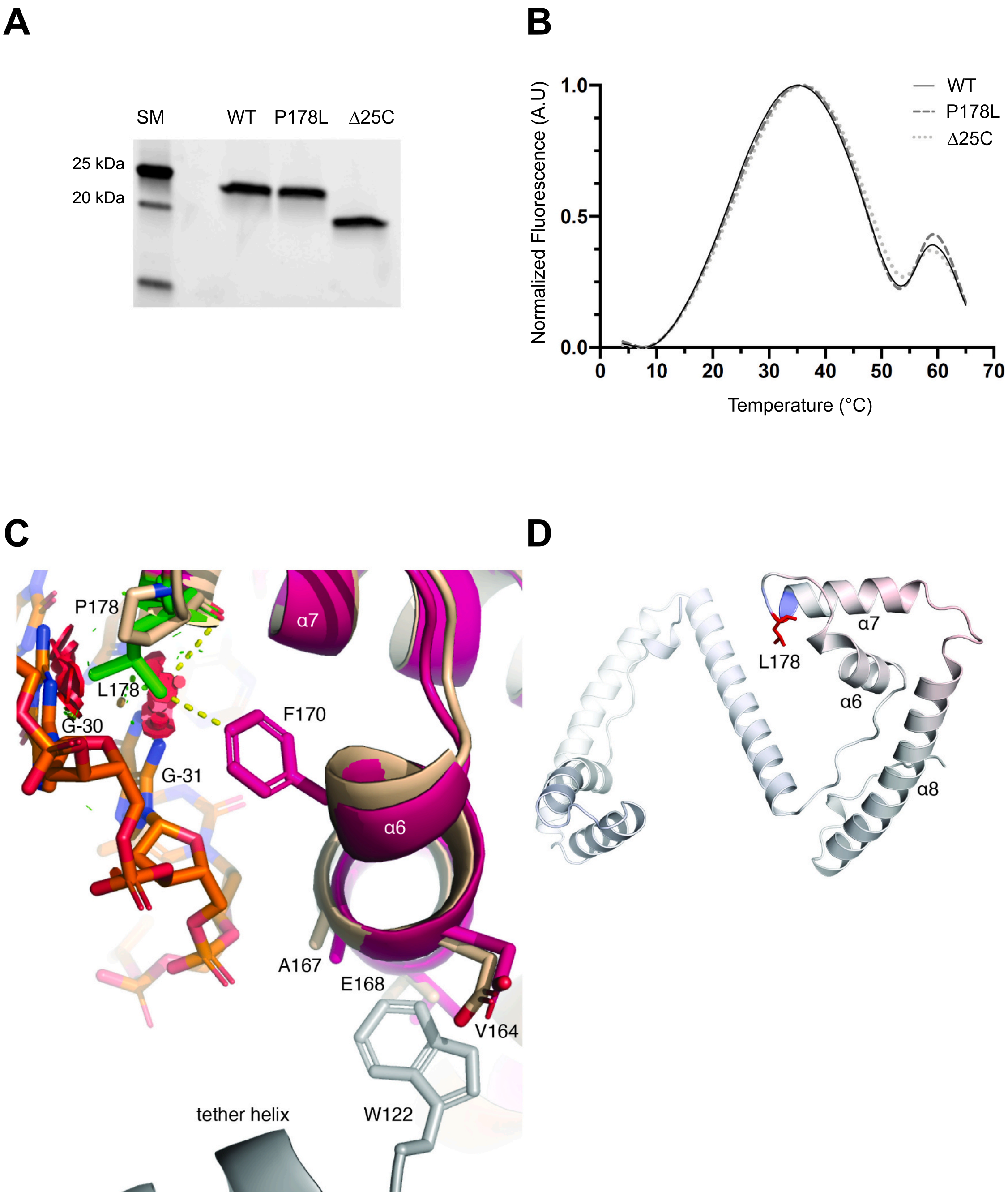

Fig. 2. Structural and stability effects of the P178L mutation. (A) Purified recombinant TFAM^{WT} (24 kDa), TFAM^{P178L} (24 kDa) and TFAM$^{\Delta 25C}$ (21 kDa) were separated by SDS-PAGE. (B) Thermofluor analysis of TFAM^{WT} and mutant variants. (C) Structural model of TFAM^{P178L}. Alignment of the TFAM^{P178L} model (hot pink) with TFAM (wheat) in a transcription initiation complex (PDB ID: 6ERP) with the least squares method on Cα atoms of α7. The L178 mutation is highlighted in green and the tether helix of POLRMT is shown in grey. DNA is shown as orange sticks. Steric clashes are highlighted with red flakes. (D) Amino acids colored according to the vibrational entropy change upon mutation. Blue represents a rigidification of the structure and red a gain in flexibility. PDB ID: 3TMM. (For interpretation of the references to colour in this figure legend, the reader is referred to the web version of this article.)

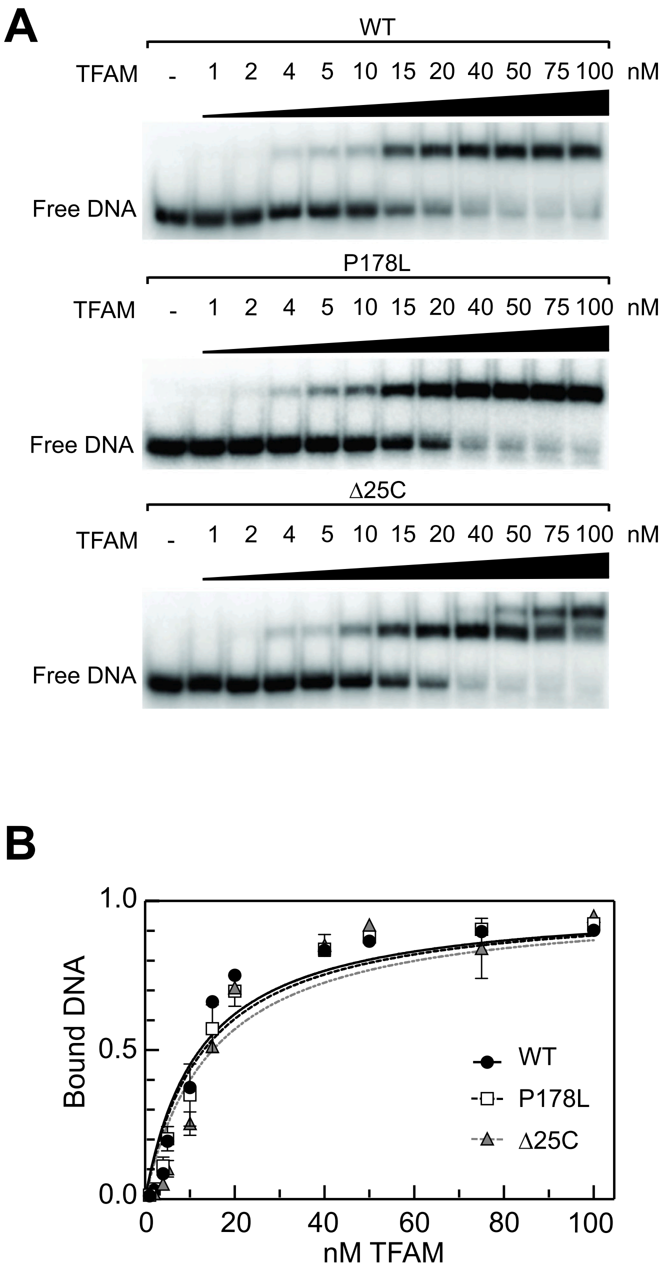

Fig. 3. P178L mutation does not affect the DNA binding capacity of TFAM. (A) TFAM binding to DNA was measured by EMSA using a 22 bp dsDNA template. Increasing WT, P178L, and Δ25C concentrations are indicated. (B) Quantification of bound DNA as a function of TFAM concentration (mean ± s.e.m., $N = 3$).

3.6. *P178L severely impairs transcription initiation*

To determine the ability of TFAM^{P178L} and TFAM$^{\Delta 25C}$ to support mtDNA transcription initiation, we employed a 772 bp linear mtDNA fragment containing HSP and LSP in a reconstituted *in vitro* transcription assay with POLRMT, TFB2M, and increasing amounts of TFAM (Fig. 5A). As expected (Farge, Mehmedovic et al. 2014), TFAM^{WT} strongly stimulated transcription initiation from both LSP and HSP, reaching a maximum activity at a ratio of ~20 bp/TFAM. At a higher ratio of 10 bp/TFAM, TFAM^{WT} then started to inhibit transcription (Fig. 5B). As demonstrated previously [33], TFAM$^{\Delta 25C}$ was not able to support transcription initiation (Fig. 5C). This is as the C-terminal tail of TFAM is essential since it directly interacts with POLRMT to recruit it to the promoter [9,33]. Interestingly, although increasing amounts of TFAM^{P178L} followed the same concentration-dependent stimulation/inhibition pattern for transcription initiation as observed with TFAM^{WT}, the TFAM^{P178L} displayed a much weaker stimulation of transcription than TFAM^{WT}. Quantification of the run-off products revealed a ~2.5-fold decreased transcription activity for the TFAM^{P178L} variant in comparison to TFAM^{WT} at both LSP and HSP (Fig. 5D and E). We thus conclude that P178L mutation impairs transcription initiation at both mitochondrial promoters.

4. Discussion

We have investigated the molecular basis of the pathogenic P178L mutation in TFAM, which is associated with a severe phenotype with onset at birth, mtDNA depletion, and early death [16]. In patient cells, we observed an ~80 % decrease in mtDNA levels, which corroborates the decrease in mtDNA levels previously reported by Stiles and colleagues [16]. Replication and transcription are linked in mitochondria. The initiation of replication at O_H depends on primers formed by transcription from LSP, which means that mutations that affect transcription initiation will also affect replication. Once DNA synthesis has been initiated at O_H, only a small fraction of all replication events continues to full-length mtDNA. Instead, about 95 % of all replication events are prematurely terminated after about 650 nt in a region called termination-associated sequence (TAS), resulting in replication product called 7S DNA [26,34]. The precise role of the 7S DNA in mtDNA maintenance is not understood, but there is evidence suggesting that termination at TAS may control the relative levels of abortive *versus* full-length mtDNA replication [35–37]. In P178L patient cells, despite the severe mtDNA depletion observed, we noticed that 7S DNA was dramatically increased relative to mtDNA. Conversely, it has been shown previously that, after removal of ddC (a nucleotide analogue that inhibits mtDNA synthesis and leads to mtDNA depletion) from cell culture media, full-length mtDNA synthesis is favored compared to 7S DNA synthesis [37,38]. In our case, the formation of 7S DNA demonstrates that mtDNA replication can be initiated at O_H, and that impaired primer synthesis thus may not be the primary cause of the observed decrease in mtDNA levels. In agreement with this, patients with disease-causing mutations in POLRMT display reduced levels of transcription initiation but maintain normal levels of mtDNA [39]. Suppose TFAM packaging of mtDNA plays an active role in regulating the switch between 7S DNA formation and full-length replication. In that case, the mildly defective ability of TFAM^{P178L} to package mtDNA could potentially impair the precise balance between these two events thus explaining the mtDNA depletion. Like Stiles et al., we observed lower TFAM protein levels in patient fibroblasts (Fig. 1D) [16]. Several studies have shown that the amount of TFAM directly regulates mtDNA copy number and that reciprocally mtDNA levels affect TFAM levels. For example, in mice with heterozygous TFAM knockout, Larsson et al. observed reduced TFAM levels associated with a ~50% decrease in mtDNA levels [40]. Conversely, moderate overexpression of TFAM results in increased mtDNA levels [41–44]. This balance is essential since high TFAM-to-mtDNA level acts as a negative repressor of mtDNA expression [13,45] The exact mechanism underlying this regulatory effect remains partially unclear. However, it has been demonstrated that LONP1, a mitochondrial protease, degrades TFAM that is not bound to mtDNA [30]. In both a thermofluor stability assay and a LONP1-mediated proteolysis assay, we could not observe any effects of the P178L mutation on TFAM stability, suggesting that protein instability does not explain the low level of TFAM^{P178L} in the patient cells. However, even if LONP1 is not more active against TFAMP^{178L} than against TFAM^{WT}, it could be that LONP1 balances the TFAM^{P178L}-to-mtDNA ratio to keep it at a normal level. Nevertheless, even if TFAM^{P178L} is degraded by LONP1, this is likely a consequence of the observed mtDNA depletion.

TFAM is also required for transcription initiation from the mitochondrial promoters, HSP and LSP. Interestingly, our *in vitro*

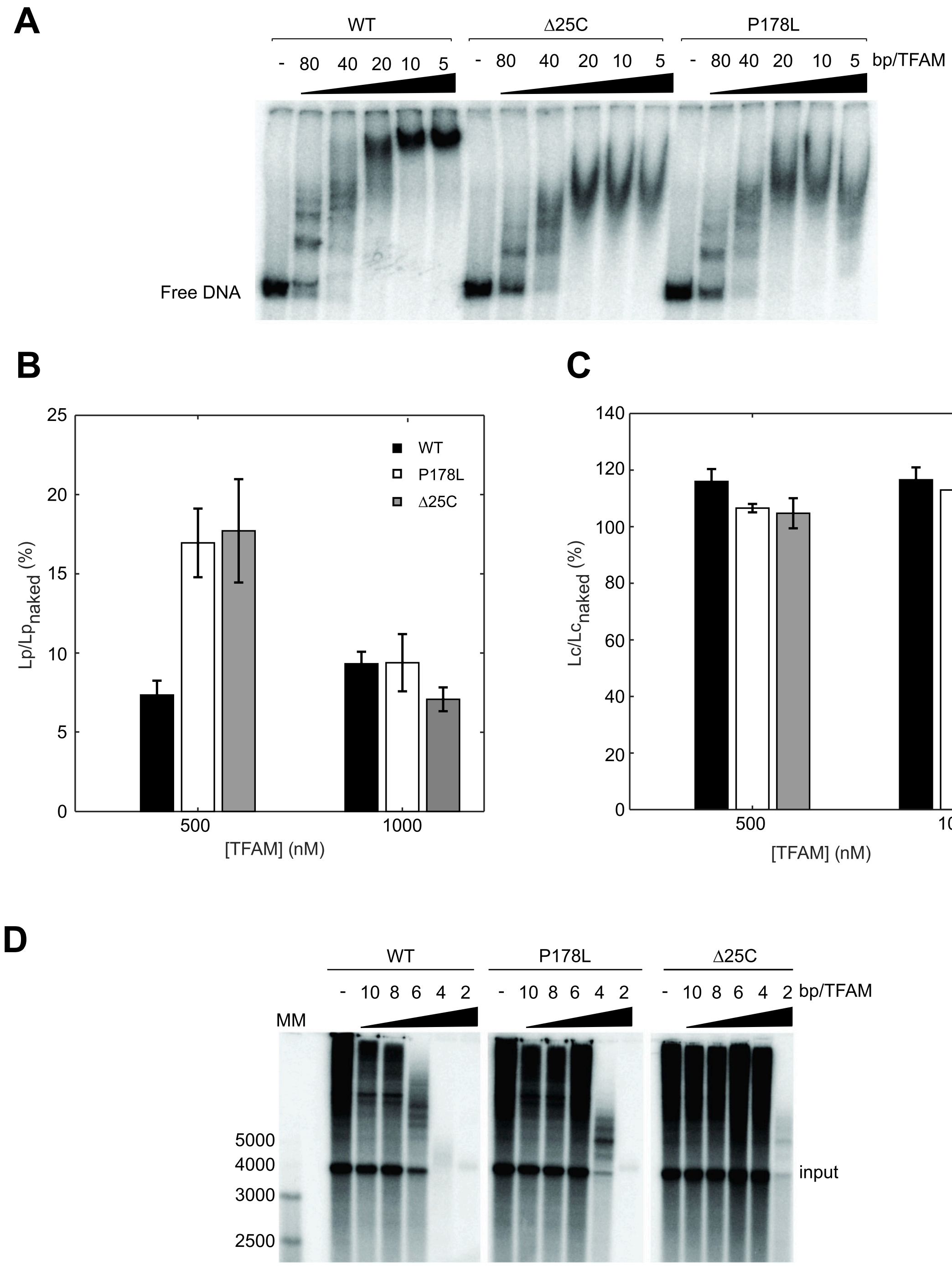

Fig. 4. TFAM^{P178L} has reduced DNA compaction activity and cannot block DNA replication progression as efficiently as TFAM^{WT}. (A) EMSAs were performed as described in 'Experimental procedures' using a 585 bp linear dsDNA template. Increasing TFAM concentrations are indicated as a TFAM:DNA ratio. (B and C) Persistence (Lp) and contour (Lc) length of DNA molecules in the presence of 500 or 1000 nM TFAM were obtained by fitting force extension curves with the extensible worm-like chain (eWLC) model as described in 'Experimental procedures' (mean ± s.e.m., $N = 20$) (D) Rolling-circle replication assays were performed in the presence of TWINKLE, POLγA, POLγB, mtSSB, and TFAM at the indicated concentrations (TFAM:DNA ratio).

transcription assay showed that the P178L mutation impairs transcription initiation at both promoters, which is supported by our structural modeling. The model suggests that the mutation affects promoter sequence recognition and causes a shift in the position of helix α6, thus affecting the interaction between TFAM and POLRMT *via* W122 in the tether helix (Fig. 2C). This shift will make the recruitment and tethering of POLRMT less efficient, making transcription initiation less effective.

In summary, we propose that transcription impairment is the most probable cause of the severe early-onset disease found in a consanguineous family with a homogenous P178L mutation in TFAM. The P178L mutation likely decreases TFAM's ability to locate recruit POLRMT for transcription initiation. This, in combination with the severe mtDNA depletion, suggests that essential genes involved in OXPHOS are not sufficiently expressed in the patients.

Supplementary data to this article can be found online at https://doi.org/10.1016/j.bbadis.2022.166467.

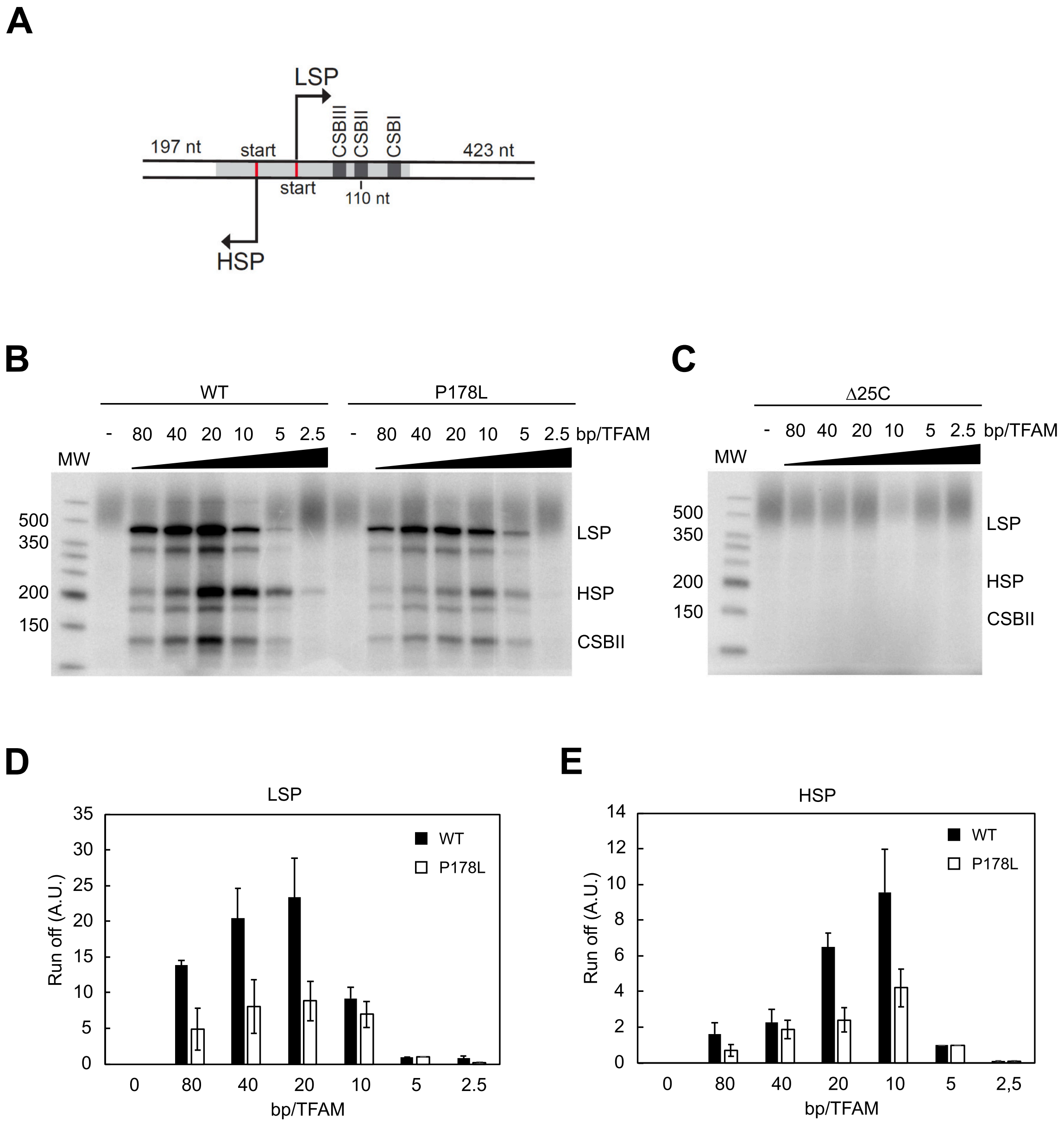

Fig. 5. TFAM^{P178L} cannot support transcription initiation as efficiently as TFAM^{WT}. (A) The template used in the transcription assay. (B) *In vitro* transcription reactions were performed using an mtDNA fragment containing the promoter sequences for LSP and HSP, in the presence of POLRMT (500 fmol), TFB2M (1 pmol), and the indicated increasing TFAM (WT, P178L) concentrations. (C) The same reaction as in (B) with TFAM$^{\Delta 25C}$. (D and E) Quantification of the run-off signal for LSP (D) and HSP (E) as a function of TFAM concentration (mean ± s.e.m., $N = 4$). MW: Molecular weight marker.

Funding

This work was supported by the Swedish Research Council (MF); Swedish Cancer Foundation (MF); European Research Council (MF); the IngaBritt and Arne Lundberg Foundation (MF); the Knut and Alice Wallenberg Foundation (MF); The Royal Swedish Academy of Sciences (MM); the Västra Götalands Regionen (MF) (ALFGBG-965954); and the Association Française Contre les Myopathies Téléthon (GF) (21411).

CRediT authorship contribution statement

MM[1] planned and conducted the cloning and purification of recombinant proteins, *in vitro* transcription, rolling circle replication, EMSA experiments and cell culture. MM[2] performed acoustic force spectrometry experiments and purified some of the TFAM protein. HS conducted the structural analysis. LI performed cell culture, Southern blot, Western blot and fluorescence microscopy. BP did the thermofluor stability assay. MSS and CPH performed the proteolysis assay and purified the LONP1. AM helped culture the cells. MM[1], SW, MF and GF analyzed the data and wrote the paper.

Declaration of competing interest

The authors declare that they have no known competing financial interests or personal relationships that could have appeared to influence the work reported in this paper.

Acknowledgements

We are grateful to Jay P. Uhler and Rebekah Hailes for the careful reading of the manuscript. We would also like to acknowledge the group of Dr. Jose E. Abdenur for providing us with patient and control cells.

References

[1] S. DiMauro, A brief history of mitochondrial pathologies, Int. J. Mol. Sci. 20 (2019).

[2] A.W. El-Hattab, W.J. Craigen, F. Scaglia, Mitochondrial DNA maintenance defects, Biochim. Biophys. Acta Mol. basis Dis. 1863 (6) (2017) 1539–1555.

[3] J.M. Fusté, S. Wanrooij, E. Jemt, C.E. Granycome, T.J. Cluett, Y. Shi, N. Atanassova, I.J. Holt, C.M. Gustafsson, M. Falkenberg, Mitochondrial RNA polymerase is needed for activation of the origin of light-strand DNA replication, Mol. Cell 37 (2010) 67–78.

[4] S. Wanrooij, J.M. Fuste, G. Farge, Y. Shi, C.M. Gustafsson, M. Falkenberg, Human mitochondrial RNA polymerase primes lagging-strand DNA synthesis in vitro, Proc. Natl. Acad. Sci. U. S. A. 105 (2008) 11122–11127.

[5] H.B. Ngo, J.T. Kaiser, D.C. Chan, The mitochondrial transcription and packaging factor Tfam imposes a U-turn on mitochondrial DNA, Nat. Struct. Mol. Biol. 18 (2011) 1290–1296.

[6] A. Rubio-Cosials, J.F. Sydow, N. Jiménez-Menéndez, P. Fernández-Millán, J. Montoya, H.T. Jacobs, M. Coll, P. Bernadó, M. Solà, Human mitochondrial transcription factor a induces a U-turn structure in the light strand promoter, Nat. Struct. Mol. Biol. 18 (2011) 1281–1289.

[7] M. Falkenberg, M. Gaspari, A. Rantanen, A. Trifunovic, N.G. Larsson, C. M. Gustafsson, Mitochondrial transcription factors B1 and B2 activate transcription of human mtDNA, Nat. Genet. 31 (2002) 289–294.

[8] D. Litonin, M. Sologub, Y. Shi, M. Savkina, M. Anikin, M. Falkenberg, C. M. Gustafsson, D. Temiakov, Human mitochondrial transcription revisited: only TFAM and TFB2M are required for transcription of the mitochondrial genes in vitro, J. Biol. Chem. 285 (2010) 18129–18133.

[9] H.S. Hillen, Y.I. Morozov, A. Sarfallah, D. Temiakov, P. Cramer, Structural basis of mitochondrial transcription initiation, Cell 171 (2017) 1072–1081.

[10] G. Farge, N. Laurens, O.D. Broekmans, S.M. van den Wildenberg, L.C. Dekker, M. Gaspari, C.M. Gustafsson, E.J. Peterman, M. Falkenberg, G.J. Wuite, Protein sliding and DNA denaturation are essential for DNA organization by human mitochondrial transcription factor a, Nat. Commun. 3 (2012) 1013.

[11] J.J. Traverso, V.S. Manoranjan, A.R. Bishop, K.O. Rasmussen, N.K. Voulgarakis, Allostery through protein-induced DNA bubbles, Sci. Rep. 5 (2015) 9037.

[12] J.N. Spelbrink, Functional organization of mammalian mitochondrial DNA in nucleoids: history, recent developments, and future challenges, IUBMB Life 62 (2010) 19–32.

[13] G. Farge, M. Mehmedovic, M. Baclayon, S.M.J.L. van den Wildenberg, W.H. Roos, C.M. Gustafsson, G.J.L. Wuite, M. Falkenberg, In vitro-reconstituted nucleoids can block mitochondrial DNA replication and transcription, Cell Rep. 8 (2014) 66–74.

[14] J. Guo, L. Zheng, W. Liu, X. Wang, Z. Wang, Z. Wang, A.J. French, D. Kang, L. Chen, S.N. Thibodeau, et al., Frequent truncating mutation of TFAM induces mitochondrial DNA depletion and apoptotic resistance in microsatellite-unstable colorectal cancer, Cancer Res. 71 (2011) 2978–2987.

[15] E.J. Tucker, R. Rius, S. Jaillard, K. Bell, P.J. Lamont, A. Travessa, J. Dupont, L. Sampaio, J. Dulon, S. Vuillaumier-Barrot, et al., Genomic sequencing highlights the diverse molecular causes of perrault syndrome: a peroxisomal disorder (PEX6), metabolic disorders (CLPP, GGPS1), and mtDNA maintenance/translation disorders (LARS2, TFAM), Hum. Genet. 139 (2020) 1325–1343.

[16] A.R. Stiles, M.T. Simon, A. Stover, S. Eftekharian, N. Khanlou, H.L. Wang, S. Magaki, H. Lee, K. Partynski, N. Dorrani, et al., Mutations in TFAM, encoding mitochondrial transcription factor a, cause neonatal liver failure associated with mtDNA depletion, Mol. Genet. Metab. 119 (2016) 91–99.

[17] J.A. Korhonen, M. Gaspari, M. Falkenberg, TWINKLE has 5' -> 3' DNA helicase activity and is specifically stimulated by mitochondrial single-stranded DNA-binding protein, J. Biol. Chem. 278 (2003) 48627–48632.

[18] J.A. Korhonen, X.H. Pham, M. Pellegrini, M. Falkenberg, Reconstitution of a minimal mtDNA replisome in vitro, EMBO J. 23 (2004) 2423–2429.

[19] G. Valentín Gesé, S. Shahzad, C. Pardo-Hernández, A. Wramstedt, M. Falkenberg, M. Hällberg, A Dual Allosteric Pathway Drives Human Mitochondrial Lon, bioRxiv, 2021, 2021.06.09.447696.

[20] J. Jumper, R. Evans, A. Pritzel, et al., Highly accurate protein structure prediction with AlphaFold, Nature 596 (2021) 583–589.

[21] C.H.M. Rodrigues, D.E.V. Pires, D.B. Ascher, DynaMut: predicting the impact of mutations on protein conformation, flexibility and stability, Nucleic Acids Res. 46 (2018) W350–W355.

[22] D. Kamsma, R. Creyghton, G. Sitters, G.J. Wuite, E.J. Peterman, Tuning the music: acoustic force spectroscopy (AFS) 2.0, Methods 105 (2016) 26–33.

[23] G. Sitters, D. Kamsma, G. Thalhammer, M. Ritsch-Marte, E.J. Peterman, G.J. Wuite, Acoustic force spectroscopy, Nat. Methods 12 (2015) 47–50.

[24] D. Kamsma, G.J.L. Wuite, Single-molecule measurements using acoustic force spectroscopy (AFS), Methods Mol. Biol. 1665 (2018) 341–351.

[25] T. Odijk, Stiff chains and filaments under tension, Macromolecules 28 (1995) 7016–7018.

[26] D. Bogenhagen, D.A. Clayton, Mechanism of mitochondrial DNA replication in mouse L-cells: kinetics of synthesis and turnover of the initiation sequence, J. Mol. Biol. 119 (1978) 49–68.

[27] J.N. Doda, C.T. Wright, D.A. Clayton, Elongation of displacement-loop strands in human and mouse mitochondrial DNA is arrested near specific template sequences, Proc. Natl. Acad. Sci. U. S. A. 78 (1981) 6116–6120.

[28] K. Ohgaki, T. Kanki, A. Fukuoh, H. Kurisaki, Y. Aoki, M. Ikeuchi, S.H. Kim, N. Hamasaki, D. Kang, The C-terminal tail of mitochondrial transcription factor a markedly strengthens its general binding to DNA, J. Biochem. 141 (2007) 201–211.

[29] T. Kanki, K. Ohgaki, M. Gaspari, C.M. Gustafsson, A. Fukuoh, N. Sasaki, N. Hamasaki, D.C. Kang, Architectural role of mitochondrial transcription factor a in maintenance of human mitochondrial DNA, Mol. Cell. Biol. 24 (2004) 9823–9834.

[30] B. Lu, J. Lee, X. Nie, M. Li, Y.I. Morozov, S. Venkatesh, D.F. Bogenhagen, D. Temiakov, C.K. Suzuki, Phosphorylation of human TFAM in mitochondria impairs DNA binding and promotes degradation by the AAA+ lon protease, Mol. Cell 10 (49) (2013) 121–132.

[31] W.S. Choi, M. Garcia-Diaz, A minimal motif for sequence recognition by mitochondrial transcription factor a (TFAM), Nucleic Acids Res. 50 (2022) 322–332.

[32] G.A. King, M. Hashemi Shabestari, K.H. Taris, A.K. Pandey, S. Venkatesh, J. Thilagavathi, K. Singh, R. Krishna Koppisetti, D. Temiakov, W.H. Roos, et al., Acetylation and phosphorylation of human TFAM regulate TFAM-DNA interactions via contrasting mechanisms, Nucleic Acids Res. 46 (2018) 3633–3642.

[33] D.J. Dairaghi, G.S. Shadel, D.A. Clayton, Addition of a 29-residue carboxyl-terminal tail converts a simple hmg box-containing protein transcriptional activator, J. Mol. Biol. 249 (1995) 11–28.

[34] T.J. Nicholls, M. Minczuk, In D-loop: 40 years of mitochondrial 7S DNA, Exp. Gerontol. 56 (2014) 175–181.

[35] G.G. Brown, G. Gadaleta, G. Pepe, C. Saccone, E. Sbisa, Structural conservation and variation in the D-loop-containing region of vertebrate mitochondrial DNA, J. Mol. Biol. 192 (1986) 503–511.

[36] M. Falkenberg, C.M. Gustafsson, Mammalian mitochondrial DNA replication and mechanisms of deletion formation, Crit. Rev. Biochem. Mol. Biol. 55 (2020) 509–524.

[37] E. Jemt, O. Persson, Y. Shi, M. Mehmedovic, J.P. Uhler, M. Davila Lopez, C. Freyer, C.M. Gustafsson, T. Samuelsson, M. Falkenberg, Regulation of DNA replication at the end of the mitochondrial D-loop involves the helicase TWINKLE and a conserved sequence element, Nucleic Acids Res. 43 (2015) 9262–9275.

[38] T.A. Brown, D.A. Clayton, Release of replication termination controls mitochondrial DNA copy number after depletion with 2',3'-dideoxycytidine, Nucleic Acids Res. 30 (2002) 2004–2010.

[39] M. Oláhová, B. Peter, Z. Szilagyi, H. Diaz-Maldonado, M. Singh, et al., POLRMT mutations impair mitochondrial transcription causing neurological disease, Nat. Commun. 12 (2021) 1135.

[40] N.G. Larsson, J. Wang, H. Wilhelmsson, A. Oldfors, P. Rustin, M. Lewandoski, G. S. Barsh, D.A. Clayton, Mitochondrial transcription factor a is necessary for mtDNA maintenance and embryogenesis in mice, Nat. Genet. 18 (1998) 231–236.

[41] M.I. Ekstrand, M. Falkenberg, A. Rantanen, C.B. Park, M. Gaspari, K. Hultenby, P. Rustin, C.M. Gustafsson, N.G. Larsson, Mitochondrial transcription factor a regulates mtDNA copy number in mammals, Hum. Mol. Genet. 13 (2004) 935–944.

[42] R. Filograna, C. Koolmeister, M. Upadhyay, A. Pajak, P. Clemente, R. Wibom, M. L. Simard, A. Wredenberg, C. Freyer, J.B. Stewart, N.G. Larsson, Modulation of mtDNA copy number ameliorates the pathological consequences of a heteroplasmic mtDNA mutation in the mouse, Sci. Adv. 4 (2019) 9824.

[43] Y. Hayashi, M. Yoshida, M. Yamato, T. Ide, Z. Wu, M. Ochi-Shindou, T. Kanki, D. Kang, K. Sunagawa, H. Tsutsui, H. Nakanishi, Reverse of age-dependent memory impairment and mitochondrial DNA damage in microglia by an overexpression of human mitochondrial transcription factor a in mice, J. Neurosci. 28 (2008) 8624–8634.

[44] M. Hokari, S. Kuroda, S. Kinugawa, T. Ide, H. Tsutsui, Y. Iwasaki, Overexpression of mitochondrial transcription factor a (TFAM) ameliorates delayed neuronal death due to transient forebrain ischemia in mice, Neuropathology 30 (2010) 401–407.

[45] N.A. Bonekamp, M. Jiang, E. Motori, R. Garcia Villegas, C. Koolmeister, I. Atanassov, A. Mesaros, C.B. Park, N.G. Larsson, High levels of TFAM repress mammalian mitochondrial DNA transcription in vivo, Life Sci. Alliance 4 (2021), e202101034.

[46] C.T. Campbell, J.E. Kolesar, B.A. Kaufman, Mitochondrial transcription factor a regulates mitochondrial transcription initiation, DNA packaging, and genome copy number, Biochim. Biophys. Acta 1819 (2012) 921–929.

[47] Matulis, Kranz, Salemme, Todd, Thermodynamic stability of carbonic anhydrase: measurements of binding affinity and stoichiometry using ThermoFluor, Biochemistry 44 (13) (2005) 5258–5266.

[48] Matsushima, Goto, Kaguni, Mitochondrial Lon protease regulates mitochondrial DNA copy number and transcription by selective degradation of mitochondrial transcription factor A (TFAM). Proc. Natl. Acad. Sci. U. S. A. 107 (43) (2010) 18410–18415.

Chapter 2.3: mtSSB R107Q disease causing mutant

2.3.1: The mtSSB mutation R107Q alters ssDNA compaction and binding dynamics (Paper III)

Single Stranded Binding proteins (SSB proteins) family binds with high specificity to ssDNA and protect the nucleic acid from oxidative damage but also from nucleolytic enzymes. Despites their role of protection of ssDNA strands, they also participate actively as main actors of the DNA maintenance. Many studies aimed at the understanding of SSBs roles and mechanism in DNA metabolism (Xu *et al.*, 2023, Jiang *et al.*, 2021; Ciesielski *et al.*, 2021; Plaza *et al.*, 2023, Morin *et al.*, 2017; Hensen *et al.*, 2019). Nevertheless, there are only few studies that were directed toward the understanding of mammalian mtSSB molecular mechanism, and particularly human mtSSB (HsmtSSB).

Since 2018, several clinical reports have described mutations of mtSSB that are associated with human diseases (Kullar *et al.*, 2018; Jurkute *et al.,* 2019; Piro-Mégy *et al.*, 2020; Del Dotto *et al.*, 2020). However, these reports lack mechanistic explanations. My project focuses on the understanding of the molecular basis for the pathogenicity of one of these mutations (R107Q). To this end, I have studied real-time interactions of mtSSB with DNA using single molecule approaches involving Total Internal Reflection Fluorescence microscopy (TIRFm) and Acoustic Force Spectroscopy (AFS). Using mass photometry, we showed that the mutation does not impair SSB variant ability to form tetramers, as we observed only one population corresponding to tetramers. Using AFS and TIRFm, we measured compaction efficiency, force and salt dependent dissociation rate, as well as binding affinity in a competition binding assay between wild-type and mutant SSB with two colours experiments. In addition, we discussed the effect of the R107Q mutation on the mtSSB structure based upon our structure modelization. All together the results suggest that the mutation could affect the binding stability, especially the wrapping state, and the compaction rate of the protein. These changes could affect the proper functioning of the protein and its ability to ensure mtDNA replication. Further investigations should aim at the interaction of this variant with protein partner such as Polγ as it was shown that mtSSB increased the polymerase processivity and that it was involved in mtDNA replication initiation. Finally, it should be noted that information about the diffusion properties of mtSSB are still missing and TIRFm is an appropriate method to address this issue.

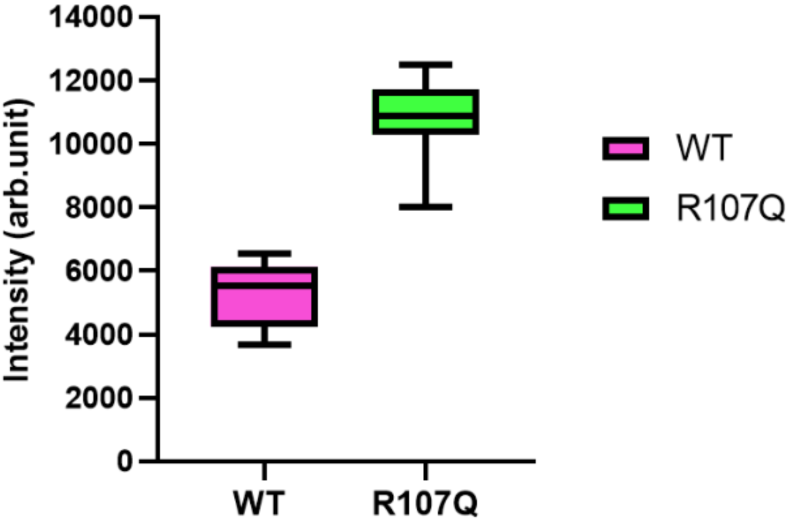

Figure 30: Absolute intensities of mtSSB Alexa 647 WT and R107Q covering separately DNA molecules. Intensity quantification was done in two different experiments, by measuring the mean of intensity of each DNA molecules covered either by WT 647 or R107Q 647 (N=21 and N=13 for WT and R107Q respectively).

It should be noted that currently there are no commercial dyes to effectively visualise ssDNA in fluorescence microscopy, and one strategy to overcome this, is to use fluorescent SSB proteins. In this paper we have used an innovative method to visualise ssDNA without the intermediate of fluorescent labelled DNA binding protein. We have used SYBR Green II dye which is normally used in quantitative PCR to detect RNA levels but can also show ssDNA sensitivity. By the use of SYBR Green II dye, we succeeded to observe ssDNA in TIRFm that is, however, dependent on salt concentration, without preventing mtSSB binding to ssDNA molecules. This could improve current protocols of fluorescence microscopy aiming at understanding ssDNA-protein interactions at the single molecule level and needs to be further investigated in the future.

2.3.2: mtSSB supplementary results and outlook

In this section, I will present and discuss preliminary and/or complementary results that were not included in the paper III.

Quantification of SSBs in competition assay support a higher DNA coverage by WT

In order to confirm the difference in ssDNA coverage by WT and R107Q mtSSB (cf. figure 2 in the publication from chapter 2.3.1), we compared proteins from a different batch and labelled with a different fluorescent dye namely Alexa 647. We used the images of mtSSB WT labelled with Alexa 647 obtained in our competition assay at 150 nM of proteins concentration without salt (competition assay ratio 1:1, WT to R107Q, cf. publication figure 5A in the publication from chapter 2.3.1), and images of mtSSB R107Q labelled with Alexa 647 obtained with preincubation of ssDNA molecules with 150 nM of mtSSB R107Q concentration without salt. Intensity quantification was done by measuring the mean of intensity of each DNA molecule exclusively covered either by WT or R107Q (N=21 and N=13 for WT and R107Q respectively) and was corrected for background noise. Results are presented in **figure 30** and show an approximately two-fold increase in intensity for DNA molecules covered by mtSSB R107Q. This supports the early finding that ssDNA coverage by R107Q is higher than for WT mtSSB that R107Q, suggesting that R107Q displays an apparent lower footprint (cf. publication figure 2).

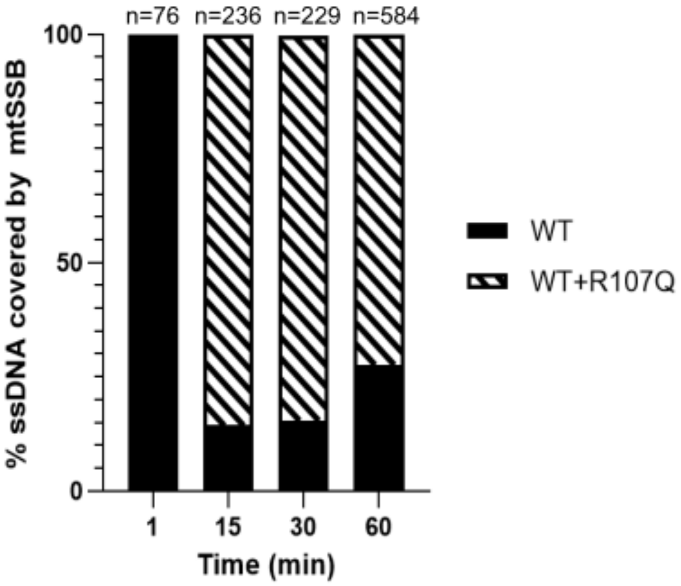

Figure 31: Number of ssDNA molecules covered by mtSSB depending on time incubation. Nucleoprotein complexes were counted depending on their coverage of SSB (1:1 ratio R107Q:WT) at several incubation times (1, 15, 30 and 60 min).

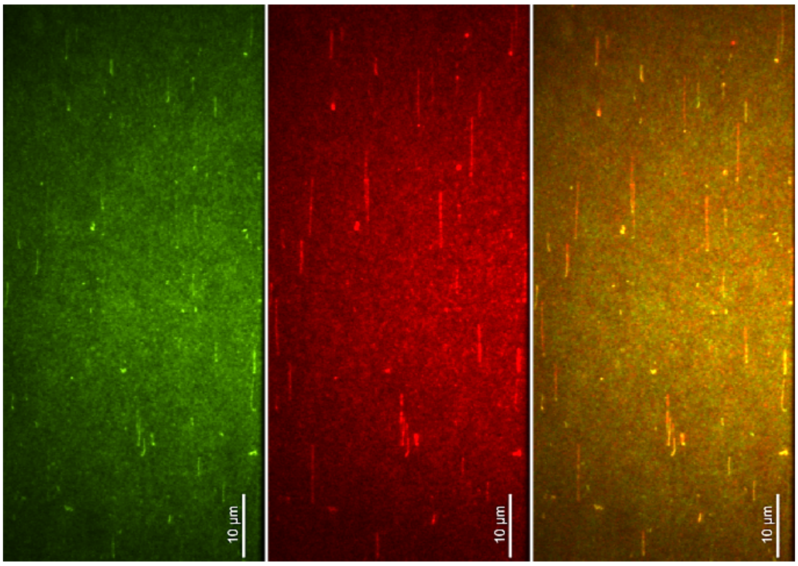

Figure 32: Binding of mtSSB WT and R107Q at 100 nM, 25 mM NaOAc, on pre-stretched DNA molecules. DNA molecules were stretched prior to add mtSSB. WT and R107Q were mixed at 100 nM each in work buffer and flushed in the microfluidic chamber, then rinsed with 25 mM NaOAc. Scale bar : 10 µm.

Real-time binding assay

In the competition assay, we noticed that the incubation time could influence the binding of mtSSB R107Q. The percentage of ssDNA coverage as a function of incubation time is presented in **figure 31** (supplementary figure S9 in the publication), it shows that for very short incubation times (~1 min) no mtSSB R107Q is bound to the ssDNA molecules and only mtSSB WT is found on the ssDNA. However, for longer incubation times (> 15 min) the percentage of ssDNA coverage by WT and R107Q appears to reach a steady state.

The limited binding of mtSSB R107Q at short times could indicate that it has a lower binding affinity (especially a lower on-rate) than mtSSB WT. Thus, we decided to perform a real-time binding assay, in which DNA molecules were stretched in the microfluidic chamber prior to adding the mtSSB. After ssDNA stretching, mtSSB WT and R107Q were then mixed at a concentration of 100 nM, with 25 mM NaOAc and added to the chamber. Unfortunately, our time resolution was not sufficient to distinguish binding rate differences. The concentration used was also a bit too high and thus enhanced the blinding effect. In future experiments the mtSSB concentration should be decreased and an optimum settings in terms of exposure time and laser power should be found in order to visualise initial fast binding events.

However, after the removal of the free mtSSB proteins from solution (by washing the flow chamber with buffer A from the publication), we notice that the distribution of mtSSB WT and R107Q were significantly different. Remarkably, on ssDNA molecules where both WT and R107Q were found, mtSSB WT was seen to coat a long (if it is not the total length) fraction of the ssDNA molecules. MtSSB R107Q did not coat ssDNA molecules to the same extent as the WT mtSSB, but appeared often located at the free end of the DNA (not biotinylated). This effect was enhanced by the NaOAc concentration (**Figure 32 and 33**). Surprisingly, when mtSSB R107Q is flushed alone on pre-stretched ssDNA molecules at 25 mM salt, the DNA coverage is very different from figure 32 (**Figure 34**) with more coated DNA.

These observations support the idea that mtSSB WT possesses a higher binding affinity than mtSSB R107Q, explaining the differences in ssDNA coverage display in **figure 31** (supplementary figure S3 in the publication). However, bio-layer interferometry assay (cf. publication section 3.3) shows that the differential in binding affinity may come from a higher off-rate of the mutant as suggested in the results.

To investigate in more detail mtSSB location on ssDNA molecules, we have preincubated ssDNA molecules with mtSSB WT or R107Q without salt, and we applied a strong flow force

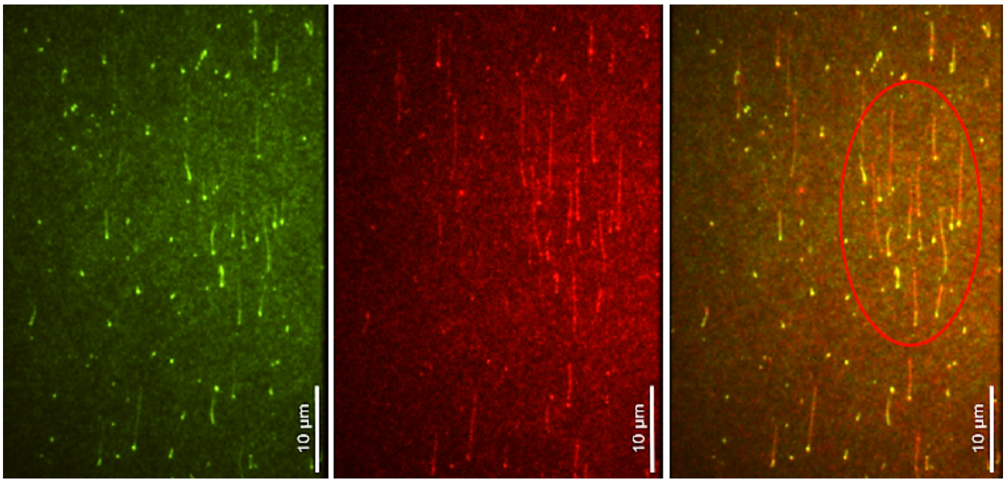

Figure 33: Binding of mtSSB WT and R107Q at 100 nM, 100 mM NaOAc, on pre-stretched DNA molecules. DNA molecules were stretched prior to add mtSSB. WT and R107Q were mixed at 100 nM each in work buffer and flushed in the microfluidic chamber, then rinsed with 100 mM NaOAc. Red circle shows multiple ssDNA molecules where mtSSB R107Q were found at the extremities. Scale bar : 10 µm.

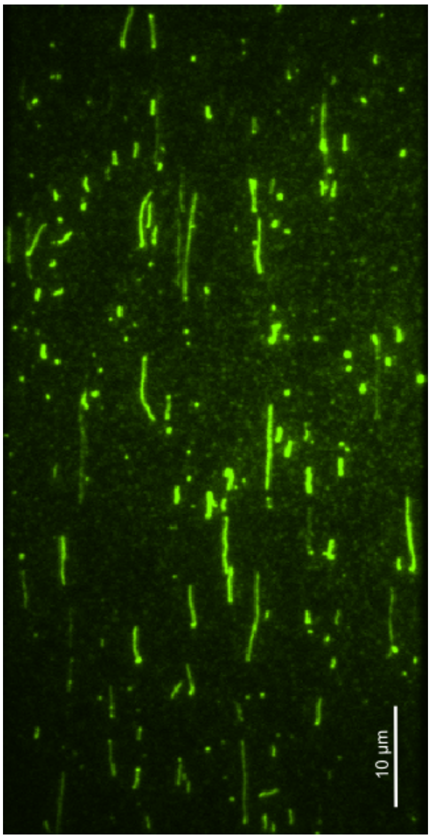

Figure 34 : Binding of mtSSB R107Q at 100 nM, 25 mM NaOAc, on pre-stretched DNA molecules. DNA molecules were stretched prior to add mtSSB. R107Q was flushed in at 100 nM in work buffer in the microfluidic chamber, then rinsed with 25 mM NaOAc. Scale bar : 10 µm

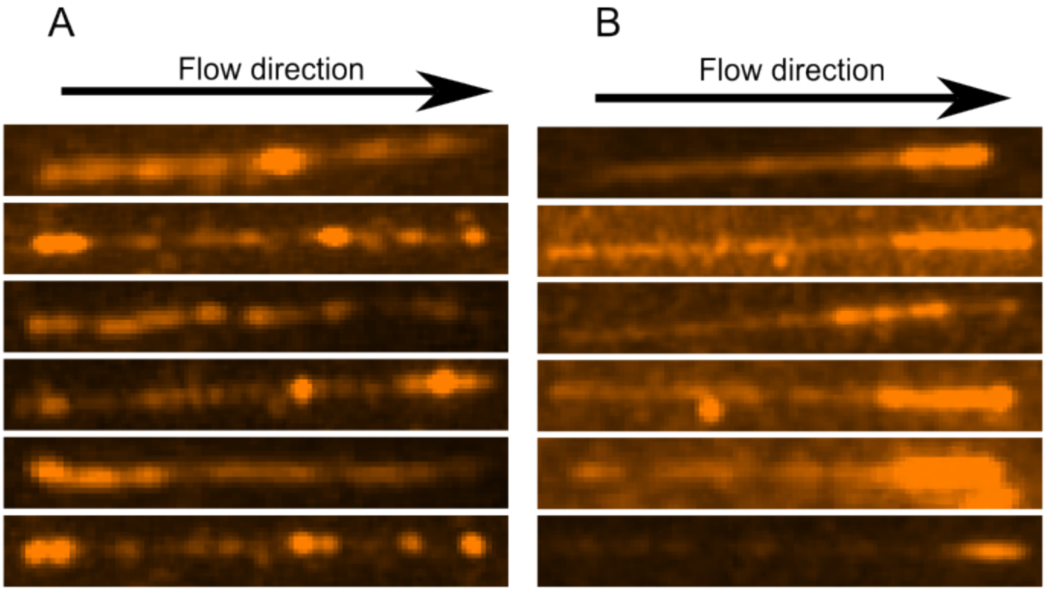

Figure 35: DNA molecules covered by mtSSB WT and R107Q stretched with high flow rate without salt. (A) DNA molecules were incubated with 150 nM mtSSB WT labelled with Alexa 555. **(B)** DNA molecules were incubated with 150 nM mtSSB R107Q labelled with Alexa 555. DNA were stretched with work buffer.

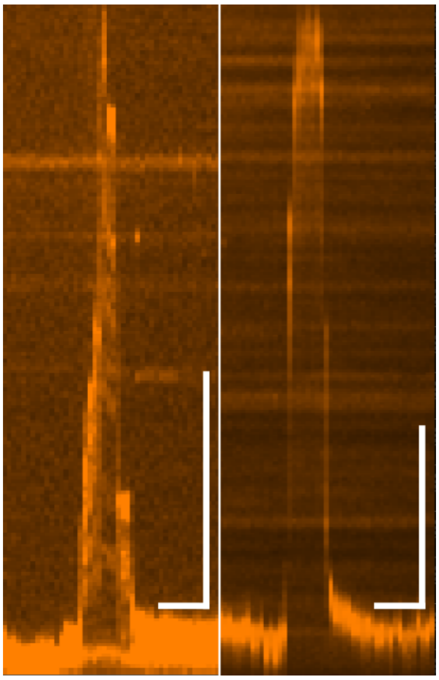

Figure 36: Kymographs of mtSSB WT and R107Q from DNA molecules pre-incubated with mtSSB proteins and stretched at maximum flow rate. Left panel: SSB WT. Right panel: SSB R107Q. Horizontal and vertical scale bars are 2 s and 5 µm respectively.

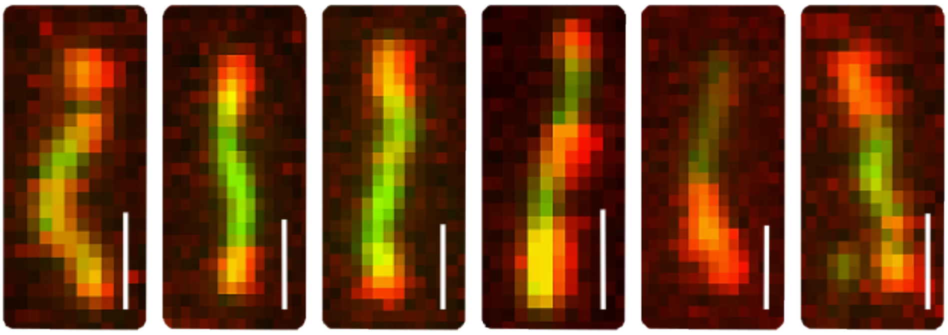

Figure 37: mtSSB WT and R107Q covering DNA molecules at ratio 1:0.1 (R107Q:WT) in competition assay. WT is in red and R107Q in green. It is noticeable that mtSSB WT bound DNA molecules in patches especially at their extremities in condition where it is 10 fold lower concentrated than R107Q. Scale bar : 1 µm.

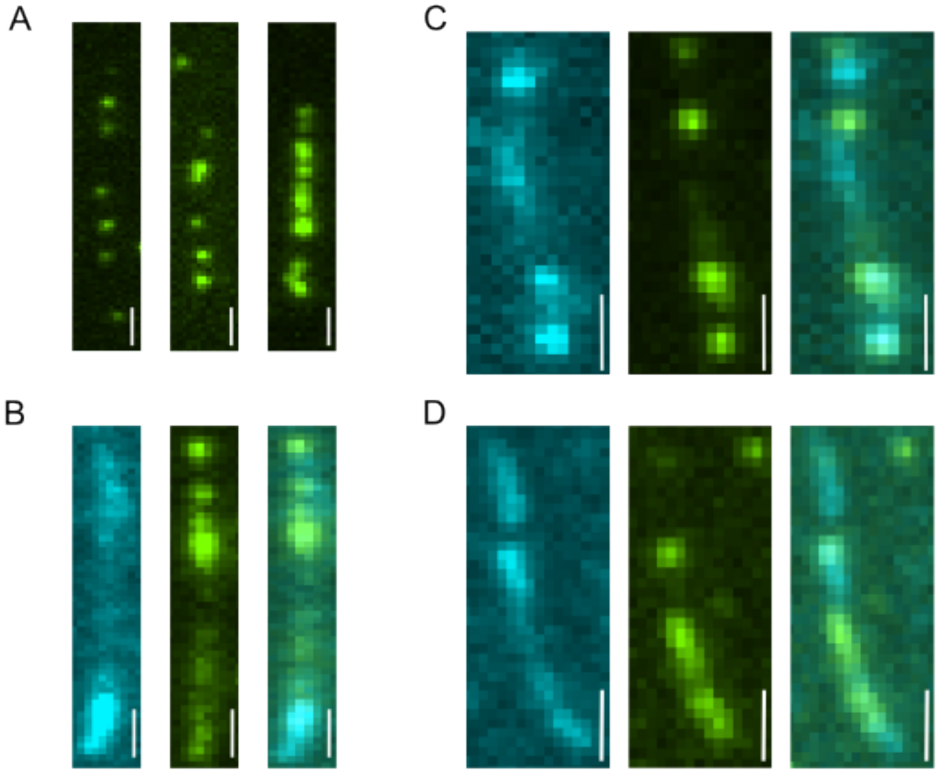

Figure 38: MtSSB WT bound to pre-stretched ssDNA. (A) MtSSB WT (1 nM, in green) bound to non-labelled and pre-stretched ssDNA molecules. (B) Pre-stretched ssDNA molecules stained with SYBR Green II (in blue) during 20 min and then rinsed with buffer A (from publication chapter 2.3.2). MtSSB WT 555 at 100 nM, in 25 mM NaOAc was added in a second step. (C) Pre-stretched DNA molecules bound with mtSSB WT 555 with 25 mM NaOAc. SYBR Green II dye was added in a second step. (D) Pre-incubated ssDNA with SYBR green II were stretched and incubated with 100 nM mtSSB WT 555 without salt. Scales bars = 1 µm.

on nucleoprotein complexes to stretch them near their full lengths. Interestingly, mtSSB WT shows a quite homogeneous coating along ssDNA molecules (**Figure 35A**), with a few small apparent patches. On the contrary, mtSSB R107Q shows a non-homogeneous coating, with a high amount of proteins located on the free ends of ssDNA molecules (**Figure 35B**). Kymographs of extension of a ssDNA molecule coated by mtSSB WT or R107Q **in figure 35A** and **35B** are presented in **figure 36**. Even though this phenomenon has also been observed with mtSSB WT, it is much less common than for the R107Q coated ssDNA.

These observations in **figure 35A and 35B** could be explained by a force dependent dissociation during the ssDNA stretching and the resulting dissociation of mtSSB R107Q except for at the free end of the ssDNA where the force tension is lowest. Indeed a more important force dependent dissociation was observed for the mtSSB R107Q in the AFS experiments (Figure 3 of the publication in chapter 2.3.1). Another reason may be the displacement of mtSSB molecules towards the free edges due to the force flow.

Finally, we note that mtSSB binding to the extremities of preincubated ssDNA molecules (without flow) has also been seen in competition assay at 1:0.1 ratio (R107Q:WT). In **figure 37**, we can see that mtSSB WT (in red, that is 10 fold lower concentrated than mtSSB R107Q in green) is often found in patches and at ssDNA extremities.

Diffusion of mtSSB

Several SSB proteins such as EcoSSB and RPA have been shown to diffuse on ssDNA (section 1.7.3). We set out to investigate if mtSSB can also diffuse on ssDNA and if so, what are the mechanism, for example reptation or intersegment transfer (section 1.7.3)? As no commercial dyes are available for staining ssDNA in microscopy experiments, we used SYBR Green II RNA stain gel dye from Invitrogen to see ssDNA molecules without SSB intermediate (Figure S1 from the publication and **Figure 38**). In our experiment, SYBR Green II RNA stain gel dye was diluted by 100 000x from the original solution (concentration not indicated by manufacturer) and incubated during 20 min with pre-stretched DNA molecules in the microfluidic chamber. Then, mtSSB WT was flushed in at 1 or 5 nM of concentration. Unfortunately, we did not succeed to see mtSSB moving on the ssDNA. Moreover, rinsing with NaOAc at 25 or 100 mM removed the SYBR Green II from the ssDNA molecules, thus limiting its use.

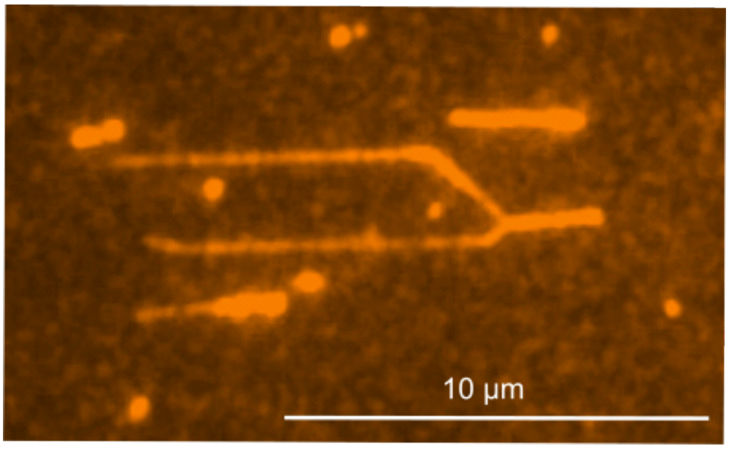

Figure 39: Bridging of ssDNA molecules coated by mtSSB R107Q. ssDNA molecules were incubated with 150 nM mtSSB R107Q without salt. Scale bar : 10 µm.

Outlook

For perspectives at short-term, real-time binding of mtSSB WT and R107Q could be optimised with the introduction of SYBR Green II dye to see ssDNA molecule, which will allow the use of lower protein concentrations and limit the background noise. Also, doing this would allow us to study mtSSB tetramers interaction with both WT and R107Q. Our diffusion experiment conditions could be controlled and validated by using a recombinant EcoSSB protein whose dynamic was already characterised. Moreover, we could also get more insight of mtSSB R107Q affinity by measuring DNA coverage as a function of protein concentrations in comparison with mtSSB WT. Finally, we have seen, for both WT and R107Q mtSSB, some bridging events in which two ssDNA molecules appear to be bridged (**Figure 39**). It would be interesting to further investigate the possible mtSSB bridging with, for example, a DNA curtain set-up. This would allow us to get insight into the potential activity of mtSSB in DNA recombination, a mechanism that is, for now, not determined within mitochondria.
In a long-term, cellular model expressing mtSSB R107Q, as was proposed for TFAM, could be done in heterozygous and homozygous cells to investigate in vivo replication status. Moreover, it would be interesting to study mtSSB R107Q in a strand unwinding mimic with a tether DNA molecule like it was done in optical tweezers by Morin *et al.* in 2017 and Plaza *et al.* in 2023. It would allow to study, for example, the mechanical unwinding of DNA by the Phi29 polymerase with mtSSB R107Q bound. In comparison with mtSSB WT, it would get insight into its impaired function in replication initiation.

The mutation R107Q alters mtSSB ssDNA compaction ability and binding dynamics

Martial Martucci[1], Amandine Moretton[1], Aleix Tarrés Solé[2,], Virginie Ropars[3] , Louise Lambert[1,4], Patrick Vernet[1], Maria Sola[2], Maria Falkenberg[4], Geraldine Farge[1#*]and Siet van den Wildenberg[1,5#]

[1] Université Clermont Auvergne, CNRS, Laboratoire de Physique de Clermont, F-63000 Clermont-Ferrand, France
[2]
[3]
[4] Department of Medical Biochemistry and Cell Biology, University of Gothenburg, P.O. Box 440, SE-405 30 Gothenburg, Sweden
[5] Université Clermont Auvergne, CNRS, IRD, Université Jean Monnet Saint Etienne, LMV, F-63000 Clermont-Ferrand, France
[#] Equal contribution
[*] Correspondence geraldine.farge@uca.fr

Abstract: Mitochondrial single-stranded DNA-binding protein (mtSSB) is essential for mitochondrial DNA (mtDNA) replication. Recently, several mtSSB variants have been associated with autosomal dominant mitochondrial optic atrophy and retinal dystrophy. Here, we have studied the functional consequence of one of the most severe variants, R107Q. We first studied the oligomeric state of this variant and observed that the mtSSB^{R107Q} mutant is still able to form stable tetramers. On the other hand, we showed, using complementary single molecule approaches, that mtSSB^{R107Q} displays a lower intramolecular ssDNA compaction ability and a higher ssDNA dissociation rate than the WT protein. We also directly visualized mtSSB^{R107Q} and mtSSB^{WT} competing in real time for ssDNA and observed a marked advantage for the mtSSB^{WT}. Combined, these results show that the R107Q mutation significantly impaired the ssDNA binding and compacting ability of mtSSB, likely by weakening mtSSB ssDNA wrapping efficiency. These features are in line with our molecular modeling of mtSSB on ssDNA showing that the R107Q mutation results in an electronegative spot that interrupts an ssDNA-interacting-electropositive patch, thus reducing the potential mtSSB-ssDNA interaction sites.

Keywords: mtSSB, R107Q, DNA compaction, single‑stranded DNA, wrapping mode

1. Introduction

Single-stranded DNA (ssDNA) intermediates are generated during common DNA maintenance processes such as replication, transcription, repair and recombination. SsDNA binding proteins (SSBs) bind those ssDNA intermediates with high affinity, preventing the formation of secondary structures and protecting them against chemical and enzymatic degradation. The mitochondrial ssDNA-binding protein (mtSSB) is a key actor of mitochondrial DNA (mtDNA) replication. It covers and stabilizes the long stretches of ssDNA formed during mtDNA replication, but also interacts with the other components of the replication machinery, which includes the heterotrimeric DNA polymerase γ (POLγ) and the replicative DNA helicase TWINKLE [Farr *et al.*, 2004; Miralles Fuste *et al.,* 2014; William and Kaguni, 1995; Korhonen *et al.*, 2003]. Although it seems that there are no physical interactions between mtSSB and POLγ [Ciesielski *et al.,* 2021], mtSSB is able to stimulate POLγ processivity and the helicase activity of TWINKLE during replication elongation [Korhonen *et al.*, 2004]. Based on single molecule assays, a mechanism has been proposed to explain how mtSSB can enhance strand displacement DNA synthesis by POLγ, in which mtSSB increases the DNA junction destabilization energy and reduces the DNA fork reannealing pressure on POLγ [Plaza *et al.,* 2023]. Recently, it was shown that mtSSB plays an additional role in regulating mtDNA replication initiation, by promoting RNA primer formation at both origins of replication thus down-regulating transcription initiation from the light-strand promoter (LSP) [Jiang *et al.*, 2021].

While POLγ and TWINKLE are related to phage replicative factors, mtSSB shares conserved domains with *Escherichia coli* SSB (*Ec*SSB) [Curth *et al.*, 1994], however, mtSSB lacks the C-terminal disordered domain that is involved in protein-protein interaction in *Ec*SSB and other species [Raghunathan *et al.*, 1997; Antony *et al.*, 2012]. In mammals, mtSSB is a 148 amino acids protein of 16 kDa that possess a mitochondrial targeting sequence (MTS) and a N-terminal ssDNA binding domain referred to as OB-fold (oligonucleotide/oligosaccharide binding-fold) domain [Wu *et al.*, 2016]. Depending on the number of OB-fold domains, SSBs can be classified into two groups, simple SSBs which contain one OB-fold domain like mtSSB or *Ec*SSB, and higher order SSBs which contain multiple OB-fold domains like RPA1, RPA2 and RPA3 [Wu *et al*, 2016]. The crystal structure of human mtSSB showed that the overall folding of the mtSSB tetramer resembles that of *Ec*SSB, forming a stable tetramer of four identical 16 kDa subunits in solution, in which a dimer contacts a second, symmetrically related, dimer [Yang *et al.*, 1997; Piro-Mégy *et al.,* 2019; Raghunathan *et al.,* 1997]. MtSSB binds ssDNA with a high specificity and in a sequence independent manner [Yang *et al.,* 1997]. However, unlike *Ec*SSB which binds ssDNA in a negative cooperativity manner, mtSSB seems to not show negative intersubunit cooperativity [Qian and Johnson, 2017].

In *Ec*SSB, several stable or semi-stable binding modes have been described, (*Ec*SSB)35, (*Ec*SSB)56, (*Ec*SSB)65 and more recently (*Ec*SSB)17, where the numbers indicate the apparent site size or footprint (i.e., nucleotides bound per tetramer) [Naufer *et al.,* 2021]. In the (*Ec*SSB)35 binding mode, mainly observed at low salt concentrations, ssDNA only interacts with two subunits of the tetramer [Lohman *et al.,* 1985; Lohman *et al.,* 1988]. In the (*Ec*SSB)65 binding mode, found preferentially at high salt concentrations, X-ray crystallographic structural studies showed that the ssDNA is fully wrapped through the association of all four *Ec*SSB subunits [Raghunathan *et al.,* 1997]. In both binding modes it was shown that *Ec*SSB diffuse rapidly on ssDNA and can 'hop or jump' across long distances of ssDNA via intersegmental transfer [Roy *et al.,* 2009; Zhou *et al.*, 2011; Antony and Lohman, 2019; Lee *et al.*, 2014]. In contrast, the T7 SSB, T7 gp2.5 protein, is relatively immobile on ssDNA [Xu *et al.,* 2023]. Similar to *Ec*SSB, two binding modes have been proposed for mtSSB: a high binding mode (SSB)60 and a low binding mode (SSB)30, [Curth *et al.*, 1994, Morin *et al.*, 2017, Qian and Johnson, 2017]. The binding mode depends on protein, salt and magnesium concentrations. The association and dissociation rates of mtSSB have been estimated by equilibrium titrations and stopped-flow kinetic measurements and it was found that the mtSSB tetramer binds ssDNA with a rate of $k{\sim}2.10^{9}$ ($M^{-1}s^{-1}$) [Qian and Johnson 2017]. The authors proposed a model in which, in the low binding mode, one mtSSB tetramer can bind two ssDNA30 molecules, whereas in the high binding mode ssDNA60 is bound and wrapped around one mtSSB tetramer. Thus, as the salt concentration is increased, the mode of binding shifts from the low mode to the higher site size mode, resulting in progressive compaction of the ssDNA. SSB binding modes can also be modulated by interacting proteins. For instance, in bacteria, the DNA helicase PriA, PriC and RecQ were shown to interact with *Ec*SSB and promote the transition from one binding mode to the other [Bhattacharyya *et al.*, 2013; Wessel *et al.*, 2013; Mills *et al.*, 2017]. Similarly, when coupled to DNA replication with the bacteriophage Phi29 DNA polymerase, human mtSSB only shows the low binding mode. The transition from the high to the low binding mode facilitated by interacting protein was suggested to facilitate the access to the buried ssDNA for the replicating proteins [Morin *et al.*, 2017].

Single-stranded DNA compaction has been visualized for *Ec*SSB using electron microscopy (EM) [Griffith *et al.,* 1984], atomic force microscopy (AFM) [Hamon *et al.,* 2007] and total internal reflection fluorescence (TIRF) microscopy [Bell *et al.*, 2015]. Surprisingly, in the TIRF experiments, this compaction is larger than what would be expected for a simple transition of binding mode. The authors proposed that this is due to the ability of EcSSB to interact with distant sites along the ssDNA, either through dimerization of SSB tetramers or through the partial wrapping of distant ssDNA sites on a single SSB tetramer [Bell *et al.*, 2015]. Recently, it was also shown that stretching the T7 gp2.5/ssDNA nucleoprotein complex significantly impacts the DNA binding parameters, with a reduction of the DNA's contour length without modification of the DNA's persistence length compared to naked ssDNA [Xu *et al.,* 2023]. Additionally in *Ec*SSB, a study by Suksombat *et al.* showed that higher applied tensions on DNA favored less wrapped states with only the (*Ec*SSB)17 mode observed at tensions above 8 pN [Suksombat *et al.*, 2015].

Recently, several mtSSB variants have been reported to cause autosomal dominant mitochondrial optic neuropathy/atrophy and retinal dystrophy with or without mitochondrial DNA depletion. These mutations have been found so far in more than 80 patients across around 20 families and with the development of whole exome sequencing (WES) and whole genome sequencing (WGS), these numbers are rapidly rising [Del Dotto *et al,* 2020, Pyro-Mégy *et al.*, 2020, Jurkute *et al.*, 2019 and 2021; Gustafson *et al.*, 2019 and 2021]. Different hypotheses could explain the molecular mechanisms of the disease : a destabilization of the mtSSB tetramer into dimers or monomers or a perturbation of the interactions of mtSSB with DNA (binding or unbinding) or with other proteins. Some initial studies in patient-derived fibroblasts suggested that the mutations R38Q and R107Q could destabilize mtSSB tetramer formation [Pyro-Mégy *et al.*, 2020; Del Dotto *et al.*, 2020]. Several of the disease-causing mutants (G40V, N62D, R107Q, E111Q and I132V) have later been studied more in detail in *in vitro* biochemistry experiments. The effect on DNA replication initiation and on the DNA binding capacities were assayed [Jiang *et al.*, 2021]. Except for the mutant I132V, all the mutants tested did not affect DNA replication elongation but rather replication initiation, from one or the two mtDNA origins of replication. As for the binding to ssDNA of two different lengths (30 and 100 nt), the three mtSSB variants G40V, N62D, and R107Q displayed decreased binding to a short 30-nt ssDNA fragment but a binding pattern similar to that seen with wild-type mtSSB on a longer 100-nt ssDNA fragment, suggesting that the disease-causing mutations could affect the low binding mode of mtSSB. An array of mtSSB variants (E27K, R38Q, G40V, N62D, R107Q, E111Q, I132V and S141N) have also been recently studied using structural analysis predictions [Gustafson *et al.*, 2021]. These molecular dynamics simulations predict that the mutations do not destabilize the tetrameric structure of mtSSB and do not induce a complete disruption of the DNA binding. Instead, they could lead to more subtle changes in ssDNA binding via local perturbations of specific ssDNA-mtSSB interactions.

Here we have investigated the pathogenesis mechanisms of mtSSB^{R107Q}, which presents one of the more severe phenotypes among all the mtSSB disease-causing mutants discovered. We first assayed the oligomeric state of the mtSSB^{R107Q} using mass photometry. We then visualized ssDNA-mtSSB interactions and quantified ssDNA compaction driven by mtSSB using single molecule fluorescence microscopy and acoustic force spectroscopy. We also determined disassembly and assembly rates. Importantly, we have visualized in real time the competition between mtSSB^{WT} and mtSSB^{R107Q} for ssDNA. Based on these results and on a structural modeling of ssDNA-wrapped mtSSB^{R107Q}, we propose a model to explain the molecular mechanism of the disease, in which the R107Q mutation alters the wrapping and compacting abilities of mtSSB.

2. Materials and Methods

2.1 Proteins purification and labeling

mtSSB lacking the mitochondrial targeting sequence (aa 1-16) and containing a N-terminal His-tag was expressed in *E.coli* and purified over HIS-Select Nickel Affinity Gel (Sigma-Alrich), HiTrap Heparin HP (GE Healthcare) and hydroxyapatite. R107Q mutation was introduced using the QuickChange Lightning site-directed mutagenesis kit (Agilent Technologies, Santa Clara, CA) and verified by sequencing before expression and purification following the same protocol as for mtSSB^{WT}. For TIRF experiments, a C-terminal cysteine residue was added to mtSSB^{WT} and mtSSB^{R107Q} before being expressed and purified as for mtSSB^{WT}. The proteins were then labeled with Maleimide Alexa Fluor™ 555 dye or Maleimide Alexa Fluor™ 647 dye (Fisher Scientific). Unreacted dye was removed from the sample with size exclusion spin-columns (MicroSpin G-25 columns - Cytiva Amersham). A labeling ratio of 1:1 (protein:dye) was verified using Nanodrop.

2.2 Mass Photometry

Mass photometry experiments were recorded on a Refeyn TwoMP system. Samples were prepared at 1 mM and diluted prior measurements at a concentration of 100 nM. Data were collected for one minute with the provided Acquire Software. Calibration of the instrument was performed in the same buffer with carbonic anhydrase, BSA, and Urease covering a range of molecular weight from 29kDa to 816kDa. Data were analyzed using the provided Discovery analysis software.

2.3 ssDNA constructs

For TIRF experiments, double-stranded Lambda DNA (48,502 bp) was biotinylated at the 5′-ends of both strands using Klenow polymerase, as described in (Gross, methods in enzymology, 2010). The labeled DNA was purified using Illustra MicroSpin S-400 HR columns (GE Healthcare). Biotinylated dsDNA was then denatured using 0.5 M NaOH for 10 min at 37°C as described in [ref eLife Bell], then diluted 40 times (0.15 ng/µL final concentration) in buffer A (20 mM TrisOAc pH8, 20 % sucrose, 20 mM DTT) and kept on ice.

For AFS experiments, DNA substrates were made by PCR amplification (PCR Long Amplification Taq PCR kit, NEB) of a 9 kb fragment of human mitochondrial genome, adding digoxigenin and biotin moieties on the same strand through the forward primer and Klenow polymerase, respectively. This labeled dsDNA was purified using NucleoSpin Gel and PCR Clean-Up (Macherey-Nagel), and then denatured, diluted at 0.1 ng/uL in cold water and kept on ice.

2.4 TIRF microscopy

The TIRF experimental setup was described in detail in [Martucci *et al.*, 2023]. For fluorescent imaging of mtSSB$^{\text{Alexa555}}$ and mtSSB$^{\text{Alexa647}}$, a 532-nm and 640-nm excitation lasers were used and imaged either on a Nikon (DS-Qi2) wide field camera (compaction assay) or on an EMCCD (iXon 888, ANDOR) camera (dissociation and competition assays). All TIRF experiments were performed in buffer A (20 mM TrisOAc pH8, 20 % sucrose, 20 mM DTT) supplemented with the amounts of NaOAc indicated in the text. In all experiments, biotinylated λ ssDNA was mixed with mtSSB$^{\text{WT}}$ and/or mtSSB$^{\text{R107Q}}$ in 400 µL of buffer A, resulting in a concentration of 0.15 ng/µL for ssDNA and the mtSSB concentrations indicated in the text. The ssDNA-mtSSB complexes formed were anchored on one end to the glass surface and subsequently flow-stretched for imaging.

2.5 Biolayer interferometry (BLI)

Biolayer interferometry experiments were performed using an Octet RED384 device (Fortebio) at 25°C and 1000 rpm shaking rate. Streptavidin-sensors were hydrated in a buffer containing 20mM Hepes pH7.6, 100mM NaCl, 0.1 mM EDTA, 0.5 mM TCEP for 10 min and the baseline was recorded for 2 min. Sensors were then functionalized with a biotinylated polyDT 30-mer or 60-mer at a concentration of 50 nM until we reached the value of 0.2 nm. Experiments were carried out subsequently in the same buffer supplemented with 0.05% Tween. Association reactions were performed for 300 seconds, and the dissociation for 600 seconds in presence of mtSSB$^{\text{WT}}$ or mtSSB$^{\text{R107Q}}$ at different concentrations ranging from 0.625 nM to 5 nM.

2.6 Acoustic Force Spectroscopy (AFS)

For AFS experiments, DNA tethers were made by attaching DNA molecules between a glass surface and 4.89 µm streptavidin polystyrene beads (Spherotech). A detailed description of the AFS instrumentation (LUMICKS B.V., Amsterdam, the Netherlands) can be found in [Martucci *et al.*, 2023]. Flow cell (LUMICKS B.V., Amsterdam, the Netherlands) functionalization was performed with anti-digoxigenin (50 µg/mL, Roche) for 20 min and passivation with PBS containing 2% BSA for at least 30 min. Beads in PBS containing 2% BSA were mixed with the ssDNA substrate diluted in water for 2 min at room temperature before injection in the flowcell and incubation for 5 min for tethering. Unattached beads were washed first with PBS containing 0.2% BSA and then with 10 mM Tris HCl pH 7.5, 100 mM NaCl and 0.2% BSA under low force. After selecting the regions of interest, making the look-up tables, and performing the force calibration, force-extension curves of the bare DNA tethers were acquired. These steps with bare DNA constituted our control and were done for each assay. Proteins of interest were then flushed in the flow cell at a flow rate of 4 µL/min for 2 min, incubated 2 min and rinsed with 10 mM Tris HCl pH 7.5, 100 mM NaCl and 0.2% BSA for 2 min, and stretching curves were generated. Data acquisition was performed using AFS Tracking G2 and analysis with AFS Analysis G2 software (LUMICKS B.V., Amsterdam, the Netherlands). The force-distance curves were fitted with the extensible Freely Jointed Chain (eFJC) model using MATLAB: L=Lc*(coth(F*2*Lp/(kBT))-((kBT)/(F*2*Lp)))*(1+(F/S)), with L being the distance between the bead and the surface (i.e. the length of the DNA), F the applied force, Lc the contour length of the DNA, Lp the persistence length, kBT the product of the Boltzmann constant and the temperature (which is 4.11 pN.nm at 25°C), and S the stretch modulus (set at 800pN for ssDNA [10.1126/science.271.5250.795]).

2.7 Structural analysis of the R107Q mutation

The DNA from *E. coli* SSB protein structure (PDB ID: 1EYG) was placed onto mitochondrial mtSSB by superposing both protein structures with Coot (Emsley et al., 2010). mtSSB^{R107Q} mutant structure was modeled as explained in **Figure 6**. Structures were represented, and the electrostatic potential surfaces calculated with default parameters, with Chimera (ref).

3. Results

3.1 The R107Q variant can form tetramers in solution

One molecular mechanism that could explain the pathogenicity of the mtSSB related diseases is a destabilization of the mtSSB tetramer into dimers or monomers. To test this hypothesis, we used mass photometry (MP) to assess the molecular mass and thus the oligomeric state of mtSSB^{R107Q} in solution (**Figure 1**). From fitting a Gaussian function to the obtained mass distribution we found a molecular mass of 67 +/- 2 kDa for mtSSB^{WT} and 60 +/- 2 kDa for mtSSB^{R107Q} (mean +/- SD). Knowing that the molecular weight of one mtSSB molecule containing the His-Tag is ~ 65 kDa, it shows that the R107Q mutation does not impair the ability of mtSSB to form tetramers in solution.

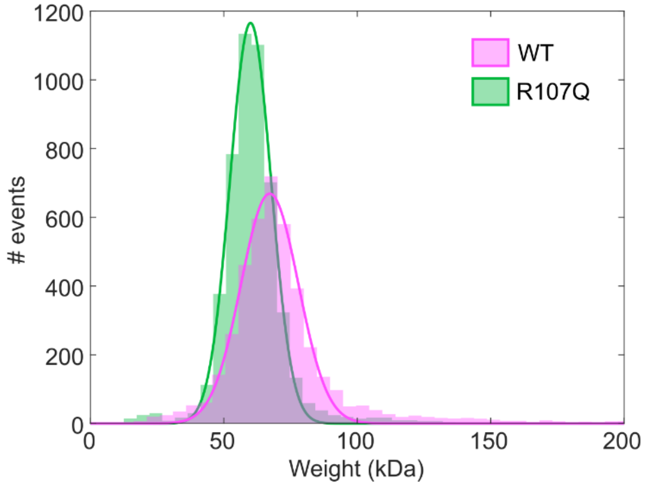

***Figure 1**: Mass photometry (MP) analysis of recombinant mtSSB^{WT} and mtSSB^{R107Q}.* *Histograms showing the population distributions of mtSSB^{WT} (magenta) and mtSSB^{R107Q} (green) were fitted with a Gaussian, yielding a mean molecular weight of 60 +/- 2 kDa for mtSSB^{R107Q} and 67 +/- 2 kDa for mtSSB^{WT}.*

3.2. The R107Q mutation alters the ability of mtSSB to compact ssDNA

Knowing that a destabilization of the tetramer is not the molecular mechanism explaining the phenotype, we then investigated the interaction of mtSSB with ssDNA. For this, we used an inverted fluorescence microscope in combination with a camera which allows imaging of a large field of view at the cost of single molecule resolution [Nikon, for details see (Martucci et al., 2023)]. We first visualized the effect of mtSSB on DNA compaction. To this end, we used 48.5 kb long biotinylated λ-phage DNA which has been converted into ssDNA using NaOH. The long ssDNA molecules were pre-incubated with fluorescence labeled mtSSB^{Alexa555} (WT or R107Q, 150 nM) and nucleoprotein complexes formed were then tethered to the glass surface of a flow-cell on one end via a biotin-streptavidin bond and gently flow-stretched. The movies were started and, subsequently, salt (100 mM or 400 mM NaOAc) was added to the flow-cell and its effect on ssDNA compaction by mtSSB was monitored. The phenomenology was as follows: First the ssDNA was stretched by the flow to a nearly constant length, then, only a few seconds after the salt was added, we observed an important shortening of the ssDNA molecules, first rapidly and then slower; both for mtSSB^{WT} and mtSSB^{R107Q} (**Figure 2A**). For each experiment, we recorded a field of view with between 10 and 40 ssDNA molecules; which all decreased in length after addition of salt.

To quantify the ssDNA compaction observed in the movies, we determined, in each frame, the "apparent" contour length (corresponding to the visible length of the DNA) and the total intensity of each ssDNA molecule. In total, we followed about ~ 30 ssDNA molecules over eight independent experiments. The initial length (L0), obtained for each ssDNA by averaging its length in the first 3 frames of the movie, was L0~2.56 µm for the WT-coated ssDNA, which was significantly shorter than the L0~4.14 µm obtained for the ssDNA coated by mtSSB^{R107Q} (**Figure 2B**). To get an idea of the length of the ssDNA under our experimental conditions in absence of mtSSB, we performed experiments with SYBR Green II. Single-stranded DNA was pre-incubated with SYBR Green II (diluted to 1X) for 20 min and the ssDNA stained with SYBR Green II was added to the flow-cell using the same conditions as used for the ssDNA-mtSSB experiments. Subsequently, the flow-cell was rinsed with buffer to remove free SYBR Green II dye. The lengths of 115 flow-stretched SYBR-ssDNA molecules were measured, which yielded an average length of ~8.5 µm (**Figure S1**). Considering that the theoretical size of a 48.5 kb naked ssDNA is 16 µm, this implies that our flow-stretch protocol stretches the ssDNA to about half of its full length. The initial (salt independent) compaction of the ssDNA by mtSSB^{WT} is thus about 70%, while for ssDNA by mtSSB^{R107Q} the initial compaction is ~ 50 %. We also quantified the initial intensity (I0) of the nucleoprotein complexes in the first 3 frames. We observe that ssDNA-mtSSB$^{R107Q\text{-}Alexa555}$ have significantly higher absolute intensities (2745 a.u.) than ssDNA-mtSSB$^{WT\text{-}Alexa555}$ (411 a.u.) for the same illumination and acquisition settings (**Figure 2C**). The higher intensities observed for the mtSSB^{R107Q} suggests that, at the same bulk concentration, ssDNA molecules are more covered by the mutant than by the WT.

We noted that rinsing with salt (100 and 400 mM) almost immediately removed the SYBR Green II from the ssDNA, it was thus not possible to follow the salt dependent compaction of the naked ssDNA with SYBR Green II. Therefore, we focus on the difference between the salt-dependent compaction in the experiments with mtSSB^{WT} and mtSSB^{R107Q}. To do so, we calculated for each ssDNA the ratio L(t)/L0 by normalizing the length of the molecule in a frame by its initial length. The time at which the salt begins to have an effect t0* was determined as described in **figure S2**. Next, L(t*)/L0 was averaged over all ssDNA molecules and represented in **figure 2D** as a function of t*, where t*=t-t0*. To describe the experimental data we fitted the exponential decay function $L/L0 = \beta \cdot exp[- kc \cdot t\ *] + Lf/L0$, where β, kc are the amplitude and rate of the salt dependent compaction, respectively, and Lf the average final length of the compacted ssDNA (**Figure 2D**). β values obtained from the fits are similar for the mtSSB^{WT} and mtSSB^{R107Q}, and appear only dependent on the salt concentration, varying from 80% at high salt (400 mM) to about 63% at lower salt (100 mM) (**Figure 2E**). In contrast, the rate of compaction kc depends both on the salt concentration and on the mtSSB used, with an almost twice faster compaction rate for mtSSB^{WT} than for mtSSB^{R107Q} (**Figure 2F**). Additionally, for both mtSSB^{WT} and mtSSB^{R107Q}, at high salt concentration the compaction is twice faster than at low salt. This suggests that ssDNA compaction by mtSSB is salt-dependent and is more efficient for mtSSB^{WT} than for mtSSB^{R107Q}.

Finally, to rule out the possibility that the nucleoprotein complexes were differently stretched in the different experiments, we also performed a two-color experiment, with ssDNA-mtSSB$^{WT\text{-}Alexa647}$ and ssDNA-mtSSB$^{R107Q\text{-}Alexa555}$ flushed and stretched simultaneously (**Figure 2B, inset**). Here again, we confirm a higher compaction of ssDNA with mtSSB^{WT} than with the mutant.

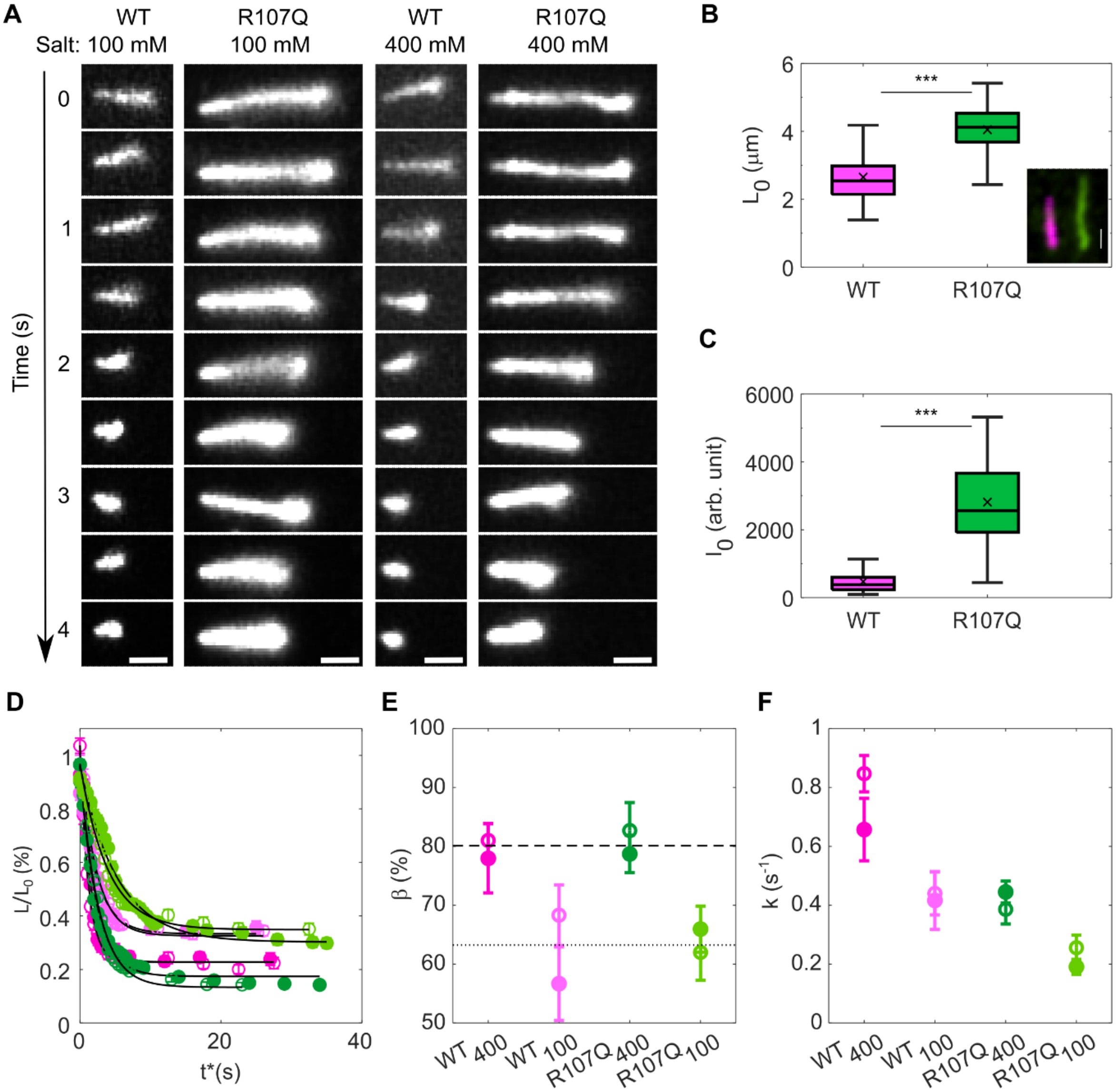

Figure 2 : mtSSB^{R107Q} has reduced ssDNA compaction activity. ***(A)*** *Selected frames from movies recording ssDNA compaction by mtSSB^{WT} or mtSSB^{R107Q} at two different salt concentrations (100 mM and 400 mM NaOAc). Colors are from an artificial filter (scale bar, 1μm).* ***(B)*** *Initial ssDNA length measurement at T0 before adding salt. Median values of L0 are 2.56 μm (n=131) and 4.14 μm (n=147) for WT and R107, respectively. Example image of a two-color experiment (inset) showing one ssDNA covered by mtSSB^{WT} (magenta) and one ssDNA molecule covered by mtSSB^{R107Q} (green) (scale bar, 1μm).* ***(C)*** *Initial intensity of mtSSB-coated ssDNA at t0 before adding salt. Median values for WT and R107Q are 411a.u. (n=59) and 2745 a.u. (n=59), respectively.* ***(D)*** *ssDNA length normalized by L0 in percentage as a function of time showing an exponential decay (dark green: WT at 400 mM salt, light green: WT at 100 mM salt, dark pink: R107Q at 400 mM salt, light pink: R107Q at 100 mM salt). Open and closed symbols of the same color represent 2 biological replicates.* ***(E)*** *Amplitude of compaction (β) in percentage of initial length for WT and R107Q at 100 mM and 400 mM salt.* ***(F)*** *Compaction rate (kc) for WT and R107Q at 100 mM and 400 mM salt. For (E) and (F), amplitude and compaction rates are obtained from an exponential fit to the data (black curves in (D)). P-values were calculated using unpaired Student's t-tests, ***P < 0.001.*

Having shown that mtSSB^{R107Q} has a default in ssDNA compaction, we set out to quantify in more detail its ability to bind ssDNA, using acoustic force spectroscopy (AFS). For these experiments, we used 9-kb long ssDNA molecules attached on one end to the glass surface and on the other end to a bead. We performed force-distance extension

(DNA stretching with an increasing force ramp) and retraction (DNA relaxation with a decreasing force ramp) experiments on bare ssDNA and on mtSSB-coated ssDNA. Each force ramp was repeated twice, which limits unspecific interactions of the ssDNA molecules with the flow-cell surface at the beginning of the extension phase for the second ramp (**Figure S3A**). We observed that the force-distance curves for mtSSB-coated ssDNA significantly deviate from the curves corresponding to bare DNA, with a clearly stronger effect for the WT than for the mutant (**Figure S3B**). We quantified the effect of mtSSB-binding on the mechanical properties of the ssDNA by fitting the force-distance retraction curves with the extensible Freely Jointed Chain model (eFJC), commonly used to model the relation between applied tensions and ssDNA extension (10.1126/science.271.5250.795). For bare ssDNA we fitted the force-distance curves from 0.1 to 15 pN and obtained values of apparent contour length Lc of 4.8 um +/- 0.2 and persistence length Lp of 1.9 nm +/- 0.3 (mean +/- SD). To estimate the Lc and Lp values after addition of mtSSB, we fitted only the first part of the force-distance curves, which deviated from the curve with bare ssDNA, from 0.1 to 2 pN, as done previously by Xu *et al* (10.1093/nar/gkad485). In the presence of mtSSB^{WT}, we observed that the Lc decreased to 1.3 um +/- 0.2 while the Lp increased to 9.3 nm +/- 1.8. In the presence of mtSSB^{R107Q}, the decrease in Lc was less drastic than in the presence of mtSSB^{WT} (Lc = 2.5 um +/- 0.8) and the Lp was only slightly higher than the Lp for bare DNA (Lc = 3.3 nm +/- 1.2) (**Figure 3A and S4B**). The Lc value for mtSSB^{WT}-coated ssDNA is thus ~4 times smaller than the Lc of bare DNA, while with mtSSB^{R107Q} the Lc is only ~twice smaller, which confirms that R107Q alters the compaction capacity of mtSSB. Meanwhile, the Lp values, which represent the bending stiffness of the ssDNA, indicate that ssDNA covered by mtSSB^{WT} is ~5 times stiffer than bare ssDNA, while ssDNA covered by mtSSB^{R107Q} has a similar rigidity than bare ssDNA. This AFS experiment can also be used to determine the energetic consequences of protein binding to DNA (10.1126/science.1071152), with the area under the force-distance curve being the work performed on the DNA that is stretched (10.7554/eLife.08646). We therefore integrated the area between the retraction curve obtained in the presence of mtSSB and the retraction curve obtained for bare ssDNA, to calculate the change in energy due to mtSSB-binding to ssDNA. The work stored in the mtSSB^{R107Q}-coated ssDNA was almost 3 times smaller than in the mtSSB^{WT}-coated ssDNA, indicating an alteration of the mtSSB-binding capacities (**Figure 3B**). Finally, we investigated the force-dependency of mtSSB-binding to ssDNA. To this aim, we applied lower amplitude force-ramps after addition of mtSSB in the flow-cell (**Figure S3C**). In this configuration, the stretching and relaxing force-distance curves overlapped for tensions below 3-4 pN (ramps R'1 and R'2 in **figure S3C**), while we observed hysteresis for higher tensions of 6-7 pN (ramps R1 and R2), for both WT and mutant proteins. Although hysteresis is observed for both WT and R107Q proteins for forces of 6-7 pN, the mtSSB^{R107Q} appears less stable on the ssDNA, as the force distance-curves obtained with two consecutive ramps at this tension do not overlap (ramps R1 and R2, **Figure S3C**), indicating that some mtSSB^{R107Q} molecules detached from the DNA. This is quantified by integrating the area between the force-distance extension and retraction curves obtained with the two successive ramps R1 and R2 (**Figure 3C**), which confirms that the change in energy due to mtSSB-ssDNA interaction is significantly lower for mtSSB^{R107Q} during the second ramp R2 compared to the first ramp R1. The force experiments thus indicate that the R107Q mutation significantly reduces mtSSB ability to compact ssDNA, by altering mtSSB-ssDNA binding and increasing its dissociation at mild tensions.

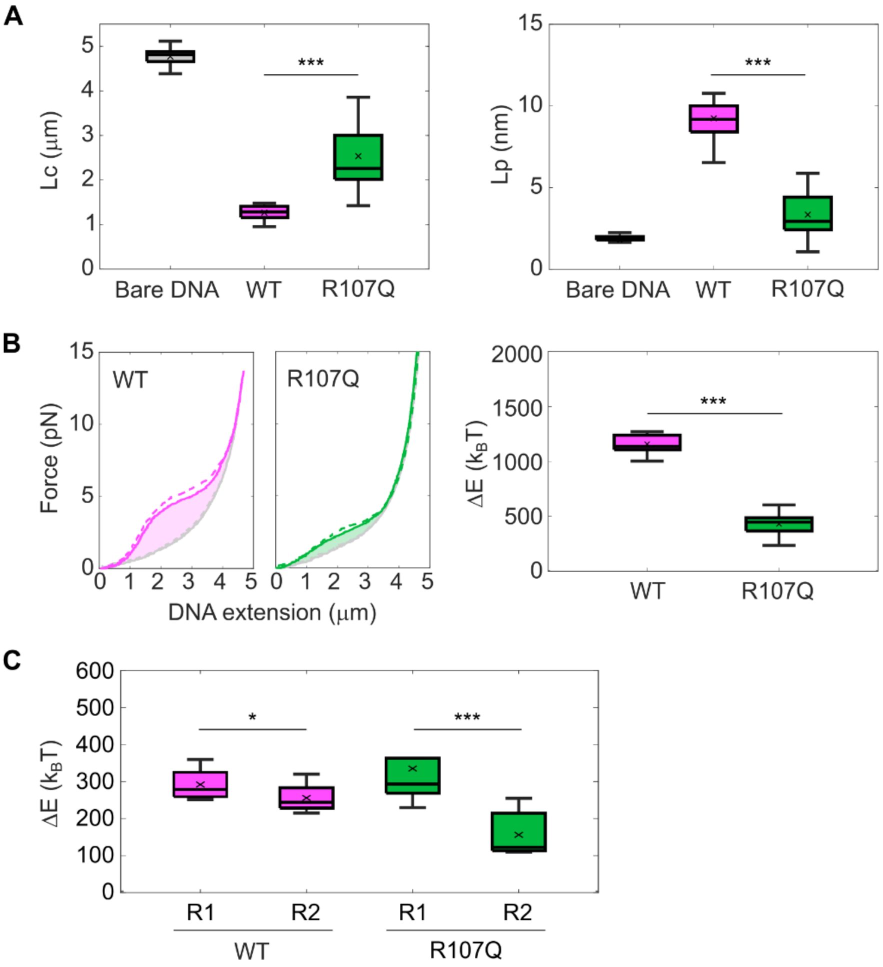

***Figure 3**: **The R107Q mutation alters the ssDNA-binding properties of mtSSB. (A)** Estimation of the contour length (Lc) and the persistence length (Lp) of bare ssDNA and ssDNA incubated with 100nM of mtSSB^{WT} or mtSSB^{R107Q}, using the eFJC model on the corresponding force-distance retraction curves obtained with AFS. Fitting range for bare DNA curve: 0.1-15 pN and for mtSSB-coated DNA: 0.1-2 pN. **(B)** Force-distance extension (dashed lines) and retraction (solid lines) curves of ssDNA in presence of mtSSB^{WT} (magenta) and mtSSB^{R107Q} (green), compared to bare DNA (gray). The area between the retraction curve obtained in the presence of mtSSB and the retraction curve obtained for bare ssDNA was used to calculate the change in energy (ΔE) due to mtSSB-binding to ssDNA. **(C)** The area between the force-distance extension and retraction curves obtained in the presence of mtSSB when stretching the DNA with two successive ramps R1 and R2 (see Figure S4C) at low force (6-7pN) was used to calculate the (ΔE) due to mtSSB-ssDNA interaction. Boxplots represent the median within the IQR for (A, B) a minimum of 20 tethers acquired in three different experiments for each condition or (C) a minimum of 8 tethers acquired in two different experiments for each condition. P-values were calculated using (A, B) unpaired Student's t-tests and (C) paired Student's t-tests, where $*P < 0.05$, $**P < 0.01$, $***P < 0.001$. The ΔE has been converted from pN•nm to k_BT (i.e. the Boltzmann constant multiplied by the absolute temperature) using the relationship $k_BT \sim 4.1$ pN•nm at 25°C (Nelson, 2004 ISBN 0716743728).*

3.3 The R107Q mutation does not alter the ability of mtSSB to bind short ssDNA templates

Next, we set out to compare the ssDNA-binding affinity of mtSSB^{WT} and mtSSB^{R107Q} using biolayer interferometry. We used sensors functionalized with either a 30mer or 60mer polydT and four different mtSSB concentrations (0.625 nM, 1.5 nM, 2.5 nM and 5 nM). In both cases, the binding traces of the four mtSSB concentrations were fitted with a 1:1 binding model (**Figure S4**). We observed closely matched Kd values for both mtSSB^{WT} (Kd = 1.17 ± 0.022 nM) and mtSSB^{R107Q} (1.18 ± 0.018 nM) when interacting with a 60mer polydT. Similarly, when a shorter

30mer polydT oligonucleotide was used, the Kd values fell within a similar range, with Kd = 2.18 ± 0.103 nM for WT and Kd = 1.35 ± 0.036 nM for mtSSB^{R107Q}. However, because these experiments were performed on short DNA templates, they did not provide information on the more complex dynamics of mtSSB-coated long ssDNA molecules that forms in vivo during mtDNA transactions. We thus moved to single molecule imaging techniques to further examine the DNA binding modes of mtSSB^{WT} and mtSSB^{R107Q} on longer, more physiological, ssDNA substrates.

3.4 Disassembly of mtSSB^{R107Q} from ssDNA

During the course of the compaction experiments, we noticed a decrease in the fluorescence intensity over time of mtSSB^{R107Q}-coated ssDNA molecules, whereas the intensity of mtSSB^{WT}-coated ssDNA remained stable, with only a slight decrease at 400 mM salt (**Figure S5**). This could suggest that, in the presence of salt, a fraction of the R107Q protein dissociates from ssDNA, and led us to investigate, in detail, the salt-dependent disassembly kinetics of mtSSB from ssDNA. To the end, pre-formed nucleoprotein complexes were flushed in a flow-cell, tethered to the glass surface on one end via a biotin-streptavidin bond and, using a high flow rate, attached to the glass surface through nonspecific interactions. This resulted in most of the ssDNA molecules being fixed and only a small fraction remaining loose or breaking. We then followed in real time for three different salt concentrations (10 mM, 100 mM and 400 mM) the decreasing intensity of the mtSSB-coated-ssDNA molecules, reflecting the dissociation from ssDNA of mtSSB^{WT} and mtSSB^{R107Q}. To limit the effect of photobleaching (**Figure S7**), we acquired fluorescence images intermittently every 5 s (Figure 4A and 4B). For each image, we converted the fluorescence intensity into numbers of mtSSB molecules on a ssDNA molecule by summing the fluorescence intensity on the DNA and dividing it by the intensity of a single fluorophore (See supplementary **Figure S6**).

The time evolution of the number of mtSSB^{WT} and mtSSB^{R107Q} molecules on ssDNA displayed two regimes: (i) first a fast decrease, followed by (ii) a slower decrease (**Figure 3 C-F and Figure S7)**. Since the fluorescence of the mtSSB-coated-ssDNA remained nearly constant after adding 10 mM salt, we focused our analysis on the salt concentrations of 100 mM and 400 mM. We estimated that, for mtSSB^{WT} , the number of molecules on ssDNA decreased over time by about 20%, independently of the salt concentration. Instead, for mtSSB^{R107Q}, this loss was ~ 40% at 100 mM salt, and ~ 77 % at the highest salt concentration (**Figure 3 D and 3F**). The sharp transition between the two regimes could not be captured by a simple one-state transition which would result in a single exponential function. Therefore, we described our data using a two-state model with a high binding mode (W, wrapping mode) and a low binding mode (B, binding mode) and assumed that dissociation happens only from the low binding mode (Qian et al JBC 2017, Naufer et al NAR 2017)): W→B→0. For each ssDNA, the number of mtSSB molecules was fitted using matlab's ode45 and the following Ordinary Differential Equations (ODE)s:d[w]/dt= k{-w}*[w] and d[b]/dt= k{-w}*[w]-k{-b}*[b], where [w] and [b] correspond to the number of molecules in the wrapping and binding state, respectively and k{-b} and k{-w}, the unbinding and unwrapping rates, respectively. We found that this simple two-state model described our data well (fit in black **Figure 3 C-F**). The obtained fitting parameters w0 and b0, corresponding to the initial number of molecules in the wrapped and bound state, and the rates k{-w} and k{-b} are depicted in **Figure 3 G-J**. The unbinding and unwrapping rates were corrected for photobleaching by subtracting the significantly smaller k{bleaching}~ 5.9 e-3 s^{-1} (see supplementary **Figure S7**). Overall, the total number of mtSSB molecules on a ssDNA before addition of salt was larger for mtSSB^{R107Q} (~2200 molecules) than for mtSSB^{WT} (~500 molecules), consistent with what we observed in our compaction experiments. For mtSSB^{R107Q}, the number of molecules in the binding mode was similar to those in the wrapping mode (b0~w0~1100 molecules), while for mtSSB^{WT} there were twice more molecules in the wrapping mode than in the binding mode (w0~2*b0~300 molecules) for both 100 mM and 400 mM (**Figure 3 G-H**). The unbinding rates k{-b} were similar for mtSSB^{WT} at 100 mM and 400 mM salt, and mtSSB^{R107Q} at 100 mM salt, however it was increased for the mtSSB^{R107Q} at high salt. As for the unwrapping rates k{-w}, they appeared not to depend on the salt, but were almost three times slower for the mtSSB^{WT} than for the mtSSB^{R107Q}. In conclusion, we observed that in general the dissociation of the mtSSB from ssDNA shows two regimes, and that fmtSSB^{R107Q} dissociates faster from ssDNA than mtSSB^{WT}.

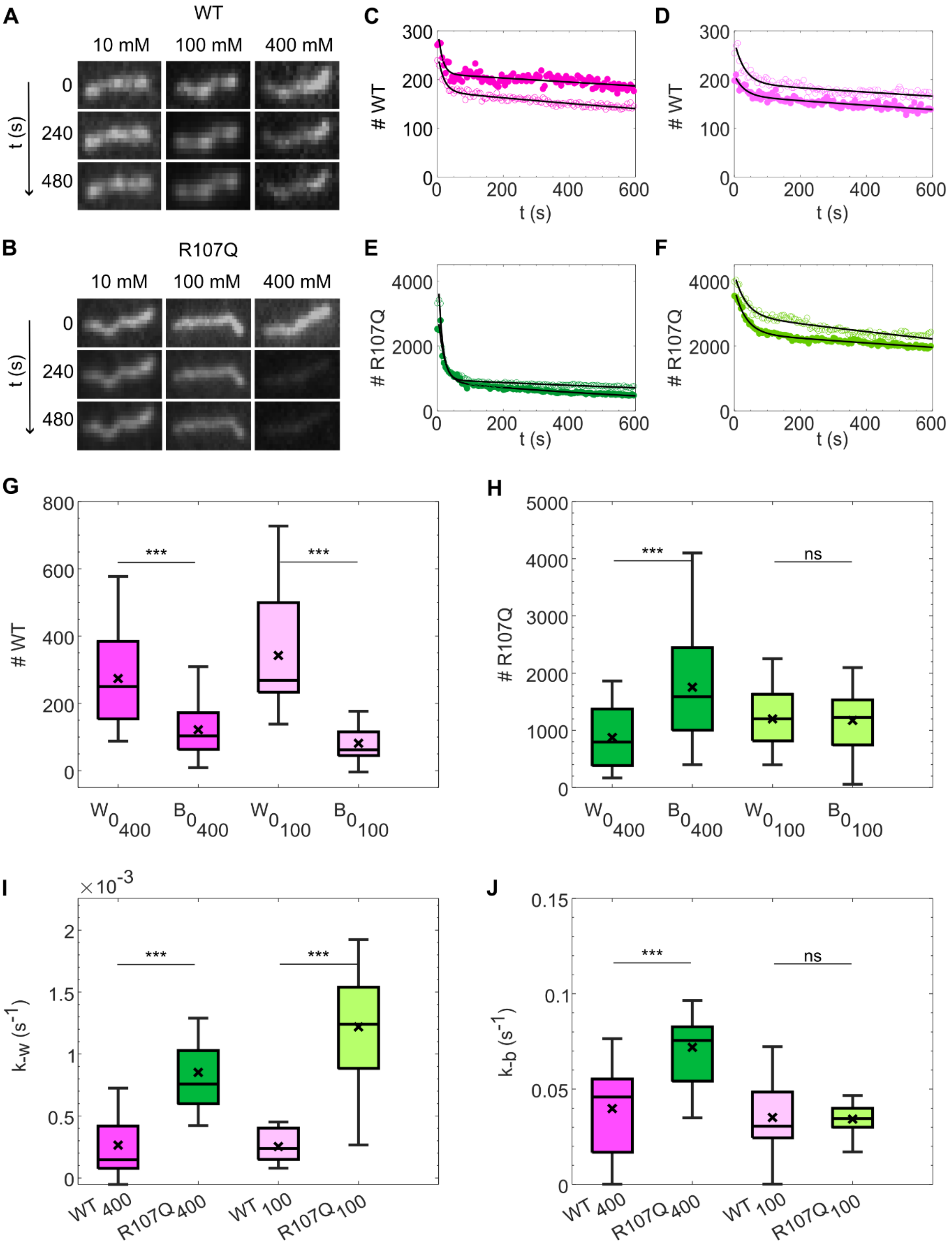

Figure 4 : Disassembly of mtSSB from ssDNA is faster for mtSSB^{R107Q} than for mtSSB^{WT}. *Typical fluorescence images of stretched mtSSB^{WT}* ***(A)*** *or mtSSB^{R107Q}* ***(B)*** *-ssDNA complexes at different NaOAc concentrations (10, 100 and 400 mM) at indicated time intervals. Images were acquired with an exposure time of 0.1 s every 5 s in order to limit the effects of photobleaching. Fluorescence intensity was converted into number of mtSSB monomers as described in* ***supplementary Figure***

***S5** and the number of mtSSB monomers bound was followed over time at different salt concentrations **(C-F)**. Example traces for mtSSB^{WT} at 400 mM NaOAc **(C)**, mtSSB^{WT} at 100 mM NaOAc **(D)**, mtSSB^{R107Q} at 400 mM NaOAc **(E)**, mtSSB^{R107Q} at 100 mM NaOAc **(F)**. Open and closed symbols of the same color represent 2 biological replicates, black curve: fit to the data. All traces are shown in **supplementary Figure S8**. (G) initial number of molecules in the wrapped state w0, **(H)** initial number of molecules in the bound state b0, **(I)** unwrapping rate k{-w} and **(J)** unbinding rate k{-b}.*

3.4 Competition assays

In patients R107Q is a dominant, heterozygous variant, which implies that the mutant protein coexists with the WT version of mtSSB. We thus performed a competition assay between mtSSB^{WT} and mtSSB^{R107Q} to examine how the two proteins behave when they are present concomitantly. mtSSB$^{R107Q\text{-}Alexa555}$ (150 nM) was mixed with increasing concentrations of mtSSB$^{WT\text{-}Alexa647}$ (1.5 nM, 15 nM, 150 nM and 300 nM; corresponding respectively to the concentration ratios 1:0.01, 1:0.1, 1:1 and 1:2). **Figure 5A** shows, for each experimental condition, typical two-color TIRF images as well as an overlay of those images. Images were analyzed as follows: for each protein ratio, we counted the DNA molecules covered with only mtSSB^{WT} (**Figure 5B**, black), both mtSSB^{WT} and mtSSB^{R107Q} (**Figure 5B**, stripes), or only mtSSB^{R107Q}(**Figure 5B**, white) and expressed them as a percentage of the total number of counted DNA molecules. In total, we counted between 210 and 345 DNA molecules for each condition. We found that, when the mtSSB^{WT} concentration is higher than the mtSSB^{R107Q} concentration (1:2 ratio, R107Q:WT), only mtSSB^{WT} was bound to ssDNA (**Figure 5B**). However, at a 1:1 ratio, we noticed that 24 % of the ssDNA molecules were covered exclusively by mtSSB^{WT} whereas 76 % of the DNA molecules were covered by both the WT and the mutant proteins (**Figure 5B**). At this ratio, we could not detect any ssDNA molecules coated exclusively with mtSSB^{R107Q}. Only when a 10-fold excess of mtSSB^{R107Q} was added, some ssDNA molecules exclusively coated by mtSSB^{R107Q} could be observed (~ 10 %) and 90 % of the ssDNA was coated by both proteins. Finally, with a 100-fold excess of mtSSB^{R107Q} (1:0.01 ratio), no mtSSB^{WT} could be detected on the DNA. We then took a closer look at the ssDNA molecules coated by both mtSSB^{WT} and mtSSB^{R107Q} (ratio 1:1 and 1:0.1). We determined the number of mtSSB^{WT} and mtSSB^{R107Q} on each DNA molecule from the total fluorescence intensity on the DNA and the intensity of a single fluorophore (**Figure 5C**). For the 1:1 ratio, we noticed that the co-coated ssDNA molecules are in fact mostly coated by the WT (73 %) (**Figure 5C**), showing that at this ratio there is mainly mtSSB^{WT} bound to DNA. For the 1:0.1 ratio, the co-coated ssDNA molecules are instead mostly covered by mtSSB^{R107Q} (94 %).

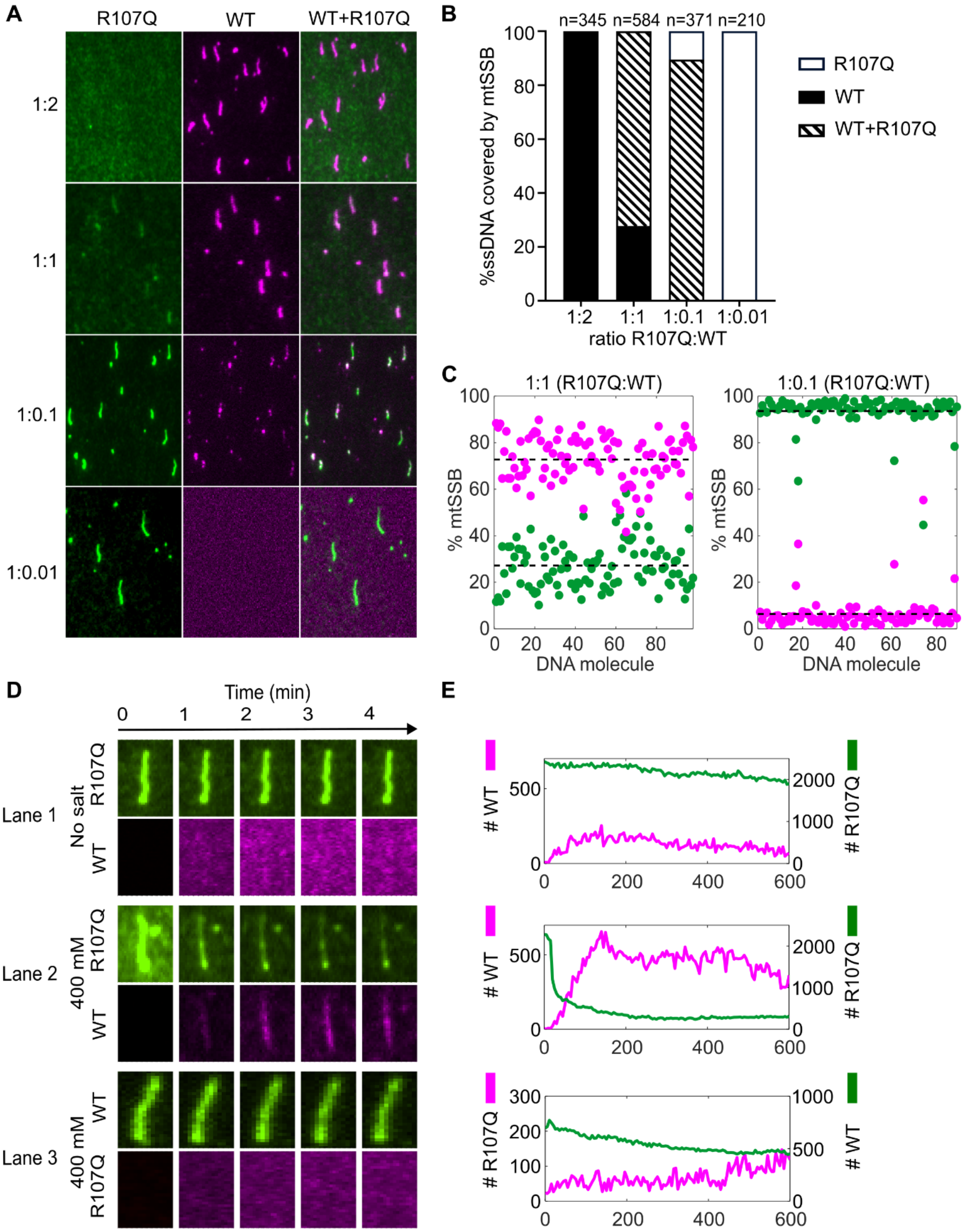

Figure 5 : Binding competition between mtSSB^{WT} and mtSSB^{R107Q} (A-C) Binding competition at different mtSSB$^{R107Q\text{-}Alexa555}$/mtSSB$^{WT\text{-}Alexa\ 647}$ protein concentration ratios (A) *Representative images of nucleoprotein complexes at different concentration ratios: 1:2, 1:1, 1:0.1, 1:0.01 (R107Q:WT). The mix of the two proteins was then incubated with ssDNA for 60 min and the nucleoprotein complexes formed were attached on the glass surface. Image contrasts were adjusted differently*

for each ratio in order to visualize low abundance proteins. ***(B)*** *Histogram showing in percentage the number of ssDNA molecules covered by only mtSSB*^{WT}*, both mtSSB*^{WT} *and mtSSB*^{R107Q} *or only mtSSB*^{R107Q} *in each condition.* ***(C)*** *Quantification of mtSSB molecules on ssDNA molecules at 1:1 (left) and 1:0.1 (right) ratios.* ***(D-E) Real-time competition between mtSSB***^{R107Q} ***and mtSSB***^{WT}*.* ***(D)*** *TIRF images of nucleoprotein complexes over time in 3 different settings. The upper line of each configuration (1 to 3) shows mtSSB*$^{R107Q\text{-}Alexa555}$ *or mtSSB*$^{WT\text{-}Alexa555}$*-ssDNA complexes stretched at the surface of the flow-cell. The lower line shows mtSSB*$^{R107Q\text{-}Alexa647}$ *or mtSSB*$^{WT\text{-}Alexa647}$ *that is added to the flow-cell in the presence of salt.* ***(E)*** *Intensity measurement of mean intensities of ssDNA-mtSSB complexes as a function of time for each configuration (1 to 3).*

Next, we set out to follow the competition between the two proteins in real-time. In this experiment, we attached preformed mtSSB$^{R107Q\text{-}Alexa555}$-ssDNA or mtSSB$^{WT\text{-}Alexa555}$-ssDNA nucleoprotein complexes at the surface of the flow-cell, then added mtSSB$^{WT\text{-}Alexa647}$ or mtSSB$^{R107Q\text{-}Alexa647}$, respectively, in the presence of different salt concentrations (0 or 400 mM) and followed the proteins on the DNA over 10 min (**Figure 5 D-E**). In the absence of salt*,* mtSSB^{WT} binds only slightly to mtSSB^{R107Q}-coated ssDNA molecules (Figure 5D lane 1). In contrast, in presence of 400 mM NaOAc, mtSSB^{R107Q} dissociates from ssDNA and free WT proteins bind rapidly on ssDNA (**Figure 5D** lane 2). When performing the opposite experiment, i.e. competing preformed mtSSB^{WT}-ssDNA complexes with free mtSSB^{R107Q} (**Figure 5D** lane 3), we observed only a slight dissociation of WT and almost no binding of mtSSB^{R107Q}. Interestingly, when we injected mtSSB$^{R107Q\text{-}Alexa647}$ in presence of 400 mM NaOAc on pre-formed ssDNA-mtSSB$^{R107Q\text{-}Alexa555}$ complexes, we noticed that, even if mtSSB$^{R107Q\text{-}Alexa555}$ dissociates from ssDNA, only a relatively small fraction of the ssDNA is coated again by mtSSB$^{R107Q\text{-}Alexa647}$ (**Figure S9** lane 1). Finally, when we injected mtSSB^{WT} in presence of 400 mM NaOAc on pre-formed ssDNA-mtSSB^{WT} complexes, some WT protein can bind even though there is nearly no dissociation, indicating that under these experimental conditions there is still some free space on the ssDNA (**Figure S9** lane 2).

3.5 Effect of R107Q on mtSSB structure

The crystal structures of mtSSB [Piro-Mégy *et al.,* 2020; Yang *et al.,* 1997; Venclovas *et al.,* 2004] show a tetramer of two dimers (dimer molA/ molB, and dimer molA'/molB', respectively, (**Figure 6A**). Each monomer is constituted by a b-barrel whose b-strands are connected by long b-hairpins and an a-helix. In the dimer, the two b-barrels are connected and form a long hydrophobic tunnel capped at either end by the a-helix of the corresponding monomer. At one side of the two connected b-barrels the strands form a continuous b-sheet that contacts the same b-sheet of the other dimer in the tetramer. The overall arrangement shows one pair of b-hairpins protruding from each dimer, whereas the other b-hairpins are on the plane of the two contacting b-sheets. Arg107 is precisely located at one edge of the flat b-sheet, at the interface between monomers in a dimer, and between the two dimers. In detail, the Arg107 guanidinium group interacts with the other monomer by i) N^{e} atom that contacts the Glu27carboxyl O2 from molB, and NH2 that contacts molB main chain carbonyl C=O of Arg28 (**Figure 6B**). A water molecule further stabilizes these contacts. With the second dimer, the contact occurs between Arg107 guanidinium group NH1 atom and the main chain C=O from molA' Phe139. In addition, the methylene groups of Arg107 side chain make van der Waals interactions with Arg38 from the same molecule, the guanidinium group of this latter further stabilized by carboxyl Oe2 from aforementioned molB Glu27. Remarkably, similar to Arg107, mutation at Arg38 is also associated to optic atrophy and foveopathy [Piro-Mégy *et al.,* 2020] . To know the potential regions of mtSSB contacted by the DNA, since no structure of human mtSSB in complex with DNA is available, we superposed the crystal structure of *E. coli* SSB protein bound to 2 poly-dC 35-mer [Raghunathan *et al.,* 2000] which, to the best of our knowledge, shows the largest ssDNA fragments bound to an SSB protein (**Figure 6A**). Remarkably, the 35-mer structure, which has a strong electronegative charge contributed principally by the phosphate backbone, covers a long electropositive patch that includes the region of Arg38 and Arg107 residues in mtSSB (**Figure 6C**), which substantiates a similar interaction of the ssDNA in both molecules. In addition, the change from Arg107 to Gln results in an electronegative spot that interrupts the electropositive patch, reducing the potential interaction sites (**Figure 6 C-E)**.

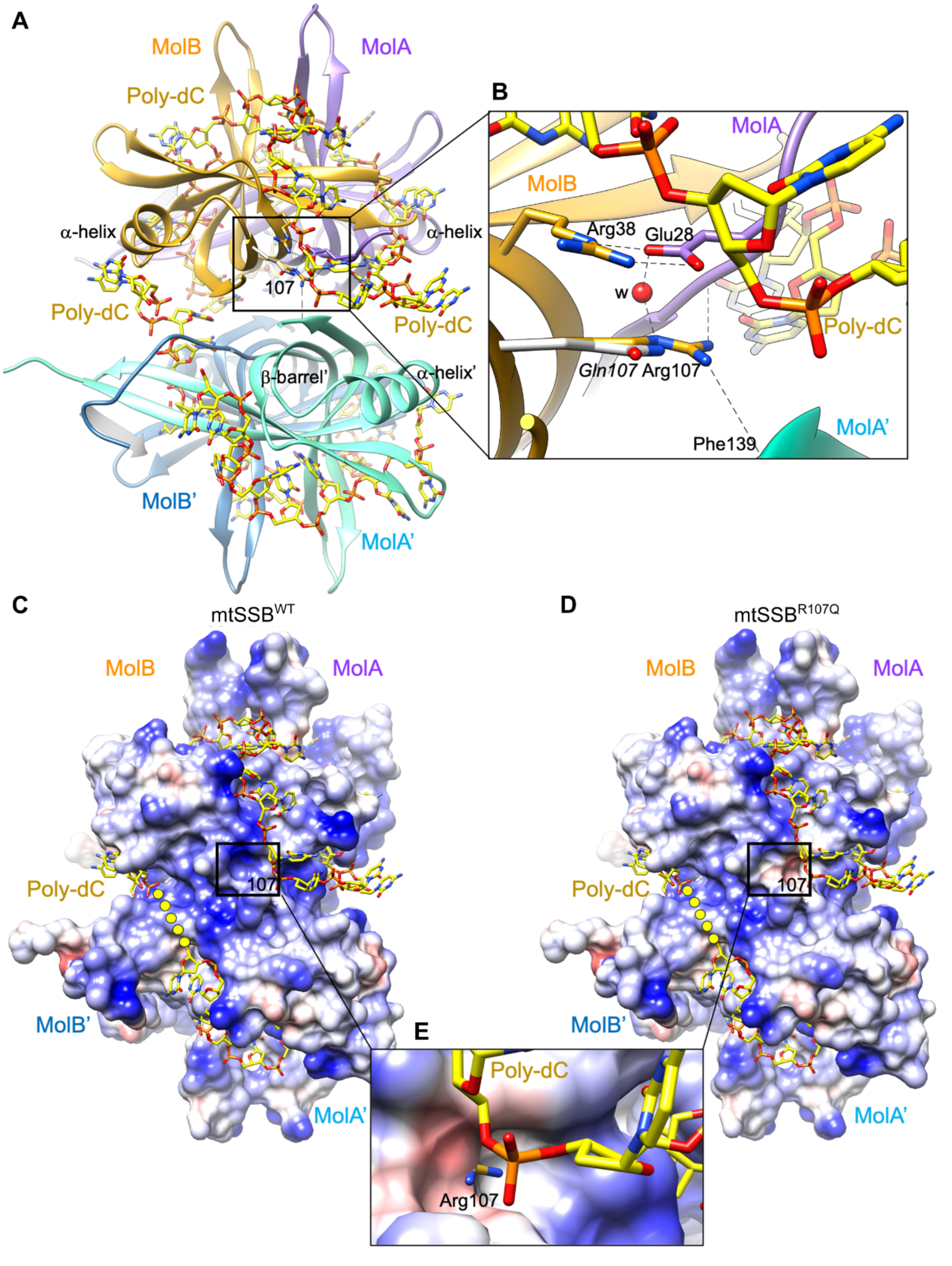

Figure 6. ***Analysis of the effects of the R107Q mutation on the structure of mtSSB****.* ***(A)*** *Two molecules MolA (colored in violet) and MolB (in gold) are related by a two-fold axis, forming a dimer that is related by crystallographic symmetry to a second dimer (MolB' and MolA', in light and dark blue, respectively), generating the physiological tetramer. By superposing the SSB protein from E.coli bound to a poly-dC 35-mer (PDB ID: 1EYG) onto the mtSSB structure (6RUP), the ssDNA fragments originally traced in SBP locate on the mitochondrial mtSSB tetramer, covering the region of Arg107 residue (framed). The b-barrel is indicated for MolA, and so is the a-helix for monomer MolA, MolB and MolA´.* ***(B)*** *Close-up view showing the interaction of Arg107 with surrounding residues, which include Arg38 from the same molecule (by van der Waals interactions between the*

methylene groups of respective side chains), Glu28 from MolA, and Phe139 amide from MolA'. A water molecule ("w" red sphere) stabilizes the interactions. The modelled R107Q mutation (Pyro-Mégy et al., 2020) shows that the Gln shorter side chain reduces two positive charges and adds a negative one. Side chains of residues are represented in the color of the own molecule, the nitrogen and oxygen atoms in blue and red, respectively. ***(C)*** *and* ***(D)*** *show the electrostatic potential represented on a Conolly surface (electronegative and positive potentials shown in red and blue, respectively) of the mtSSB^{WT} and modeled R107Q structures, respectively. The surface at position 107 is framed, and the connection between DNA fragments represented as yellow dots. Note that the positive electrostatic potential in the WT changes to negative potential in the mutant, near the ssDNA.* ***(E)*** *Close-up view of the R107Q electrostatic surface superposed to the WT structure. The surface around shorter Gln107 is electronegative and cannot allocate Arg107 positive side chain, whose positively charged tip protrudes.*

4. Discussion

The R107Q mutation has been identified as a pathogenic mutation in 2019 in two back-to-back studies [Piro-Mégy *et al*., 2020; Del Dotto *et al.,* 2020]. The mutation was shown to lead to a reduction of mtDNA content, a lower amount of 7S DNA, and a slower DNA repopulation after EtBr treatment. EMSA experiments also showed later that mtSSB^{R107Q} displayed decreased binding to a short 30-nt ssDNA fragment but a binding pattern similar to that seen with mtSSB^{WT} on a 100-nt ssDNA fragment [Jiang *et al.*, 2021]. Here we have determined Kd values on 30-nt and 60-nt templates using BLI and found very similar Kd for mtSSB^{WT} and mtSSB^{R107Q} ($Kd_{30\text{-nt}}$ = 1.17 nM and 1.18 nM and $Kd_{60\text{-nt}}$ = 2.2 nM and 1.4 nM for mtSSB^{WT} and mtSSB^{R107Q} , respectively). These values are very similar to the values found for mtSSB^{WT} using a 40-nt ssDNA and either fluorescence polarization methods (Kd = 1.8 ± 0.9 nM) [Kaur *et al*., 2018] (DREEM) or EMSA (Kd = 2.3 nM) [Ciesielski and Kaguni, 2015]. However, studies on short templates are limited to the interactions on DNA of one or a few proteins. We thus moved to longer, more biologically-relevant DNA lengths to better understand mtSSB binding dynamics.

It was shown that, depending on the mtSSB and salt concentrations, there are two binding modes for mtSSB to ssDNA, namely a wrapping mode and a binding mode [Lohman *et al.,* 1985; Lohman *et al,*. 1988, Qian and Johnson, 2017, Naufer *et al.,* 2021]. These modes have their own rates and footprints: the footprint in the binding mode is 30 bp while the footprint in the wrapping mode is 60 bp [Qian and Johnson, 2017]. Our dissociation experiments revealed that mtSSB binding to ssDNA can indeed be modeled by a generic two state binding model SSB + ssDNA←SSB.ssDNA(bound)← SSB.ssDNA(WRAPPED). The wrapping and binding states have their own rate constants, and the hypothesis is that dissociation of mtSSB from ssDNA occurs only from the bound state. The addition of salt modulates the transition of mtSSB from the wrapped state to the bound state from which the mtSSB may dissociate from the ssDNA. Using this simple model we found that there are initially an average of about 350 WT molecules bound per ssDNA molecule, of which 26% are in the binding mode and 74% in the wrapping mode (corresponding to 25 and 70 tetramers, respectively). Taking the footprint of a SSB tetramer in the binding mode of 30 bp and in the wrapping mode 60 bp [Qian and Johnson, 2017], this suggests that only about 10% of the 16 µm ssDNA is coated by the mtSSB^{WT}. Instead we found that around 2200 mtSSB^{R107Q} molecules are on the ssDNA in the dissociation experiments, and half of these are in the binding state while the other half is in the wrapping state. Therefore, there are about 275 mtSSB^{R107Q} tetramers in the wrapping state, while for mtSSB^{WT} there are only about 70 tetramers in the wrapping state, and yet the compaction of the ssDNA is more important for mtSSB^{WT} . This could suggest that the apparent footprint of mtSSB^{R107Q} is smaller than the footprint of mtSSB^{WT}. We suggest that, in fact, this lower apparent footprint of mtSSB^{R107Q} is more likely related to a more transient wrapping state, as indicated by the 3-fold larger unwrapping rate calculated for mtSSB^{R107Q} and by the force experiments, as we will discuss later. We therefore considered the same footprints for mtSSB^{R107Q} and mtSSB^{WT}, which yielded a coverage of about 50 % of the ssDNA for mtSSB^{R107Q}. This higher coverage of the ssDNA was also qualitatively observed in the compaction experiments where the ssDNA-mtSSB^{R107Q} complexes had a higher intensity than those with mtSSB^{WT}.

The question is then, in the same experimental conditions, to what degree can human mtSSB compact ssDNA? To address this we first used Syber II and showed that, in our experimental flow-stretch conditions, lambda ssDNA (16 µm) is stretched to 8.5 µm corresponding to ~53 % of its full length. For ssDNA coated with mtSSB the length of the nucleoprotein complex reduced to 2.56 µm for mtSSB^{WT} and 4.14 µm for mtSSB^{R107Q}, corresponding to 70% and

50%, respectively, of the length of bare ssDNA under the same experimental conditions. This demonstrates that, in the absence of salt, even though the protein coverage is higher for mtSSB^{R107Q}, the compaction ability of mtSSB^{R107Q} is significantly reduced compared to mtSSB^{WT}. The addition of salt induced a further compaction (β) of ~80% for high salt and 62% for low salt for both mtSSB^{WT} and mtSSB^{R107Q}. This corresponds for mtSSB^{WT} -coated-ssDNA to a salt dependent compaction of dL~1.59 µm, resulting in a final length Lf~0.97 µm at 100 mM salt. At higher salt (400 mM), the compaction increased to dL~2 µm and the final length decreased to Lf~0.56 µm. For mtSSB^{R107Q}-coated-ssDNA the salt dependent compaction is dL~2.57 µm resulting in a Lf~1.57 µm at 100 mM salt, and dL~3.3 µm resulting in a Lf~0.85 µm at 400 mM salt. Thus, even though the final length of mtSSB^{R107Q}-coated-ssDNA is larger than the length of mtSSB^{WT}-coated-ssDNA, the salt dependant length-change dL is larger for mtSSB^{R107Q} than for mtSSB^{WT}. This could be explained by the fact that there are more tetramers in the bound state that could transfer to the wrapped state. In the fluorescence compaction experiments we do not have the resolution to accurately determine the number of mtSSB molecules on the ssDNA. However, as the initial experimental conditions in the compaction experiments were similar to those in the dissociation experiments, we thus assumed that the initial number of tetramers in the two binding modes are similar in the compaction and dissociation experiments. In the dissociation experiments we find that for the mtSSB^{WT} there are only 25 tetramers that can go from the bound to the wrapped state, while for mtSSB^{R107Q} 275 tetramers can undergo this transition. If the salt dependent compaction would be due to the 25 mtSSB^{WT} tetramers that go from the binding states to the wrapping state, this would result in a theoretical decrease of the length of the ssDNA; dL_th= 25* (60-30)*0.3 e-9 ~0.23 µm. This is clearly not enough to explain the experimentally measured dL, which suggests that there is an additional mechanism that enhances the compaction of ssDNA by mtSSB^{WT}. We can not rule out the effect of secondary structures that may form in the regions of the nucleoprotein complex not covered by mtSSB^{WT}. Indeed, the sparser coating of ssDNA by mtSSB^{WT} may result in a more important contribution of secondary structure formation than for the more densely covered mtSSB^{R107Q}-ssDNA. Nevertheless, we note that condensation of nucleoprotein complexes larger than expected based on a simple wrapping transition was also observed in EcSSB-ssDNA [Bell *et al.,* 2015]. The authors proposed that EcSSB engages in long-range reversible intramolecular interactions via the formation of EcSSB octamers, which may bridge different sites on the ssDNA resulting in enhanced condensation of the EcSSB-ssDNA complexes. For mtSSB^{R107Q}, considering that 275 tetramers could go from the binding to the wrapping state, the theoretical maximum length change dL_th= 275* (60-30)*0.3 e-9 ~2.5 µm, which is close to the measured compaction. We thus do not observe the same enhanced wrapping as observed for the mtSSB^{WT}, which would suggest that mtSSB^{R107Q} may miss the cooperative mechanism between tetramers to form octamers.

The remaining question is then how it is possible that the R107Q mutation reduces ssDNA compaction, even though the coverage of ssDNA by mtSSB^{R107Q} is higher than for mtSSB^{WT}? We suspect that this is due to a reduced ssDNA wrapping efficiency of mtSSB^{R107Q}. In the compaction assays, for a given salt concentration, we found that the wrapping rate (k) is almost a factor 2 higher for mtSSB^{WT} than for mtSSB^{R107Q}. At intermediate salt concentration (100 mM), the dissociation rates (k(-b)) are similar for mtSSB^{WT} and mtSSB^{R107Q}, therefore, the apparent faster wrapping rate should be only related to the wrapping state and not to a possible mtSSB dissociation from the ssDNA. Moreover, the rates (k(-w)) measured in the dissociation experiments are 3 times higher for the mtSSB^{R107Q} than for mtSSB^{WT}. These results suggest the mutation R107Q mainly affects the wrapping state, resulting in a less efficient and less stable wrapping of ssDNA by mtSSB^{R107Q} than by mtSSB^{WT}.

Our competition assays showed that at a 1:1 ratio of mtSSB^{WT}: mtSSB^{R107Q}, about 76 % of the ssDNA is co-covered by mtSSB^{WT} and mtSSB^{R107Q} and about 24 % is exclusively covered by mtSSB^{WT}. At this ratio, 73 % of the mtSSB on the co-covered ssDNA is mtSSB^{WT} and 27 % is mtSSB^{R107Q}. If we extrapolate to an *in vivo* situation, this would imply that for a heterozygous patient, ssDNA should be predominantly interacting with mtSSB^{WT}. Only when there is a 10-fold excess of mtSSB^{R107Q} the large majority of the ssDNA is co-covered with 90 % mtSSB^{R107Q} and 10 % mtSSB^{WT}. There should thus exist a sharp threshold above which mtSSB^{R107Q} becomes dominant. However, it is also

possible that, *in vivo*, heterotetramers containing WT and mutated subunits are formed, leading to the dominant negative effect observed in patients. We also showed that in the absence of salt mtSSB^{R107Q} does not dissociate much from the ssDNA and mtSSB^{WT} appears not to be able to bind. This would suggest that the ssDNA is completely covered by mtSSB^{R107Q}. However, the total number of mtSSB^{R107Q} molecules (~2200) corresponds to a ssDNA coverage of about 50 %, which implies that there should be 50 % of free ssDNA for mtSSB^{WT} to bind to. The observation that no mtSSB^{WT} can bind may indicate that the free ssDNA is divided into small stretches between neighboring mtSSB^{R107Q} molecules and that those stretches are too small for the footprint of mtSSB^{WT} (~60 bp). In the presence of salt, mtSSB^{R107Q} dissociates rapidly from the ssDNA making space for mtSSB^{WT} to attach to ssDNA. On the contrary, ssDNA preincubated with mtSSB^{WT} is more stable, and the addition of salt does not induce the dissociation of the mtSSB^{WT}. Even though these nucleoprotein complexes are not saturated, the mtSSB^{R107Q} can not stably bind under the high salt conditions.

Force spectroscopy is a powerful tool to study the mechanical properties of polymers, such as DNA, and the interactions and binding forces with other molecules, such as proteins. Here we used AFS, and we fitted the obtained force-distance curves with the eFJC model. This model can be applied to our data, as the DNA remains flexible between bound mtSSB molecules [Cashen *et al.,* 2023], and allowed us to retrieve the changes in contour length Lc and persistence length Lp after adding mtSSB to bare ssDNA (**Figure 3A**). Binding of mtSSB^{WT} to ssDNA significantly reduced the Lc at low forces, indicating shortening of the DNA molecules through compaction, probably involving the wrapping mode of mtSSB. These results are in line with Kaur et al., where a shortening of the Lc of DNA was observed in presence of mtSSB, that was attributed to DNA wrapping around human mtSSB [Kaur et al., 2018]. This reduction was less striking after addition of mtSSB^{R107Q}, confirming the alteration of DNA compaction ability, also seen with single-molecule fluorescence microscopy. For the persistence length Lp, we obtained a value of 1.9 nm for bare ssDNA in presence of 100 mM salt, which is consistent with the literature (1.3 nm for Tinland *et al.* [Tinland *et al.,* 1997] and 2.5 nm for Murphy et *al.* [Murphy *et al.,* 2004], at the same salt concentration). mtSSB^{WT}-binding increased the Lp ~5 times, to 9.3 nm, indicating that protein-binding strongly decreases the flexibility of the ssDNA. However, the Lp value after addition of mtSSB^{R107Q} is only slightly increased compared to the Lp value of bare ssDNA, to 3.3 nm. The persistence length is directly linked to the Kuhn length, which corresponds to the length of the inflexible segment of the polymer chain. In the case of bare ssDNA, this inflexible subunit is the nucleotide, while after binding of mtSSB, it is the footprint of the protein. The significantly lower Lp value for mtSSB^{R107Q} compared to mtSSB^{WT} indicates a smaller apparent footprint of the mutated protein, which can be explained by a less stable wrapping state for mtSSB^{R107Q} , as we discussed previously.

For the Lc and Lp estimations, we used the force-retraction curves rather than the force-extension curves, as ssDNA can bind non-specifically to the flow-cell at very low forces. We did not observe the formation of important ssDNA secondary structures, which would be indicated by hysteresis between the force-extension and the force-retraction curves of the bare ssDNA, as reported before. For example, in the paper from Bell *et al*, this hysteresis event was seen already for a salt concentration above 25-50 mM [Bell *et al.,* 2015]. However, their ssDNA template is different and approximately twice longer as ours, which might give more possibilities for secondary structure formation. Former work also showed that SSB-binding had an impact on secondary structure formation or removal. The T7 SSB gp2.5 was for example not able to resolve pre-formed secondary structures, but it could bind slightly stretched ssDNA and prevent the formation of hairpins that would otherwise appear when decreasing the force [Xu *et al.,* 2023]. As for *Ec*SSB, hysteresis observed between the force-extension and the force-retraction curves for bare ssDNA in presence of salt was absent after adding the protein, which suggests that *Ec*SSB removes and prevents secondary structures [Bell *et al.,* 2015]. In our setup, it was not possible to assess the effect of mtSSB^{WT} and mtSSB^{R107Q} on hairpin formation, as bare ssDNA was not forming such secondary structures, but it would have been interesting to see how the mutant protein compared to the WT.

Additionally, we investigated the force-dependent stability of the mtSSB-ssDNA bound. It was previously shown that *Ec*SSB wrapping state is destabilized at high forces (20 pN) while unwrapped binding modes are favored, since

they do not require the ssDNA to bend and adopt specific conformations as for wrapping [Naufer *et al.* 2021]. Thus, ssDNA compaction is limited at high forces, but increases when the force is lowered. mtSSB presents the same behavior, and the force at which ssDNA starts to unwrap can be deducted from the force-distance curves, by applying cycles of stretch-relax with increasing forces to the ssDNA-protein complexes [Morin *et al.,* 2017]. Indeed, at low forces, the force-distance curves are reversible, but above a threshold corresponding to the minimum force triggering the overall unwrapping, hysteresis between the force-extension and the force-retraction curves is observed. These hysteresis events represent unwrapping and re-wrapping of the mtSSB tetramers, as the tetramers in the wrapped state are rather stables, while ssDNA shortening by mtSSB-wrapping necessitates DNA to be flexible and bend, and can therefore only happen at lower forces. With this method, we started seeing hysteresis at forces of 6-7 pN for both mtSSB^{WT} and mtSSB^{R107Q}, which is consistent with the results of Morin *et al.*, who found an unwrapping force of 8 pN using optical tweezers, for a [mtSSB]/[NaCl] ratio of 1.10^6 as in our experimental conditions [Morin *et al.,* 2017]. The authors were also able to extract the minimum force that begins to promote protein detachment, which is the force above which the force-extension curves of two consecutive ramps do not overlap anymore, and they found a value of ~13 pN for mtSSB^{WT}. In another study using T7 SSB gp2.5 and optical tweezers combined with confocal fluorescence microscopy, the SSB molecules started detaching at 20 pN in the extension phase, with only half of the coverage remaining at 35 pN [Xu *et al.,* 2023]. In our experiment, we observed unbinding of mtSSB^{R107Q} at forces as low as 6-7 pN, when we start seeing unwrapping, suggesting that a part of the unwrapped mtSSB molecules then fall off the ssDNA, and confirming that the ssDNA-mtSSB^{R107Q} bound is rather unstable. We were not able to detect force disassembly for mtSSB^{WT}, but our AFS setup did not allow us to apply forces higher than 20-25 pN, as the bound between anti-digoxigenin and its ligand is probably not strong enough to maintain the ssDNA molecules tethered to the surface [Neuert *et al.,* 2006].

R107Q patient fibroblasts exhibit an important mtDNA depletion, suggesting a defect in mtDNA replication processes [Del Dotto *et al.,* 2020; Piro-Mégy *et al.,* 2020]. This was confirmed by *in vitro* assays, which revealed that while the mutation does not impact mtDNA replication elongation, it impairs mtDNA replication initiation [Jiang *et al.,* 2021]. Single-molecule experiments have shown that during mtDNA synthesis, the low site-size binding mode of mtSSB is favored at the replication fork [Morin *et al.,* 2017]. As our results indicate that mtSSB low binding mode is seemingly little affected by the R107Q mutation, this is thus consistent that mtDNA replication elongation is not affected in patients. On the contrary, mtSSB^{R107Q} ssDNA complexes in the wrapped mode are unstable, which may suggest a role for this binding mode in mtDNA replication initiation.

One hypothesis that has been proposed previously to explain the role of mtSSB disease-causing mutations is a lower stability of the tetramer. Previous *in-silico* modeling analysis of mtSSB^{R107Q} showed that shortening the side chain from Arg to Gln results in loss of the intra and inter dimer contacts that, considering these interactions occur in the four subunits, could lead to tetramer destabilization [Piro-Mégy *et al.,* 2020]. However, using mass photometry, we observed that mtSSB^{WT} and mtSSB^{R107Q} were present in solution only in the tetramer form. Similarly, Gustafson [Gustafson *et al.,* 2021] using molecular dynamics simulation predicted a very stable tetrameric structure for mtSSB^{R107Q}. The superposition of the ssDNA from *Ec*SSB structure strongly suggests that the DNA locates right above Arg107 and also very close to Arg38, a mutation also involved in mitochondrial disease. Our structural model suggests that R107Q induces a change in the electrostatics precisely at this region, from positive to negative, plausibly creating a surface less prone to interact with the DNA, which could slow the transition to a stable, wrapped state. Overall, our results suggest that the R107Q mutation does not destabilize the formation of tetramers but instead affect the stable binding of mtSSB to ssDNA in a wrapped state, leading to a faster dissociation and a lower compaction ability. This is consistent with the phenotype observed in patients, where the mutation does not drastically compromise mtDNA maintenance but rather leads to adult-onset optic myopathy.

Funding statement: This work was supported by the Association Française Contre les Myopathies Téléthon [grant numbers 24167 (GF) and xxx (AM);

Conflict of interest: The authors declare no conflict of interest. The funders had no role in the design of the study; in the collection, analyses, or interpretation of data; in the writing of the manuscript; or in the decision to publish the results.

Acknowledgements: We thank Bertrand Raynal of Plateforme de Biophysique Moléculaire of Institut Pasteur C2RT for mass photometry measurements, Eugen Ostrofet (Lumicks) for his help with the AFS setup and Adèle Porcan for technical help.

References

Antony, E., & Lohman, T. M. (2019, February). Dynamics of E. coli single stranded DNA binding (SSB) protein-DNA complexes. In *Seminars in cell & developmental biology* (Vol. 86, pp. 102-111). Academic Press.

Antony, E., Weiland, E. A., Korolev, S., & Lohman, T. M. (2012). Plasmodium falciparum SSB tetramer wraps single-stranded DNA with similar topology but opposite polarity to E. coli SSB. *Journal of molecular biology*, *420*(4-5), 269-283.

Bell, J. C., Liu, B., & Kowalczykowski, S. C. (2015). Imaging and energetics of single SSB-ssDNA molecules reveal intramolecular condensation and insight into RecOR function. *Elife*, *4*, e08646.

Bhattacharyya, B., George, N. P., Thurmes, T. M., Zhou, R., Jani, N., Wessel, S. R., ... & Keck, J. L. (2014). Structural mechanisms of PriA-mediated DNA replication restart. *Proceedings of the National Academy of Sciences*, *111*(4), 1373-1378.

Cashen, B. A., Morse, M., Rouzina, I., Karpel, R. L., & Williams, M. C. (2023). Dynamic structure of T4 gene 32 protein filaments facilitates rapid noncooperative protein dissociation. *Nucleic Acids Research*, *51*(16), 8587-8605.

Ciesielski, G. L., Bermek, O., Rosado-Ruiz, F. A., Hovde, S. L., Neitzke, O. J., Griffith, J. D., & Kaguni, L. S. (2015). Mitochondrial single-stranded DNA-binding proteins stimulate the activity of DNA polymerase γ by organization of the template DNA. *Journal of Biological Chemistry*, *290*(48), 28697-28707.

Ciesielski, G. L., Kim, S., de Bovi Pontes, C., & Kaguni, L. S. (2021). Physical and functional interaction of mitochondrial single-stranded DNA-binding protein and the catalytic subunit of DNA polymerase gamma. *Frontiers in Genetics*, *12*, 721864.

Curth, U., Urbanke, C., Greipel, J., Gerberding, H., Tiranti, V., & Zeviani, M. (1994). Single‐stranded‐DNA‐binding proteins from human mitochondria and Escherichia coli have analogous physicochemical properties. *European journal of biochemistry*, *221*(1), 435-443.

Del Dotto, V., Ullah, F., Di Meo, I., Magini, P., Gusic, M., Maresca, A., ... & Carelli, V. (2020). SSBP1 mutations cause mtDNA depletion underlying a complex optic atrophy disorder. *The Journal of clinical investigation*, *130*(1), 108-125.

Farr, C. L., Matsushima, Y., Lagina, A. T., Luo, N., & Kaguni, L. S. (2004). Physiological and biochemical defects in functional interactions of mitochondrial DNA polymerase and DNA-binding mutants of single-stranded DNA-binding protein. *Journal of Biological Chemistry*, *279*(17), 17047-17053.

Griffith, J. D., Harris, L. D., & Register, J. I. I. I. (1984, January). Visualization of SSB-ssDNA complexes active in the assembly of stable RecA-DNA filaments. In *Cold Spring Harbor Symposia on Quantitative Biology* (Vol. 49, pp. 553-559). Cold Spring Harbor Laboratory Press.

Gustafson, M. A., McCormick, E. M., Perera, L., Longley, M. J., Bai, R., Kong, J., ... & Falk, M. J. (2019). Mitochondrial single-stranded DNA binding protein novel de novo SSBP1 mutation in a child with single large-scale mtDNA deletion (SLSMD) clinically manifesting as Pearson, Kearns-Sayre, and Leigh syndromes. *PLoS One*, *14*(9), e0221829.

Gustafson, M. A., Perera, L., Shi, M., & Copeland, W. C. (2021). Mechanisms of SSBP1 variants in mitochondrial disease: Molecular dynamics simulations reveal stable tetramers with altered DNA binding surfaces. *DNA repair*, *107*, 103212.

Hamon, L., Pastre, D., Dupaigne, P., Breton, C. L., Cam, E. L., & Pietrement, O. (2007). High-resolution AFM imaging of single-stranded DNA-binding (SSB) protein—DNA complexes. *Nucleic acids research*, *35*(8), e58.

Jiang, M., Xie, X., Zhu, X., Jiang, S., Milenkovic, D., Misic, J., ... & Falkenberg, M. (2021). The mitochondrial single-stranded DNA binding protein is essential for initiation of mtDNA replication. *Science Advances*, *7*(27), eabf8631

Jurkute, N., D'Esposito, F., Robson, A. G., Pitceathly, R. D., Cordeiro, F., Raymond, F. L., ... & Genomics England Research Consortium. (2021). SSBP1-disease update: expanding the genetic and clinical spectrum, reporting variable penetrance and confirming recessive inheritance. *Investigative ophthalmology & visual science*, *62*(15), 12-12.

Jurkute, N., Leu, C., Pogoda, H. M., Arno, G., Robson, A. G., Nürnberg, G., ... & Votruba, M. (2019). SSBP1 mutations in dominant optic atrophy with variable retinal degeneration. *Annals of neurology*, *86*(3), 368-383.

Kaur, P., Longley, M. J., Pan, H., Wang, H., & Copeland, W. C. (2018). Single-molecule DREEM imaging reveals DNA wrapping around human mitochondrial single-stranded DNA binding protein. *Nucleic Acids Research*, *46*(21), 11287-11302.

Korhonen, J. A., Gaspari, M., & Falkenberg, M. (2003). TWINKLE has 5′→ 3′ DNA helicase activity and is specifically stimulated by mitochondrial single-stranded DNA-binding protein. *Journal of Biological Chemistry*, *278*(49), 48627-48632.

Korhonen, J. A., Pham, X. H., Pellegrini, M., & Falkenberg, M. (2004). Reconstitution of a minimal mtDNA replisome in vitro. *The EMBO journal*, *23*(12), 2423-2429.

Lee, K. S., Marciel, A. B., Kozlov, A. G., Schroeder, C. M., Lohman, T. M., & Ha, T. (2014). Ultrafast redistribution of E. coli SSB along long single-stranded DNA via intersegment transfer. *Journal of molecular biology*, *426*(13), 2413-2421.

Loeff, L., Kerssemakers, J. W., Joo, C., & Dekker, C. (2021). AutoStepfinder: A fast and automated step detection method for single-molecule analysis. *Patterns*, *2*(5).

Lohman, T. M., & Bujalowski, W. (1988). Negative cooperativity within individual tetramers of Escherichia coli single strand binding protein is responsible for the transition between the (SSB) 35 and (SSB) 56 DNA binding modes. *Biochemistry*, *27*(7), 2260-2265.

Lohman, T. M., & Overman, L. B. (1985). Two binding modes in Escherichia coli single strand binding protein-single stranded DNA complexes. Modulation by NaCl concentration. *Journal of Biological Chemistry*, *260*(6), 3594-3603.

Martucci, M., Debar, L., van den Wildenberg, S., & Farge, G. (2023). How to Quantify DNA Compaction by TFAM with Acoustic Force Spectroscopy and Total Internal Reflection Fluorescence Microscopy. In Mitochondrial DNA: Methods and Protocols (pp. 121-137). New York, NY: Springer US.

Mills, M., Harami, G. M., Seol, Y., Gyimesi, M., Martina, M., Kovács, Z. J., ... & Neuman, K. C. (2017). RecQ helicase triggers a binding mode change in the SSB–DNA complex to efficiently initiate DNA unwinding. *Nucleic acids research*, *45*(20), 11878-11890.

Miralles Fusté, J., Shi, Y., Wanrooij, S., Zhu, X., Jemt, E., Persson, Ö., ... & Falkenberg, M. (2014). In vivo occupancy of mitochondrial single-stranded DNA binding protein supports the strand displacement mode of DNA replication. *PLoS genetics*, *10*(12), e1004832.

Morin, J. A., Cerron, F., Jarillo, J., Beltran-Heredia, E., Ciesielski, G. L., Arias-Gonzalez, J. R., ... & Ibarra, B. (2017). DNA synthesis determines the binding mode of the human mitochondrial single-stranded DNA-binding protein. *Nucleic acids research*, *45*(12), 7237-7248.

Murphy, M. C., Rasnik, I., Cheng, W., Lohman, T. M., & Ha, T. (2004). Probing single-stranded DNA conformational flexibility using fluorescence spectroscopy. *Biophysical journal*, *86*(4), 2530-2537.

Naufer, M. N., Morse, M., Möller, G. B., McIsaac, J., Rouzina, I., Beuning, P. J., & Williams, M. C. (2021). Multiprotein E. coli SSB–ssDNA complex shows both stable binding and rapid dissociation due to interprotein interactions. *Nucleic acids research*, *49*(3), 1532-1549.

Neuert, G., Albrecht, C., Pamir, E., & Gaub, H. E. (2006). Dynamic force spectroscopy of the digoxigenin–antibody complex. *FEBS letters*, *580*(2), 505-509.

Piro-Mégy, C., Sarzi, E., Tarrés-Solé, A., Péquignot, M., Hensen, F., Quilès, M., ... & Delettre, C. (2020). Dominant mutations in mtDNA maintenance gene SSBP1 cause optic atrophy and foveopathy. *The Journal of clinical investigation*, *130*(1), 143-156.

Plaza-GA, I., Lemishko, K. M., Crespo, R., Truong, T. Q., Kaguni, L. S., Cao-García, F. J., ... & Ibarra, B. (2023). Mechanism of strand displacement DNA synthesis by the coordinated activities of human mitochondrial DNA polymerase and SSB. *Nucleic Acids Research*, *51*(4), 1750-1765.

Qian, Y., & Johnson, K. A. (2017). The human mitochondrial single-stranded DNA-binding protein displays distinct kinetics and thermodynamics of DNA binding and exchange. *Journal of Biological Chemistry*, *292*(31), 13068-13084.

Raghunathan, S., Kozlov, A. G., Lohman, T. M., & Waksman, G. (2000). Structure of the DNA binding domain of E. coli SSB bound to ssDNA. *Nature structural biology*, *7*(8), 648-652.

Raghunathan, S., Ricard, C. S., Lohman, T. M., & Waksman, G. (1997). Crystal structure of the homo-tetrameric DNA binding domain of Escherichia coli single-stranded DNA-binding protein determined by multiwavelength x-ray diffraction on the selenomethionyl protein at 2.9-Å resolution. *Proceedings of the National Academy of Sciences*, *94*(13), 6652-6657.

Roy, R., Kozlov, A. G., Lohman, T. M., & Ha, T. (2009). SSB protein diffusion on single-stranded DNA stimulates RecA filament formation. *Nature*, *461*(7267), 1092-1097.

Suksombat, S., Khafizov, R., Kozlov, A. G., Lohman, T. M., & Chemla, Y. R. (2015). Structural dynamics of E. coli single-stranded DNA binding protein reveal DNA wrapping and unwrapping pathways. *elife*, *4*, e08193.

Tinland, B., Pluen, A., Sturm, J., & Weill, G. (1997). Persistence length of single-stranded DNA. *Macromolecules*, *30*(19), 5763-5765.

Venclovas, Č., Ginalski, K., & Kang, C. (2004). Sequence‐structure mapping errors in the PDB: OB‐fold domains. *Protein science*, *13*(6), 1594-1602.

Wessel, S. R., Marceau, A. H., Massoni, S. C., Zhou, R., Ha, T., Sandler, S. J., & Keck, J. L. (2013). PriC-mediated DNA replication restart requires PriC complex formation with the single-stranded DNA-binding protein. *Journal of Biological Chemistry*, *288*(24), 17569-17578.

Williams, A. J., & Kaguni, L. S. (1995). Stimulation of Drosophila Mitochondrial DNA Polymerase by Single-stranded DNA-binding Protein (∗). *Journal of Biological Chemistry*, *270*(2), 860-865.

Wu, Y., Lu, J., & Kang, T. (2016). Human single-stranded DNA binding proteins: guardians of genome stability. *Acta biochimica et biophysica Sinica*, *48*(7), 671-677.

Xu, L., Cabanas-Danés, J., Halma, M. T., Heller, I., Stratmann, S. A., van Oijen, A. M., Lee, S-J., Peterman, E. J. G., & Wuite, G. J. L. (2023). Regulation of T7 gp2. 5 binding dynamics by its C-terminal tail, template conformation and sequence. *Nucleic Acids Research*, gkad485.

Yang, C., Curth, U., Urbanke, C., & Kang, C. (1997). Crystal structure of human mitochondrial single-stranded DNA binding protein at 2.4 Å resolution. *Nature structural biology*, *4*(2), 153-157.

Zhou, R., Kozlov, A. G., Roy, R., Zhang, J., Korolev, S., Lohman, T. M., & Ha, T. (2011). SSB functions as a sliding platform that migrates on DNA via reptation. *Cell*, *146*(2), 222-232.

Supplementary figures

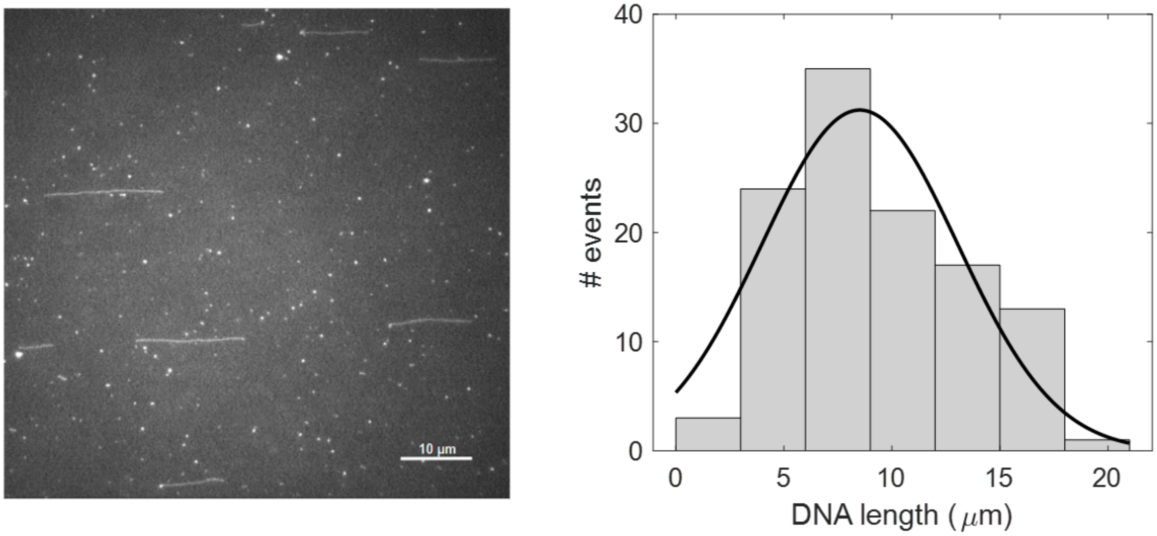

Figure S1 : Determination of ssDNA molecules length under our flow conditions using SYBR Green II staining. (A) Typical image of a field of view showing several ssDNA molecules stained with SYBR Green II and stretched under a constant flow. (B) Distribution of ssDNA lengths. A Gaussian fit to the histogram yielded an average length of ~8.5 µm (n=115).

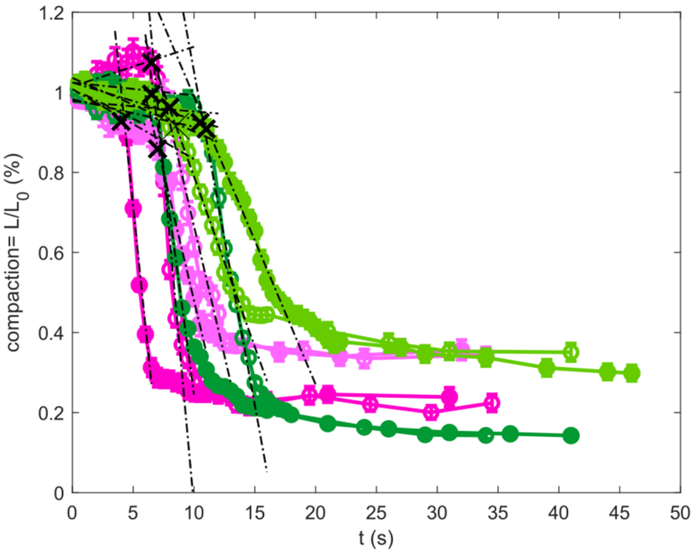

Figure S2 : Determination of t0*. The time at which the salt begins to have an effect t0* is marked with a cross and is inferred from the intercept of a linear fit to the first (constant) part and a second linear fit to the first five points of the fast decaying part of the normalized compaction curve (dark green: WT at 400 mM salt, light green: WT at 100 mM salt, dark pink: R107Q at 400 mM salt, light pink: R107Q at 100 mM salt). Open and closed symbols of the same color represent 2 biological replicates.

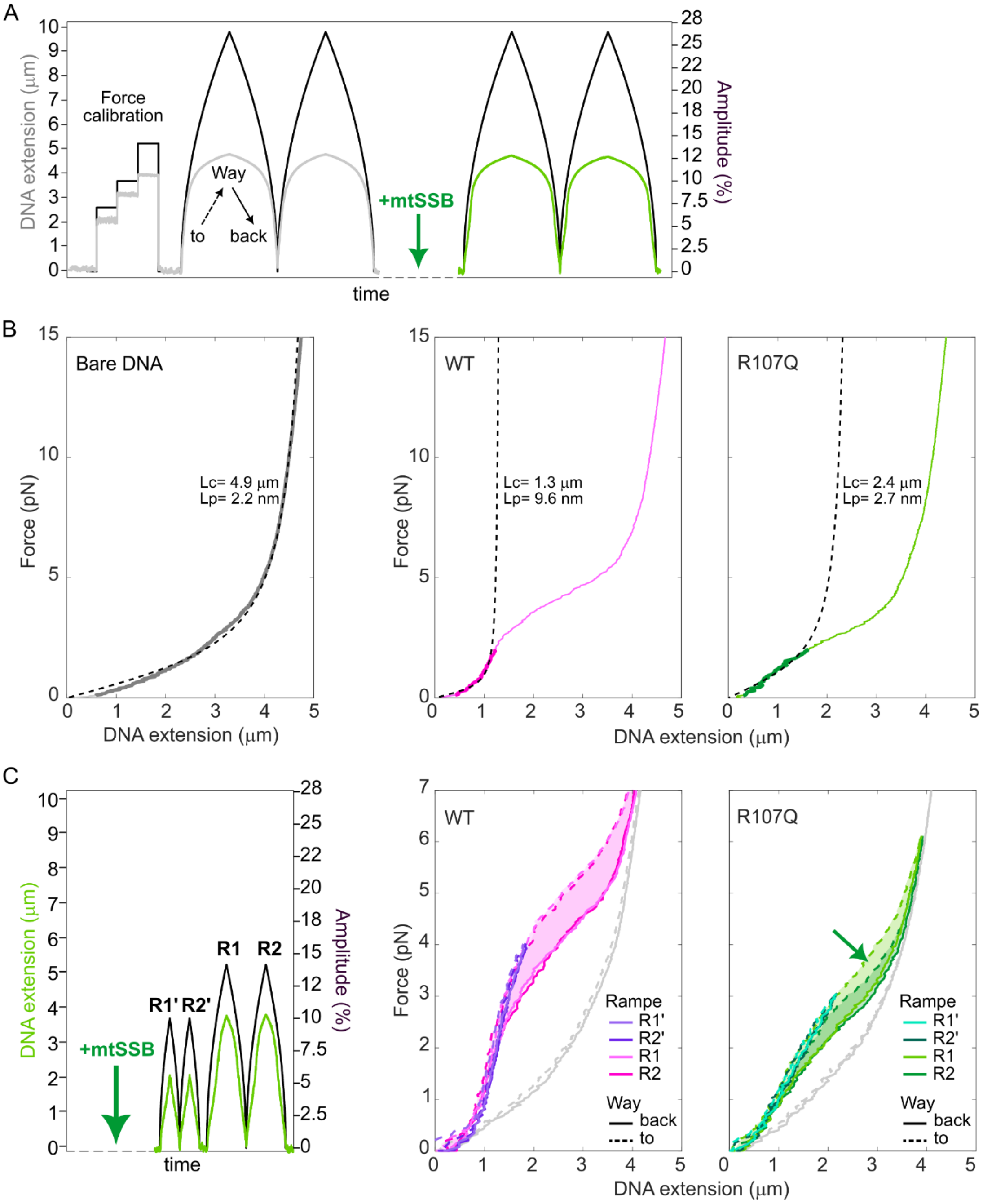

Figure S3: The R107Q mutation alters the ssDNA-binding properties of mtSSB. (A) Schematic of a typical AFS experiment. Following force calibration on bare ssDNA, force stretching (way to) and relaxation (way back) of the bare DNA is performed using two successive identical force ramps. The force ramps are then repeated after addition of the mtSSB protein. **(B)** Experimental force-retraction curves (from the second ramps in (A)) of bare ssDNA (gray), or ssDNA coated with mtSSB WT (magenta) or R107Q (green), and corresponding fits to the eFJC model (black dashed lines) in order to estimate the Lc and Lp parameters. Fitting range for bare DNA curve: 0.1-15 pN and for mtSSB-coated DNA: 0.1-2 pN. **(C)** A schematic of the force-dependence AFS experiment is shown on the left. After addition of the mtSSB protein, successive force ramps with low amplitudes are applied, first with 3-4 pN (R'1 and R'2) and then with 6-7 pN (R1 and R2). The corresponding force-distance extension (dashed lines) and retraction (solid lines) curves are shown on the right for two representative DNA tethers coated with mtSSB WT or mutant.

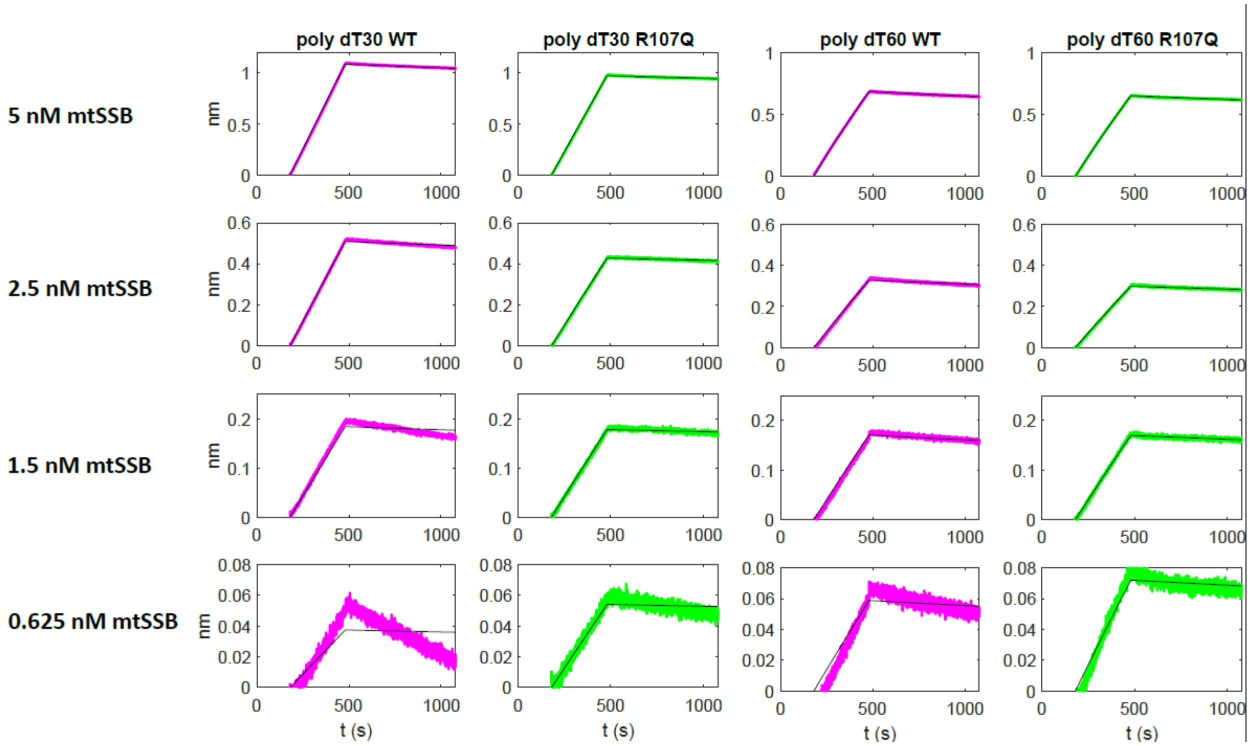

Figure S4 : The affinity of WT and R107Q for ssDNA assessed by biolayer interferometry. Two ssDNA (polydT30 and polydT) and four different SSB concentrations ((0.625 nM, 1.5 nM, 2.5 nM and 5 nM) were used. The raw binding traces (green and magenta) were fitted with a 1:1 binding model (black curve).

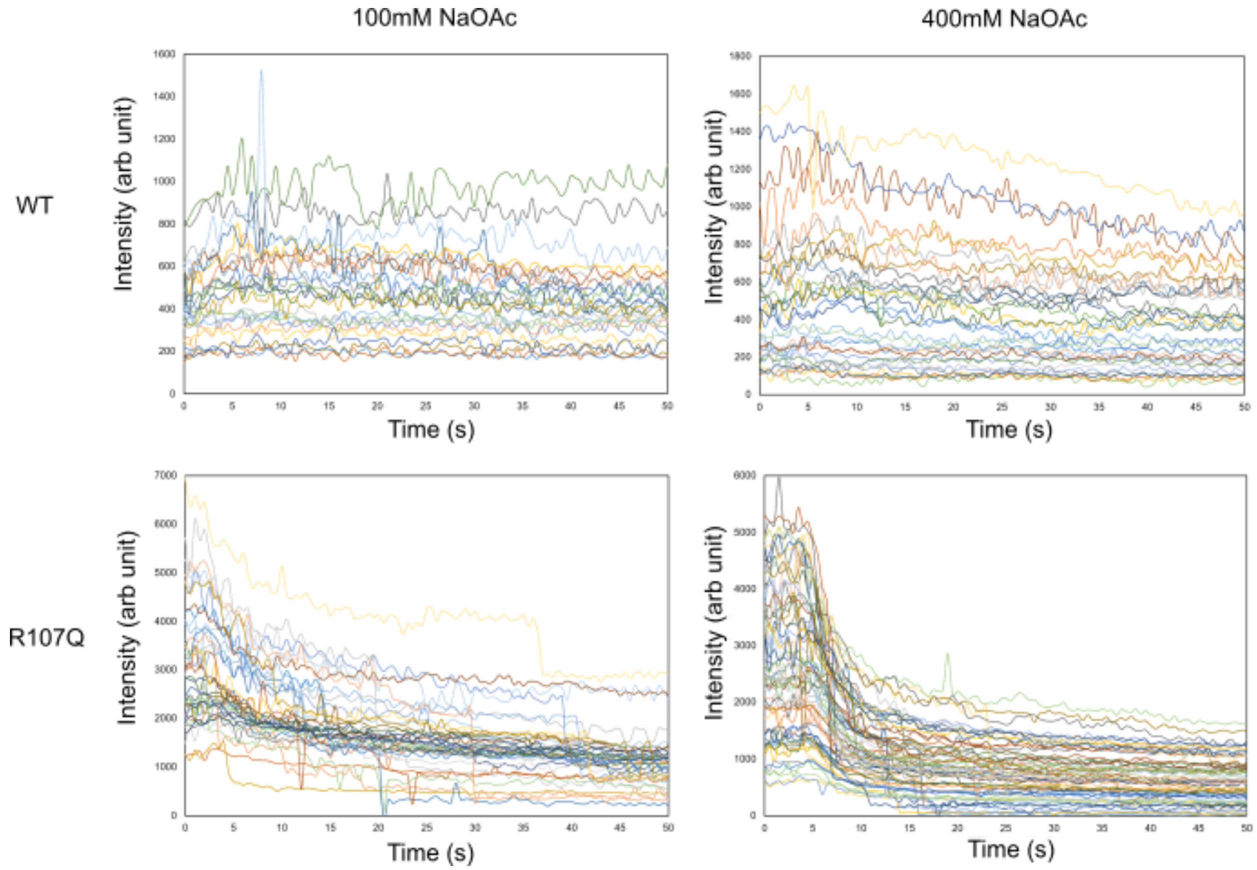

Figure S5 : Total fluorescence intensity of SSB-coated-ssDNA molecules over time. To quantify total fluorescence intensity, a region of interest (ROI) that encompasses the entire fluorescent intensity along the DNA was selected at each time point and a local background subtraction correction was performed .

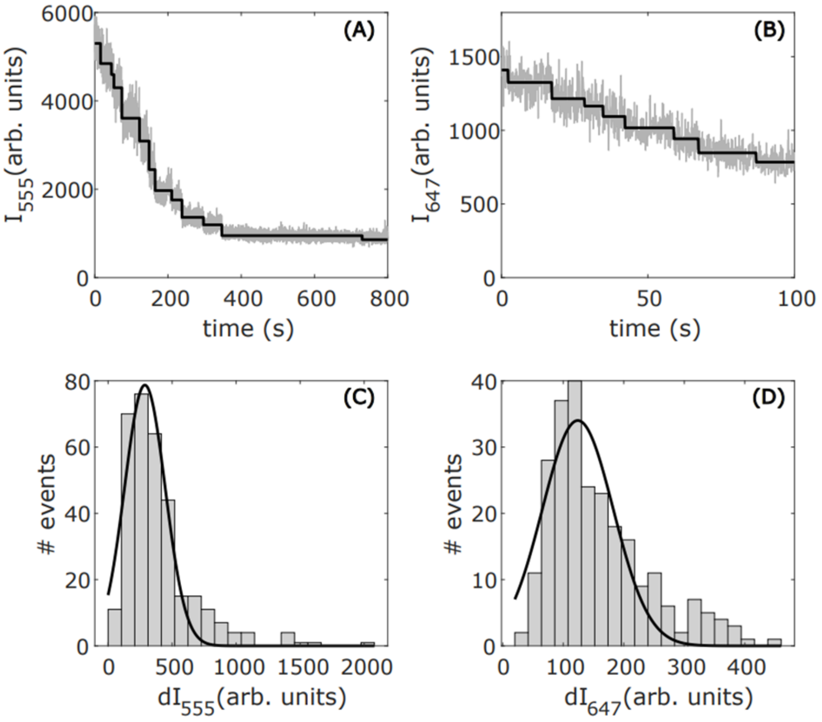

Figure S6 : Quantification of the intensity of a mtSSB monomer. Fluorescence signal of a mtSSB-Alexa555 **(A)** and mtSSB-Alexa **(B)** complex as a function of time, showing single-step photobleaching events. Assays were performed using 100 ms exposure time and 4 mW and 11,4 mW laser power for 532 nm and 638 nm laser, respectively. The intensity of SSB coated-ssDNA was retrieved from kymographs and analyzed using AutoStepFinder v2.1.0 from Loeff-Kerssemakers et al [Loeff *et al.,* 2021], yielding the intensity loss during a photobleaching step, which is shown in the intensity histogram of single mtSSB-Alexa555 and mtSSB-Alexa647 complexes represented in **(C) and (D)**, respectively. The intensity distribution was fitted with a Gaussian, yielding a mean fluorescence value (dI) of 287 ± 51 a.u. (mean ± SE) (N= 328) for a single SSB-Alexa-555 complex and 124 ± 26 a.u. (mean ± SE) (N= 294) for a single SSB-Alexa-647.

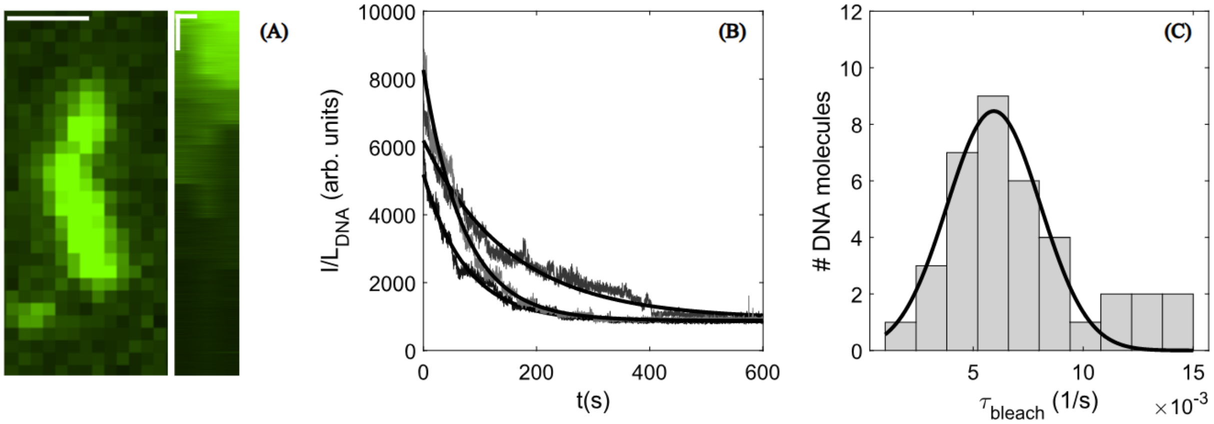

Figure S7: Photobleaching rate of SSB-WT-Alexa 555. (A) Typical fluorescence image (left) and kymograph (right) of a SSBWT-Alexa555-ssDNA nucleoprotein under continuous illumination, with an exposure time of 100 ms and a laser power of 4 mW. Images are typical examples of two identical experiments. Scale bars : 1 µm (horizontal) and 2 min (vertical). **(B)** Fluorescence intensity over time from the kymograph displayed in (A). From exponential fit to such data from a Gaussian fit to the obtained histogram we obtained a mean photobleaching rate with a standard deviation; k{bleaching}= 5.9e-3 +/- 1.3 e-3 1/s (N=38). The dissociation experiments were performed with a factor 2 less laser power and with a delay between frames.

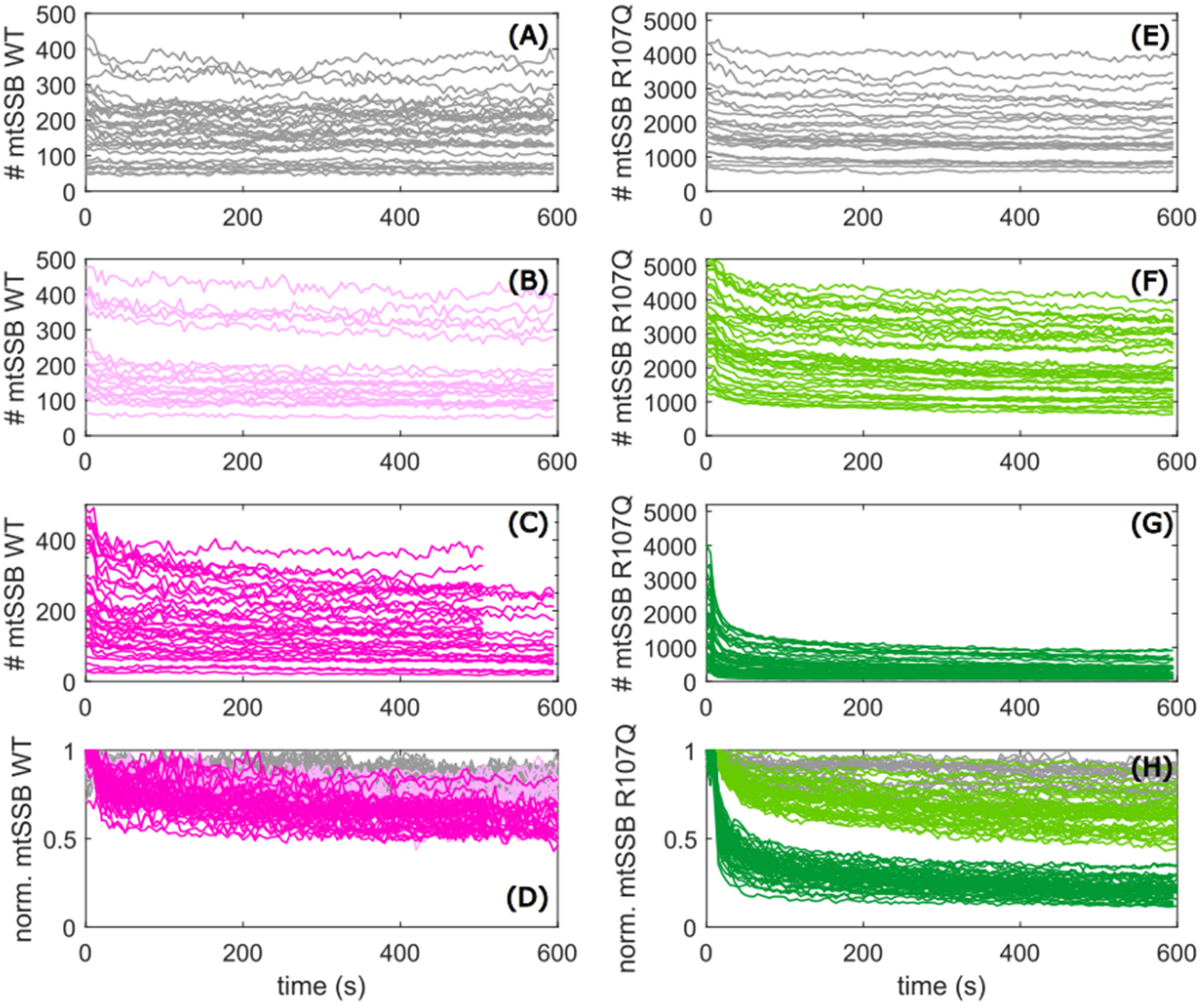

Figure S8: Number of WT or R107Q SSB monomers bound to ssdNA over time at different salt concentrations. (A) WT, 10 mM NaOAc, **(B)** WT,100 mM NaOAc, **(C)** WT, 400 mM NaOAc, **(D)** WT, all traces superimposed, **(E)** R107Q, 10 mM NaOAc, **(F)** R107Q, 100 mM NaOAc, **(G)** R107Q, 400 mM NaOAc, **(H)** R107Q, all traces superimposed. For each experimental condition, only ssDNA molecules larger than 1 µm were considered, which corresponds to ~30-40 ssDNA molecules per condition.

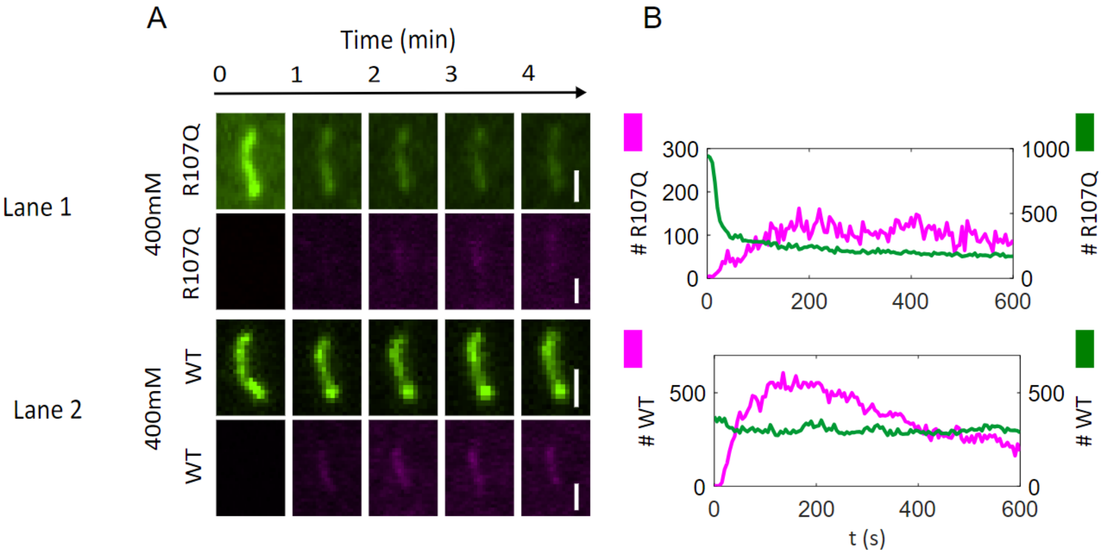

Figure S9 : Real time competition assays. (A) Fluorescence images of nucleoprotein complexes over time. The upper line of each configuration shows R107Q-Alexa 555 (lane 1) or WT-Alexa 555-ssDNA (lane 2) complexes stretched at the surface of the flow-cell. The lower line shows R107Q-Alexa 647 or WT-Alexa 647 that is added to the flow-cell in the presence of salt. **(B)** Intensity measurement of mean intensities of ssDNA-mtSSB complexes as a function of time for each competition assay.

Concluding remarks

Since the rise of next-generation sequencing and whole genome sequencing, the medical diagnosis of mitochondrial mutation in sickness has increased. Therefore, interest towards the understanding of mitochondria has increased. However, there are still grey area to discover, for instance in mtDNA maintenance. In the past decades, single molecule techniques have been developed and aim to the understanding of molecular mechanisms performed by individual molecules. This thesis may help to understand the disease-causing mechanisms of two variants of two main actors of the mtDNA maintenance namely TFAM P178L and mtSSB R107Q. We performed biochemical characterisation and used two single molecules methods: the acoustic force spectroscopy (AFS) and the total internal reflection fluorescence microscopy (TIRFm). A guide to perform such single molecule experiments on TFAM can be found in this thesis.

TFAM P178L was shown to be involved in mtDNA depletion in patients. We demonstrated that the mutation has no effect on DNA binding nor on TFAM motion. However, the mutation mildly affects DNA compaction and severely impairs mtDNA transcription initiation at both HSP and LSP. Molecular modeling suggests that promoter sequence recognition and interaction between TFAM's HMGB box and POLRMT could be main factors in the hindrance of transcription. In addition, the mutation appears to affect TFAM dimerization and may be involved in the decreased of compaction and transcription levels. The structure of this variant remains to be elucidated.

The human mitochondrial SSB variant R107Q was recently clinically investigated and shown to be involved in mitochondrial maintenance defects associated with autosomal dominant mitochondrial optic atrophy and retinal dystrophy. We showed that the R107Q mutant is still able to form stable tetramers. In addition, we have demonstrated that the R107Q mutation significantly impaired the ssDNA binding affinity (with higher dissociation rate) and compacting ability of SSB. These disabilities are likely due to a less stable and incomplete wrapping state in comparison to the WT. These features are in line with our molecular modeling of SSB on ssDNA showing that the R107Q mutation reduces the potential SSB-ssDNA interaction sites. However, information on the binding footprint are still missing. In addition, motion of human mtSSB is still not addressed in the literature. Human mtSSB has been shown to display its low binding mode when supporting strand displacement with Phi29 polymerase (Morin *et al.*, 2017). How mtSSB R107Q behaviour in this kind of experiment (Plaza *et al.*,

2023) could be interesting to study the mechanism that leads to a decrease in replication initiation (Jiang *et al.*, 2021).

Last, cellular models expressing the mutant proteins could be done by gene editing with CRISPr cassettes and could constitute good supports to study *in vivo* effects on replication and transcription levels.

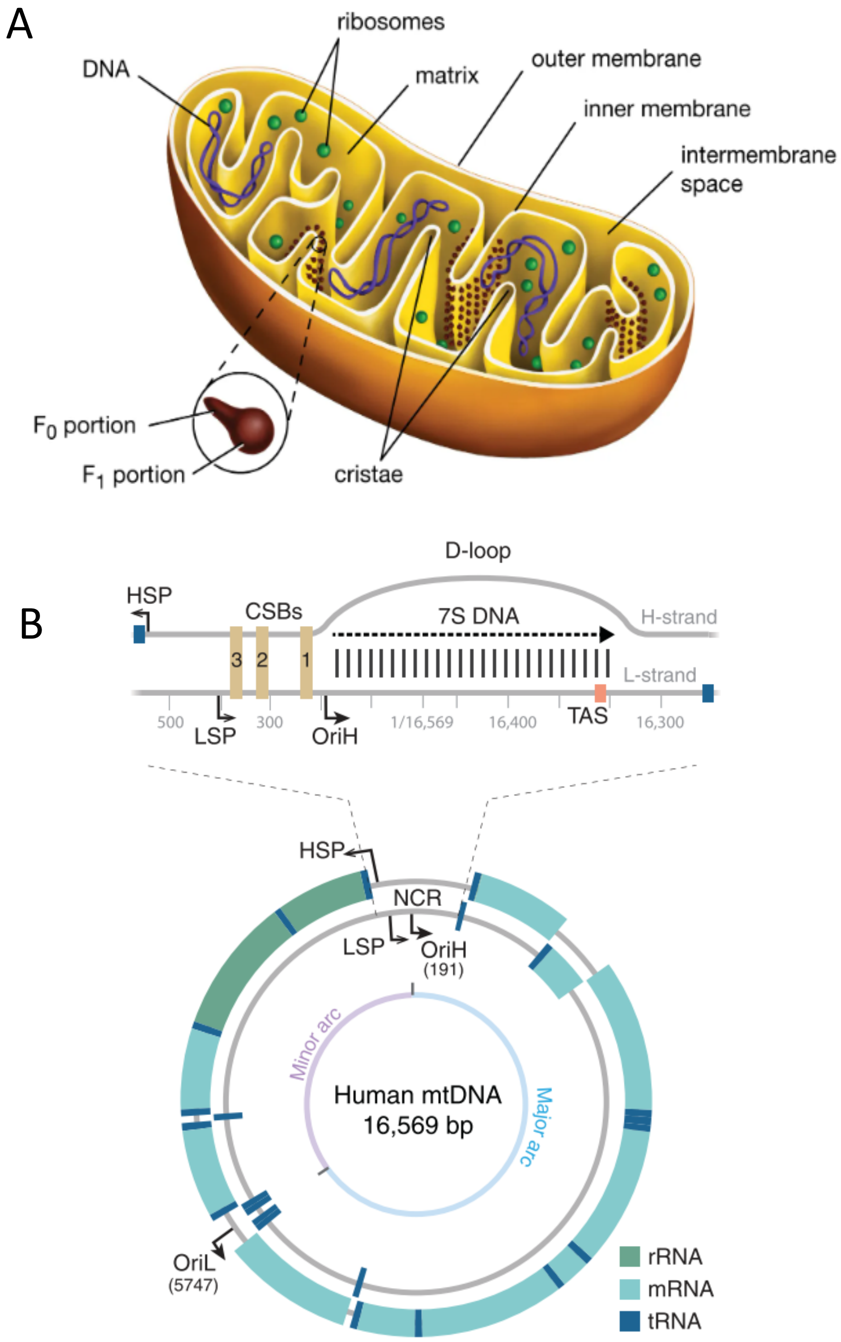

Figure 40: La mitochondrie et son génome chez l'humain. (**A**) Dessin d'une coupe transversale d'une mitochondrie avec ses doubles membranes (la membrane interne formant les crêtes et la membrane externe) qui séparent l'espace inter-membranaire et la matrice mitochondriale. L'ADN mitochondrial réside dans la matrice et la chaîne de transport d'électrons symbolisée par l'ATP synthase (en forme de poire brune) est ancrée dans la membrane interne. (**B**) Le génome mitochondrial est circulaire et mesure 16,6 kpb. Il est composé d'un brin lourd (brin H, cercle extérieur) et d'un brin léger (brin L, cercle intérieur) qui hébergent tous deux une séquence promotrice HSP et LSP respectivement ainsi qu'une origine de réplication OriH et OriL. Un zoom de la région non codante (NCR) est représentée en haut (Sources : https://www.britannica.com/science/cell-biology/Regulation-of-RNA-after-synthesis et Falkenberg et Gustafsson, 2020).

Résumé en français

Structure et génome des mitochondries chez les mammifères

L'origine des mitochondries serait associée à un changement atmosphérique global il y a environ deux milliards d'années, où l'oxygène s'est peu à peu accumulé dans une atmosphère composée principalement de soufre, d'azote et de carbone (Andersson et al, 2002). En 1970, Lynn Margulis a publié un livre intitulé « Origin of Eukaryotic Cells » dans lequel elle propose que les organites eucaryotes comme les mitochondries et les chloroplastes ont évolué à partir d'une endosymbiose entre une bactérie et une cellule eucaryote (Roger et al, 2017).

Les mitochondries sont des organites essentiels présents dans la plupart des cellules eucaryotes. Elles sont connues pour être « les centrales électriques » qui fournissent de l'énergie aux cellules sous la forme de molécules d'ATP, utilisées par les cellules pour couvrir leurs besoins énergétiques. Le nombre moyen de mitochondries par cellule peut varier de plusieurs centaines à plusieurs milliers, selon les besoins énergétiques des tissus. La mitochondrie est composée de deux membranes: (i) une membrane externe séparant les mitochondries du cytoplasme de la cellule et (ii) une membrane interne formée d'invaginations appelées crêtes où s'effectue la “respiration” (**Figure 40A**). Bien que les mitochondries effectuent la synthèse de l'ATP, elles sont impliquées dans de nombreuses autres voies cellulaires, notamment l'apoptose via la régulation du calcium cellulaire et du cytochrome C, le métabolisme des acides aminés et des nucléotides et le catabolisme des acides gras (Andrew J. Roger et al, 2017). De plus, les mitochondries possèdent leur propre génome localisé dans la matrice. Chez l'Homme, l'ADN mitochondrial est circulaire, mesure 16,5 kb et possède une région régulatrice non codante appelée “NCR” pour non-coding region. Il code seulement 13 protéines alors que son protéome est estimé à plus de 1000 protéines (Nils Wiedemann et al, 2017). Cette différence illustre un lien étroit entre la cellule et la mitochondrie où la majorité des protéines mitochondriales sont en effet synthétisées dans le noyau et exportées vers les mitochondries. L'ADN mitochondrial est composé d'un brin lourd (heavy ou H) et d'un brin léger (light ou L) possédant chacun un promoteur (HPS et LSP) ainsi qu'une origine de réplication (OriH et OriL) (**Figure 40B**).

Le métabolisme

L'oxydation de molécules se produisant notamment lors des processus de catabolisme tels que la glycolyse, l'oxydation des acides gras β ou le cycle de l'acide citrique, est utilisée pour synthétiser des molécules d'ATP lors de la phosphorylation oxydative. Ces oxydations permettent également de réduire des cofacteurs tels que le NADH ou le $FADH_2$ qui céderont leurs électrons au niveau de la chaîne de transport d'électrons (ETC) localisée dans la membrane interne mitochondriale (van der Bliek et al, 2017).

Les acides gras (AG) sont utilisés comme substrats par l'organisme pour générer de l'énergie. Les AG sont dégradés via une voie d'oxydation appelée la β-oxydation. Celle-ci se déroule dans les mitochondries où l'oxydation de la chaîne carbonée des AG entraîne la libération un acétyl-CoA et d'un acide avec deux carbones en moins, en plus de réduire du NAD^+ et du FAD. Au cours du cycle de Krebs, l'acétyl-CoA est utilisé comme substrat dans une série de réaction d'oxydo-réduction au sein de la matrice mitochondriale et où du NAD^+ et du FAD sont également réduits.

La phosphorylation oxydative englobe à la fois l'ETC et l'ATP synthase. Les électrons issus des cofacteurs réduits sont transportés à travers une série de complexes (I-IV) jusqu'à un accepteur d'électrons final qui est l'oxygène. À mesure que les électrons traversent les complexes, ils perdent de l'énergie potentielle qui est utilisée par les complexes pour pomper les protons de la matrice vers l'espace intermembranaire. Comme la membrane interne est imperméable aux protons, un gradient électrochimique est créé, entraînant la synthèse d'ATP par l'ATP synthase avec phosphorylation de l'ADP en ATP, avec formation d'eau dans la matrice (Judge et Dodd, 2020).

Réplication et réparation de l'ADN mitochondriale (ADNmt)

L'ADNmt des mammifères est répliqué par des facteurs de réplication différents de ceux nécessaires à la réplication de l'ADN nucléaire, bien qu'ils aient une origine nucléaire. Beaucoup de ces facteurs de réplication appartiennent à la famille des bactériophages comme la polymérase mitochondriale réplicative POLγ, l'hélicase TWINKLE ou l'ARN polymérase POLRMT (Gustafsson et al, 2016). La synthèse des brins H et L est effectuée uniquement par POLγ. Cependant, pour initier la synthèse de l'ADNmt, POLγ a besoin d'une amorce d'ARN comme matrice de départ (Fusté et al, 2010). Cette amorce est synthétisée par POLRMT,

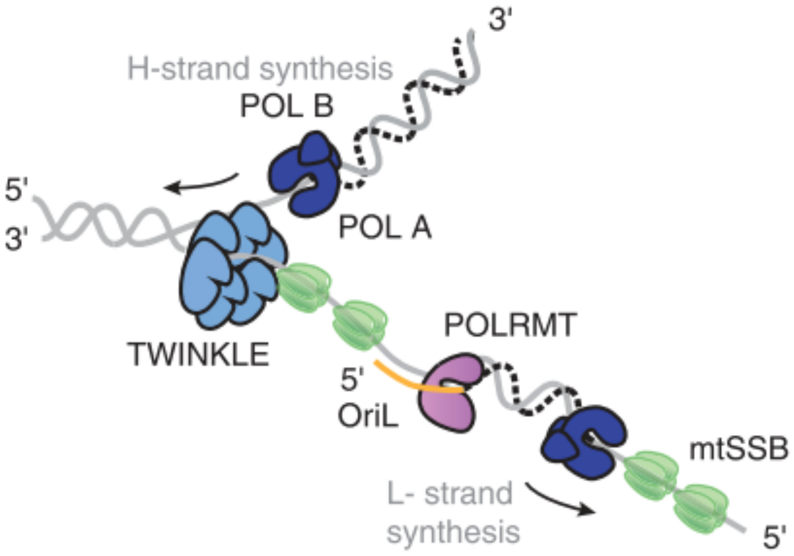

Figure 41: La fourche de réplication. L'hélicase TWINKLE (**en bleu clair**) dirige le déroulement de l'ADNdb dans la direction 5'-3'. MtSSB (**en vert**) se lie à l'ADNsb et stimule la synthèse de l'ADN par POLγ (**en bleu foncé**). POLRMT (**en violet**) synthétise les amorces d'ARN nécessaires à POLγ pour l'initiation de la réplication (Source : Falkenberg et Gustafsson, 2020).

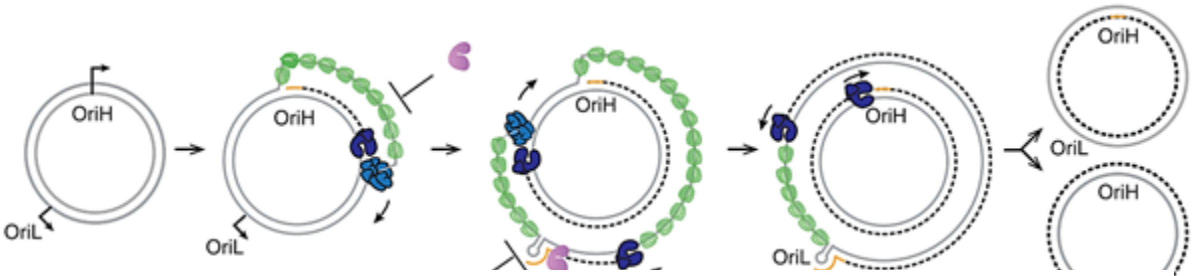

Figure 42: La réplication du brin H naissant est initiée à OriH et se déroule de manière unidirectionnelle de 5 'vers 3'. Le brin H parental est déplacé et couvert par mtSSB. En atteignant OriL, le brin H se plie en une structure tige-boucle qui est utilisée par POLRMT pour amorcer la synthèse du brin L par POLγ jusqu'à ce qu'un cercle complet et deux nouvelles molécules filles soient formées (Source : Falkenbeg et Gustafsson, 2020).

impliquée dans la transcription de l'ADNmt (Gaspari et al, 2004, Wanrooij et al, 2008). De plus, POLγ est incapable de progresser sur de l'ADN double brin (ADNdb) et l'hélicase mitochondriale TWINKLE est nécessaire pour dérouler l'ADNmt au niveau de la fourche de réplication (**Figure 41)** (Korhonen et al, 2003). Un autre facteur essentiel dans la réplication de l'ADNmt est la protéine de liaison mitochondriale simple brin (mtSSB). Il empêche la réhybridation et la dégradation du brin déplacé, et améliore également la réplication de l'ADNmt en stimulant l'activité TWINKLE et en améliorant la processivité de POLγ au niveau de la fourche de réplication. Au niveau de cette dernière, TWINKLE utilise de l'énergie pour dérouler l'ADNdb, suivi de POLγ synthétisant le brin naissant lié par mtSSB afin de le protéger contre les nucléases et empêcher la formation de structures secondaires (Falkenberg 2018). Vinograd et al. en 1972 a proposé un modèle de réplication de l'ADNmt connu sous le nom de "Strand displacement model (SDM)" (Robberson et al, 1972). Dans ce modèle, le brin H est déplacé lors de l'initiation de la réplication et la synthèse des brins H et L se produit en continu. La réplication du brin H naissant est initiée à OriH et se déroule de manière unidirectionnelle de 5 'à 3' (**Figure 42**). Au cours de l'élongation de la réplication, TWINKLE se déplace sur le brin H parental et déroule l'ADNmt, dont le brin L est couvert par mtSSB. En atteignant OriL, le brin H forme une structure tige-boucle, utilisée par POLRMT pour amorcer la synthèse du brin L par POLγ jusqu'à ce qu'un cercle complet soit effectué. A la fin de la réplication deux nouvelles molécules filles d'ADN circulaires sont ainsi obtenues (Falkenbeg and Gustafsson, 2020).

Au cours des processus métaboliques, les acides nucléiques peuvent être endommagés par divers agents chimiques ou physiques. Par exemple, les espèces réactives de l'oxygène (ROS) sont des molécules hautement réactives formées à partir de l'oxygène diatomique (O2) et peuvent modifier ou casser la structure de l'ADN; au même titre que les ultraviolets et les radiations. Les ROS sont particulièrement présentes dans les mitochondries en raison de la phosphorylation oxydative dans la matrice où réside l'ADNmt. Par conséquent, l'environnement dans lequel l'ADNmt est manipulé pourrait être à l'origine de dommages au sein de l'ADNmt qui pourraient se manifester par des mutations ponctuelles ou des cassures de brins. Il est également important de noter que l'ADNmt est répliqué en permanence et indépendamment du cycle cellulaire, ce qui augmente les risques d'endommagement de l'ADNmt. Dans le noyau, les dommages de l'ADN peuvent être réparés par plusieurs mécanismes de réparation robustes. Parmi ces mécanismes, on trouve la réparation par excision de base (BER), la réparation par excision de nucléotides (NER), la réparation par

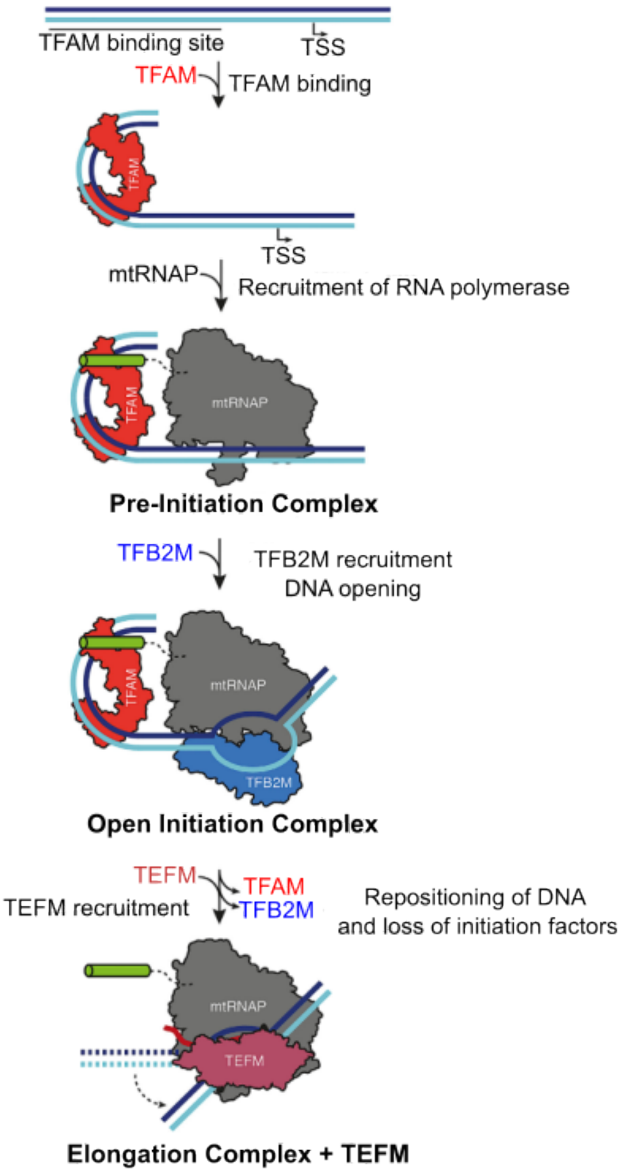

Figure 43: Modèle du complexe d'initiation de la transcription chez l'humain. TFAM se lie aux promoteurs en amont du site d'initiation de la transcription (le TSS pour transcription start site), plie l'ADN à 180° et recrute l'ARN polymérase (mtRNAP) pour former le complexe de pré-initiation. Ensuite, TFB2M est recruté et assiste mtRNAP dans l'ouverture de l'ADN. Ensuite, TFAM et TFB2M se dissocient et TEFM interagit avec mtRNAP pour former le complexe d'élongation. La manière dont se termine la transcription n'est toujours pas claire, mais il est proposé que MTERF soit impliqué dans le processus (Source : Hillen et al, 2017).

mésappariement (MMR), la réparation de cassures simples et doubles brins telles que la recombinaison homologue (HR) ou encore la jonction d'extrémités non homologues (NHEJ) (Chatterjee et al, 2017). Le BER est le seul mécanisme qui a été nettement caractérisé chez les mitochondries des mammifères. Il consiste en l'excision d'une base azoté par des glycosylases dont le type varie en fonction de la nature du dommage, comme une oxydation, alkylation ou encore une déamination.

D'autres mécanismes de réparation de l'ADNmt ont cependant lieu dans les mitochondries. Par exemple, chez Saccharomyces cerevisiae, les cassures double brins (DSB) peuvent être réparées par recombinaison homologue (HR) (Stein et coll., 2015). Néanmoins, il n'est toujours pas clair si la réparation des DSB existe dans les mitochondries de mammifères.

Dans les mitochondries des mammifères, contrairement au noyau, les molécules d'ADNmt fortement endommagées (comme les cassures de brins) subissent souvent une dégradation rapide (Bayona-Bafaluy et al, 2005). En effet, le caractère multi-copie de l'ADNmt permet la dégradation des molécules d'ADNmt endommagées sans générer de problèmes au sein des mitochondries. La voie de dégradation pourrait être moins énergétique qu'un mécanisme de réparation complexe, préférant répliquer des copies saines d'ADNmt (Nissanka et al, 2019). Les acteurs de la dégradation de l'ADNmt linéaire n'ont pas encore été clairement mis en évidence, mais des études ont montré que l'inactivation des nucléases POLγ, Twinkle et MGME1 a un impact sur la dégradation des molécules d'ADNmt (Peeva et al, 2018, Nissanka et al, 2018).

Transcription de l'ADN mitochondrial

La machinerie de transcription mitochondriale est composée de plusieurs protéines qui sont traduites dans le cytosol et exportées dans les mitochondries. Les principales protéines impliquées dans la transcription de l'ADNmt sont l'ARN polymérase mitochondriale POLRMT, le facteur de transcription mitochondrial A (TFAM), B2 (TFB2M), le facteur d'élongation mitochondrial (TEFM) et le facteur de terminaison mitochondriale 1 (MTERF1) (Gaspari et al, 2004 ; Gustafsson et Falkenberg, 2016). La transcription mitochondriale conduit à la formation de deux longs transcrits polycistroniques sans introns qui correspondent à la transcription du brin lourd et léger, à partir des promoteurs HSP et LSP, tous deux localisés dans la région NCR (Gustafsson et al, 2016). L'initiation de la transcription commence par la reconnaissance des promoteurs par TFAM (**Figure 43**). TFAM, en se liant aux promoteurs,

courbe le squelette de l'ADN à 180° (Ngo et al, 2011; Rubio-Cosials et al, 2011). Ensuite, TFAM recrute POLRMT et le stabilise au niveau de la région promotrice via l'interaction du domaine HMG Box B avec la queue N-terminale de POLRMT appelée la «tether helix» (Hillen et al, 2017). Ensuite TFB2M est recruté et assiste POLRMT dans l'ouverture de l'ADN. La transition entre l'initiation et l'élongation de la transcription se fait par un changement de conformation de l'ADN avec la dissociation de TFAM et de TFB2M qui est remplacé par TEFM. La terminaison de la transcription reste toutefois encore floue.

Maladies mitochondriales et thérapies

En raison de l'ubiquité des mitochondries, les troubles mitochondriaux peuvent affecter n'importe quel système organique et se manifester à tout âge, présentant des syndromes multisystémiques; mais peuvent également entraîner des symptômes tissus-spécifiques. Pour ces raisons, les maladies mitochondriales sont particulièrement difficiles à diagnostiquer. Les maladies mitochondriales, définies comme des troubles dus à un défaut de la chaîne de phosphorylation oxydative (OXPHOS), sont les maladies métaboliques les plus courantes (Jardel et Rucheton, 2018). Etant donné que ces troubles altèrent le processus OXPHOS, (entraînant un déficit de production d'énergie) les organes et tissus qui ont besoin d'une grande quantité d'énergie sont affectés les premiers. Par exemple, il s'agit souvent du système nerveux, des muscles cardiaques et squelettiques ou du foie. C'est pourquoi les maladies mitochondriales impliquent souvent des troubles neurologiques et une faiblesse musculaire. Les manifestations des troubles mitochondriaux observées peuvent être, par exemple, des troubles cognitifs, une atrophie optique, une encéphalomyopathie, l'épilepsie, des myopathies cardiaques et squelettiques, des néphropathies, des hépatopathies ou des endocrinopathies (El Hattab et al, 2017). Une caractéristique des troubles mitochondriaux directement liée à la nature multicopie de l'ADNmt est que les cellules peuvent contenir à la fois des copies d'ADNmt saines et mutantes. Ce phénomène est appelé hétéroplasmie. Par conséquent, dans les mitochondries, un certain nombre d'ADNmt pourraient être endommagés, conduisant à des protéines mutées. Mais cela pourrait être compensé par des protéines de type sauvage produites par des copies saines d'ADNmt, jusqu'à ce qu'un certain seuil de tolérance soit dépassé.

De plus, les troubles mitochondriaux humains sont des maladies génétiques dues à la mutation de gènes très divers situés soit sur l'ADN mitochondrial (ADNmt) soit sur le génome nucléaire, conduisant à des dysfonctionnements mitochondriaux à plusieurs stades. Par exemple, des défauts au niveau de la maintenance de l'ADNmt, de la dynamique mitochondriale (fusion-

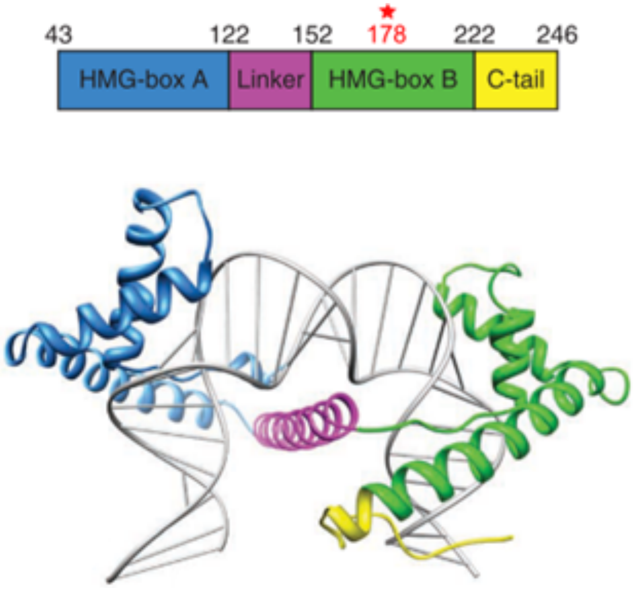

Figure 44: Séquence et structure de TFAM. (**En haut**) TFAM est une protéine de 246 acides aminés qui héberge deux domaines HMG (**A et B en bleu et vert**), un domaine reliant les deux (**en violet**) et une queue C-terminale (**en jaune**). La mutation P178L est indiquée en rouge. Notez que le peptide signal n'est pas représenté et correspond aux acides aminés de 1 à 43. (**En bas**) Est illustrée la structure de TFAM liée à un ADNdb lors de l'initiation de la transcription, dans laquelle les couleurs correspondent à celles dans la séquence protéique (Source Ngo et al, 2011).

fission) ou au niveau de la maintenance d’un pool de nucléotides (El-Hattab et al, 2017). Les troubles mitochondriaux peuvent survenir à tout âge et sont généralement progressifs. De nos jours, il n’existe toujours pas de traitement curatif efficace contre les troubles mitochondriaux. Les thérapies se concentrent principalement sur des stratégies réparatrices ou préventives telles que la supplémentation en coenzyme Q10 ou la restauration des niveaux de NAD+, la régulation positive de la biogenèse mitochondriale ou l'augmentation de la mitophagie pour réduire les niveaux d'hétéroplasmie (Russel et al, 2020). Une autre approche prometteuse développée au cours des dernières décennies est la thérapie génique. La thérapie génique représente une approche thérapeutique attractive pour les maladies monogéniques récessives. Cependant, la délivrance et l’expression d’un gène ectopique dans tout le corps restent encore un défi. Différentes approches sont en cours, utilisant des systèmes viraux ou non viraux, parmi lesquels l’approche virale est pour l'instant la plus efficace. D’autres approches basées sur la dégradation sélective des molécules d’ADN endommagées ou alors basées sur la réparation des ARNs mitochondriaux semblent également prometteuses.

Facteur de transcription A mitochondrial (TFAM)

TFAM est considéré comme l’un des composants essentiels du nucléoïde mitochondrial. Dans les mitochondries des mammifères, environ 1 000 molécules de TFAM sont présentes par molécule d'ADNmt, impliquant 1 TFAM pour 16 à 17 pb d'ADNmt (Farge et Falkenberg, 2019). TFAM appartient au “High Mobility Group (HMG)”, plus précisément au groupe HMGB (Malarkey et Churchill, 2012). Il s'agit d'une protéine de 24 kDa et de 246 acides aminés codée par l'ADN nucléaire et exportée vers la matrice mitochondriale via la reconnaissance de son peptide signal, qui est clivé à son arrivée dans les mitochondries. La structure de TFAM a été révélée par cristallographie. Cette dernière a montré que TFAM est composé de deux domaines HMG nommées HMG A et B (parfois appelées 1 et 2) qui se lient à l'ADN, d'une région de liaison qui relie ces deux domaines et d'une queue C-terminal impliquée dans l'activation de la transcription et la reconnaissance des séquences promotrices (Gangelhoff et al, 2009; Ngo et al, 2011; Rubio-Cosials et al, 2011) (**Figure 44**).

TFAM peut se lier de manière spécifique à l’ADN mitochondrial, via la reconnaissance des séquences promotrices dans l’initiation de la transcription, ou bien de manière aspécifique. Ce dernier mode de liaison permet à TFAM de compacter l’ADN par des mécanismes divers comme la dénaturation locale des brins rendant l’ADN plus souple, des courbures de l’ADN à 180°, des boucles et des rapprochements physiques de brins d’ADN. La compaction de l’ADN

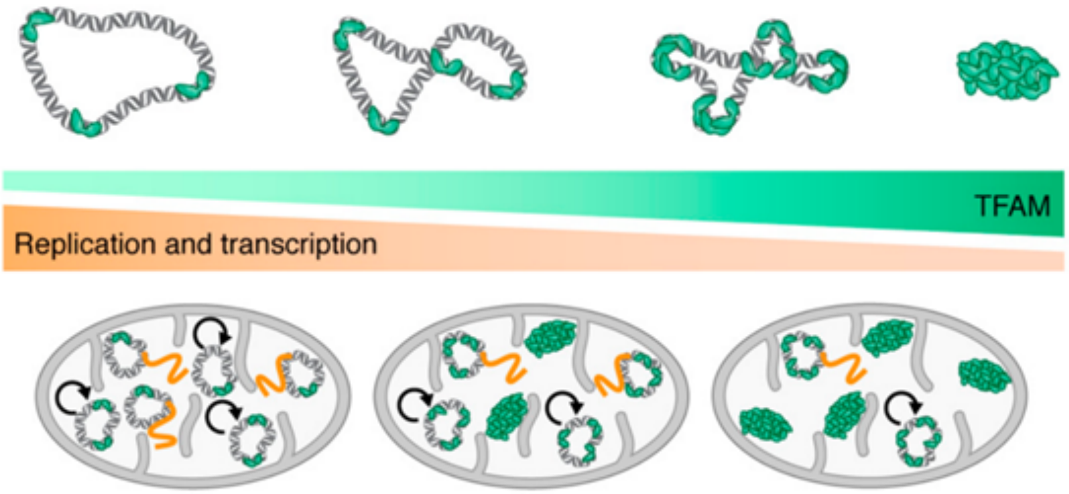

Figure 45: TFAM régule la réplication et la transcription en contrôlant la compaction de l'ADNmt. (**En haut**) Modèle illustrant la compaction de l'ADNmt en fonction de la concentration en TFAM. (**En bas**) Il est proposé que le compactage de l'ADNmt par TFAM régule à la fois la réplication et la transcription en fonction du degré de compaction de l'ADNmt. Il est suggéré que les nucléoïdes compactés soient une forme de stockage coexistant avec les nucléoïdes actifs (**ci-dessus**) (Source Farge et Falkenberg, 2019).

mitochondrial par TFAM, outre le fait de pallier l'encombrement des molécules d'ADN, est également un moyen de réguler l'activité des nucléoides. Les nucléoides possédant un faible nombre de TFAM seront plutôt actifs, menant des processus de réplication et de transcription, tandis que les nucléoides possédant un grand nombre de TFAM seront plus dans un état de "dormance" et serviront plutôt de stock d'ADN (**Figure 45**) (Brown *et al,* 2011; Kukat *et al*, 2015; Farge *et al*, 2014).

TFAM a été observé diffusant sur l'ADN double-brin par un mécanisme de "glissade" (Farge *et al*, 2012; Heller *et al*, 2013). La diffusion de TFAM pourrait-être un moyen de scanner et repérer les séquences promotrices rapidement. Qui plus-est, la diffusion de TFAM permet à d'autres TFAM de se rejoindre et de former des agrégats qui sont impliqués dans la compaction de l'ADN mitochondrial. Les fonctions de TFAM ci-dessus peuvent être finement régulées par des modifications telles que des acétylations ou des phosphorylations qui ont pour conséquence de réduire l'affinité de TFAM pour l'ADN ainsi que sa diffusion. De ce fait, TFAM pourrait servir de facteur épigénétique.

Un variant TFAM (TFAM P178L) a été identifiée chez une fratrie qui était atteint d'une insuffisance hépatique néonatale évoluant vers la disparition et une déplétion de l'ADNmt dans le foie et les muscles squelettiques (Stiles et al, 2016). Ce mutant a fait l'objet d'études expérimentales dans cette thèse. Il a été démontré que les niveaux de TFAM et le nombre de copies d'ADNmt sont directement liés. Chez la souris, la mutation hétérozygote de TFAM génère une diminution d'environ 40 % du nombre de copies d'ADNmt *in vivo*, et la mutation homozygote s'est avérée mortelle au niveau embryonnaire (Kang et al, 2018). De plus, une diminution importante des niveaux d'ADNmt ou de TFAM a été observée dans les populations de patients touchées par la maladie de Parkinson, de Huntington et d'Alzheimer et même simplement avec le vieillissement, décrivant une association des niveaux d'ADNmt et de TFAM avec la neurodégénérescence (Kang et al, 2018). Récemment, il a été démontré qu'un variant récessif de TFAM (Arg232Cys) provoquait une déplétion de l'ADNmt associée à une insuffisance ovarienne primaire, des convulsions, une déficience intellectuelle et une perte auditive dans une famille consanguine, ce qui élargit le répertoire des phénotypes de maladies mitochondriales (Ullah et al, 2021).

Figure 46: Structure HsmtSSB. HsmtSSB est assemblé sous la forme d'un homotétramère, dans lequel les quatre monomères (molA, A', B et B') forment une structure dimère à dimère, avec une symétrie centrale. Dans l'encadré, certaines positions de mutation retrouvées dans les désordres mitochondriaux (relatifs à mtSSB) y sont indiquées. Elles se situent à l'interface entre les dimères (Source : Piro-Mégy et al, 2020).

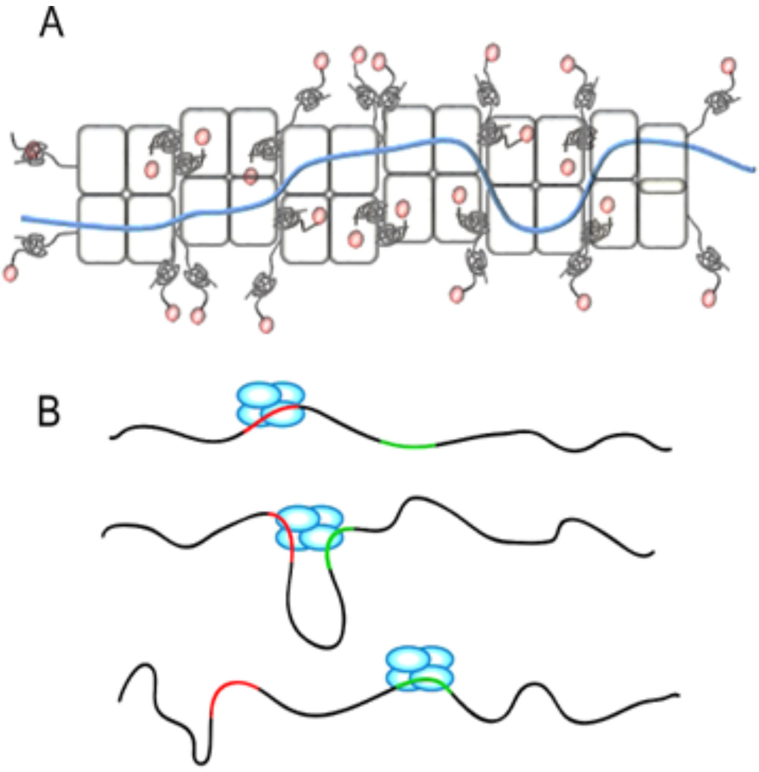

Figure 47: Modèle illustrant la coopérativité et la diffusion d'EcoSSB. (**A**) Schéma illustrant la coopérativité d'EcoSSB en mode de liaison faible sur l'ADNsb (**en bleu**) via des interactions entre tétramères (**carrés)** et par leur IDL (segment globulaire noir). La queue C-terminale d'EcoSSB est représentée en **rose**. Le mécanisme de diffusion pourrait être imagé par des tétramères EcoSSB glissant sur l'ADNsb (diffusion par reptation). (**B**) Modèle du mécanisme de transfert intersegmental dans lequel EcoSSB (**en bleu**) lié à un site d'ADNsb (**en rouge**) interagit avec un autre site distant de la même molécule d'ADNsb (**en vert**) et se dissocie du site d'origine, conduisant à de grands déplacements (Source : Lee et al 2008 et Antony et Lohman, 2019).

Protein de liaison à l'ADN simple-brin mitochondrial (mtSSB)

Les protéines de liaison à l'ADN simple brin (SSB) sont présentes dans les trois domaines de la vie, à savoir les eucaryotes, les eubactéries, les archées ainsi que dans les virus. Selon l'organisme, les SSB sont impliqués dans le métabolisme de l'ADN à différentes échelles, notamment dans la réplication et la transcription, la recombinaison de l'ADN et sa réparation. La structure cristalline de la protéine de liaison à l'ADN simple brin (ADNsb) mitochondrial humain (HsmtSSB) a été résolue en 1997, mettant en évidence une structure homotétramère formée de deux dimères en "tête-à-tête" (Yang et al, 1997) (**Figure 46**). Chez les mammifères, mtSSB est une protéine de 148 acides aminés et de 16 kDa (monomère), qui possède un peptide signal vers la mitochondrie et héberge par monomère un domaine oligonucleotide/oligosaccharide (OB) de liaison à l'ADNsb, permettant à l'ADNsb d'être enroulé autour du tétramère (Wu et al, 2016).

Le nombre de nucléotides d'ADNsb liés par les SSB peut être modulé par les conditions environnementales, telles que la concentration et le type de sel, le pH et la température, le rapport SSB/ADNsb, ainsi que les partenaires de liaison (Antony et Lohman, 2019). En fonction de ces conditions, il a été constaté que HsmtSSB présente au moins deux modes de liaison: un mode de liaison partiel (low binding-mode) et un mode de liaison complet (high binding mode) dans lesquels le nombre de nucléotides enroulés varie (Curth et al, 1994). La structure ainsi que certaines fonctions de mtSSB (comme les différents modes de liaison) sont très similaires à celles de SSB chez *Escherichia coli* (EcoSSB) qui a été beaucoup caractérisé dans la littérature (Webster et al, 1997; Kaur et al, 2017; Antony and Lohman, 2019; Bell et al, 2015; Kozlov *et al*, 2017) . C'est pourquoi EcoSSB constitue un bon modèle d'étude pour mtSSB.

De plus, plusieurs SSB ont été observés se déplaçant sur une molécule d'ADN comme EcoSSB, la protéine de réplication A (RPA) chez les eucaryotes ou alors la protéine gp2.5 du phage T7 (Lee *et al*, 2014; Zhou *et al*, 2011; Nguyen *et al*, 2014). Des modèles de mécanismes de diffusion ont été proposés pour EcoSSB comme le modèle de déplacement par reptation ou par transfert intersegmental (**Figure 47**). Cependant, la dynamique de mtSSB n'a toujours pas été caractérisée.

Les propriétés de liaison de SSB, telles que son empreinte, son affinité avec sa vitesse de dissociation et d'association, peuvent être étudiées à la fois par des techniques d'analyse en

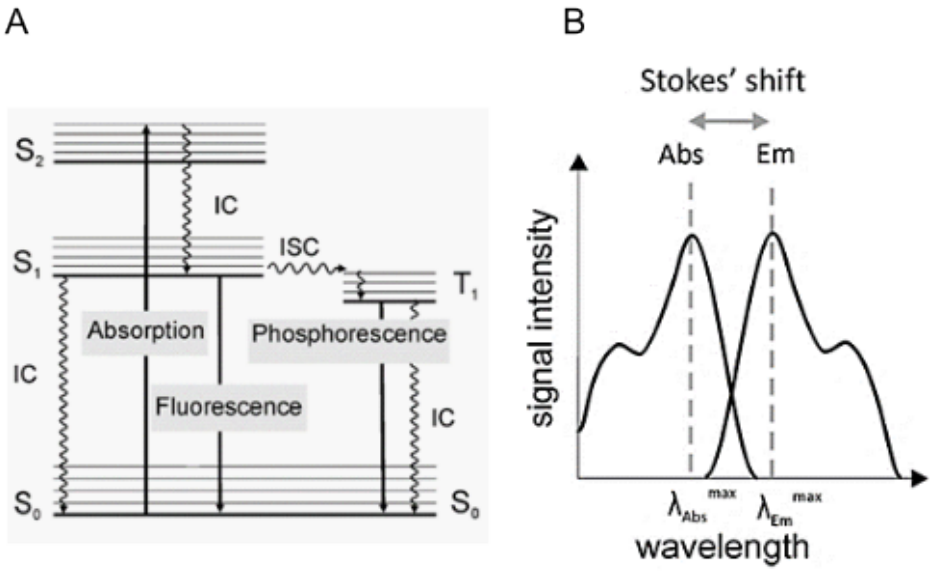

Figure 48: Schéma du diagramme de Jablonski et du décalage de Stoke. (**A**) Diagramme de Jablonski. Les états électroniques (S_0, S_1, S_2) et leurs états vibrationnels correspondant sont affichés sous forme de lignes horizontales. Les lignes ondulées illustrent une transition non radiative tandis que les lignes droites montrent une émission radiative. (**B**) Illustration du décalage de Stoke. La longueur d'onde d'excitation requise pour qu'un fluorophore absorbe la lumière (λ_{Abs}) est inférieure à la longueur d'onde d'émission de la lumière émise par le même fluorophore (λ_{Em}). Les pics auxquels la quantité maximale de lumière est absorbée et émise sont séparés par une distance appelée décalage de Stoke (Schémas tirés de van den Wildenberg, 2011).

masse et par des techniques à l'échelle de la molécule unique dites "single molecule". Cependant, la mécanique de liaison des protéines SSB à l'ADN simple brin sous tension peut être étudiée exclusivement avec des outils de spectroscopie de force à l'échelle de la molécule unique. L'étude de la mécanique de liaison peut être réalisée en analysant l'étirement des complexes mtSSB-ADNsb en fonction de la force appliquée. L'étirement forcé de l'ADNsb peut être obtenu à l'aide de méthodes de manipulation de l'ADN telles que les pinces optiques et magnétiques ("optical and magnetic tweezers") ou la spectroscopie de force acoustique (AFS).

Concernant les pathologies associées à mtSSB, il a été récemment rapporté que plusieurs variants de mtSSB provoquent une neuropathie/atrophie optique d'origine mitochondriale à caractère autosomique dominant et une dystrophie rétinienne avec ou sans déplétion de l'ADN mitochondrial. Jusqu'à présent, ces mutations ont été découvertes chez plus de 80 patients répartis dans une vingtaine de familles, et avec le développement de nouvelles méthodes de séquençage telles que le "whole exome sequencing (WES)" et les "next-generation sequencing (NGS)", ces chiffres augmentent rapidement (Kullar et al, 2018); Del Dotto et al, 2019 ; Pyro-Mégy et al, 2019 ; Jurkute et al, 2019 ; Gustafson et al, 2021).

Principe de la fluorescence

La fluorescence est un processus par lequel la matière absorbe la lumière et la réémet à une longueur d'onde différente. Le processus de fluorescence a été introduit pour la première fois par Sir George Gabriel Stoke en 1852 et expliqué en 1933 par le professeur Aleksander Jablonski dans le diagramme qui porte son nom : le diagramme de Jablonski (**Figure 48A**). Lorsqu'un fluorophore absorbe des photons, ses électrons vont passer par plusieurs états électroniques de différents niveaux d'énergie (S_0, S_1, S_2); d'un état de relaxation (état fondamental S_0) à un état excité (S_1, S_2). Lorsque les électrons sont excités dans des états électroniques singulets supérieurs (S_1, S_2), ils se détendent spontanément par différents mécanismes tels que la relaxation vibratoire à l'intérieur du même état électronique, par conversion interne (IC), par ré-émission de photons qui caractérise la fluorescence ou par croisement intersystème (ISC). Lorsque les électrons se détendent d'un état électronique supérieur à un état électronique inférieur, ils perdent de l'énergie. De ce fait, l'énergie de la lumière d'excitation est toujours inférieure à l'énergie de la lumière émise par le fluorophore.

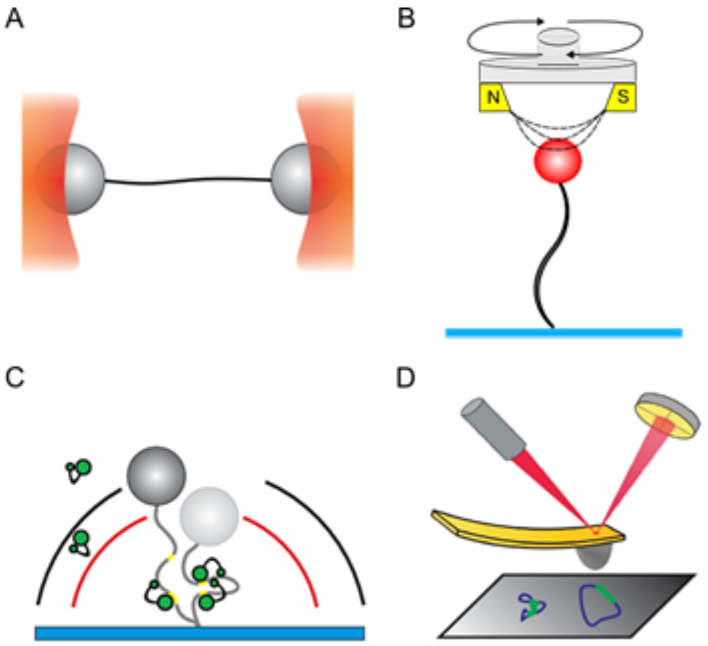

Figure 49: Techniques courantes dites de « single molecule ». (**A**) Double pinces optiques. (**B**) Pinces magnétiques. (**C**) Mouvement de particules captives (TPM). (**D**) Microscopie à force atomique (AFM) (Schéma de la pince magnétique adapté de Takahashi et al, 2021).

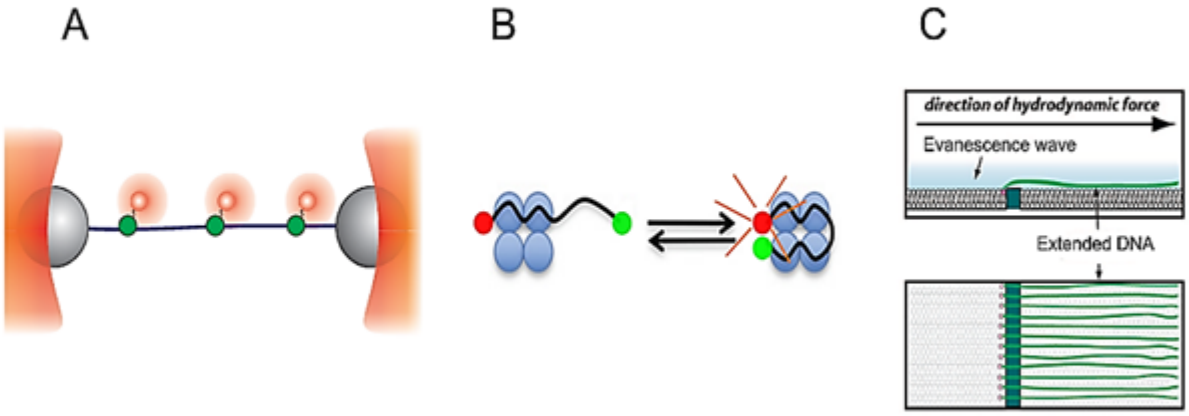

Figure 50: Techniques courantes de microscopie à fluorescence à l'échelle de la molécule unique. (**A**) Schéma d'une double pince optique. Une molécule d'ADN est piégée à ses deux extrémités par des microbilles qui interagissent généralement avec la liaison biotine-streptavidine. Les deux microbilles sont ensuite manipulées par des faisceaux laser (faisceau rouge) permettant la manipulation de l'ADN. La protéine fluorescente d'intérêt peut être utilisée et visualisée par différents types de microscopie à fluorescence telles que la microscopie à champ large, la microscopie confocal ou de super-résolution. (**B**) Illustration de la technique FRET avec un couple de fluorophores. Le changement conformationnel de la protéine en bleu est observé lorsque les deux fluorophores atteignent une distance suffisante pour permettre au fluorophore vert de transférer son énergie au fluorophore rouge qui émet alors une fluorescence. (**C**) Dessin de la méthode des rideaux d'ADN. Dans une chambre microfluidique fonctionnalisée avec une bicouche lipidique, les molécules d'ADN y sont attachées. Ces ADN sont poussés par un courant hydrodynamique vers une nanobarrière qui va stopper leur progression et conduire à l'alignement des molécules d'ADN (Illustration FRET adaptée de Qian et Johnson, 2017 et schéma des rideaux d'ADN de Fazio et al, 2008).

C’est pourquoi les fluorophores affichent toujours une longueur d'onde d'excitation inférieure à la longueur d'onde d'émission illustrée par le décalage de Stoke (**Figure 48B**).

Un aspect crucial de la conduite d’une expérience de microscopie est le choix du fluorophore adéquat. Les fluorophores peuvent être classés selon leur nature. On peut distinguer (i) les colorants synthétiques tels que les colorants Cy3, Alexa Fluors et ATTO, ou l'isothiocyanate de fluorescéine (FITC), (ii) les protéines fluorescentes comme la protéine fluorescente verte améliorée (eGFP) ou la protéine fluorescente jaune (YFP) qui contiennent une structure chimique aux propriétés fluorescentes, (iii) les “quantum dots” qui sont des structures nanocristallines semi-conductrices et (iv) des fluorophores naturels tels que la chlorophylle ou la flavine (van den Wildenberg et al, 2011). Les fluorophores ont des propriétés importantes qui ont une influence sur les expériences et les résultats, et doivent donc être choisis avec soin. Parmi ces propriétés, on trouve le spectre d’absorption et d’émission du fluorophore, sa taille, son coefficient d’extinction molaire, son rendement quantique et son temps de vie à l’état excité. Toutefois, les caractéristiques des fluorophores peuvent également être affectées par l'environnement local, comme le pH, la polarité, les ions ou l'interaction avec d'autres molécules qui pourraient éteindre le fluorophore ou entraver sa capacité à pénétrer dans la cellule.

Étudier les interactions ADN-protéines avec des méthodes à l’échelle de la molécule unique (“single molecule”)

La biophysique des molécules uniques est née avec un défi expérimental : est-il possible d'examiner et d'étudier une seule molécule biologique ? Au cours de la dernière décennie, les techniques de molécules uniques ont connu une croissance remarquable dans le domaine de la biologie et peuvent être divisées en deux catégories principales : (i) la spectroscopie de force (**Figure 49**) et (ii) la spectroscopie de fluorescence **(Figure 50**). La recherche sur des molécules uniques en biophysique a été récompensée par un prix Nobel de chimie partagé en 2014 décerné à Stefan Hell, Eric Betzig et William Moerner, et en 2018 par un prix Nobel de physique décerné à Arthus Ashkin pour ses travaux sur les pinces optiques.

Les méthodes dites “single molecule” fournissent des informations complémentaires aux expériences biochimiques classiques. Ces techniques, comme la micromanipulation ou l'imagerie de fluorescence, permettent d'éliminer les effets de moyenne spatiale et temporelle inhérents aux mesures globales et donnent accès à des événements rares ou transitoires,

difficiles à observer par des mesures globales. Le terme “single molecule” fait référence aux expériences qui se concentrent sur l’étude des propriétés de molécules individuelles. Au cours des deux dernières décennies, des techniques de biophysiques ont émergé et ont rendu possible la manipulation de l’ADN et l’imagerie des complexes ADN-protéines en temps réel.

La spectroscopie de force à l’échelle de la molécule unique, telles que les pinces optiques (**Figure 49A**) et magnétiques (**Figure 49B**), est couramment utilisée pour étudier les propriétés mécaniques des biopolymères comme l'ADN et leurs interactions avec d'autres molécules. Ces méthodes permettent, entre autres, d'étudier les paramètres mécaniques de l'ADN (comme sa flexibilité ou sa longueur) mais elles peuvent également donner des informations sur la cinétique et la mécanique d’interaction des protéines liées comme les ADN polymérases par exemple (Gross et al, 2010). La combinaison des méthodes de manipulation par la force et de visualisation par la fluorescence, telle que les pinces optiques couplées avec la microscopie à fluorescence (**Figure 50A**) ou le transfert d'énergie par résonance (FRET) (**Figure 50B**) sur molécule unique (smFRET), a amélioré notre connaissance des mécanismes d'interaction ADN-protéine. Cela a permis de mieux comprendre les événements biologiques en visualisant et en analysant le comportement de biomolécules individuelles interagissant avec d'autres. Aujourd’hui, certaines de ces techniques ont été standardisées, avec de nombreuses solutions commerciales et supports techniques disponibles.

Les techniques dites “single molecule” ont connu un engouement, notamment car dans les tests en masse (comme l'électrophorèse sur gel), des millions de biomolécules sont soumises à l'analyse et, par conséquent, les résultats révèlent le comportement moyen d'un grand nombre de molécules (Takahashi et al, 2021). En revanche, les techniques “single molecule” révèlent non seulement le comportement moyen, mais fournissent également des informations sur la dynamique de ces molécules au cours d'un processus biologique dans lequel la même molécule peut agir de manières différentes.

L’une des principales limites des techniques de “single molecule” est que de nombreuses expériences sont souvent nécessaires pour fournir un grand nombre d’observations et étudier de manière adéquate la distribution des échantillons, les sous-populations et les événements rares (Hill et al, 2017). Pour pallier cette limitation, des techniques sur molécule unique ont été développées, qui sont compétitives dans l'analyse de données à haut débit, comme les rideaux d'ADN (**Figure 50C**), la spectroscopie de force acoustique ou encore les pinces magnétiques.

Les techniques de fluorescence à l'échelle de la molécule unique se sont révélées particulièrement pertinentes pour visualiser et quantifier le mouvement des protéines. Le mouvement des molécules individuelles peut être quantifié en calculant le déplacement moyen au carré (MSD). De plus, les méthodes "single molecule" couplées à la fluorescence procurent des informations sur l'emplacement et la dynamique des protéines se liant à un ligand, telles que leur affinité de liaison, ou les changements de conformation au sein des molécules (Gross et al, 2010).

La microscopie à fluorescence est devenue un outil indispensable et courant pour les biologistes, car elle peut être utilisée pour observer et localiser des biomolécules dans les cellules. Cependant, ce que l'on observe en microscopie à fluorescence standard, ce sont des millions de molécules. Dès lors, une question se pose : est-il possible d'observer avec précision la fluorescence émise par une seule molécule ? Pour cela, les molécules doivent être manipulées séparément et l'illumination doit être contrôlée pour exciter uniquement les molécules souhaitées. La microscopie à fluorescence d'une seule molécule repose ainsi sur la détection précise de la fluorescence émise par une ou plusieurs molécules uniques en temps réel, tout en s'efforçant de limiter le bruit de fond afin d'augmenter le rapport signal sur bruit. En effet, pour récolter des informations plus détaillées et plus claires, il est important d'avoir un rapport signal sur bruit le plus élevé possible. Les approches pour y parvenir incluent la conception de fluorophores à haut rendement quantique et le développement de méthodes de microscopie pour diminuer le signal de fond et exciter uniquement de petits volumes autour de la molécule d'intérêt.

La microscopie à fluorescence sur molécules uniques peut être classée en deux grandes catégories qui sont (i) la microscopie à fluorescence confocale où une image est générée en balayant un échantillon avec un laser focalisé, tandis qu'un "pinhole" devant le détecteur bloque la lumière qui ne provient pas du plan focal et (ii) microscopie à fluorescence à grand champ où une plus grande région autour de l'échantillon est excitée (Gross et al, 2010). Mais comment pouvons-nous réduire le signal de fond en microscopie à fluorescence à grand champ ? Une méthode efficace est la microscopie à fluorescence par réflexion interne totale (TIRF) qui a été développée par Axelrod *et al* (Axelrod et al, 1983). La microscopie TIRF s'appuie sur la loi de Snell et Descartes selon laquelle un faisceau laser peut être totalement réfléchi au contact d'une surface s'il arrive avec un angle particulier appelé angle critique. Au point de contact, une onde

d'évanescence est générée et son énergie décroît de façon exponentielle à mesure qu'elle traverse le milieu dans lequel réside l'échantillon. En conséquence, seules les molécules situées dans la région entre la surface et 100 à 200 nm au-dessus de celle-ci sont excitées, ce qui améliore considérablement le rapport signal/bruit de fond puisque les molécules en solution ne sont pas excitées. La microscopie TIRF est bien adaptée à la manipulation de l'ADN nécessitant un ancrage de l'ADN sur une surface. Combinées aux techniques de manipulation de l’ADN, les techniques de microscopie à fluorescence sur molécule unique ont amélioré notre compréhension des mécanismes sous-jacents aux interactions ADN-protéine et protéine-protéine.

Objectifs de la thèse

Il reste encore beaucoup à savoir sur le métabolisme de l’ADN mitochondrial et sur les fonctions des mitochondries au sein des cellules. Les mitochondries ont suscité davantage d'intérêt depuis le développement des “NGS”, qui facilitent grandement le diagnostic des maladies mitochondriales. Les maladies mitochondriales sont des maladies génétiques rares, généralement héréditaires, avec une prévalence estimée à 1 sur 5 000 nouveau-nés. Elles présentent une grande hétérogénéité clinique en raison de l’ubiquité des mitochondries dans les organes et tissus. Les mutations génétiques conduisant à des maladies mitochondriales peuvent affecter soit l'ADN nucléaire, soit l'ADN mitochondrial. Cela a pour conséquence d’affecter un grand nombre de protéines impliquées dans de nombreux processus différents, tels que le maintien de l'ADN mitochondrial, la fusion mitochondriale, la synthèse d'ATP par la chaîne de transport d'électrons, le maintien d'un pool équilibré de nucléotides, ou la régulation de l'homéostasie.

Les maladies peuvent être étudiées à différents niveaux, qui peuvent être au niveau des organes et des tissus, au niveau des cellules ou au niveau moléculaire. Au cours des deux dernières décennies, des méthodes “single molecule” sont apparues et ont permis de comprendre les mécanismes d’interaction ADN-protéine au niveau d’une seule molécule. Ils sont donc utiles pour comprendre le mécanisme de protéines mutantes identifiées comme étant impliquées dans des maladies. Dans cette thèse, nous avons utilisé deux techniques dites “single molecule” : la spectroscopie de force acoustique (AFS) et la microscopie à fluorescence par réflexion interne totale (TIRFm) couplées avec l'étirement d'ADN par force de courant fluidique, ainsi que la caractérisation biochimique de deux variantes de protéines de maintenance mitochondriale, à

savoir TFAM P178L et mtSSB R107Q afin de donner un aperçu des mécanismes impliqués dans le défaut de la maintenance mitochondriale.

Le premier chapitre de cette thèse concerne la description et la configuration des expériences TIRF et AFS afin d'analyser le mouvement des protéines et l'interaction avec les molécules d’ADN. Dans ce chapitre sont également abordés les problèmes qui peuvent être rencontrés lors de ces expériences ainsi que des conseils pour les éviter ou les surmonter.

Le deuxième chapitre traite de l'étude du mutant TFAM P178L, pathogène, qui s'est révélé impliqué dans la déplétion de l'ADNmt chez les patients. Nous avons réalisé des expériences biochimiques telles qu'un test de réplication in vitro (“rolling circle”), la transcription in vitro avec HSP et LSP, des tests de déplacement d'électromobilité (EMSA), ainsi qu'une modélisation de structure et un test de stabilité thermique. Ceci a permis de caractériser les fonctions de TFAM P178L dans la réplication et la transcription, sa stabilité et son affinité de liaison spécifique et non spécifique, ainsi que sa dégradation par LONP1. Ensuite, nous avons analysé sa capacité à lier et à compacter l’ADN en utilisant la spectroscopie de force acoustique (AFS). Enfin, nous avons mené des expériences de microscopie TIRF pour évaluer et quantifier sa dynamique en déterminant les événements de diffusion caractéristiques ainsi que son coefficient de diffusion.

Le troisième chapitre était axé sur l'étude du variant SSB humain R107Q qui a récemment fait l'objet d'une étude clinique et qui est également impliquée dans des défauts de maintenance mitochondriale tels que l'épuisement et la délétion de l'ADNmt conduisant à des troubles mitochondriaux. L'objectif était de caractériser le mécanisme moléculaire des interactions ADN-SSB R107Q par rapport au SSB WT afin de connaître les effets de la mutation sur le mécanisme de mtSSB. Les techniques utilisées étaient les mêmes techniques que pour l’étude de TFAM P178L, à savoir l'AFS et la microscopie TIRF.

Chapitre 2.1 : Quantifier la compaction de l'ADN et la dynamique de TFAM à l'aide de la microscopie TIRF et de l’AFS

La microscopie à fluorescence par réflexion interne totale (TIRF) a été développée en réponse à une problématique : comment améliorer le rapport signal sur bruit en microscopie à fluorescence en champ large? La microscopie confocale améliore considérablement le rapport

signal sur bruit en bloquant les photons qui ne proviennent pas du plan focal, augmentant ainsi la résolution axiale. Cependant, le temps d'acquisition peut être long et la puissance d'illumination est généralement élevée, ce qui limite l'utilisation de faibles concentrations de fluorophores ou bien l'enregistrement de vidéos qui sont utiles pour étudier le mouvement de particule. C'est en ce point que la microscopie TIRF se démarque. La microscopie TIRF repose sur un faisceau laser qui sort de l'objectif sous un angle particulier (appelé angle critique) conduisant à une réflexion totale du laser à l'interface entre le verre et l'échantillon. Au point de contact, une onde d'évanescence est générée dont son énergie décroît de façon exponentielle au fur et à mesure qu'elle traverse l'échantillon, excitant les fluorophores sur 200 nm de profondeur avec une faible puissance. Par conséquent, la microscopie TIRF améliore considérablement la résolution axiale et le rapport signal sur bruit en excitant seulement une petite région d'intérêt. Associé à la manipulation d'ADN, la microscopie TIRF est un puissant outil pour visualiser simultanément un grand nombre de molécules d'ADN ancrées sur une surface de verre, et avec une faible puissance d'illumination. C'est donc une excellente méthode pour étudier le mouvement d'une molécule isolée en interaction avec l'ADN.

La spectroscopie de force acoustique (AFS) est une technique de spectroscopie de force sur molécule unique qui permet la manipulation simultanée de plusieurs brins d'ADN ancrés sur une surface et dans une chambre microfluidique. Permettant les échanges de tampons, c'est un excellent outil pour analyser les interactions ADN-protéine avec des variations de composition du milieu et en ajoutant d'autres protéines d'intérêt. Une extrémité des ADN est attachée à la surface en verre de la chambre et l'autre extrémité à une microbille. En exerçant une force acoustique sur les billes, il est possible de manipuler indirectement les ADN, en les étirant ou en les maintenant statiques à une force constante. En corrélant le déplacement des billes avec les forces appliquées, on obtient une courbe force-distance qui renseigne sur les propriétés mécaniques des ADN, avec ou sans protéines.

Ici, nous avons décrit en détail, étape par étape, deux méthodologies pour étudier la liaison, la compaction et le mouvement de TFAM sur des molécules d'ADN double brin individuelles avec la microscopie TIRF et l'AFS. Nous avons décrit étape par étape comment obtenir des ADN ancrés sur la surface avec des templates d'ADN par PCR et comment mesurer les effets de TFAM sur l'ADN via l'analyse du "root mean square" (RMS) et de la courbe force-distance. Dans un second temps, nous avons décrit étape par étape comment réaliser une microscopie TIRF à deux couleurs avec notre dispositif expérimental personnalisé, du marquage de TFAM

avec un fluorophore, à la manipulation de l'ADN par étirement par courant fluidique dans une chambre microfluidique, pour finir par le suivi de TFAM sur l'ADN. De plus, cet article donne un aperçu des problèmes qui peuvent être rencontrés lors de telles expériences ainsi que des conseils pour éviter certains problèmes expérimentaux (publication 2.1).

Chapitre 2.2 : Etude du variant pathogène TFAM P178L

Le facteur de transcription mitochondrial A (TFAM) est un composant essentiel du nucléoïde mitochondrial des mammifères et participe activement à l'organisation et à l'expression de l'ADN mitochondrial (ADNmt). Récemment, un variant homozygote pathogène du TFAM (P178L) a été associé à un syndrome grave de déplétion de l'ADNmt conduisant à une insuffisance hépatique néonatale et à une mort précoce. Nous avons effectué une caractérisation biochimique et biophysique du variant TFAM P178L afin de comprendre les bases moléculaires de la pathogénicité de cette mutation. Nos résultats ont révélé une grave déplétion en ADNmt dans les cellules du patient, accompagnée d'une diminution du niveau de TFAM. Il est intéressant de noter que le niveau de l'ADN 7S est augmenté par rapport au niveau d'ADNmt dans les cellules du patient. Avec la spectroscopie de force acoustique, nous avons comparé les changements de flexibilité de l'ADN du mutant par rapport au WT, en mesurant la longueur de persistance et la longueur du contour de molécules d'ADN individuelles. Les résultats suggèrent que la flexibilité de l'ADN n'est que légèrement affectée par le changement d'acide aminé P178L. En revanche, la mutation altère gravement l'initiation de la transcription de l'ADNmt au niveau des promoteurs des brins lourds et légers. La modélisation moléculaire suggère que la mutation P178L affecte la reconnaissance des séquences promotrices et l'interaction entre TFAM et la "tether helix" de POLRMT, expliquant ainsi la diminution du niveau de la transcription (publication 2.2.1).

De plus, nous avons étudié la dynamique d'interaction en temps réel de TFAM WT et P178L sur l'ADN en utilisant la microscopie TIRF. Nous avons constaté que les coefficients de diffusion de TFAM sauvage et du variant P178L sont similaires. Pour les deux TFAM, il a été observé que les monomères s'associaient et se dissociaient à partir de groupe de TFAM, restaient statiques ou bien "rebondissaient" sans association. Des expériences à deux couleurs ont également montré que TFAM WT et le mutant interagissaient de la même manière. Une légère diminution du nombre de dimères chez TFAM P178L a été observée, ce qui indiquerait que la mutation P178L pourrait affecter la dimérisation de TFAM, même si des expériences plus poussées sont nécessaires pour confirmer ce résultat. Ce défaut de dimérisation pourrait

également être impliqué dans l'altération de l'initiation de la transcription. Le rôle de la dimérisation de TFAM dans la transcription étant sujet à débat (Gangelhoff et al, 2009 ; Ngo et al, 2014). De plus, une autre étude a montré que les niveaux de TFAM présentant un défaut de dimère étaient restaurés *in vivo* lors de l'inhibition de la protéase Lon et du protéasome du cytosol 20S, ce qui suggère que la dimérisation de TFAM pourrait être impliquée dans sa stabilité (Kasashima et Endo, 2015). Enfin, comme les interactions TFAM-TFAM sont importantes pour compacter efficacement les molécules d'ADNmt (Kukat et al, 2015), la dimérisation de TFAM ainsi que la formation d'états oligomériques supérieurs pourraient expliquer, dans une certaine mesure, la diminution de TFAM observé chez les patients (partie 2.2.2).

Chapitre 2.3 : Etude du variant pathogène mtSSB R107Q

L'ADN mitochondrial est continuellement répliqué et exprimé par une population de nucléoïdes actifs, indépendamment du cycle cellulaire. Comme les mitochondries hébergent la phosphorylation oxydative, elles sont en première ligne des dommages oxydatifs. Lors de la réplication, de la transcription ou lors d'une réparation de brin, l'ADNdb est transitoirement simple brin, donc plus vulnérable. Il existe une famille de protéines appelées protéines de liaison à l'ADN simple brin (protéines SSB) qui se lient avec une grande spécificité à l'ADN simple brin, le protégeant ainsi des dommages oxydatifs mais également des enzymes nucléolytiques. Malgré leur rôle de protection, ils participent également activement en tant qu'acteurs principaux à la maintenance de l'ADN. De nombreuses études visent à comprendre les rôles et les mécanismes des SSB dans le métabolisme de l'ADN (Xu et al, 2023, Jiang et al, 2021 ; Ciesielski et al, 2021 ; Plaza et al, 2023, Morin et al, 2017 ; Hensen et al, 2019). Néanmoins, seules quelques études ont été orientées vers la compréhension du mécanisme moléculaire de mtSSB chez les mammifères, et en particulier de mtSSB humain (HsmtSSB).

Depuis 2018, plusieurs rapports cliniques ont décrit des mutations de mtSSB associées à des maladies humaines (Kullar et al, 2018 ; Jurkute et al, 2019 ; Piro-Mégy et al, 2020 ; Del Dotto et al, 2020). Cependant, ces rapports manquent d'explications mécanistiques. Mon projet porte sur la compréhension des bases moléculaires de la pathogénicité d'une de ces mutations (R107Q). Pour cela, nous avons étudié les interactions de mtSSB avec l'ADN en utilisant des approches dites “single molecule” impliquant la microscopie TIRF et la spectroscopie de force acoustique (AFS). Nous avons quantifié sa compaction vis à vis de la teneur en sel du milieu et le taux de dissociation. De plus, nous avons étudié par compétition, l'affinité entre SSB

sauvage et mutant pour l'ADNsb. Dans l'ensemble, les résultats suggèrent que la mutation pourrait affecter les modes de liaison de la protéine ainsi que la compaction de l'ADNsb. Ces changements pourraient affecter le bon fonctionnement de la protéine et sa capacité à assurer la réplication de l'ADNmt. Des recherches plus approfondies devraient être menées visant à étudier son interaction avec un partenaire protéique tel que Polγ. En effet, il a été démontré que mtSSB augmentait la processivité de la polymérase et qu'il était impliqué dans l'initiation de la réplication de l'ADNmt. Enfin, la dynamique de diffusion de mtSSB reste encore à être déterminée. Cela pourrait être réalisé au laboratoire avec la microscopie TIRF (publication 2.3.1).

Actuellement, il n'existe aucun colorant commercial permettant de visualiser efficacement l'ADNsb en microscopie à fluorescence. Une stratégie pour surmonter ce problème consiste à utiliser des protéines SSB fluorescentes. Dans cet article, nous avons utilisé une méthode innovante pour visualiser l'ADNsb sans l'intermédiaire d'une protéine de liaison marquée par fluorescence. Ici, nous avons utilisé le colorant SYBR Green II qui est normalement utilisé dans la PCR quantitative pour détecter les niveaux d'ARN, mais il possède également une sensibilité pour l'ADNsb. Grâce à l'utilisation du fluorophore SYBR Green II, nous avons réussi à observer l'ADNsb en TIRF. Toutefois, son utilisation dépend de la concentration en sel. Cela pourrait améliorer la méthodologie actuelle de microscopie à fluorescence visant à comprendre les interactions ADNsb-protéine à l'échelle de la molécule unique et mériterait d'être étudiée plus en détail à l'avenir.

References

Agaronyan, K., Morozov I., Y., Anikin, M., & Temiakov, D. (2018). Replication-transcription switch in human mitochondria. *Physiology & Behavior*, *176*(5), 139–148. https://doi.org/10.4049/jimmunol.1801473.The

Andersson, S. G. E., Karlberg, O., Canbäck, B., Kurland, C. G., Whatley, F. R., Van Der Giezen, M., Martin, W., Tielens, A. G. M., Allen, J. F., & Raven, J. A. (2003). On the origin of mitochondria: A genomics perspective. *Philosophical Transactions of the Royal Society B: Biological Sciences*, *358*(1429), 165–179. https://doi.org/10.1098/rstb.2002.1193

Antony, E., & Lohman, T. M. (2019). Dynamics of E. coli single stranded DNA binding (SSB) protein-DNA complexes. *Seminars in Cell and Developmental Biology*, *86*, 102–111. https://doi.org/10.1016/j.semcdb.2018.03.017

Antony, E., Weiland, E. A., Korolev, S., & Lohman, T. M. (2012). Plasmodium falciparum SSB Tetramer Wraps Single Stranded DNA with Similar Topology but Opposite Polarity to E. coli SSB. *Journal of Molecular Biology*, *420*(0), 269–283. https://doi.org/10.1016/j.jmb.2012.04.021.Plasmodium

Archetti, A., Glushkov, E., Sieben, C., Stroganov, A., Radenovic, A., & Manley, S. (2019). Waveguide-PAINT offers an open platform for large field-of-view super-resolution imaging. *Nature Communications*, *10*(1). https://doi.org/10.1038/s41467-019-09247-1

Ashkin, A. (1992). Forces of a single-beam gradient laser trap on a dielectric sphere in the ray optics regime. *Biophysical Journal*, *61*(2), 569–582. https://doi.org/10.1016/S0006-3495(92)81860-X

Asin-Cayuela, J., Schwend, T., Farge, G., & Gustafsson, C. M. (2005). The human mitochondrial transcription termination factor (mTERF) is fully active in vitro in the non-phosphorylated form. *Journal of Biological Chemistry*, *280*(27), 25499–25505. https://doi.org/10.1074/jbc.M501145200

Axelrod, D., Thompson, N. L., & Burghardt, T. P. (1983). Total internal reflection fluorescent microscopy. *Journal of Microscopy*, *129*(1), 19–28. https://doi.org/10.1016/B978-012164730-8/50130-1

Bartlett, K., & Eaton, S. (2004). *European Journal of Biochemistry 1993 Hakkola.pdf* (pp. 462–469). Eur.J.Biochem.

Bayona-Bafaluy, M. P., Blits, B., Battersby, B. J., Shoubridge, E. A., & Moraes, C. T. (2005). Rapid directional shift of mitochondrial DNA heteroplasmy in animal tissues by a mitochondrially targeted restriction endonuclease. *Proceedings of the National Academy of Sciences of the United States of America*, *102*(40), 14392–14397. https://doi.org/10.1073/pnas.0502896102

Bell, J. C., Liu, B., & Kowalczykowski, S. C. (2015). Imaging and energetics of single SSB-ssDNA molecules reveal intramolecular condensation and insight into RecOR function. *Elife*, *4*. https://doi.org/10.7554/eLife.08646.001

Betzig, E., Patterson, G. H., Sougrat, R., Lindwasser, O. W., Olenych, S., Bonifacino, J. S., Davidson, M. W., Lippincott-Schwartz, J., & Hess, H. F. (2006). Imaging intracellular fluorescent proteins at nanometer resolution. *Science*, *313*(5793), 1642–1645. https://doi.org/10.1126/science.1127344

Bhattacharyya, B., George, N. P., Thurmes, T. M., Zhou, R., Jani, N., Wessel, S. R., Sandler, S. J., Ha, T., & Keck, J. L. (2014). Structural mechanisms of PriA-mediated DNA replication restart. *Proceedings of the National Academy of Sciences of the United States of America*, *111*(4), 1373–1378. https://doi.org/10.1073/pnas.1318001111

Bianco, P. R. (2017). The tale of SSB. In *Progress in Biophysics and Molecular Biology* (Vol. 127, pp. 111–118). Elsevier Ltd. https://doi.org/10.1016/j.pbiomolbio.2016.11.001

Bogenhagen, D. F., Wang, Y., Shen, E. L., & Kobayashi, R. (2003). Protein components of mitochondrial DNA nucleoids in higher eukaryotes. *Molecular & Cellular Proteomics : MCP*, *2*(11), 1205–1216. https://doi.org/10.1074/mcp.M300035-MCP200

Bogenhagen, D., & Clayton, D. A. (1978). Mechanism of mitochondrial DNA replication in mouse L-cells: RNA priming during the initiation of heavy-strand synthesis. *Journal of Molecular Biology*, *135*(2), 353–368. https://doi.org/10.1016/0022-2836(79)90441-8

Boguszewska, K., Kazmierczak-baranska, J., & Karwowski, B. T. (2020). The Similarities between Human Mitochondria and Bacteria in the Context of Structure, Genome, and Base Excision Repair System. *Molecules*, *25*(12), 2857. https://doi.org/10.3390/molecules25122857

Bonen, L., Cunningham, R. S., Gray, M. W., & Doolittle, W. F. (1977). Wheat embryo mitochondrial 18S ribosomal RNA: Evidence for its prokaryotic nature. *Nucleic Acids Research*, *4*(3), 663–671. https://doi.org/10.1093/nar/4.3.663

Boore, J. L. (1999). Animal mitochondrial genomes. *Nucleic Acids Research*, *27*(8), 1767–1780. https://doi.org/10.1093/nar/27.8.1767

Broderick, S., Rehmet, K., Concannon, C., & Nasheuer, H. P. (2010). Eukaryotic single-stranded dna binding proteins: Central factors in genome stability. *Sub-Cellular Biochemistry*, *50*, 143–163. https://doi.org/10.1007/978-90-481-3471-7_8

Brown, T. A., Tkachuk, A. N., Shtengel, G., Kopek, B. G., Bogenhagen, D. F., Hess, H. F., & Clayton, D. A. (2011). Superresolution Fluorescence Imaging of Mitochondrial Nucleoids Reveals Their Spatial Range, Limits, and Membrane Interaction. *Molecular and Cellular Biology*, *31*(24), 4994–5010. https://doi.org/10.1128/mcb.05694-11

Brüser, C., Keller-Findeisen, J., & Jakobs, S. (2021). The TFAM-to-mtDNA ratio defines inner-cellular nucleoid populations with distinct activity levels. *Cell Reports*, *37*(8). https://doi.org/10.1016/j.celrep.2021.110000

Bustamante, C., Bryant, Z., & Smith, S. B. (2003). Ten years of tension: single-molecule DNA mechanics. *Nature*, *421*(January), 423–427.

Byrnes, J., Hauser, K., Norona, L., Mejia, E., Simmerling, C., & Garcia-Diaz, M. (2016). Base Flipping by MTERF1 Can Accommodate Multiple Conformations and Occurs in a Stepwise Fashion. *Journal of Molecular Biology*, *428*(12), 2542–2556. https://doi.org/10.1016/j.jmb.2015.10.021

Campbell, C. T., Kolesar, J. E., & Kaufman, B. A. (2012). Mitochondrial transcription factor A regulates mitochondrial transcription initiation, DNA packaging, and genome copy number. *Biochimica et Biophysica Acta - Gene Regulatory Mechanisms*, *1819*(9–10), 921–929. https://doi.org/10.1016/j.bbagrm.2012.03.002

Canceill, D., & Ehrlich, S. D. (1996). Copy - Choice recombination mediated by DNA polymerase III holoenzyme from Escherichia coli. *Proceedings of the National Academy of Sciences of the United States of America*, *93*(13), 6647–6652. https://doi.org/10.1073/pnas.93.13.6647

Candelli, A., Hoekstra, T. P., Farge, G., Gross, P., Peterman, E. J. G., & Wuite, G. J. L. (2013). A toolbox for generating single-stranded DNA in optical tweezers experiments. *Biopolymers*, *99*(9), 611–620. https://doi.org/10.1002/bip.22225

Canugovi, C., Maynard, S., Bayne, A.-C. V., Sykora, P., Tian, J., de Souza-pinto, N. C., Croteau, D. L., & Bohr, V. A. (2010). THE MITOCHONDRIAL TRANSCRIPTION FACTOR A FUNCTIONS IN MITOCHONDRIAL BASE EXCISION REPAIR. *DNA Repair*, *9*(10), 1080–1089. https://doi.org/10.1016/j.dnarep.2010.07.009.THE

Chatterjee, N., & Walker, G. C. (2017). Mechanisms of DNA damage, repair, and mutagenesis. *Environmental and Molecular Mutagenesis*, *58*(5), 235–263. https://doi.org/10.1002/em.22087

Chinnery, P. F., Howell, N., Lightowlers, R. N., & Turnbull, D. M. (1997). *MELAS and MERRF*. 1713–1721.

Chung, J. W., Shin, D., Kwak, J. M., & Seog, J. (2013). Direct force measurement of single DNA-peptide interactions using atomic force microscopy. *Journal of Molecular Recognition*, *26*(6), 268–275. https://doi.org/10.1002/jmr.2269

Ciesielski, G. L., Bermek, O., Rosado-Ruiz, F. A., Hovde, S. L., Neitzke, O. J., Griffith, J. D., & Kaguni, L. S. (2015). Mitochondrial single-stranded DNA-binding proteins stimulate the activity of DNA polymerase γ by organization of the template DNA. *Journal of Biological Chemistry*, *290*(48), 28697–28707. https://doi.org/10.1074/jbc.M115.673707

Ciesielski, G. L., Kim, S., de Bovi Pontes, C., & Kaguni, L. S. (2021). Physical and Functional Interaction of Mitochondrial Single-Stranded DNA-Binding Protein and the Catalytic Subunit of DNA Polymerase Gamma. *Frontiers in Genetics*, *12*(September). https://doi.org/10.3389/fgene.2021.721864

Craig, K., Young, M. J., Blakely, E. L., Longley, M. J., Turnbull, D. M., Copeland, W. C., & Taylor, R. W. (2012). A p.R369G POLG2 mutation associated with adPEO and multiple mtDNA deletions causes decreased affinity between polymerase γ subunits. *Mitochondrion*, *12*(2), 313–319. https://doi.org/10.1016/j.mito.2011.11.006

Cuppari, A., Fernández-Millán, P., Battistini, F., Tarrés-Solé, A., Lyonnais, S., Iruela, G., Ruiz-López, E., Enciso, Y., Rubio-Cosials, A., Prohens, R., Pons, M., Alfonso, C., Tóth, K., Rivas, G., Orozco, M., & Solà, M. (2019). DNA specificities modulate the binding of human transcription factor A to mitochondrial DNA control region. *Nucleic Acids Research*, *47*(12), 6519–6537. https://doi.org/10.1093/nar/gkz406

CURTH, U., URBANKE, C., GREIPEL, J., GERBERDING, H., TIRANTI, V., & ZEVIANI, M. (1994). Single-stranded-DNA-binding proteins from human mitochondria and Escherichia coli have analogous physicochemical properties. *European Journal of Biochemistry*, *221*(1), 435–443. https://doi.org/10.1111/j.1432-1033.1994.tb18756.x

D'Souza, A. R., & Minczuk, M. (2018). Mitochondrial transcription and translation: Overview. In *Essays in Biochemistry* (Vol. 62, Issue 3, pp. 309–320). Portland Press Ltd. https://doi.org/10.1042/EBC20170102

Del Dotto, V., Ullah, F., Di Meo, I., Magini, P., Gusic, M., Maresca, A., Caporali, L., Palombo, F., Tagliavini, F., Baugh, E. H., MacAo, B., Szilagyi, Z., Peron, C., Gustafson, M. A., Khan, K., La Morgia, C., Barboni, P., Carbonelli, M., Valentino, M. L., … Carelli, V. (2020). SSBP1 mutations cause mtDNA depletion underlying a complex optic atrophy disorder. *Journal of Clinical Investigation*, *130*(1), 108–125. https://doi.org/10.1172/JCI128514

Di Donfrancesco, A., Massaro, G., Di Meo, I., Tiranti, V., Bottani, E., & Brunetti, D. (2022). Gene Therapy for Mitochondrial Diseases: Current Status and Future Perspective. *Pharmaceutics*, *14*(6). https://doi.org/10.3390/pharmaceutics14061287

Dickey, T. H., Altschuler, S. E., & Wuttke, D. S. (2013). Single-stranded DNA-binding proteins: Multiple domains for multiple functions. *Structure*, *21*(7), 1074–1084. https://doi.org/10.1016/j.str.2013.05.013

Doda, J. N., Wright, C. T., & Clayton, D. A. (1981). Elongation of displacement-loop strands in human and mouse mitochondrial DNA is arrested near specific template sequences. *Proceedings of the National Academy of Sciences of the United States of America*, *78*(10 I), 6116–6120. https://doi.org/10.1073/pnas.78.10.6116

Driessen, R. P. C., Sitters, G., Laurens, N., Moolenaar, G. F., Wuite, G. J. L., Goosen, N., & Dame, R. T. (2014). Effect of temperature on the intrinsic flexibility of DNA and its interaction with architectural proteins. *Biochemistry*, *53*(41), 6430–6438. https://doi.org/10.1021/bi500344j

El-Hattab, A. W., Craigen, W. J., & Scaglia, F. (2017). Mitochondrial DNA maintenance defects. *Biochimica et Biophysica Acta - Molecular Basis of Disease*, *1863*(6), 1539–1555. https://doi.org/10.1016/j.bbadis.2017.02.017

El-Hattab, A. W., & Scaglia, F. (2013). Mitochondrial DNA Depletion Syndromes: Review and Updates of Genetic Basis, Manifestations, and Therapeutic Options. *Neurotherapeutics*, *10*(2), 186–198. https://doi.org/10.1007/s13311-013-0177-6

Endo, T., & Yamano, K. (2010). Transport of proteins across or into the mitochondrial outer membrane. *Biochimica et Biophysica Acta - Molecular Cell Research*, *1803*(6), 706–714. https://doi.org/10.1016/j.bbamcr.2009.11.007

Falkenberg, M. (2018). Mitochondrial DNA replication in mammalian cells: Overview of the pathway. *Essays in Biochemistry*, *62*(3), 287–296. https://doi.org/10.1042/EBC20170100

Falkenberg, M., & Gustafsson, C. M. (2020). Mammalian mitochondrial DNA replication and mechanisms of deletion formation. *Critical Reviews in Biochemistry and Molecular Biology*, *55*(6), 509–524. https://doi.org/10.1080/10409238.2020.1818684

Farge, G., & Falkenberg, M. (2019). Organization of DNA in mammalian mitochondria. *International Journal of Molecular Sciences*, *20*(11), 2770. https://doi.org/10.3390/ijms20112770

Farge, G., Laurens, N., Broekmans, O. D., Van Den Wildenberg, S. M. J. L., Dekker, L. C. M., Gaspari, M., Gustafsson, C. M., Peterman, E. J. G., Falkenberg, M., & Wuite, G. J. L. (2012). Protein sliding and DNA denaturation are essential for DNA organization by human mitochondrial transcription factor A. *Nature Communications*, *3*. https://doi.org/10.1038/ncomms2001

Farge, G., Mehmedovic, M., Baclayon, M., vandenWildenberg, S. M. J. L., Roos, W. H., Gustafsson, C. M., Wuite, G. J. L., & Falkenberg, M. (2014). In Vitro-reconstituted nucleoids can block mitochondrial DNA replication and transcription. *Cell Reports*, *8*(1), 66–74. https://doi.org/10.1016/j.celrep.2014.05.046

Fazio, T., Visnapuu, M. L., Wind, S., & Greene, E. C. (2008). DNA curtains and nanoscale curtain rods: High-throughput tools for single molecule imaging. *Langmuir*, *24*(18), 10524–10531. https://doi.org/10.1021/la801762h

Feric, M., Demarest, T. G., Tian, J., Croteau, D. L., Bohr, V. A., & Misteli, T. (2021). Self-assembly of multi-component mitochondrial nucleoids via phase separation. *The EMBO Journal*, *40*(6). https://doi.org/10.15252/embj.2020107165

Flynn, R. L., & Zou, L. (2010). Oligonucleotide/oligosaccharide-binding fold proteins: A growing family of genome guardians. *Critical Reviews in Biochemistry and Molecular Biology*, *45*(4), 266–275. https://doi.org/10.3109/10409238.2010.488216

Frey, T. G., Renken, C. W., & Perkins, G. A. (2002). *Insight into mitochondrial structure and function from electron tomography*. *1555*, 196–203.

Fusté, J. M., Wanrooij, S., Jemt, E., Granycome, C. E., Cluett, T. J., Shi, Y., Atanassova, N., Holt, I. J., Gustafsson, C. M., & Falkenberg, M. (2010). Mitochondrial RNA Polymerase Is Needed for Activation of the Origin of Light-Strand DNA Replication. *Molecular Cell*, *37*(1), 67–78. https://doi.org/10.1016/j.molcel.2009.12.021

Gangelhoff, T. A., Mungalachetty, P. S., Nix, J. C., & Churchill, M. E. A. (2009). Structural analysis and DNA binding of the HMG domains of the human mitochondrial transcription factor A. *Nucleic Acids Research*, *37*(10), 3153–3164. https://doi.org/10.1093/nar/gkp157

Gaspari, M., Larsson, N. G., & Gustafsson, C. M. (2004). The transcription machinery in mammalian mitochondria. *Biochimica et Biophysica Acta - Bioenergetics*, *1659*(2–3), 148–152. https://doi.org/10.1016/j.bbabio.2004.10.003

Gibb, B., Silverstein, T. D., Finkelstein, I. J., & Greene, E. C. (2012). Single-stranded DNA curtains for real-time single-molecule visualization of protein-nucleic acid interactions. *Analytical Chemistry*, *84*(18), 7607–7612. https://doi.org/10.1021/ac302117z

Goffart, S., Cooper, H. M., Tyynismaa, H., Wanrooij, S., Suomalainen, A., & Spelbrink, J. N. (2009). Twinkle mutations associated with autosomal dominant progressive external ophthalmoplegia lead to impaired helicase function and in vivo mtDNA replication stalling. *Human Molecular Genetics*, *18*(2), 328–340. https://doi.org/10.1093/hmg/ddn359

Gray, M. W. (2012). Mitochondrial Evolution. *Mitochondrial Evolution*, *4*(9), a011403.

Gross, P., Farge, G., Peterman, E. J. G., & Wuite, G. J. L. (2010). Combining Optical Tweezers, Single-Molecule Fluorescence Microscopy, and Microfluidics for Studies of DNA-Protein Interactions. In *Methods in Enzymology* (1st ed., Vol. 475, Issue C). Elsevier Inc. https://doi.org/10.1016/S0076-6879(10)75017-5

Gunn, K. H., Marko, J. F., & Mondragón, A. (2018). Single-molecule magnetic tweezer analysis of topoisomerases. *Methods in Molecular Biology*, *1703*, 139–152. https://doi.org/10.1007/978-1-4939-7459-7_10

Guo, J. T., & Malik, F. (2022). Single-Stranded DNA Binding Proteins and Their Identification Using Machine Learning-Based Approaches. *Biomolecules*, *12*(9). https://doi.org/10.3390/biom12091187

Gustafson, M. A., Perera, L., Shi, M., & Copeland, W. C. (2021). Mechanisms of SSBP1 variants in mitochondrial disease: Molecular dynamics simulations reveal stable tetramers with altered DNA binding surfaces. *DNA Repair*, *107*, 103212. https://doi.org/10.1016/j.dnarep.2021.103212

Gustafsson, C. M., Falkenberg, M., & Larsson, N. G. (2016). Maintenance and Expression of Mammalian Mitochondrial DNA. *Annual Review of Biochemistry*, *85*, 133–160. https://doi.org/10.1146/annurev-biochem-060815-014402

Gustafsson, C. M., Falkenberg, M., & Larsson, N. G. (2016). Maintenance and Expression of Mammalian Mitochondrial DNA. *Annual Review of Biochemistry*, *85*, 133–160. https://doi.org/10.1146/annurev-biochem-060815-014402

Hamon, L., Pastré, D., Dupaigne, P., Le Breton, C., Le Cam, E., & Piétrement, O. (2007). High-resolution AFM imaging of single-stranded DNA-binding (SSB) protein - DNA complexes. *Nucleic Acids Research*, *35*(8), 1–7. https://doi.org/10.1093/nar/gkm147

Hamon, L., Pastré, D., Dupaigne, P., Le Breton, C., Le Cam, E., & Piétrement, O. (2007). High-resolution AFM imaging of single-stranded DNA-binding (SSB) protein - DNA complexes. *Nucleic Acids Research*, *35*(8). https://doi.org/10.1093/nar/gkm147

Heller, I., Sitters, G., Broekmans, O. D., Farge, G., Menges, C., Wende, W., Hell, S. W., Peterman, E. J. G., & Wuite, G. J. L. (2013). STED nanoscopy combined with optical tweezers reveals protein dynamics on densely covered DNA. *Nature Methods*, *10*(9), 910–916. https://doi.org/10.1038/nmeth.2599

Henneman, B., Heinsman, J., Battjes, J., & Dame, R. T. (2018). Quantitation of DNA-Binding Affinity Using Tethered Particle Motion. *Bacterial Chromatin: Methods and Protocols*, 257–275.

Hensen, F., Potter, A., Van Esveld, S. L., Tarrés-Solé, A., Chakraborty, A., Solà, M., & Spelbrink, J. N. (2019). Mitochondrial RNA granules are critically dependent on mtDNA replication factors Twinkle and mtSSB. *Nucleic Acids Research*, *47*(7), 3680–3698. https://doi.org/10.1093/nar/gkz047

Hill, F. R., Monachino, E., & Van Oijen, A. M. (2017). The more the merrier: High-throughput single-molecule techniques. *Biochemical Society Transactions*, *45*(3), 759–769. https://doi.org/10.1042/BST20160137

Hillen, H. S., Morozov, Y. I., Sarfallah, A., Temiakov, D., & Cramer, P. (2017). Structural Basis of Mitochondrial Transcription Initiation. *Cell*, *171*(5), 1072.e10-1081.e10. https://doi.org/10.1016/j.cell.2017.10.036

Hillen, H. S., Morozov, Y. I., Sarfallah, A., Temiakov, D., & Cramer, P. (2017). Structural Basis of Mitochondrial Transcription Initiation. *Cell*, *171*(5), 1072.e10-1081.e10. https://doi.org/10.1016/j.cell.2017.10.036

Holland, H. D. 1994 Early proterozoic atmospheric change. In Early life on earth (ed. S. Bengtson), pp. 237–244. New York: Columbia University Press.

Holmes, J. B., Akman, G., Wood, S. R., Sakhuja, K., Cerritelli, S. M., Moss, C., Bowmaker, M. R., Jacobs, H. T., Crouch, R. J., & Holt, I. J. (2015). Primer retention owing to the absence of RNase H1 is catastrophic for mitochondrial DNA replication. *Proceedings of the National Academy of Sciences of the United States of America*, *112*(30), 9334–9339. https://doi.org/10.1073/pnas.1503653112

Holt, I. J., Lorimer, H. E., & Jacobs, H. T. (2000). Coupled Leading-and Lagging-Strand Synthesis of Mammalian Mitochondrial DNA eubacteria. Replication of the H strand on this model is proposed to initiate at a single site (O H), and to proceed unidirectionally until two-thirds of the way around the These. *Cell*, *100*, 515–524.

Houten, S. M., & Wanders, R. J. A. (2010). A general introduction to the biochemistry of mitochondrial fatty acid β-oxidation. *Journal of Inherited Metabolic Disease*, *33*(5), 469–477. https://doi.org/10.1007/s10545-010-9061-2

Ibarra, B., Chemla, Y. R., Plyasunov, S., Smith, S. B., Lázaro, J. M., Salas, M., & Bustamante, C. (2009). Proofreading dynamics of a processive DNA polymerase. *EMBO Journal*, *28*(18), 2794–2802. https://doi.org/10.1038/emboj.2009.219

Jansen, J. J., Maassen, J. A., Van Der Woude, F. J., Lemmink, H. A. J., Van Den Ouweland, J. M. W., 'T Hart, L. M., Smeets, H. J. M., Bruijn, J. A., & Lemkes, H. H. P. J. (1997). Mutation in mitochondrial tRNA(Leu(UUR)) gene associated with progressive kidney disease. *Journal of the American Society of Nephrology*, *8*(7), 1118–1124. https://doi.org/10.1681/asn.v871118

Jardel, C., & Rucheton, B. (2018). Diagnostic des maladies mitochondriales. *Revue Francophone Des Laboratoires*, *2018*(501), 36–48. https://doi.org/10.1016/s1773-035x(18)30119-9

Jemt, E., Persson, Ö., Shi, Y., Mehmedovic, M., Uhler, J. P., López, M. D., Freyer, C., Gustafsson, C. M., Samuelsson, T., & Falkenberg, M. (2015). Regulation of DNA replication at the end of the mitochondrial D-loop involves the helicase TWINKLE and a conserved sequence element. *Nucleic Acids Research*, *43*(19), 9262–9275. https://doi.org/10.1093/nar/gkv804

Jiang, M., Xie, X., Zhu, X., Jiang, S., Milenkovic, D., Misic, J., Shi, Y., Tandukar, N., Li, X., Atanassov, I., Jenninger, L., Hoberg, E., Albarran-Gutierrez, S., Szilagyi, Z., Macao, B., Siira, S. J., Carelli, V., Griffith, J. D., Gustafsson, C. M., … Falkenberg, M. (2021). The mitochondrial single-stranded DNA binding protein is essential for initiation of mtDNA replication. *Science Advances*, *7*(27). https://doi.org/10.1126/sciadv.abf8631

Jiang, S., Koolmeister, C., Misic, J., Siira, S., Kühl, I., Silva Ramos, E., Miranda, M., Jiang, M., Posse, V., Lytovchenko, O., Atanassov, I., Schober, F. A., Wibom, R., Hultenby, K., Milenkovic, D., Gustafsson, C. M., Filipovska, A., & Larsson, N. (2019). TEFM regulates both transcription elongation and RNA processing in mitochondria. *EMBO Reports*, *20*(6), 1–18. https://doi.org/10.15252/embr.201948101

Joung, J. K., & Sander, J. D. (2013). *Nat Rev Mol Cell Biol. 14*. *14*(1), 49–55. https://doi.org/10.1038/nrm3486.TALENs

Judge, A., & Dodd, M. S. (2020). *Metabolism*. *0*(July), 607–647.

Juette, M. F., Terry, D. S., Wasserman, M. R., Zhou, Z., Altman, R. B., Zheng, Q., & Blanchard, S. C. (2014). The bright future of single-molecule fluorescence imaging. *Current Opinion in Chemical Biology*, *20*(1), 103–111. https://doi.org/10.1016/j.cbpa.2014.05.010

Jurkute, N., Leu, C., Pogoda, H. M., Arno, G., Robson, A. G., Nürnberg, G., Altmüller, J., Thiele, H., Motameny, S., Toliat, M. R., Powell, K., Höhne, W., Michaelides, M., Webster, A. R., Moore, A. T., Hammerschmidt, M., Nürnberg, P., Yu-Wai-Man, P., & Votruba, M. (2019). SSBP1 mutations in dominant optic atrophy with variable retinal degeneration. *Annals of Neurology*, *86*(3), 368–383. https://doi.org/10.1002/ana.25550

Kamiyama, D., & Huang, B. (2012). Development in the STORM. *Developmental Cell*, *23*(6), 1103–1110. https://doi.org/10.1016/j.devcel.2012.10.003

Kamsma, D., Bochet, P., Oswald, F., Alblas, N., Goyard, S., Wuite, G. J. L., Peterman, E. J. G., & Rose, T. (2018). Single-Cell Acoustic Force Spectroscopy: Resolving Kinetics and Strength of T Cell Adhesion to Fibronectin. *Cell Reports*, *24*(11), 3008–3016. https://doi.org/10.1016/j.celrep.2018.08.034

Kang, I., Chu, C. T., Kaufman, B. A., & Protein, C. (2018). neurodegeneration : Emerging evidence and mechanisms. *FEBS Letters*, *592*(5), 793–811. https://doi.org/10.1002/1873-3468.12989.The

Kasashima, K., & Endo, H. (2015). Interaction of human mitochondrial transcription factor A in mitochondria: Its involvement in the dynamics of mitochondrial DNA nucleoids. *Genes to Cells*, *20*(12), 1017–1027. https://doi.org/10.1111/gtc.12306

Kaur, G., Lewis, J. S., & Van Oijen, A. M. (2019). Shining a spotlight on DNA: Single-molecule methods to visualise DNA. *Molecules*, *24*(3), 1–20. https://doi.org/10.3390/molecules24030491

Kaur, P., Longley, M. J., Pan, H., Wang, H., & Copeland, W. C. (2018). Single-molecule DREEM imaging reveals DNA wrapping around human mitochondrial single-stranded DNA binding protein. *Nucleic Acids Research*, *46*(21), 11287–11302. https://doi.org/10.1093/nar/gky875

Kaur, P., Longley, M. J., Pan, H., Wang, W., Countryman, P., Wang, H., & Copeland, W. C. (2020). Single-molecule level structural dynamics of DNA unwinding by human mitochondrial Twinkle helicase. *Journal of Biological Chemistry*, *295*(17), 5564–5576. https://doi.org/10.1074/jbc.RA120.012795

King, G. A., Hashemi Shabestari, M., Taris, K. K. H., Pandey, A. K., Venkatesh, S., Thilagavathi, J., Singh, K., Krishna Koppisetti, R., Temiakov, D., Roos, W. H., Suzuki, C. K., & Wuite, G. J. L. (2018). Acetylation and phosphorylation of human TFAM regulate TFAM-DNA interactions via contrasting mechanisms. *Nucleic Acids Research*, *46*(7), 3633–3642. https://doi.org/10.1093/nar/gky204

Korhonen, J. A., Gaspari, M., & Falkenberg, M. (2003). TWINKLE has 5′ → 3′ DNA helicase activity and is specifically stimulated by mitochondrial single-stranded DNA-binding protein. *Journal of Biological Chemistry*, *278*(49), 48627–48632. https://doi.org/10.1074/jbc.M306981200

Korhonen, J. A., Pande, V., Holmlund, T., Farge, G., Pham, X. H., Nilsson, L., & Falkenberg, M. (2008). Structure-Function Defects of the TWINKLE Linker Region in Progressive External Ophthalmoplegia. *Journal of Molecular Biology*, *377*(3), 691–705. https://doi.org/10.1016/j.jmb.2008.01.035

Kovari, D. T., Yan, Y., Finzi, L., & Dunlap, D. (2018). Tethered particle motion: An easy technique for probing DNA topology and interactions with transcription factors. In *Methods in Molecular Biology* (Vol. 1665, pp. 317–340). Humana Press Inc. https://doi.org/10.1007/978-1-4939-7271-5_17

Kozlov, A. G., Shinn, M. K., Weiland, E. A., & Lohman, T. M. (2017). Glutamate promotes SSB protein-protein Interactions via intrinsically disordered regions. *Journal of Molecular Biology*, *429*(18), 2790–2801. https://doi.org/10.1016/j.jmb.2017.07.021.Glutamate

Kukat, C., Davies, K. M., Wurm, C. A., Spåhr, H., Bonekamp, N. A., Kühl, I., Joos, F., Polosa, P. L., Park, C. B., Posse, V., Falkenberg, M., Jakobs, S., Kühlbrandt, W., & Larsson, N. G. (2015). Cross-strand binding of TFAM to a single mtDNA molecule forms the mitochondrial nucleoid. *Proceedings of the National Academy of Sciences of the United States of America*, *112*(36), 11288–11293. https://doi.org/10.1073/pnas.1512131112

Kukat, C., Wurm, C. A., Spåhr, H., Falkenberg, M., Larsson, N. G., & Jakobs, S. (2011). Super-resolution microscopy reveals that mammalian mitochondrial nucleoids have a uniform size and frequently contain a single copy of mtDNA. *Proceedings of the National Academy of Sciences of the United States of America*, *108*(33), 13534–13539. https://doi.org/10.1073/pnas.1109263108

Kullar, P. J., Gomez-Duran, A., Gammage, P. A., Garone, C., Minczuk, M., Golder, Z., Wilson, J., Montoya, J., Häkli, S., Kärppä, M., Horvath, R., Majamaa, K., & Chinnery, P. F. (2018). Heterozygous SSBP1 start loss mutation co-segregates with hearing loss and the m.1555A>G mtDNA variant in a large multigenerational family. *Brain*, *141*(1), 55–62. https://doi.org/10.1093/brain/awx295

Kyung Suk Lee, Amanda B. Marciel, Alexander G. Kozlov, Charles M. Schroeder, Timothy M. Lohman, and Taekjip Ha. (2008). Ultrafast Redistribution of E. coli SSB Along Long Single- Stranded DNA via Intersegment Transfer. *J Mol Biol*, *23*(1), 1–7. https://doi.org/10.1016/j.jmb.2014.04.023.Ultrafast

Lakshmipathy, U., & Campbell, C. (1999). The Human DNA Ligase III Gene Encodes Nuclear and Mitochondrial Proteins. *Molecular and Cellular Biology*, *19*(5), 3869–3876. https://doi.org/10.1128/mcb.19.5.3869

Lee, H. S., Yun, C. H., Kim, H. M., & Lee, C. J. (2007). Persistence length of multiwalled carbon nanotubes with static bending. *Journal of Physical Chemistry C*, *111*(51), 18882–18887. https://doi.org/10.1021/jp075062r

Lee, H., Lee, S., Baek, G., Kim, A., Kang, B. C., Seo, H., & Kim, J. S. (2021). Mitochondrial DNA editing in mice with DddA-TALE fusion deaminases. *Nature Communications*, *12*(1), 10–15. https://doi.org/10.1038/s41467-021-21464-1

Le Dantec, Y., Baris, O., & Lenaers, G. (2022). OPA1 trans-splicing: A gene therapy approach to treat OPA1-related optic neuropathies. Acta Ophthalmologica, 100.

Lenaers, G., Hamel, C., Delettre, C., Amati-Bonneau, P., Procaccio, V., Bonneau, D., Reynier, P., & Milea, D. (2012). Dominant optic atrophy. *Orphanet Journal of Rare Diseases*, *7*(1), 1–12. https://doi.org/10.1186/1750-1172-7-46

Lin, S., Qin, L., Wuite, G. J. L., & Dame, R. T. (2018). Bacterial Chromatin: Methods and Protocols, Methods in Molecular Biology. *Methods in Molecular Biology*, *1837*, 177–197. https://doi.org/10.1007/978-1-4939-8675-0

Litonin, D., Sologub, M., Shi, Y., Savkina, M., Anikin, M., Falkenberg, M., Gustafsson, C. M., & Temiakov, D. (2010). Human mitochondrial transcription revisited: Only TFAM and TFB2M are required for transcription of the mitochondrial genes in vitro. *Journal of Biological Chemistry*, *285*(24), 18129–18133. https://doi.org/10.1074/jbc.C110.128918

Loeff, L., Kerssemakers, J. W. J., Joo, C., & Dekker, C. (2021). AutoStepfinder: A fast and automated step detection method for single-molecule analysis. *Patterns*, *2*(5), 100256. https://doi.org/10.1016/j.patter.2021.100256

Lohman, T. M., & Ferrari, M. E. (1994). ESCHERICHIA COLI SINGLE STRANDED DNA-BINDING PROTEIN : Multiple Cooperati vities identified in bacteria [Serratia marcescens SSB (1 6)], conjugative bacterial. *Proteins*.

Lu, B., Lee, J., Nie, X., Li, M., Morozov, Y. I., Venkatesh, S., Bogenhagen, D. F., Temiakov, D., & Suzuki, C. K. (2013). Phosphorylation of Human TFAM in Mitochondria Impairs DNA Binding and Promotes Degradation by the AAA+ Lon Protease. *Molecular Cell*, *49*(1), 121–132. https://doi.org/10.1016/j.molcel.2012.10.023

Ma, C. ., Steinfeld, J. ., & Greene, E. . (2017). Single-Stranded DNA Curtains for Studying Homologous Recombination. *Methods in Enzymology*, *582*, 193–219. https://doi.org/10.1016/bs.mie.2016.08.005.Single-Stranded

Malarkey, C. S., & Churchill, M. E. . (2012). The high mobility group box: the ultimate utility player of a cell. *Trends in Biochemical Sciences*, *37*(12), 553–562. https://doi.org/10.4049/jimmunol.1801473.The

Matic, S., Jiang, M., Nicholls, T. J., Uhler, J. P., Dirksen-Schwanenland, C., Polosa, P. L., Simard, M. L., Li, X., Atanassov, I., Rackham, O., Filipovska, A., Stewart, J. B., Falkenberg, M., Larsson, N. G., & Milenkovic, D. (2018). Mice lacking the mitochondrial exonuclease MGME1 accumulate mtDNA deletions without developing progeria. *Nature Communications*, *9*(1). https://doi.org/10.1038/s41467-018-03552-x

Matsushima, Y., Goto, Y. I., & Kaguni, L. S. (2010). Mitochondrial Lon protease regulates mitochondrial DNA copy number and transcription by selective degradation of mitochondrial transcription factor A (TFAM). *Proceedings of the National Academy of Sciences of the United States of America*, *107*(43), 18410–18415. https://doi.org/10.1073/pnas.1008924107

McGhee, J., & von Hippel, P. H. (1974). Theoretical Aspects of DNA-Protein Interactions : Co-operative and Non-co-operative Binding of Large Ligands to a One-dimensional Homogeneous Lattice. *Journal of Molecular Biology*, *86*, 469–489. https://doi.org/10.1007/bfb0017199

Mehmedović, M., Martucci, M., Spåhr, H., Ishak, L., Mishra, A., Sanchez-Sandoval, M. E., Pardo-Hernández, C., Peter, B., van den Wildenberg, S. M., Falkenberg, M., & Farge, G. (2022). Disease causing mutation (P178L) in mitochondrial transcription factor A results in impaired mitochondrial transcription initiation. *Biochimica et Biophysica Acta - Molecular Basis of Disease*, *1868*(10). https://doi.org/10.1016/j.bbadis.2022.166467

Meyer, J. N., Leuthner, T. C., & Luz, A. L. (2017). Mitochondrial fusion, fission, and mitochondrial toxicity. *Toxicology*, *391*(March), 42–53. https://doi.org/10.1016/j.tox.2017.07.019

Meyerson, C., Van Stavern, G., & McClelland, C. (2015). Leber hereditary optic neuropathy: Current perspectives. *Clinical Ophthalmology*, *9*, 1165–1176. https://doi.org/10.2147/OPTH.S62021

Mills, M., Harami, G. M., Seol, Y., Gyimesi, M., Martina, M., Kovács, Z. J., Kovács, M., & Neuman, K. C. (2017). RecQ helicase triggers a binding mode change in the SSB–DNA complex to efficiently initiate DNA unwinding. *Nucleic Acids Research*, *45*(20), 11878–11890. https://doi.org/10.1093/nar/gkx939

Miyakawa, I. (2017). Organization and dynamics of yeast mitochondrial nucleoids. *Proceedings of the Japan Academy Series B: Physical and Biological Sciences*, *93*(5), 339–359. https://doi.org/10.2183/pjab.93.021

Modesti, M. (2011). Fluorescent Labeling of proteins. *Methods in Molecular Biology*, *783*, 101–120. https://doi.org/10.1007/978-1-4939-7271-5

Moraes, C. T., Ricci, E., Bonilla, E., DiMauro, S., & Schon, E. A. (1992). The mitochondrial tRNA(Leu(UUR)) mutation in mitochondrial encephalomyopathy, lactic acidosis, and strokelike episodes (MELAS): Genetic, biochemical, and morphological correlations in skeletal muscle. *American Journal of Human Genetics*, *50*(5), 934–949.

Moretton, A., Morel, F., Macao, B., Lachaume, P., Ishak, L., Lefebvre, M., Garreau-Balandier, I., Vernet, P., Falkenberg, M., & Farge, G. (2017). Selective mitochondrial DNA degradation following double-strand breaks. *PLoS ONE*, *12*(4), 1–17. https://doi.org/10.1371/journal.pone.0176795

Morfill, J., Blank, K., Zahnd, C., Luginbühl, B., Kühner, F., Gottschalk, K. E., Plückthun, A., & Gaub, H. E. (2007). Affinity-matured recombinant antibody fragments analyzed by single-molecule force spectroscopy. *Biophysical Journal*, *93*(10), 3583–3590. https://doi.org/10.1529/biophysj.107.112532

Morin, J. A., Cao, F. J., Lázaro, J. M., Arias-Gonzalez, J. R., Valpuesta, J. M., Carrascosa, J. L., Salas, M., & Ibarra, B. (2012). Active DNA unwinding dynamics during processive DNA replication. *Proceedings of the National Academy of Sciences of the United States of America*, *109*(21), 8115–8120. https://doi.org/10.1073/pnas.1204759109

Morin, J. A., Cerrón, F., Jarillo, J., Beltran-Heredia, E., Ciesielski, G. L., Arias-Gonzalez, J. R., Kaguni, L. S., Cao, F. J., & Ibarra, B. (2017). DNA synthesis determines the binding mode of the human mitochondrial single-stranded DNA-binding protein. *Nucleic Acids Research*, *45*(12), 7237–7248. https://doi.org/10.1093/nar/gkx395

Murzin, A. G. (1993). OB(oligonucleotide/oligosaccharide binding)-fold: Common structural and functional solution for non-homologous sequences. *EMBO Journal*, *12*(3), 861–867. https://doi.org/10.1002/j.1460-2075.1993.tb05726.x

NASS, M. M., & NASS, S. (1963). Intramitochondrial Fibers With Dna Characteristics. I. Fixation and Electron Staining Reactions. *The Journal of Cell Biology*, *19*, 593–611. https://doi.org/10.1083/jcb.19.3.593

Naufer, M. N., Morse, M., Möller, G. B., McIsaac, J., Rouzina, I., Beuning, P. J., & Williams, M. C. (2021). Multiprotein E. coli SSB-ssDNA complex shows both stable binding and rapid dissociation due to interprotein interactions. *Nucleic Acids Research*, *49*(3), 1532–1549. https://doi.org/10.1093/nar/gkaa1267

Ngo, H. B., Kaiser, J. T., & Chan, D. C. (2011). The mitochondrial transcription and packaging factor Tfam imposes a U-turn on mitochondrial DNA. *Nature Structural and Molecular Biology*, *18*(11), 1290–1296. https://doi.org/10.1038/nsmb.2159

Ngo, H. B., Lovely, G. A., Phillips, R., & Chan, D. C. (2014). Distinct structural features of TFAM drive mitochondrial DNA packaging versus transcriptional activation. *Nature Communications*, *5*(1), 3077. https://doi.org/10.1038/ncomms4077.Distinct

Nguyen, B., Sokoloski, J., Galletto, R., Elson, E. L., Wold, M. S., & Lohman, T. M. (2014). Diffusion of human Replication Protein A along single stranded DNA. *Journal of Molecular Biology*, *426*(19), 3246–3261. https://doi.org/10.1016/j.jmb.2014.07.014.Diffusion

Nicholls, T. J., & Minczuk, M. (2014). In D-loop: 40 years of mitochondrial 7S DNA. *Experimental Gerontology*, *56*(September), 175–181. https://doi.org/10.1016/j.exger.2014.03.027

Nicholls, T. J., Nadalutti, C. A., Motori, E., Sommerville, E. W., Gorman, G. S., Basu, S., Hoberg, E., Turnbull, D. M., Chinnery, P. F., Larsson, N. G., Larsson, E., Falkenberg, M., Taylor, R. W., Griffith, J.

D., & Gustafsson, C. M. (2018). Topoisomerase 3α Is Required for Decatenation and Segregation of Human mtDNA. *Molecular Cell*, *69*(1), 9-23.e6. https://doi.org/10.1016/j.molcel.2017.11.033

Nicholls, T. J., Zsurka, G., Peeva, V., Schöler, S., Szczesny, R. J., Cysewski, D., Reyes, A., Kornblum, C., Sciacco, M., Moggio, M., Dziembowski, A., Kunz, W. S., & Minczuk, M. (2014). Linear mtDNA fragments and unusual mtDNA rearrangements associated with pathological deficiency of MGME1 exonuclease. *Human Molecular Genetics*, *23*(23), 6147–6162. https://doi.org/10.1093/hmg/ddu336

Nissanka, N., Bacman, S. R., Plastini, M. J., & Moraes, C. T. (2018). The mitochondrial DNA polymerase gamma degrades linear DNA fragments precluding the formation of deletions. *Nature Communications*, *9*(1). https://doi.org/10.1038/s41467-018-04895-1

Nissanka, N., Minczuk, M., & Moraes, C. T. (2019). Mechanisms of Mitochondrial DNA Deletion Formation. *Trends in Genetics*, *35*(3), 235–244. https://doi.org/10.1016/j.tig.2019.01.001

Nunnari, J., & Suomalainen, A. (2012). Mitochondria: In sickness and in health. *Cell*, *148*(6), 1145–1159. https://doi.org/10.1016/j.cell.2012.02.035.Mitochondria

Odijk, T. (1995). Stiff Chains and Filaments under Tension. *Macromolecules*, *28*(20), 7016–7018. https://doi.org/10.1021/ma00124a044

Omura, T. (1998). Mitochondria-Targeting Recognized at All Steps Sequence , of Protein a Multi-Role Import into Sorting Sequence Mitochondria The intracellular sorting of newly synthesized precursor proteins (preproteins) to mito chondria depends on the " mitoc. *J Biochem*, *123*, 1010–1016.

PALADE, G. E. (1953). An electron microscope study of the mitochondrial structure. *Journal of Histochemistry & Cytochemistry*, *1*(22), 188–211. http://jhc.sagepub.com/content/1/4/188.short

Peeva, V., Blei, D., Trombly, G., Corsi, S., Szukszto, M. J., Rebelo-Guiomar, P., Gammage, P. A., Kudin, A. P., Becker, C., Altmüller, J., Minczuk, M., Zsurka, G., & Kunz, W. S. (2018). Linear mitochondrial DNA is rapidly degraded by components of the replication machinery. *Nature Communications*, *9*(1), 1–11. https://doi.org/10.1038/s41467-018-04131-w

Piro-Mégy, C., Sarzi, E., Tarrés-Solé, A., Péquignot, M., Hensen, F., Quilès, M., Manes, G., Chakraborty, A., Sénéchal, A., Bocquet, B., Cazevieille, C., Roubertie, A., Müller, A., Charif, M., Goudenège, D., Lenaers, G., Wilhelm, H., Kellner, U., Weisschuh, N., … Delettre, C. (2020). Dominant mutations in mtDNA maintenance gene SSBP1 cause optic atrophy and foveopathy. *Journal of Clinical Investigation*, *130*(1), 143–156. https://doi.org/10.1172/JCI128513

Plaza-G.a, I., Lemishko, K. M., Crespo, R., Truong, T. Q., Kaguni, L. S., Cao-García, F. J., Ciesielski, G. L., & Ibarra, B. (2023). Mechanism of strand displacement DNA synthesis by the coordinated activities of human mitochondrial DNA polymerase and SSB. *Nucleic Acids Research*, *51*(4), 1750–1765. https://doi.org/10.1093/nar/gkad037

Posse, V., Al-Behadili, A., Uhler, J. P., Clausen, A. R., Reyes, A., Zeviani, M., Falkenberg, M., & Gustafsson, C. M. (2019). RNase H1 directs origin-specific initiation of DNA replication in human mitochondria. *PLoS Genetics*, *15*(1), 1–20. https://doi.org/10.1371/journal.pgen.1007781

Posse, V., Shahzad, S., Falkenberg, M., Hällberg, B. M., & Gustafsson, C. M. (2015). TEFM is a potent stimulator of mitochondrial transcription elongation in vitro. *Nucleic Acids Research*, *43*(5), 2615–2624. https://doi.org/10.1093/nar/gkv105

Prakash, A., & Doublié, S. (2015). Base Excision Repair in the Mitochondria. *Journal of Cellular Biochemistry*, *116*(8), 1490–1499. https://doi.org/10.1002/jcb.25103

Qi, Z., & Greene, E. C. (2016). Visualizing recombination intermediates with single-stranded DNA curtains. *Methods*, *105*, 62–74.

Qian, H., Sheetz, M. P., & Elson, E. L. (1991). Single particle tracking. Analysis of diffusion and flow in two-dimensional systems. *Biophysical Journal*, *60*(4), 910–921. https://doi.org/10.1016/S0006-3495(91)82125-7

Qian, Y., & Johnson, K. A. (2017). The human mitochondrial single-stranded DNA-binding protein displays distinct kinetics and thermodynamics of DNA binding and exchange. *Journal of Biological Chemistry*, *292*(31), 13068–13084. https://doi.org/10.1074/jbc.M117.791392

RAGHUNATHAN, S., RICARD, C. S., LOHMAN, T. M., & WAKSMAN, G. (1997). Crystal structure of the homo-tetrameric DNA binding domain of Escherichia coli single-stranded DNA-binding protein determined by multiwavelength x-ray diffraction on the selenomethionyl protein at 2.9-Å resolution. *The National Academy of Sciences*, *94*, 6652–6657.

Rashighi, M., & Harris, J. E. (2017). A Novel Processive Mechanism for DNA Synthesis Revealed by Structure, Modeling and Mutagenesis of the Accessory Subunit of Human Mitochondrial DNA Polymerase. *Physiology & Behavior*, *176*(3), 139–148. https://doi.org/10.1053/j.gastro.2016.08.014.CagY

Ravichandran, V., Vasquez, G. B., Srivastava, S., Verma, M., Petricoin, E., Lubell, J., Sriram, R. D., Barker, P. E., & Gilliland, G. L. (2004). Data standards for proteomics: Mitochondrial two-dimensional polyacrylamide gel electrophoresis data as a model system. *Mitochondrion*, *3*(6), 327–336. https://doi.org/10.1016/j.mito.2004.02.006

Reyes, A., Kazak, L., Wood, S. R., Yasukawa, T., Jacobs, H. T., & Holt, I. J. (2013). Mitochondrial DNA replication proceeds via a “bootlace” mechanism involving the incorporation of processed transcripts. *Nucleic Acids Research*, *41*(11), 5837–5850. https://doi.org/10.1093/nar/gkt196

Ringel, R., Sologub, M., Morozov, Y. I., Litonin, D., Cramer, P., & Temiakov, D. (2011). Structure of human mitochondrial RNA polymerase. *Nature*, *478*(7368), 269–273. https://doi.org/10.1038/nature10435

Robberson, D. L., Kasamatsu, H., & Vinograd, J. (1972). Replication of mitochondrial DNA. Circular replicative intermediates in mouse L cells. *Proceedings of the National Academy of Sciences of the United States of America*, *69*(3), 737–741. https://doi.org/10.1073/pnas.69.3.737

Roger, A. J., Muñoz-Gómez, S. A., & Kamikawa, R. (2017). The Origin and Diversification of Mitochondria. *Current Biology*, *27*(21), R1177–R1192. https://doi.org/10.1016/j.cub.2017.09.015

Rossmanith, W., & Karwan, R. M. (1998). Impairment of tRNA processing by point mutations in mitochondrial tRNALeu(UUR) associated with mitochondrial diseases. *FEBS Letters*, *433*(3), 269–274. https://doi.org/10.1016/S0014-5793(98)00928-4

Rousso, I., & Deshpande, A. (2022). Applications of Atomic Force Microscopy in HIV-1 Research. *Viruses*, *14*(3), 1–14. https://doi.org/10.3390/v14030648

Roy, R., Kozlov, A. G., Lohman, T. M., Ha, T., Biology, C., & Biophysics, M. (2010). SSB diffusion on single stranded DNA stimulates RecA filament formation. *Nature*, *461*(7267), 1092–1097. https://doi.org/10.1038/nature08442.SSB

Rubey, W. W. (1951). Geologic history of sea water: an attempt to state the problem. Geological Society of America Bulletin, 62(9), 1111-1148.

Rubio-Cosials, A., Sidow, J. F., Jiménez-Menéndez, N., Fernández-Millán, P., Montoya, J., Jacobs, H. T., Coll, M., Bernadó, P., & Solà, M. (2011). Human mitochondrial transcription factor A induces a U-turn structure in the light strand promoter. *Nature Structural and Molecular Biology*, *18*(11), 1281–1289. https://doi.org/10.1038/nsmb.2160

Ruhanen, H., Borrie, S., Szabadkai, G., Tyynismaa, H., Jones, A. W. E., Kang, D., Taanman, J. W., & Yasukawa, T. (2010). Mitochondrial single-stranded DNA binding protein is required for maintenance of mitochondrial DNA and 7S DNA but is not required for mitochondrial nucleoid organisation. *Biochimica et Biophysica Acta - Molecular Cell Research*, *1803*(8), 931–939. https://doi.org/10.1016/j.bbamcr.2010.04.008

Russell, O. M., Gorman, G. S., Lightowlers, R. N., & Turnbull, D. M. (2020). Mitochondrial Diseases: Hope for the Future. *Cell*, *181*(1), 168–188. https://doi.org/10.1016/j.cell.2020.02.051

Sbalzarini, I. F., & Koumoutsakos, P. (2005). Feature point tracking and trajectory analysis for video imaging in cell biology. *Journal of Structural Biology*, *151*(2), 182–195. https://doi.org/10.1016/j.jsb.2005.06.002

Sbalzarini, I. F., & Koumoutsakos, P. (2005). Feature point tracking and trajectory analysis for video imaging in cell biology. *Journal of Structural Biology*, *151*(2), 182–195. https://doi.org/10.1016/j.jsb.2005.06.002

Schubert, M. B., & Vilarinho, L. (2020). Molecular basis of Leigh syndrome: A current look. *Orphanet Journal of Rare Diseases*, *15*(1), 1–14. https://doi.org/10.1186/s13023-020-1297-9

Schwinghammer, K., C.M. Cheung, A., I. Morozov, Y., Agaronyan, K., Temiakov, D., & Cramer, P. (2013). Structure of human mitochondrial RNA polymerase elongation complex. *Nature Structural & Molecular Biology*, *20*(11), 1298–1303. https://doi.org/10.1038/nsmb.2683.Structure

Shi, Y., Posse, V., Zhu, X., Hyvärinen, A. K., Jacobs, H. T., Falkenberg, M., & Gustafsson, C. M. (2016). Mitochondrial transcription termination factor 1 directs polar replication fork pausing. *Nucleic Acids Research*, *44*(12), 5732–5742. https://doi.org/10.1093/nar/gkw302

Shutt, T. E., & Gray, M. W. (2006). Bacteriophage origins of mitochondrial replication and transcription proteins. *Trends in Genetics*, *22*(2), 90–95. https://doi.org/10.1016/j.tig.2005.11.007

Silverstein, T. D., Gibb, B., & Greene, E. C. (2014). Visualizing Protein Movement on DNA at the Single-molecule Level using DNA Curtains. *DNA Repair*, *20*, 94–109. https://doi.org/10.1016/j.dnarep.2014.02.004.Visualizing

Sitters, G., Kamsma, D., Thalhammer, G., Ritsch-Marte, M., Peterman, E. J. G., & Wuite, G. J. L. (2014). Acoustic force spectroscopy. *Nature Methods*, *12*(1), 47–50. https://doi.org/10.1038/nmeth.3183

Sjöstrand, F. S. (1953). Electron microscopy of mitochondria and cytoplasmic double membranes: ultra-structure of rod-shaped mitochondria. Nature, 171(4340), 30-31

Smith, S. B., Cui, Y., & Bustamante, C. (1996). Overstretching B-DNA: The elastic response of individual double-stranded and single-stranded DNA molecules. *Science*, *271*(5250), 795–799. https://doi.org/10.1126/science.271.5250.795

Sokoloski, J. E., Kozlov, A. G., Galletto, R., & Lohman, T. M. (2016). Chemo-mechanical pushing of proteins along single-stranded DNA. *Proceedings of the National Academy of Sciences of the United States of America*, *113*(22), 6194–6199. https://doi.org/10.1073/pnas.1602878113

Spinazzola, A. (2011). Mitochondrial DNA mutations and depletion in pediatric medicine. *Seminars in Fetal and Neonatal Medicine*, *16*(4), 190–196. https://doi.org/10.1016/j.siny.2011.04.011

Stein, A., Kalifa, L., & Sia, E. A. (2015). Members of the RAD52 Epistasis Group Contribute to Mitochondrial Homologous Recombination and Double-Strand Break Repair in Saccharomyces cerevisiae. *PLoS Genetics*, *11*(11), 1–20. https://doi.org/10.1371/journal.pgen.1005664

Stiles, A. R., Simon, M. T., Stover, A., Eftekharian, S., Khanlou, N., Wang, H. L., Magaki, S., Lee, H., Partynski, K., Dorrani, N., Chang, R., Martinez-Agosto, J. A., & Abdenur, J. E. (2016). Mutations in TFAM, encoding mitochondrial transcription factor A, cause neonatal liver failure associated with mtDNA depletion. *Molecular Genetics and Metabolism*, *119*(1–2), 91–99. https://doi.org/10.1016/j.ymgme.2016.07.001

Suksombat, S., Khafizov, R., Kozlov, A. G., Lohman, T. M., & Chemla, Y. R. (2015). Structural dynamics of E. Coli singlestranded DNA binding protein reveal DNA wrapping and unwrapping pathways. *ELife*, *4*(AUGUST2015), 1–23. https://doi.org/10.7554/eLife.08193

Takahashi, S., Oshige, M., & Katsura, S. (2021). DNA manipulation and single-molecule imaging. *Molecules*, *26*(4), 1–28. https://doi.org/10.3390/molecules26041050

Tan, B. G., Mutti, C. D., Shi, Y., Xie, X., Zhu, X., Silva-Pinheiro, P., Menger, K. E., Díaz-Maldonado, H., Wei, W., Nicholls, T. J., Chinnery, P. F., Minczuk, M., Falkenberg, M., & Gustafsson, C. M. (2022). The human mitochondrial genome contains a second light strand promoter. *Molecular Cell*, *82*(19), 3646-3660.e9. https://doi.org/10.1016/j.molcel.2022.08.011

Tang, J. X., Thompson, K., Taylor, R. W., & Oláhová, M. (2020). Mitochondrial OXPHOS biogenesis: Co-regulation of protein synthesis, import, and assembly pathways. *International Journal of Molecular Sciences*, *21*(11), 1–32. https://doi.org/10.3390/ijms21113820

Terzioglu, M., Ruzzenente, B., Harmel, J., Mourier, A., Jemt, E., López, M. D., Kukat, C., Stewart, J. B., Wibom, R., Meharg, C., Habermann, B., Falkenberg, M., Gustafsson, C. M., Park, C. B., & Larsson, N. G. (2013). MTERF1 Binds mtDNA to prevent transcriptional interference at the light-strand promoter but is dispensable for rRNA gene transcription regulation. *Cell Metabolism*, *17*(4), 618–626. https://doi.org/10.1016/j.cmet.2013.03.006

Tiranti, V., Rossi, E., Ruiz-Carrillo, A., Rossi, G., Rocchi, M., Didonato, S., Zuffardi, O., & Zeviani, M. (1995). Chromosomal localization of mitochondrial transcription factor A (TCF6), single-stranded DNA-binding protein (SSBP), and Endonuclease G (ENDOG), three human housekeeping genes involved in mitochondrial biogenesis. *Genomics*, *25*(2), 559–564. https://doi.org/10.1016/0888-7543(95)80058-T

Tomáška, L., Nosek, J., & Kucejová, B. (2001). Mitochondrial single-stranded DNA-binding proteins: In search for new functions. *Biological Chemistry*, *382*(2), 179–186. https://doi.org/10.1515/BC.2001.025

Uhler, J. P., Thörn, C., Nicholls, T. J., Matic, S., Milenkovic, D., Gustafsson, C. M., & Falkenberg, M. (2016). MGME1 processes flaps into ligatable nicks in concert with DNA polymerase γ during mtDNA replication. *Nucleic Acids Research*, *44*(12), 5861–5871. https://doi.org/10.1093/nar/gkw468

Ullah, F., Rauf, W., Khan, K., Khan, S., Bell, K. M., de Oliveira, V. C., Tariq, M., Bakhshalizadeh, S., Touraine, P., Katsanis, N., Sinclair, A., He, S., Tucker, E. J., Baig, S. M., & Davis, E. E. (2021). A recessive variant in TFAM causes mtDNA depletion associated with primary ovarian insufficiency, seizures, intellectual disability and hearing loss. *Human Genetics*, *140*(12), 1733–1751. https://doi.org/10.1007/s00439-021-02380-2

van den Wildenberg, Siet MJL and Prevo, Bram and Peterman, E. J. (2011). Single - protein motion on microtubules and in cell membranes. *Single Molecule Analysis*, 93–113.

Van Der Bliek, A. M., Sedensky, M. M., & Morgan, P. G. (2017). Cell biology of the mitochondrion. *Genetics*, *207*(3), 843–871. https://doi.org/10.1534/genetics.117.300262

Van Dyck, E., Foury, F., Stillman, B., & Brill, S. J. (1992). A single-stranded DNA binding protein required for mitochondrial DNA replication in S. cerevisiae is homologous to E. coli SSB. *EMBO Journal*, *11*(9), 3421–3430. https://doi.org/10.1002/j.1460-2075.1992.tb05421.x

Van Rosmalen, M. G. M., Kamsma, D., Biebricher, A. S., Li, C., Zlotnick, A., Roos, W. H., & Wuite, G. J. L. (2020). Revealing in real-time a multistep assembly mechanism for SV40 virus-like particles. *Science Advances*, *6*(16), 1–8. https://doi.org/10.1126/sciadv.aaz1639

Waldman, V. M., Weiland, E., Kozlov, A. G., & Lohman, T. M. (2016). Is a fully wrapped SSB-DNA complex essential for Escherichia coli survival? *Nucleic Acids Research*, *44*(9), 4317–4329. https://doi.org/10.1093/nar/gkw262

Wang, K. Z. Q., Zhu, J., Dagda, R. K., Uechi, G., Cherra, S. J., Gusdon, A. M., Balasubramani, M., & Chu, C. T. (2014). ERK-mediated phosphorylation of TFAM downregulates mitochondrial transcription: Implications for Parkinson's disease. *Mitochondrion*, *17*, 132–140. https://doi.org/10.1016/j.mito.2014.04.008

Wanrooij, P. H., Uhler, J. P., Shi, Y., Westerlund, F., Falkenberg, M., & Gustafsson, C. M. (2012). A hybrid G-quadruplex structure formed between RNA and DNA explains the extraordinary stability of the mitochondrial R-loop. *Nucleic Acids Research*, *40*(20), 10334–10344. https://doi.org/10.1093/nar/gks802

Wanrooij, S., Fusté, J. M., Farge, G., Shi, Y., Gustafsson, C. M., & Falkenberg, M. (2008). Human mitochondrial RNA polymerase primes lagging-strand DNA synthesis in vitro. *Proceedings of the National Academy of Sciences of the United States of America*, *105*(32), 11122–11127. https://doi.org/10.1073/pnas.0805399105

Wanrooij, S., Goffart, S., Pohjoismäki, J. L. O., Yasukawa, T., & Spelbrink, J. N. (2007). Expression of catalytic mutants of the mtDNA helicase Twinkle and polymerase POLG causes distinct replication stalling phenotypes. *Nucleic Acids Research*, *35*(10), 3238–3251. https://doi.org/10.1093/nar/gkm215

Webster, G., Genschel, J., Curth, U., Urbanke, C., Kang, C. H., & Hilgenfeld, R. (1997). A common core for binding single-stranded DNA: Structural comparison of the single-stranded DNA-binding proteins (SSB) from E. coli and human mitochondria. *FEBS Letters*, *411*(2–3), 313–316. https://doi.org/10.1016/S0014-5793(97)00747-3

Wessel, S. R., Marceau, A. H., Massoni, S. C., Zhou, R., Ha, T., Sandler, S. J., & Keck, J. L. (2013). PriC-mediated DNA replication restart requires PriC complex formation with the single-stranded DNA-binding protein. *Journal of Biological Chemistry*, *288*(24), 17569–17578. https://doi.org/10.1074/jbc.M113.478156

Wiedemann, N., & Pfanner, N. (2017). Mitochondrial machineries for protein import and assembly. *Annual Review of Biochemistry*, *86*, 685–714. https://doi.org/10.1146/annurev-biochem-060815-014352

Wong, T. S., Rajagopalan, S., Townsley, F. M., Freund, S. M., Petrovich, M., Loakes, D., & Fersht, A. R. (2009). Physical and functional interactions between human mitochondrial single-stranded DNA-binding protein and tumour suppressor p53. *Nucleic Acids Research*, *37*(2), 568–581. https://doi.org/10.1093/nar/gkn974

Wu, Y., Lu, J., & Kang, T. (2016). Human single-stranded DNA binding proteins: Guardians of genome stability. *Acta Biochimica et Biophysica Sinica*, *48*(7), 671–677. https://doi.org/10.1093/abbs/gmw044

Xu, L., Cabanas-dan, J., Halma, M. T. J., Heller, I., Stratmann, S. A., Oijen, A. M. Van, Lee, S., Peterman, E. J. G., & Wuite, G. J. L. (2023). Regulation of T7 gp2 . 5 binding dynamics by its C-terminal tail , template conformation and sequence. *Nucleic Acids Research*, *51*(13), 6540–6553.

Xu, L., Halma, M. T. J., & Wuite, G. J. L. (2023). Unravelling How Single-Stranded DNA Binding Protein Coordinates DNA Metabolism Using Single-Molecule Approaches. *International Journal of Molecular Sciences*, *24*(3). https://doi.org/10.3390/ijms24032806

Yang, C., Curth, U., Urbanke, C., & Kang, C. (1997). Crystal structure of human mitochondrial single-stranded DNA binding protein at 2.4 A resolution. *Nature*, *4*(2), 153–157.

Yang, Y., & Walsh, C. E. (2005). Spliceosome-mediated RNA trans-splicing. *Molecular Therapy*, *12*(6), 1006–1012. https://doi.org/10.1016/j.ymthe.2005.09.006

Yasukawa, T., Reyes, A., Cluett, T. J., Yang, M. Y., Bowmaker, M., Jacobs, H. T., & Holt, I. J. (2006). Replication of vertebrate mitochondrial DNA entails transient ribonucleotide incorporation throughout the lagging strand. *EMBO Journal*, *25*(22), 5358–5371. https://doi.org/10.1038/sj.emboj.7601392

Yildiz, A., & Selvin, P. R. (2005). Fluorescence imaging with one nanometer accuracy: Application to molecular motors. *Accounts of Chemical Research*, *38*(7), 574–582. https://doi.org/10.1021/ar040136s

Yin, Y. W., & Steitz, T. A. (2002). Structural basis for the transition from initiation to elongation transcription in T7 RNA polymerase. *Science*, *298*(5597), 1387–1395. https://doi.org/10.1126/science.1077464

Young, M. J., Longley, M. J., Li, F. Y., Kasiviswanathan, R., Wong, L. J., & Copeland, W. C. (2011). Biochemical analysis of human POLG2 variants associated with mitochondrial disease. *Human Molecular Genetics*, *20*(15), 3052–3066. https://doi.org/10.1093/hmg/ddr209

Yu, H., Xue, C., Long, M., Jia, H., Xue, G., Du, S., Coello, Y., & Ishibashi, T. (2018). TEFM Enhances Transcription Elongation by Modifying mtRNAP Pausing Dynamics. *Biophysical Journal*, *115*(12), 2295–2300. https://doi.org/10.1016/j.bpj.2018.11.004

Zhou, R., Kozlov, A. G., Roy, R., Zhang, J., Korolev, S., Lohman, T. M., & Ha, T. (2011). SSB functions as a sliding platform that migrates on DNA via reptation. *Cell*, *146*(2), 222–232. https://doi.org/10.1016/j.cell.2011.06.036

Zhu, X., Xie, X., Das, H., Tan, B. G., Shi, Y., Al-Behadili, A., Peter, B., Motori, E., Valenzuela, S., Posse, V., Gustafsson, C. M., Hällberg, B. M., & Falkenberg, M. (2022). Non-coding 7S RNA inhibits transcription via mitochondrial RNA polymerase dimerization. *Cell*, *185*(13), 2309-2323.e24. https://doi.org/10.1016/j.cell.2022.05.006

Web source: https://www.britannica.com/science/cell-biology/Regulation-of-RNA-after-synthesis

Abstract

Mitochondria are organelles within eukaryotic cells that are essential to produce energy by the oxidative phosphorylation process, that synthesises ATP required for metabolism reactions. Mitochondria possess their own genome of 16,5 kb of which its replication and expression are independent of the nucleus and which is permanently bound with proteins, forming a nucleoprotein structure called nucleoid. Among these proteins, some are found to form a core component of the mitochondrial nucleoids and have been well characterised such as the polymerase POLγ, the helicase TWINKLE, the RNA polymerase POLRMT, the mitochondrial transcription factor A TFAM or more recently the mitochondrial single stranded binding protein mtSSB. Mutations within these proteins greatly affect mtDNA integrity and copy number, leading to mtDNA deletion and depletion going with often severe diseases. With the development of DNA molecule manipulation techniques and fluorescence microscopy in the past two decades, single molecule methods have arisen and enable the understanding of DNA-protein interaction mechanisms at a single molecule level. In this thesis, we employed two single molecule techniques: the acoustic force spectroscopy (AFS) and the total internal reflection fluorescence microscopy (TIRFm) coupled with DNA fluid flow manipulation in order to give insight about the disease related mechanism of two mitochondrial maintenance protein variants involved in mitochondrial maintenance defect, namely TFAM P178L and mtSSB R107Q.

Résumé

Les mitochondries sont des organites présentes chez les cellules eucaryotes et sont essentielles à la production d'énergie via la phosphorylation oxydative, qui synthétise de l'ATP nécessaire aux réactions du métabolisme. Les mitochondries possèdent leur propre génome de 16,5 kb de long et dont la réplication et l'expression se font indépendamment du noyau et qui est associé en permanence avec des protéines, formant une structure nucléoprotéique appelée le nucléoide. Parmi ces protéines, certaines sont considérées comme étant des acteurs principaux du nucléoide mitochondrial et ont été étudiées en profondeur comme l'ADN polymérase POLγ, l'hélicase TWINKLE, l'ARN polymérase POLRMT, le facteur de transcription mitochondrial A TFAM et plus récemment la protéine de liaison à l'ADN mitochondrial simple brin SSB. Des mutations au sein de ces protéines altèrent grandement l'intégrité de l'ADN mitochondrial et le nombre de ses copies, entraînant des délétions au niveau de cet ADN ou une déplétion allant avec des pathologies souvent graves. Avec le développement de méthodes permettant la manipulation individuelle de molécules d'ADN ainsi que l'essor de la microscopie à fluorescence, des techniques dites "single molecule" ont émergées dans les vingt dernières années et ont permis la compréhension des mécanismes d'interaction ADN-protéines au niveau de la molécule. Dans cette thèse, nous avons utilisé deux single molecule techniques: la spectroscopie de force acoustique (AFS) et la microscopie à fluorescence par réflexion interne total (TIRFm) couplée avec la manipulation de molécules d'ADN par courant micro-fluidique dans le but d'étudier les mécanismes d'interaction avec l'ADN de deux variants à l'origine de défaillances dans la maintenance de l'ADNmt, à savoir TFAM P178L et mtSSB R107Q.